Development of Novel Optical Planar Waveguide-based Biosensors using a Nanotechnology Approach

Ali Madlool Al-Jawdah

A thesis submitted in partial fulfilment of the requirements of
Sheffield Hallam University
for the degree of Doctor of Philosophy

July 2019

DECLARATION

I hereby declare that:

1. I have not been enrolled for another award of the University, or other academic

or professional organisation, whilst undertaking my research degree.

2. None of the material contained in the thesis has been used in any other

submission for an academic award.

3. I am aware of and understand the University's policy on plagiarism and certify

that this thesis is my own work. The use of all published or other sou rces of

material consulted have been properly and fully acknowledged.

4. The work undertaken towards the thesis has been conducted in accordance with

the SHU Principles of Integrity in Research and the SHU Research Ethics Policy.

5. The word count of the thesis is 47,662.

Name	Ali Madlool Al-Jawdah
Date	July 2019
Award	PhD
Faculty	Science Technology and Art
Director(s) of Studies	Professor Alexie Nabok

To my parents and my sons

ABSTRACT

This work aims at the development of novel biosensor based on optical planar waveguide (OPW) for detection of mycotoxins, which are common contaminants in agriculture products (grains, beans, nuts, fruits) and associated food and feed. These low molecular weight toxins produced by various fungi species possess a substantial danger to human and animals, and thus are under strict legislated limits in sub-ppm (part per million) level. The detection of mycotoxins in such low concentrations is of great interest nowadays.

A novel detection principle of polarization interferometry (PI) exploited in this system (which can be considered as a logical continuation of ellipsometry) in based on tracking changes in the polarization state of a laser beam passing through the waveguide and affected by immobilized in the waveguide sensing window. The key element of this sensor is a planar optical waveguide consisting of 190 nm thick silicon nitride core layer sandwiched between two 3 μm thick layers of silicon dioxide; a sensing window was etched in the top silicon oxide layer to allow monitoring molecular adsorption. A 630 nm polarized light from a laser diode coupled through the slant edge of the waveguide experiences a large number of reflections (about 500 per mm) when propagating through the waveguide. The p- component of polarized light is affected by changes in refractive index in the sensing window, while s- component is less affected and thus serves as a reference. Therefore, the changes in either the medium refractive index or molecular adsorption cause the phase shift between p- and s- components. The observation of the light polarization state is enabled by a polarizer converting the changes in polarization to variations of light intensity which is then recoded with CCD linear array interfaced to PC. The refractive index sensitivity of the OPW PI sensor of about 1600 rad/RIU/mm (the highest value known for optical detection) was found by both the theoretical modelling and experimental testing.

The developed experimental set-up was used for detection of mycotoxins, i.e. aflatoxin B1 (AFT B1), ochratoxin A (OTA), and zearalenone (ZEN), in direct assay with two types of bio-receptors immobilized within the sensing window: (i) antibodies electrostatically bound onto silicon nitride surface via layers of poly-allylamine hydrochloride and protein A, or (ii) aptamers covalently bound via SH groups on aminated surface of silicon nitride. The outcome of such biosensing tests was successful; all three mycotoxins were detected in a wide concentration range from10 pg/ml up to 1 μg/ml in direct immunoassays with their respective antibodies. The use of specific aptamers as bioreceptors in the latest upgrade of the OPW PI set-up has resulted in much lower detected concentrations of AFT B1 and OTA down to 1pg/ml, with LDL estimated as 0.6 -0.7 pg/ml.

The obtained sensitivity in sub-ppt (part per trillion) level is the highest known for optical biosensors, and it is particularly remarkable for a label-free detection of low molecular weight analyte molecules in direct assay format. The developed OPW PI biosensor is universal and can be easily adapted for detection of different analyte molecules by choosing suitable bio-receptors. It can be used equally for detection of small and large molecules, and in different assay formats, e.g. direct, sandwich, and competitive assays, and therefore can be considered as a platform biosensing technology for a wide range of applications, i.e. environmental monitoring, security, agriculture and food industry, and biomedical.

ACKNOWLEDGEMENT

I would like to express my special appreciation and thanks to my supervisor Prof. Alexei Nabok for his guidance and advices. And for introducing me to the world of biosensing and nanotechnology by engage me to attend to a lot of international conferences. Furthermore, I would like to thank Prof. Jean-Louis Marty and Dr. Gaelle Catanante from Perpignan University for their cooperation and participation for the success of this project. Special thanks and gratitude to Mr. Ian in university workshop for his cooperation and assistance.

I would especially like to thank Babylon University for the award of the scholarship, and Iraqi Cultural Attache in London to facilitate all matters related to the study and make it possible.

Finally, I would like to thanks to all MERI administration staff due to their kindly cooperation and helping.

TABLE OF CONTENTS

LIST OF PUBLICATIONS OF THE CANDIDATE

1. Nabok, A., Al-Jawdah, A. M., & Tsargorodska, A. (2017). Development of planar waveguide-based immunosensor for detection of low molecular weight molecules such as mycotoxins. *Sensors and Actuators B: Chemical*, *247*, 975-980.
2. Al-Jawdah, A., Nabok, A., Jarrah, R., Holloway, A., Tsargorodska, A., Takacs, E., & Szekacs, A. (2018). Mycotoxin biosensor based on optical planar waveguide. *Toxins*, *10*(7), 272.
3. Nabok, A., Al-Rubaye, A. G., Al-Jawdah, A. M., Tsargorodska, A., Marty, J. L., Catanante, G., ... & Takacs, E. (2019). Novel optical biosensing technologies for detection of mycotoxins. *Optics & Laser Technology*, *109*, 212-221.
4. Alexei Nabok, Ali Al-Jawdah, Anna Tsargorodska, Development of planar waveguide-based immunosensor for detection of low molecular weight molecules such as mycotoxins. Conference on Optical Chemical Sensor and biosensor, Graz, Austria, march 20-23, 2016.
5. Ali Al-Jawdah, Alexei Nabok, Anna Tsargorodska, Development of polarization interferometer immunosensor based on planar waveguide, MERI Symposium 17th-18th May 2016 Sheffield Hallam University; 2016
6. Alexei Nabok, Ali Al-Jawda, Anna Tsargorodska, Development of planar waveguide-based immunosensor for detection of low molecular weight molecules such as mycotoxins, Sensors and Actuators B: Chemical.
7. Ali Al-Jawdah, Alexei Nabok, Alan Holloway, Anna Tsargorodska, Nanotech Middle East international conference, 4th - 6th December 2017, Dubai, U.A.E.
8. Ali Al-Jawdah, Alexei Nabok, Alan Holloway, and Anna Tsargorodska, Development of Polarization Interferometer Biosensor for Detection of Mycotoxins, SPIE European Conference on Optics and Optoelectronics, 23th - 27th April 2017 Prague, Czech Republic.

9. Ali Al-Jawdah, Alexei Nabok, Anna Tsargorodska, Development of optical planar waveguide biosensor for detection of mycotoxins, 5th International Conference on bio-Sensing Technology, 7th - 10th May 2017, Riva del Garda, Italy.
10. A. M. Al-Jawdah, A. Nabok, Radhyah Jarrah, A. Holloway, A. Tsargorodska, E. Takacs, A. Szekacs, Novel bio-sensing platform based on planar waveguide polarization interferometer: detection of mycotoxins, 25th - 28th March 2018, Naples, Italy.
11. A. Al-Jawdah, A. Nabok, R. Jarrah, A. Holloway, G. Catanant, Mycotoxins bio-sensing platform based on optical planar waveguide and Specific Aptamers. the 6th Nano Today Conference, 16-20 June 2019, Lisbon, Portugal.
12. A. Al-Jawdah, A. Nabok, R. Jarrah, A. Holloway, G. Catanant, Highly sensitive label-free detection of aflatoxin B1 using optical waveguide operating as polarization interferometer, Biotech France 2019 26-28 June 2019, Paris, France.

LIST OF FIGURES

LIST OF TABLES

LIST OF ABBREVIATIONS

AFT B1	Aflatoxin B1
BIMW	Bimodal Waveguide interferometer
CCD	Charge-coupled device
CVD	Chemical vapor deposition technology
DNA	Deoxyribonucleic acid
DNA	Deoxyribonucleic acid
DPI	Dual polarization interferometry
DTT	Dithiothreitol
EC	European Commission
EIA	Enzyme immunoassay assay
ELISA	Enzyme-linked immune-sorbent assay
EW	Electromagnetic wave
FBG	Fibre Bragg Grating
FBGS	Fibre Bragg grating sensors
FDA	US Food and Drug Administration
FFT	Fourier transform
FPIA	Fluorescence polarization immunoassay
GC	Gas chromatography
HI	Hartman interferometer
HPLC	High-performance liquid chromatography
HPLC-FD	High-performance liquid chromatography fluorescence detection
HPLC-UV	High-Performance Liquid Chromatography-Ultraviolet
IgG	Immunoglobulin (antibodies)
LbL	Layer-by-layer (LbL) deposition technique
LC	Liquid chromatography
LDL	Low detection limit
LED	Light emitting diode

LFD	Lateral flow device
LOD	Limit of detection
LPCVD	Low pressure chemical vapor deposition technology
LPGS	Long-period gratings sensors
LSPR	Local surface Plasmon Resonance
MIP	Molecular Inversion Probe
MS	Mass spectrometry technique
MZI	Mach-Zehnder Interferometer
NPs	Nano particles
OPW	optical planar waveguide
OPW PI	Optical planar waveguide polarization interferometry
OTA	Ochratoxin A
PAH	Polycyclic aromatic hydrocarbon
PBB	PBS binding buffer
PCR	Polymerase chain reaction
PEI	Polyetherimide
PI	polarization interferometry
ppb	Parts per billion
PS	Porous silicon
PSS	poly-sterylsulphonate sodium
PTFE	polytetrafluoroethylene
RF	Retention factor
RIS	Refractive index sensitivity
RIU	Refractive index unit
RNA	Ribonucleic acid
SELEX	Sequential Evolution of Ligands by Exponential Enrichment
SERS	Surface-enhanced Raman Spectroscopy
SH group	organosulfur compound
SMCC	4-(N-maleimidomethyl) cyclohexanecarboxylic acid)
SPR	Surface Plasmon Resonance
TE	Transverse electric TE mode

TIRE	Total internal reflection ellipsometry
TLC	Thin layer chromatography
TLC	Thin layer chromatography
TM	Transverse magmatic TE mode
UV	Ultraviolet light electromagnetic waves
WHO	The World Health Organization
YI	Young interferometer
ZEN	Zearalenone

LIST OF GREECE SYMBLES

k	wave vector
k_i	component of the incident light wave vector parallel to the interface
k_{sp}	wave vector of the surface plasmon mode
c	light speed
ε_i	dielectric functions of medium i
θ_i	Light incidence angle
n	Refractive index
I	Intensity of the light
λ	Light wavelength
χ	Electromagnetic field decay
φ_s	The phase of s- component of polarized light
φ_p	The phase of p- component of polarized light
Ψ	The ratio of the reflection amplitudes rp and rs of polarized light
Δ	Phase different between s ,p components of polarized light
Λ	The period of Bragg grating
ε_r	Relative permittivity
ε	Permittivity
ε_r'	Real part of permittivity
ε_r''	Imaginary part of permittivity
ω	Angular frequency
ω_o	Angular resonant frequency
γ	Evanescent absorption coefficient
σ	Conductivity

δ	Skin depth
ϵ	Dielectric function
θ_B	Brewster angle
θ_c	Critical angle

Chapter 1: Introduction

1.1 General background

The environmental pollution is one of the main problems of our civilization nowadays. Contamination of water resources by industrial wastes such as heavy metal ions and agricultural pesticides is one of the worst cases [1]. Another type of pollutants attracted attention recently are mycotoxins, which are the products of metabolism of large varieties of fungi species grown typically on different agriculture products, i.e. grains, spices, nuts, coffee beans, fruits, and respective derivative food products [2]. Mycotoxins being toxic, carcinogenic and endocrine disruptive agents are of particular concern for agriculture and food industry [2]. Monitoring these pollutants on low concentrations in sub-ppb (part per billion) range is a task of great importance nowadays. This of course could be done using modern analytical methods of chromatography and mass spectroscopy, though such analysis will be too expensive and not suitable for in-field detection of mycotoxins. Optical sensors combining high sensitivity with other advantages, such as non-invasiveness, low power consumption, and remote access [3], is perhaps a right choice for this task. However, the toxins mentioned above are usually small molecules which are quite difficult to detect using conventional optical sensing technologies such as SPR (surface plasmon resonance). Much lover detection limit (down to 0.1 ppb) can be achieved using the method of total internal reflection ellipsometry (TIRE) which was developed in the last decade in Prof. Nabok's research group at Sheffield Hallam University [4-7]. The TIRE method, however, is a laboratory-based analytical technique which required expensive equipment, e.g. spectroscopic ellipsometer, and highly qualified technical personnel. Further enhancement of the sensitivity could achieve by exploiting multiple reflections of light. This could be done with the use optical waveguide or optical fiber. As well as work towards development of portable

sensor devices having high sensitivity in ppt (part-per trillion) range can be achieved using interferometry principles in combination with planar waveguide geometry [7]. Recent developments in planar waveguide technology using Mach-Zehnder interferometry [8] or ring-resonators [9] principles are very promising. An interesting concept of fully integrated sensor was recently demonstrated by Misiakos [10] which combines multichannel planar waveguide, avalanche LEDs as light source, and p-n junction photo-detectors as well as microfluidics in one silicon chip. The relative drawback of Mach Zehnder biosensor is the complexity of its design. In this work we propose much simpler design of the optical waveguide devices. Another possibility was based on earlier sensor development which utilized a silicon oxide - silicon nitride planar waveguide operating in polarization interferometry (PI) regime [7, 11, 12]. Both the modelling and preliminary experiments showed 2-3 order increase in sensitivity as compared to TIRE methods [7, 12] due to a multiple reflection of light in the waveguide. The same waveguides, though operating in the light attenuation regime, were successfully utilized in optical enzyme sensor array capable of detection of traces (in sub-ppb) range of heavy metals and pesticides [13, 14]. The proposed optical planar waveguide planar interferometer (OPW PI) sensors can be quite small in size and capable of detecting low molecular weight toxins in ppt range of concentrations.

1.2 Motivation for research

Due to the adverse health effects of mycotoxins that range from acute poisoning to long-term effects such as immune deficiency and cancer and their widespread in agriculture products and associated food and feed, they are considered as a real threat

to public health and require efforts to control them. The World Health Organization (WHO) set quite strict limits (typically in ppb range) on the allowed concentration of mycotoxins [15]. The first step in reducing of the mycotoxin contamination to the safe level is providing means for their detection and monitoring.

The traditional analytical methods such as chromatography and mass-spectroscopy are capable of detection of low molecular weight molecules of mycotoxins in such low concentrations, however they require advance analytical instrumentation in specialized laboratories and highly skillful personnel which makes the analysis quire expensive and time consuming. Biosensors are considered as the most promising way to bridge the gap between the high WHO requirements and a current state of analytical capabilities. In the last decade, several bio-sensing methods for mycotoxins detection were demonstrated; however, they still utilize bulky and expensive laboratory equipment and require great deal of experience in their use. Therefore, the development of low cost, portable, though highly sensitive bio-sensors is in great demand nowadays. This was the main motivation behind my PhD project.

1.3 Aim and objectives

The main aim of my PhD project is to develop a novel optical bio-sensing technology based on planar waveguides capable of detection of mycotoxins in low concentrations down to ppt level and also to provide a platform for further commercial development of portable biosensors for in-field detection of mycotoxins.

The objectives are:

1. To develop an experimental setup for optical planar waveguide (OPW) biosensing based on the principle of polarization interferometry (PI).
2. To test the experimental set-up, to evaluate its sensitivity, and to develop data processing system.
3. To develop the experimental methodologies of (i) the immobilization of bio-receptors (antibodies and aptamers) on the waveguide surface, and (ii) the detection of mycotoxins in direct assay with their specific antibodies and aptamers.
4. To perform a series of biosensing experiments using the developed OPW PI experimental setup for *in-vitro* detection of several mycotoxins, i,e, aflatoxin B1, zearalenone, ochratoxin A, in direct assay with respective antibodies and aptamers.
5. To carry out preliminary work for the development of a portable OPW PI biosensor.

1.4 The proposed research

In this work, the simplified design of a planar waveguide sensor was explored. Instead using a reference arm or channel as in other previously developed interferometers second, we use the two polarization components p- and s- which are affected differently by the medium. In the proposed one channel design, the s-polarized component (which is less affected by the medium) is used as a reference.

Another element of novelty was the use of simple light coupling via slanted angle. Within this project, theoretical analysis of light propagation through planer

waveguide was done. The theory was used to model the waveguide optimize, its geometric and evaluate refractive index sensitivity.

The major experimental part of the work was the practical implementation of OPW design, which went through several stages of experimental set-up upgrading. The final version of OPW set-up provided the record high RIS of about 10,000 rad/RIU.

Selection of suitable bio receptors (antibody or aptamers) and their immobilization on the waveguide was essential part of the project.

Finally, the experimental detection of three different mycotoxins (aflatoxin b, ochratoxin A and zearalenone) was successfully achieved. The LDL limit in sub ppt range is the best among the other optical sensors reported.

1.5 References

1. Onder, S., Dursun, S., Gezgin, S., & Demirbas, A. (2007). Determination of heavy metal pollution in grass and soil of city centre green areas (Konya, Turkey), Polish Journal of Environmental Studies, 16(1), 145.
2. Peraica, M., Radic, B., Lucic, A., & Pavlovic, M. (1999). Toxic effects of mycotoxins in Humans, Bulletin of the World Health Organization, 77(9), 754-766.
3. Ahuja, D., & Parande, D. (2012). Optical sensors and their applications, Journal of Scientific Research and Reviews, 1(5), 060-068.
4. Nabok, A V., Tsargorodskaya, A., Hassan, A. K., Starodub, N. F., (2005). Total internal reflection ellipsometry and SPR detection of low molecular weight environmental toxins, Applied Surface Science, 246 (4), 381-386
5. Nabok, A.V., Tsargorodskaya, A., Holloway, A., Starodub, N.F., Gojster, O. (2007). Registration of T-2 mycotoxin with total internal reflection ellipsometry and QCM impedance methods, Biosensors & Bioelectronics, 22 (6) , 885-890
6. Nabok, A., Tsargorodskaya, A. (2008). The method of total internal reflection ellipsometry for thin film characterisation and sensing, Thin Solid Films, 516 (24), 8993 9001
7. Nabok, A., Tsargorodskaya, A., Mustafa, M.K., Szekacs, I., Starodub, N.F., Szekacs, A. (2011). Detection of low molecular weight toxins using optical phase detection techniques, Sensors and Actuators B, Chemical , 154(2), 232-237.
8. Mehra, R., & Tripathi, J. (2010). Machzehnder Interferometer and it's Applications, International Journal of Computer Applications, 1(9), 110-118.
9. Guider, R., Gandolfi, D., Chalyan, T., Pasquardini, L., Samusenko, A., Pucker, G., ... & Pavesi, L. (2015). Design and Optimization of SiON Ring Resonator-Based Biosensors for Aflatoxin M1 Detection, Sensors, 15(7), 17300-17312.
10. Lechuga, L. M., Sepulveda, B., del Rio, J. S., Blanco, F., Calle, A., & Dominguez, C. (2004, July). Integrated micro-and nano-optical biosensor silicon devices CMOS compatible. In Integrated Optoelectronic Devices 2004 (pp. 96-110). International Society for Optics and Photonic, 2004 (pp. 96-110).

11. Shirshov, Y.M., Snopok, B.A., Samoylov, A.V., Kiyanovskij, A.P., Venger, E.F., Nabok, A.V., & Ray, A.K. (2001). Analysis of the response of planar polarization interferometer to 18 molecular layer formation: fibrinogen adsorption on silicon nitride surface. Biosensors and Bioelectronics, 16(6), 381-390
12. Nabok, A.Organic and Inorganic nanostructure, 2005, Arteh House, Boston
13. Nabok, A., Haron, S., & Ray, A. (2004). Registration of heavy metal ions and pesticides with ATR planar waveguide enzyme sensors. Applied Surface Science, 238(1), 423-428. 49
14. Nabok, A., Tsargorodskaya, A., Haron, S., & Travis, J. (2006, April). Planar waveguide enzyme sensor array for water pollution monitoring. In MEMS Sensors and Actuators, 2006. The Institution of Engineering and Technology Seminar on (pp. 119-126). IET.

Chapter 2: Mycotoxin detection techniques:

Review

2.1 Introduction

This chapter provides a brief outline of the project starting with the motivation and current state of work in the field of detection of low molecular weight toxins, and mycotoxins in particular. The comparison of traditional laboratory based analytical methods, such as HPLC and mass-spectroscopy, and biosensors are presented here to justify the subject of PhD project, its aims and objectives.

2.2 Traditional mycotoxin detection methods

2.2.1 Introduction:

Contamination of agricultural products and associated food and feed is very common these days which causes a number of economic and health problems, as mentioned in the previous chapter. Therefore, national and international institutions and organizations, such as the European Commission (EC), the US Food and Drug Administration (FDA), the World Health Organization (WHO) and the Food and Agriculture Organization recognized the potential harmful impact of mycotoxins and set up regulatory limits for major classes. [6, 7]. For example, European Union Mycotoxin Legislation limits range from 10 to 0.5 ng/g (or ppb) depending on the type of mycotoxin and the type of product [1, 2]. In order to avoid the dangers and control the spread of those contaminants, there is an urgent requirement of providing means of detection and monitoring of these toxins. Mycotoxin detection is considered a scientific challenge, due to their high toxicity, widespread and the small size of the molecules molecular weight (50-500), [3, 4, 5].

Continuous analysis of mycotoxin contaminants in agriculture products, food and feed requires analytical methods capable of their detection at the concentration level indicated above. The most common analytical method for almost all varieties of mycotoxins uses the immune-affinity clean-up combined with high-performance liquid chromatography (HPLC). HPLC is based on the separation of a mixture into several components depending on their differences in the interaction with absorbent material which leads to different flow rates; HPLC is usually combined with UV or fluorescence detection, [8, 9]. Another commonly used technology is thin layer chromatography (TLC), which gives qualitative or semi-quantitative results. These

analytical methods required long hours of preparation and processing to yield the results of a particular sample. The production of antibodies for majority of mycotoxins has led to emerging and an increasing use of enzyme-linked immune-sorbent assays (ELISAs), which rely on use the specific antibodies to bind the mycotoxin molecules, and give the estimated result of the sample in less than 30 min. Most of these traditional analytical methods have sufficient sensitivity to detect mycotoxins at the required concentrations, however the complexity of instrumentation and the analysis procedures make those methods very expansive and time consuming. Therefore, there is great demand of development of alternative solutions for cost-effective, in-field detection of mycotoxins. Up to now, there is no ideal solution for this problem; several bio-sensing technologies developed recently cannot meet all the requirements of high sensitivity, reliability, portability, low cost, and ease of use. This PhD project is attempted to develop such a biosensor [10].

2.2.2 Chromatography:

Chromatography is a technique to separate mixtures of substances into their components on the basis of their molecular composition and molecular structure. There are many kinds of chromatography techniques, such as gas chromatography (GC), liquid chromatography (LC), thin layer chromatography (TLC) and high performance liquid chromatography (HPLC). All chromatographic types operate on the same basic principle of separation the sample into its compound based on the difference in the relative affinities of the compound molecules [11].

2.2.2.1 Thin Layer Chromatography (TLC)

This method separates the components in the mobile phase depending on their relative variance of affinity towards the stationary phase. In this technique, the components travel as mobile phase over the surface of the stationary phase, the separation start when the mobility of the compound is affected by the compound affinity to the stationary phase, so that the compound which have the highest affinity towards stationary phase move slowly, while lowest affinity compound move faster. As shown in Fig. 2.1, the separation of compounds can be visualized as different spots at the travel path on the plate that hold the solution.

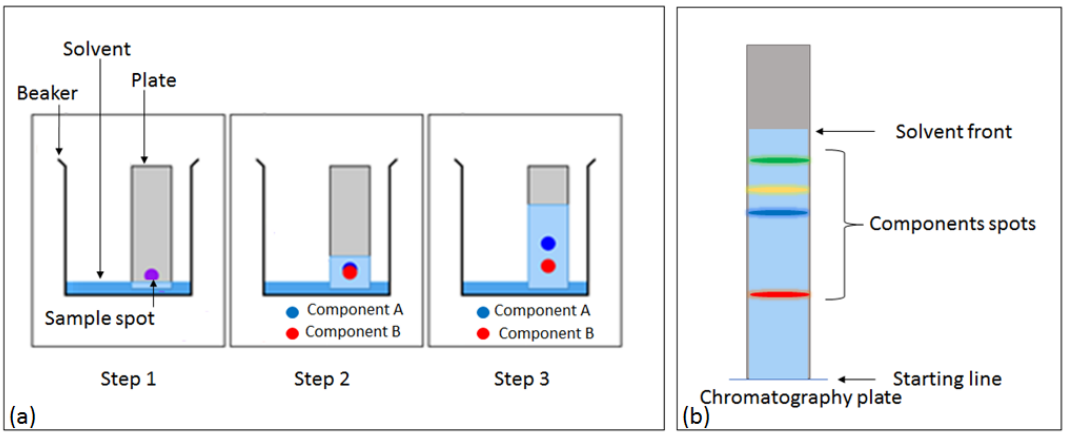

Figure 2.1 Thin Layer Chromatography: (a) compounds separation mechanism, (b) components color bands on chromatographic plate.

TLC is usually performed on a sheet of glass, plastic, or aluminum, which is covered with a thin layer of adsorbent material, such as silica gel, or cellulose as a stationary phase. In the end of the process, the plate will be dried and visualized under UV light to visualize the traveling distance of the component to calculate the flow rate and to find out the separation results. As shown in Fig. 2.2, the ratio of the traveling

distance of the substance that of the solvent is used to estimate the substance movement, and called as retention factor RF value, which is the ratio of the distance moved by the solute and the distance moved by the solvent along the paper, from the common Origin. The value of the RF factor can be zero when the solute remains fixed at its origin and one when moves as far as the solvent, so the value of RF ranging between zero and one [11]. The ratio of the traveling distance of the substance that of the solvent is used to estimate the substance movement and called as retention factor RF value. Knowing RF value one can make the tentative identification of the compound [12-15].

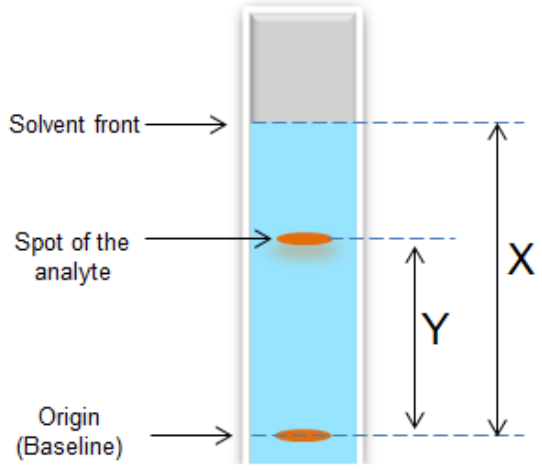

Figure 2.2 Retention factor of thin layer chromatography.

This approach can be used to detect the mycotoxins by dropping the sample onto TLC plate, and then the plate is developed, by dipping into an aluminum chloride solution and heating. The presence of mycotoxins then can be visualized by

irradiation the plate by long-wave UV light. Comparison to the standard sample allows estimation of the level of the mycotoxin's consecration. The detection limit is about 0.5 µg/kg (0.5 ppb). TLC using silica gel impregnated with organic acid has been reported as appropriate method to detect common mycotoxins (aflatoxins, citrinin, fumonisin) [16] TLC has been reported to detect 2µg/kg (2ppb) of mycotoxin in various cereal grains [17].

2.2.2.2 High Performance Liquid Chromatography (HPLC):

High performance liquid chromatography is an improved form of column liquid chromatography. This method shown in Fig. 2.3 can be considered as a mass transfer process involving absorption. In this technique the move of the sample analytes through a column by gravity have been replaced by the high pressures pump (of up to 400 atmospheres) to generate and measure a specific flow rate of mobile phase (typically milliliters per minute).This approach make the separation process faster.

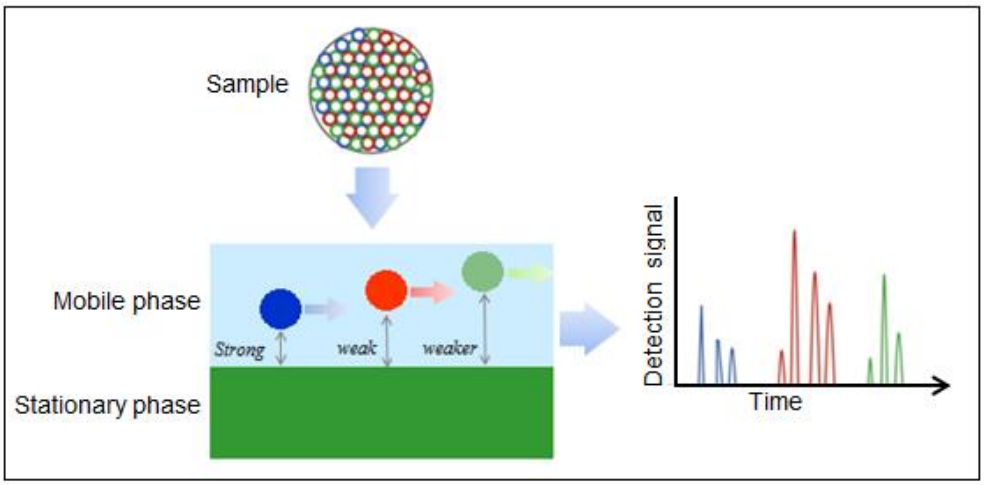

Figure 2.3 Principles of HPLC

The separation process starts with pumping the liquid solvent that contains the sample mixture through a column containing a solid adsorbent material. During that process, each component in the sample interacts slightly differently with the adsorbent material, and small variations in the interaction lead to the difference in the flow rates of components flowing, eventually, leading to separation of the components as they flow out of the column, [16,17,18]. HPLC have many advantages over traditional chromatography, such as higher speed (most analysis take 30 min or less), higher resolution and sensitivity, and easy sample recovery. There are plenty of publications with good results demonstrating the ability to detect mycotoxins in low concentrations. The HPLC system shown schematically in Fig. 2.4 consists of the following main parts [19, 20, 21]:

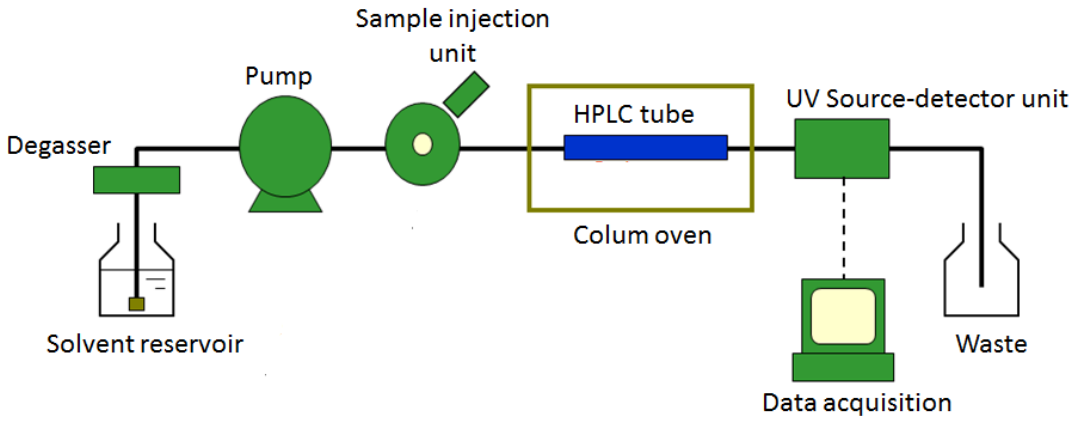

Figure 2.4 Main parts of High-performance liquid chromatography

Solvent: a sample must first be dissolved in a liquid solvent, usually one with known HPLC spectra so that its data can be distinguished from the sample.

Solvent Delivery System (Pump): to provide the pressure, which drives the sample through the column (pressure of up to 400-600 bar).

Column: is a usually stainless steel tube with a diameter of 3 to 5mm and a length ranging from 10 to 30cm. The separation of the compounds occurs in this tube (column). The stationary phase is packed in this tube

Injector: this element injects the sample into the high-pressure flow, (about 5-20 μL). The accuracy of HPLC performance is largely affected by the reproducibility of sample injection, so that the design of the injector is an important factor. The most widely used injection method is autosampler (auto-injector) system, which allows repeated injections in a set scheduled-timing.

Detector: which feeds the information to a computer (recorder and data collector) to quantify and identify the sample components. The detector measures the change in the composition of the eluent, due to present of the analyte and, converts this change to the form of electronic signal.

According to the separation mechanism (type of the column) there are four types of HPLC:

Normal Phase HPLC: In this type of HPLC the separation relies on the polarity of the compounds. The stationary phase has a polarity, so the least polar will separate first and its more polar compounds will separate later.

Reverse Phase HPLC: This method uses stationary phase as hydrophobic or nonpolar, while the mobile phase has a polarity. So, the nonpolar material will be retained longer.

Size-exclusion HPLC: in this method the substrate molecules are incorporating within a column and the separation of constituents depends on the difference in molecular sizes.

Ion-exchange HPLC: in this strategy the stationary phase possesses ionically charged surface opposite to the charge of the sample, so the compounds are separated by the ion force interaction.

In general, the chromatography is capable of analysing most of mycotoxin types, while ion-exchange chromatography is more suited for acidic mycotoxins like β-nitropropionic acid, ochratoxin A, mycophenolic acid, viridicatumtoxin and tenuazonic acid, [23]. HPLC is typically coupled with UV and called (HPLC-UV), or fluorescence detector and named (HPLC-FD). HPLC-UV employs a UV-detector to measure the absorbance A (no unit) at particular wavelength to obtain compound concentration C (mol/litter) using the Beer-Lambert's Law:

$$A = \epsilon C b \tag{2.1}$$

where ϵ is the absorption coefficient (L $mol^{-1}cm^{-1}$), and b is the light path through the liquid sample length.

The fluorescence detector (HPLC-FD) is one of the most sensitive detectors can be coupled to liquid chromatography. The excitation and emission fluorescence spectra can help to characterize individual compounds. Excitation spectra are identical to UV/Visible absorption spectra, while emission spectra can give additional information [24].

2.2.2.3 Gas chromatography (GC)

Gas chromatography is considered one of the most popular methods for analyzing and separating compounds, because of its low detection limit and high resolution. Gas chromatography (GC) is a chromatography technique in which the mobile phase is a gas, the gaseous mobile phase is forced by using pressure to pass through the stationary phase, [25,26]. This method is more suitable for analyzing and testing the purity of the compounds that can be vaporized without decomposition. The stationary phase is a microscopic layer of polymer or liquid on a solid support inside the column, while the mobile phase is an inert gas such as helium or an unreactive gas such as nitrogen. The mobile phase which is a gaseous compound passed through the column and analyzed by interacting with the walls of the column [27].

The schematic diagram of GC is shown in Fig. 2.5 the gas source (usually high purity He, Ar, or N_2) has the pressure and flow control. The gas flows into the injector, through the column and then into the detector. The injector heats the sample to vaporize it and introduce into the injector. The vaporized solutes transport through the column by the carrier gas, while the column is maintained in a temperature controlled oven to keep the sample in vapor phase. The solutes travels through the column at a various rate speed depending on their physical properties. The fastest solute exits from the column first followed by the remaining solutes according to their speed. As each solute exits from the column, it meets the detector. An electronic signal is generated upon interaction of the solute with the detector. The amplitude of the signal is plotted against elapsed time to produce a chromatogram. The time and size of a peak are used to identify and measure the amount of the compound in the sample. The size of the resulting peak is proportional to the amount of the compound in the sample [28].

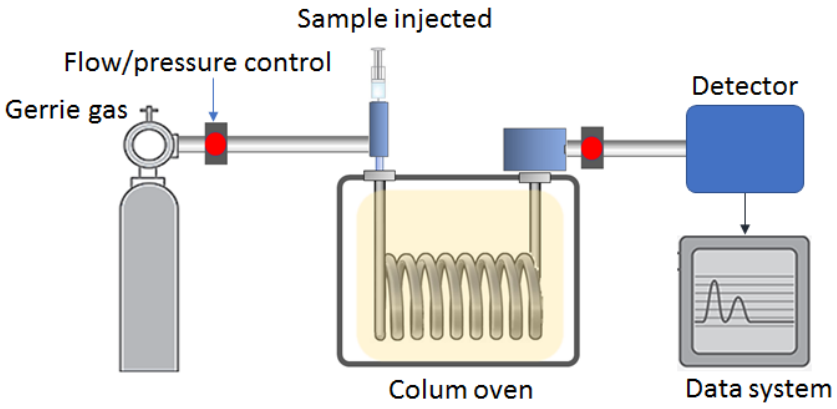

Figure 2.5 Schematic Diagram of GC.

Teruhisa GoTo*i, Masami MATSUI*2, and Takaharu KITSUWA and others have been demonstrated the detection aspergillus mycotoxins using gas chromatography with fused silica capillary column. Also gas chromatographic methods are used for quantitative simultaneous determination of trichothecenes in cereals and cereal-based products.

2.2.3 The enzyme-linked immunosorbent assay (ELISA):

This method uses the specific binding of antibody-antigen to select the target molecules, then the target molecules are detected and quantified, [29,30]. ELISA (enzyme-linked immunosorbent assay) or enzyme immunoassay (EIA) (as another name) is a plate-based assay technique used to detect and quantify substances such as peptides, proteins, antibodies and hormones. It is also suitable for use to detect mycotoxins. The process involves immobilizing the antigen on a solid surface and then complex it with an antibody that is linked to an enzyme (this secondary antibody is usually labeled with an enzyme). As illustrated in Fig. 2.6 the detection is done via a substratum which is added to the plate, the reaction of the substratum

decomposition catalyzed by the enzyme releases colored products, which is converted to measurable signal using photo detector [31, 32]. The ELISA techniques can be classified depending on the antigen-antibody combination into a direct ELISA, indirect ELISA, sandwich ELISA, competitive ELISA.

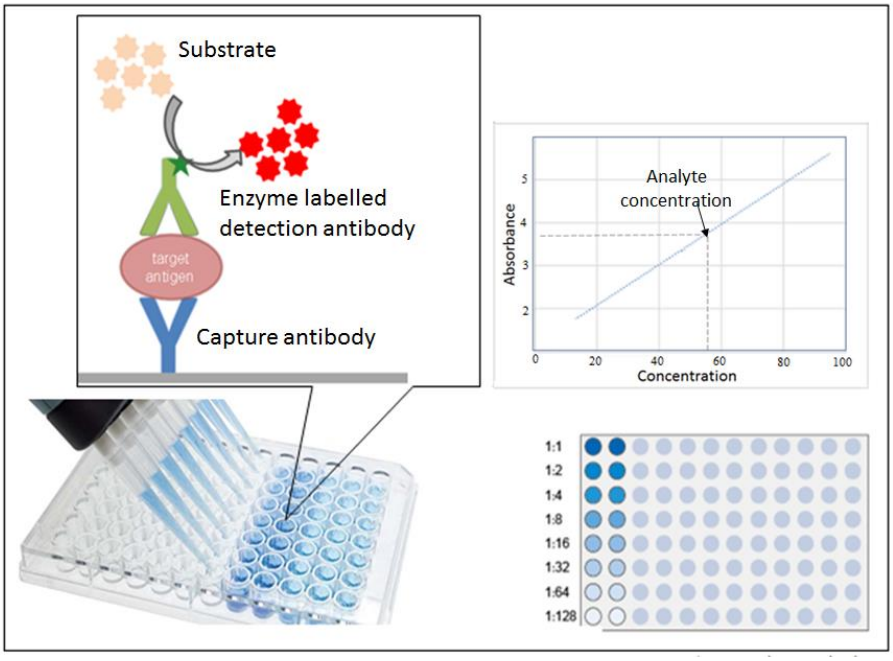

Figure 2.6 Enzyme-linked immunosorbent assay (ELISA).

2.2.4 Lateral flow devices (LFD)

This method relies on the formation of immune complex of the antigen with a dried format of bio-active particles immobilized on a micro-structured strip which has the capacity to transport fluid spontaneously through series of capillary beads. As shown in Fig. 2.7 the first element acts as a sponge and holds an excess of a sample fluid. The sample moves along the strip through capillary tubes to the part that contains the dried labeled reagents, which recognize pathogens in the sample, then the antigen binds with the reagents. After a while, when more and more fluid has passed through the stripes, the stripe-area changes its color. The density of the line will vary

depending on the quantity of the target present. Accumulation of labeled conjugate on test line and control line by immunological recognition system generates detectable signals and results are visualized either by naked eye or using a lateral flow strip reader. LFD has demonstrated the detection of aflatoxins in concentrations down to range 1µg/kg (1 ppb) and dynamic range from 2 to 40µg/ kg) [33, 34, 35, 36].

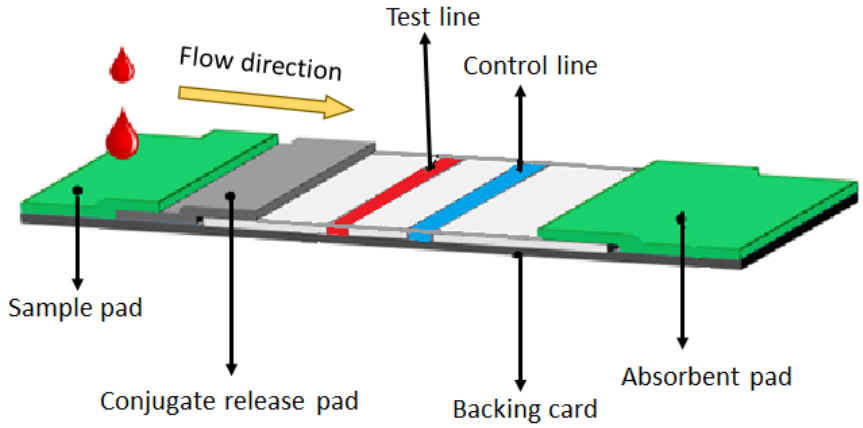

Figure 2.7 Basic component of lateral flow test

2.2.5 Fluorescence polarization immunoassay (FPIA)

This technique employs a fluorophore bound antigen that bound to the antibody of interest. The principles of FPIA are illustrated in Fig. 2.8. Polarized light used to produce a polarized fluorescent emission from the analyte-tracer, the average polarization of the emitted fluorescence will be related to the speed of rotation of the molecule. The rate of speed of molecule rotation in liquid is related to the size of the molecule. Therefore, the polarization of the fluorescent emission is related to the size of the molecule. Such relation is used in this method to make the polarized of the

fluorescent emission from the analyte-tracer molecules as indicator to its binding to antibody, because that binding leads to increase in the size and thus reduces the polarization ratio [37]. The changes in polarization is therefore proportional to the amount of antigen in the sample, and it can be accurately measured with FPIA. This method was used to detect aflatoxin B1 in beer and showed 1ng/mL (1ppb) as detection limit [38, 39, 40].

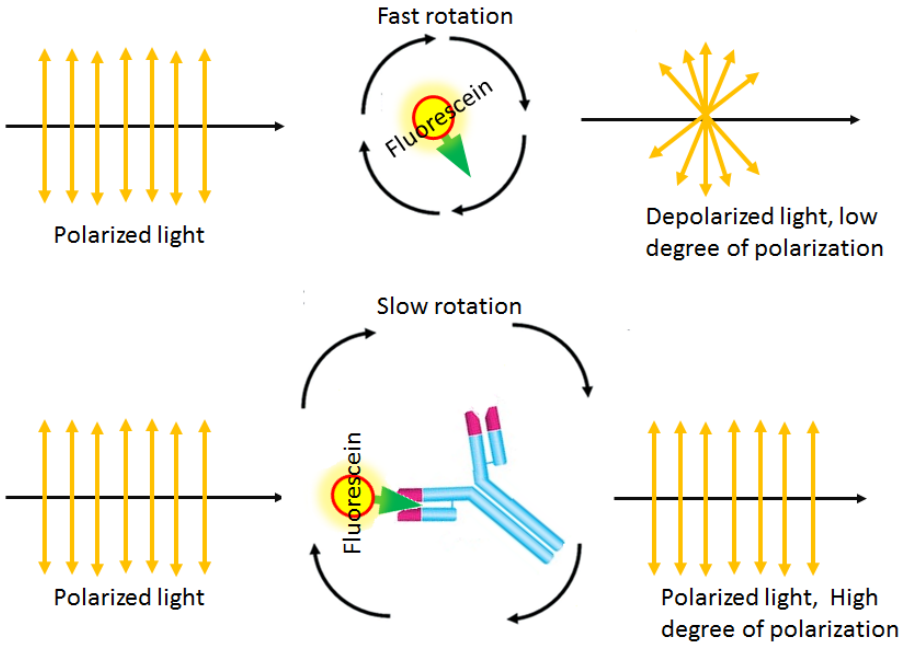

Figure 2.8 Principles of FPIA

2.2.6 Infrared spectroscopy

Infrared spectroscopy (IR spectroscopy or vibrational spectroscopy) is spectroscopic technique based on the interaction of infrared light with the sample to provide information about the molecule identity, [41]. The electromagnetic radiation in the infrared range gives rise to excitation of molecular vibrations or rotations. Different functional group absorbs characteristic frequency of IR radiation, hence showing the characteristic IR spectral bands. Therefore, a particular substance or

molecules system can be identified from its IR spectrum finger print [42, 43]. Infrared spectroscopy has proved to be a powerful tool for the study of biological molecules, including proteins, lipids, carbohydrates, and nucleic acids. This spectroscopic approach enables such molecules to be identified and changes to their chemical structures to be characterized.

As shown in Fig. 2.9, the basic components of an IR spectrometer are the radiation source, monochromator, sample and reference cells, detector, amplifier and recorder [44].

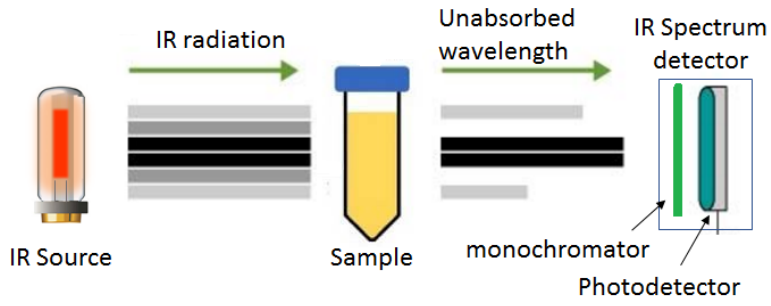

Figure 2.9 Principles of IR spectroscopy

2.2.7 Molecular Inversion Probe

This method uses single-stranded oligonucleotides (oligos) having a sequence that are complementary to the target in the genome. The target molecules are captured using circularization molecular technique. When the probe hybridizes to the target, it undergoes an inversion in configuration (as suggested by the name of the technique) and circularizes. Specifically, the two target complementary regions at the 5' and 3' ends of the probe become adjacent to one another while the internal linker region forms a free hanging loop (see Fig. 2.10). The key strengths of the MIP technology

include its high specificity to the target and its scalability for high-throughput, multiplexed analyses where tens of thousands of genomic loci are assayed simultaneously [45, 46].

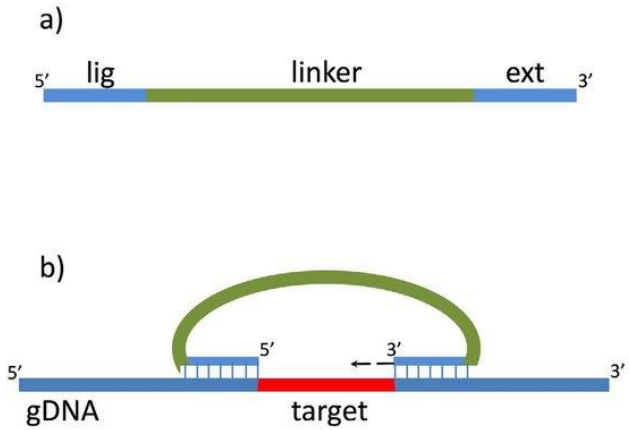

Figure 2.10 Principles of Molecular Inversion Probe, In the MIP method, target-specific oligo probe sequences are hybridized to the target region of genomic DNA and the probe is circularized by DNA polymerase and ligase such that the target sequence is incorporated into the circular molecule [45].

2.2.8 Mass spectrometry

Mass spectrometry (MS) technique relies on ionization of the sample, and then the separation of the ionic species in electro-magnetic field on the bases of their mass-to-charge ratio. Mass spectrometry is an analytical technique capable of identifying compounds and evaluating its concentration. These days the methods of chromatography and MS are combined in one piece of instrumentation [47, 48, 49], and such combination can provide additional information on chemical structure of affinity-bound ligands which is missing in chromatography.

The complete MS process involves the ionization of the sample with or without fragmentation; the ions are then characterized by their mass to charge ratios (m/z) and relative abundances, using electric and magmatic fields (see Fig. 2.11).

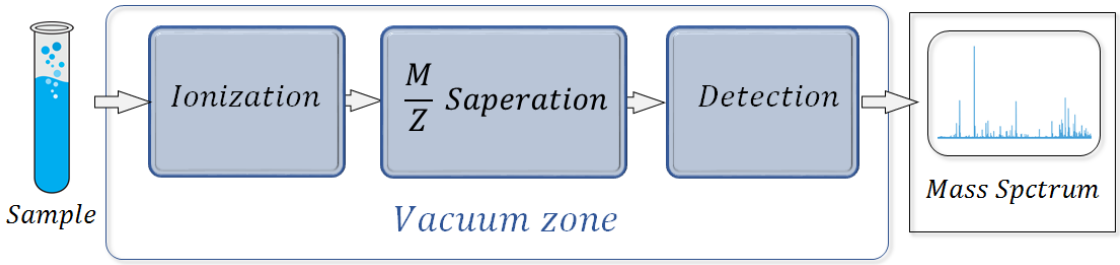

Figure 2.11 Mass Spectrometry principles.

The MS analytical technique is fast, requires no sample preparation and no derivatization or chromatographic separation. MS have been used for detection of mycotoxins, such as aflatoxins B1, B2, G1, and G2, and demonstrated very high sensitivity with LOD as low as 50 fmol [50]. The drawback of this method is, obviously, high cost of instrumentation.

Table 2.1 Properties of mycotoxins traditional analytical methods., [51].

Method	Advantages	Disadvantage	LOD	LOQ

TCL	Simple and inexpensive Can be used as a rapid screening method	Poor sensitivity Poor precision Quantitative approach only if coupled with a densitometer	$30ng.mL^{-1}$	$100ng.mL^{-1}$
HPLC-FLD	Good selectivity Accurate identification Short analysis time Automatic analysis (autosampler) Official methods available	Expensive equipment Specialist expertise required Derivatization may be required	$0.04ng.mL^{-1}$	$0.15ng.mL^{-1}$
LC-MS	Selective and sensitive detection Capability to generate structural information of the target analyte Low detection limits Simultaneous analysis of multiple mycotoxins Minimum sample pre-treatment steps	Expensive equipment Specialist expertise required Sensitivity depends on ionization technique	$2\mu g.kg^{-1}$	$3.5\mu g.kg^{-1}$
GC	Simultaneous analysis of multiple mycotoxins Selective and sensitive detection	Expensive equipment Specialist expertise required Derivatization required Non-linear calibration curve Carry over effects from previous Sample	$0.5\mu g.kg^{-1}$	$1\mu g.kg^{-1}$
ELISA	Convenient and sensitive detection Ease of operation Rapid sample screening Simultaneous analysis of multiple mycotoxins Low use of organic solvents	Matrix interference problems Cross-reactivity with related mycotoxins Possible false positive/negative results Narrow operating range	$4.0ng.mL^{-1}$	$Not\ specifed$

2.3 Biosensors

2.3.1 The concept of biosensor

A biosensor is an analytical device which can detect molecules of inorganic, organic or biological types through their interaction with bi-receptors, such as antibodies, enzymes, organelles, whole cells or tissues. Such interactions can be

converted to some kind of physical parameters using a suitable transducer, which can be electrical, electrochemical, optical, piezoelectric, thermometric, ion-sensitive, magnetic, or acoustic, and resulted in a measurable signal. According to the above definition, a biosensor consists of the following main parts as shown in Fig. 2.12 [52, 53, 54]:

Bioreceptor is the element consisting of a bio-component which is able to capture a specific target analyte, i.e. ion, molecule, cell, virus, bacteria, etc., and to perform some kind of biochemical reaction, for example, decomposition, or binding, formation of molecular complexes, polymerizations, etc. There are many types of biological molecules which can act as sensing element or receptor, the list includes antibodies, enzymes, nucleic acids, organelle, cell, etc. Some of these receptors, for example enzymes, may act as catalyst decomposition of certain analytes; some others, e.g. antibodies have binding ability with specifically target molecules. Observation and recording of such interactions between the bioreceptor and the analyte will be providing the information on the presence of the analyte and its and concentration. The reaction between the bioreceptor and analyte may result in the production of new chemicals, release of heat, flow of electrons, changes in pH, optical properties of the medium. *Transducer* is the element that converts such changes into some physical measurable signals, i.e. mass, temperature, electric current or potential, oscillation frequency, optical properties, etc.

Signal processing system is the part which processes the signal produced by transducer by converting it to electronic signal, amplifying it, transforming it to a format suitable for the user, and finally identifying the analyte and establishing a correlation between the output signal and the analyte concentration [55,56,57]. Signal processing is typically carried out by computer.

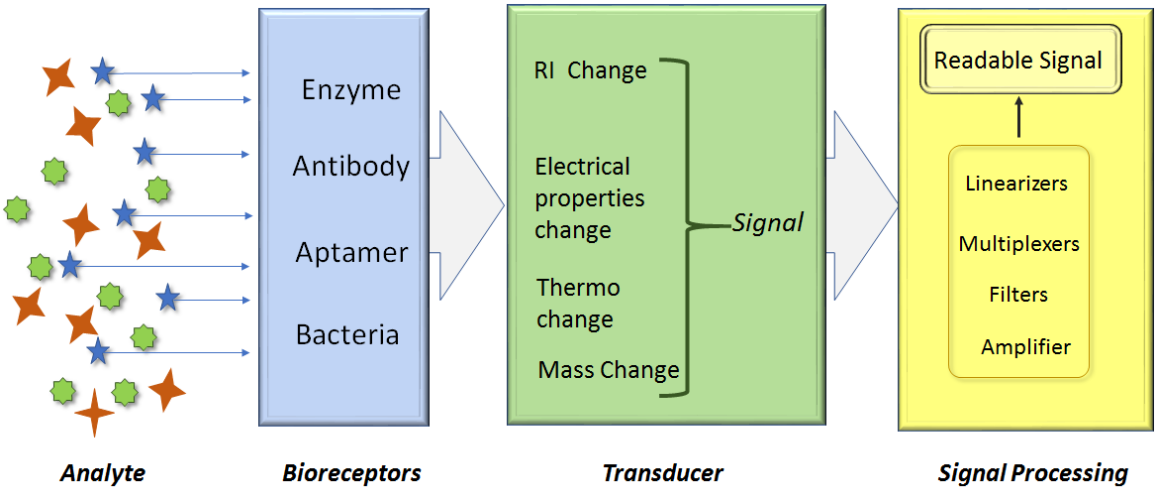

Figure 2.12 Schematic diagram of optical biosensors

2.3.2 Classification of biosensor

Biosensors can be classified by their bio-receptor element or by the transduction type. Biological elements include antibodies, enzymes, DNA oligomers, aptamers, organelles, cells, micro-organisms, and biological tissue. The choice of transduction method depends on the physicochemical changes resulting from the sensing event. Biosensing methods can be split into three main classes according to their transduction types, i.e. optical detection methods, electrochemical detection methods, and mass detection methods. Optical biosensors having a number of advantages over the other biosensing technologies (see more detailed description in the following sections) is the subject of this project, therefore the main attention will be focused on optical biosensing methods.

2.3.3 Optical biosensors

2.3.3.1 Introduction

Optical biosensors offer great advantages over traditional analytical methods due to their ability to direct, real-time and label-free detection of many biological and chemical substances. Moreover, they provide additional advantages including high specificity, sensitivity, small size and cost-effectiveness. Optical biosensors are the most commonly reported category of biosensors. Optical biosensors can be designed as label-free when the detected signal is generated directly by the interaction of the analysed material with the transducer. Alternatively, optical biosensors could the labels, e.g. chromophores or fluorophores, to generate the optical signal.

The properties of electromagnetic waves, e.g. light, can be characterized by the amplitude frequency, phase, and polarization state, and all of these parameters can be utilized in optical detection of chemical and biological reactions. More specifically, the transduction principles of the optical biosensors could be based on changes in the amplitude, frequency, phase, or polarization of light in response to the physical or chemical changes during bio-recognition processes. In general, optical transducers can be classified into two main groups: so-called passive and active optical devices. In "passive" devices the thickness (d) and/or real part of refractive index (n) of the sensitive layer are detected, while in "active" optical devices, the imaginary part of the refractive index related to either light losses or light emission (i.e. fluorescence or luminescence) are recorded. The first group includes ellipsometry, SPR, interferometry, and fiber optics; the second group includes absorption and luminescent spectroscopy.

The key behind the ability of optical biosensors to detect the biological analytes lies on the fact that biological molecules have dielectric permittivity greater than that of buffer solution and water. Therefore, biomolecules possess the intrinsic ability to reduce the propagation velocity of electromagnetic waves that propagate through them, which is sensed as change in the refractive index of the medium [58].

Typical advantages offered by optical biosensors are high sensitivity, possibility of remote sensing, isolation from electromagnetic interferences, fast and real-time measurements, multiplexing, non-invasive in-vivo measurements, and bio compatibility. The main components of an optical biosensor are the light source, optical transmission medium (sample tube, glass slide, fiber, waveguide, etc.), immobilized biological recognition element (enzymes, antibodies, cells or bacteria), and optical detection system.

Optical biosensors can be broadly classified on the bases on transducing principles and their designs as shown in Fig. 2.13 [59]. Most of these methods are outlined in more details in the following sections in this chapter.

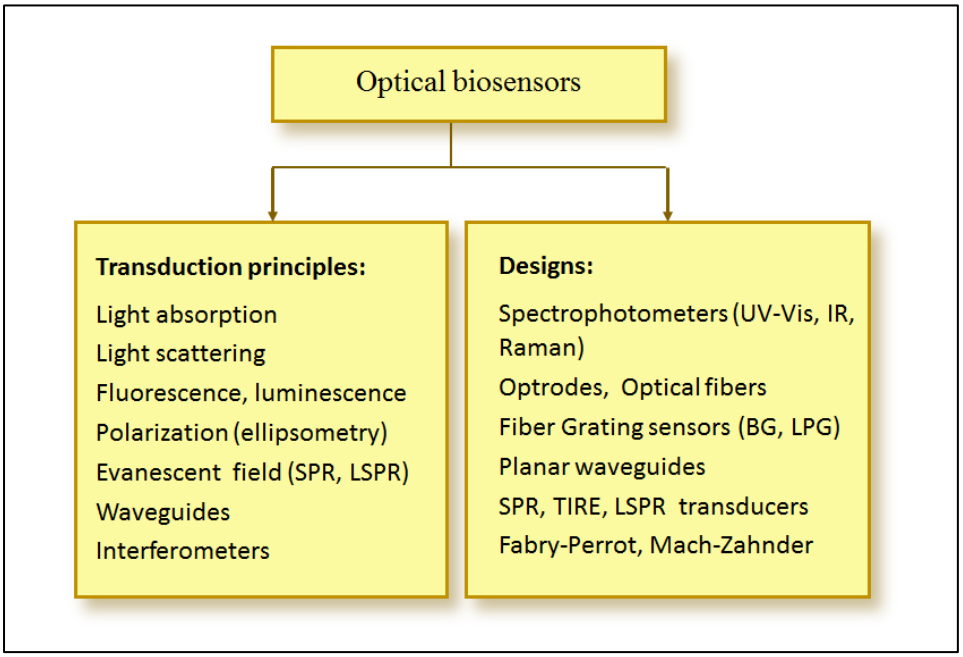

Figure 2.13 Classification of optical biosensors

2.3.4 The phenomenon of surface plasmon resonance (SPR)

The phenomenon of surface plasmon resonance (SPR) is associated with coherent electron oscillations that can be stimulated by electromagnetic waves (light) at the interface between two materials, typically on a metal-dielectric interface where the real part of the dielectric function changes its sign. In this (light-electron) interaction, free electrons in metal respond collectively by oscillating in resonance with the electromagnetic wave. Such electron oscillations, however, decay exponentially into both materials with the decay length in range of wavelength of light. This resonance state is very sensitive to any changes of dielectric function (or refractive index) in the vicinity of the interface and therefore can be used as a sensing method for detection of small changes in the external medium refractive index caused, for example, by molecular adsorption.

The condition of resonance interaction between the free electrons and the electromagnetic field is achieved when the component of the incident light wave vector parallel to the interface (k_i) is equal to the wave vector of the surface plasmon mode (k_{sp}).

$$k_{sp} = \left(\frac{2\pi}{\lambda}\right)\sqrt{\frac{\varepsilon_1\varepsilon_2}{\varepsilon_1+\varepsilon_2}}, \tag{2.2}$$

where ε_1 and ε_2 are dielectric functions of metal and insulator, respectively.

The incident light wave vector parallel to the interface k_i will be:

$$k_i = k\sin\theta_i \tag{2.3}$$

Where θ_i is the incidence angle of the light, the component of light wave vector (k_i) can be increased to match that of the surface plasmons (k_{sp}) using the methods of either total internal reflection or diffraction. Such coupling between light and surface plasmons is performed by coupling devices. The most common coupling devices in SPR sensors include a prism coupler, a waveguide coupler, and a grating coupler. Kretcschmann configuration which uses high refractive index prism coupler is the most frequently used method for optical excitation of surface plasmons. In this technique, the light passed through a high refractive index prism is totally reflected at the base of the prism, generating evanescent wave which penetrates in a thin metal film deposited on the prism base. The evanescent wave propagates along the interface with the propagation constant:

$$k_i = nk \sin \theta_i \tag{2.4}$$

The angle of incidence θ_i can be adjusted to make the wavevector k_i matching k_{sp} of surface plasmons. The k-vector matching condition is very sensitive to any changes in the refraction index of the dielectric medium closed to the thin metallic film, [60,61,62], which constitutes the main principle of SPR biosensing.

2.3.5 SPR biosensors

The surface plasmon resonance (SPR) method found its main application in chemical and biosensing, because of its relatively easy and inexpensive experimental realization. The SPR method can be considered as the detection of coupling the incident electromagnetic wave into the surface plasmons. One of the easiest experimental implementations of SPR is based on so-called Kretschmann

configuration [63,64] shown in Fig. 2.16. The main element of this experimental set-up is a glass prism coated with a thin (40-50nm) film of noble metal (e.g. gold, silver, or cooper); alternatively. Metal film could be deposited on glass slide which is in optical contact with the prism via index matching fluid. When a collimated p-polarized light beam from a laser experienced total internal reflection at a glass/medium interface the reflected light intensity registered with photo-detector reaches its maximum. It has to be noted that the metal film should be thin enough of not affecting the total internal reflection condition. If the frequency of the evanescent wave matches the frequency of oscillations of surface plasmons in metal, the energy of the incident light will be transferred to plasmons, and the reflected light intensity will be reduced. Such conditions are often referred to as surface plasmon resonance (SPR).

SPR can be recorded by monitoring the intensity of reflected light during the scanning of the beam over the range of angles of incidence, and thus changing the x-component (in the plane of the sample) of k-vector. A typical SPR curve in Fig. 2-16 (b) demonstrates the characteristic points of the resonance minimum, as well as the point of total internal reflection. The position of minimal reflectance and half-width of SPR peak of the SPR curve strongly depend on the optical characteristics of the metal film (i.e. thickness, refractive index, and extinction coefficient) as well as optical characteristics of the medium because the evanescent wave can extend through the thin metal film into the medium. Therefore, the presence of a coating on top of the metal film will cause further changes (shift) in the SPR curve, as shown in Fig. 2.14 Furthermore, molecular adsorption on the surface causes further SPR shift. The optical parameters of both the metal and coating are linked with the position and half-width of SPR curve. Therefore, the optical parameters of the coating can be

obtained by fitting of the experimental SPR curve to Fresnel's theory using least-square minimization techniques.

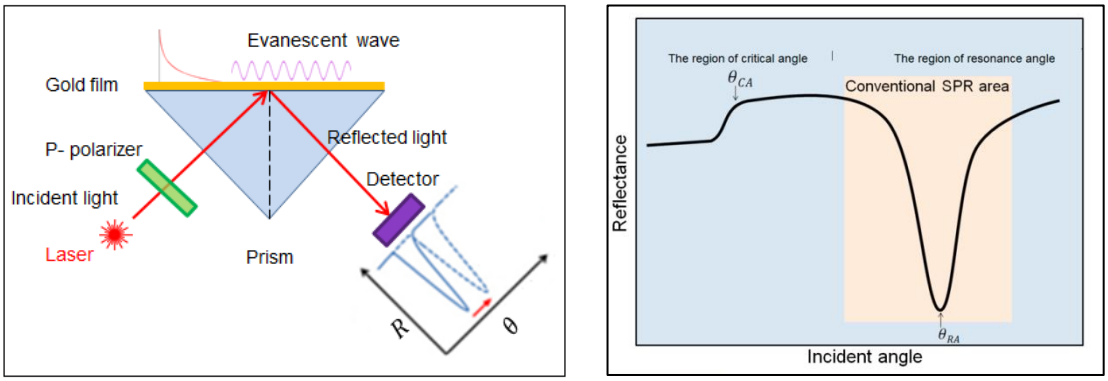

(a) (b)

Figure 2.14 SPR Krechmann configuration (a) and the angular dependence of the reflected light intensity (b).

The reflection coefficient for a p-polarized light beam in the glass prism/metal film/ambient (air) three-layer system (figure 2) is described as [65]:

$$r_{123} = r_{12}\frac{b_{23}+a_{23}[Re(r_{12})-iIm(r_{12})]e^{2idk_{x2}}}{b_{23}+a_{23}[Re(r_{12})+iIm(r_{12})]e^{2idk_{x2}}}$$

(2.5)

where $r_{ij} = \frac{a_{ij}}{b_{ij}} = Re(r_{ij}) + iIm(r_{ij})$ are reflection coefficients at the interface between layers i and j, k_x is the x-component (in the plane of the film) of the k-vector of the light incident at an angle θ:

$$k_x = k_o \varepsilon_1^{1/2} \sin\theta = \frac{2\pi}{\pi} n_1 \sin\theta \tag{2.6}$$

The function $R(k_x) = |r_{123}|^2$ experiences a minimum when $b_{23} = 0$; the surface plasmon resonance is, therefore, observed at:

$$k_x^o = k_o \sqrt{\frac{\varepsilon_1 \varepsilon_3}{\varepsilon_1 + \varepsilon_3}} \tag{2.7}$$

where $\varepsilon_1$and ε_3 are dielectric permittivities of the glass prism and the ambient, respectively, k_o is wave vector of the incident light in the plane of the surface, and k_x^o wave vector of the surface plasmon in metallic films.

The reflectivity spectrum $R(k)$ or its angular dependence $R(\theta)$ can be calculated from the parameters of the reflective system using Fresnel's formulas. Optical parameters of metal film can be found by fitting the experimental SPR curve to the Fresnel theory using the least-square technique. Using certain approximations, the relations between optical parameters of metal film (dielectric permittivity ε_2 and the thickness d_2) and the parameters of the SPR curve (position of the resonance r_{min} , minimum reflectivity R_{min} , and half-width of wave vector of evanescent field Δk) have been established in the following form [66]:

$$\varepsilon_{2r} = \frac{\varepsilon_3 k_{min}^2}{k_{min}^2 - \varepsilon_3 k_o^2} \quad , \quad \varepsilon_{2i} = \frac{\Delta k}{4A}\left(1 \pm \sqrt{R_{min}}\right) \tag{2.8}$$

$$d_2 = \frac{1}{\emptyset} \ln\left[\frac{\Delta k}{4B}\left(1 \pm \sqrt{R_{min}}\right)\right] \tag{2.9}$$

Where, ε_{2r} , ε_{2i} are the real part and imaginary part of the dielectric constant respectively, k_{min} is the minimum value of the wave vector of evanescent field, A, B are constant.

The equation (2.7) and (2.8) show that the position of SPR minimum depends entirely on the real part of the dielectric constant (ε_{2r}) , while R_{min} and Δk depend on a linear combination of the imaginary part of the dielectric constant (ε_{2i}) and the film thickness (d). That gives a simple method of estimation of thin metal film parameters; however, this could be done more precisely using data fitting software.

The response of the SPR transducer to chemical or bio-chemical reactions (including molecular adsorption) can be monitored as the time dependence of the reflected light intensity at a fixed angle of incidence. In the case of detection of rather large biomolecules, such as proteins, it is more appropriate to use the value of the refractive index fixed to 1.42 at 633 nm (which is a typical value for proteins), and only consider changes in the molecular layer thickness. In the case of the adsorption of small molecules in the bulk of the sensitive membrane, the thickness can be considered to be constant; thus, the shift of the SPR curve is associated with changes in the refractive index. The broadening and dumping of the SPR minimum can be interpreted as an increase in the k-value. The interpretation of changes in SPR curves depends largely on the preliminary knowledge of the system and requires a great deal of experience. The SPR response due to chemical reactions, biochemical reactions, or molecular adsorption can be monitored as the time dependence of the reflected light intensity at a fixed angle of incidence. It is worth mentioning that the choice of the angle of incidence is important for maintaining the linearity and wide

dynamic range of the response. To fulfill the linearity, the angle of incidence is usually chosen on the left side of the SPR, on its linear part, and as choose as possible to the SPR minimum, as shown in the typical SPR curve (Figure 2.15), the linear dynamic range ΔR can be defined as a vertical projection of a left linear part of the SPR curve. The SPR method has found numerous applications as a film characterization technique capable of measuring n and k with an accuracy ranging from 10^{-4} to 10^{-5}, and the thickness with an accuracy of 10^{-2} nm. Because of a high sensitivity towards n, k, and d, as well as convenient geometry of measurements, which does not involve light propagation through the ambient, SPR has become very popular in chemical and biosensing applications.

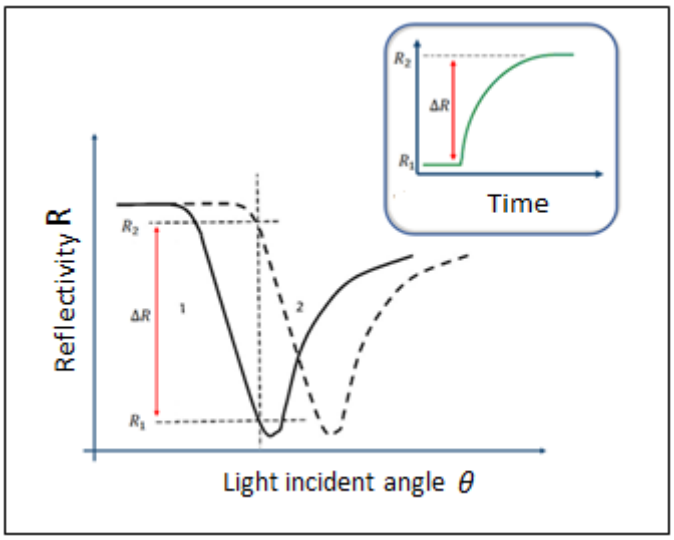

Figure 2.15 The illustration of kinetic SPR measurements at a fixed angle of incidence.

There are several practical realizations of SPR methods, which can be split into two principally different groups, namely, spectral SPR and angular SPR. In a typical

angular SPR experimental-set-up, shown in Fig. 2.16, a light beam from a HeNe laser goes through the aperture and becomes p-polarized after passing the polarizer is then modulated with the chopper. Part of the beam reflected from the beam splitter and captured with the photo-detector serves as a reference signal channel. The other part of the beam targets the semi cylindrical prism, with the gold-coated glass slide attached to the back via index matching fluid. The prism is maintained on rotating stage. The reflected light is collected with the photo-detector and forms the main signal channel. The signals of the main and reference channels are fed into the lock-in amplifier which is fed into PC via the IEEE card. The dedicated software controls the stepper motor, which turns the stage.

The angular dependence of the reflected light intensity $I_{(\theta)}$ is therefore recorded with the PC. There exist many other modifications of angular SPR techniques having different methods of the detection of $I_{(\theta)}$. For example, as shown in Fig. 2.17, the use of a fan-beam allows the registration of the $I_{(\theta)}$ curve instantly with the photodiode.

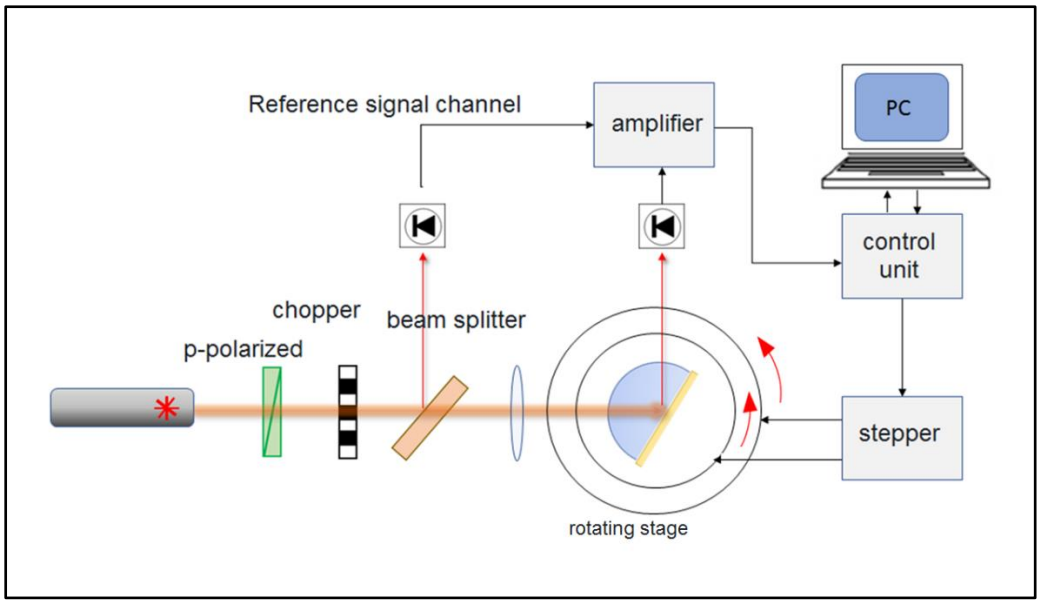

Figure 2.16 Typical angular SPR experiment set-up

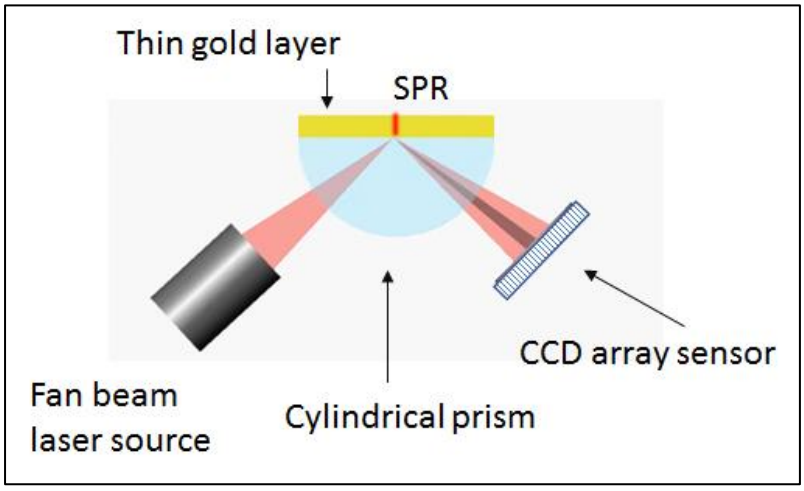

Figure 2.17 Angular SPR experiment using fan beam light.

Spectral SPR instruments depend on recording the spectrum of the reflected light, when irradiating the gold-coated glass slide through glass prism with white light and examining the spectra of reflected light. Molecular binding events will lead to

changes in the wavelength at which resonance occurs, and this can be detected via changes in the intensity across the spectrum.

2.3.6 Localized surface plasmon resonance based biosensor

The interaction of light with nanometer-sized (sizes smaller than the wavelength of light) structures of noble metal produces a collective oscillation of conduction electrons known as the localized surface plasmons, as illustrated in Fig. 2.18. The resonance conditions are established when the frequency of electromagnetic wave matches the natural frequency of oscillation of free electrons in metal nanostructures, e.g. nanoparticles; this phenomenon is called as localized surface plasmon resonance (LSPR). This situation is completely different from conventional SPR when the evanescent electromagnetic wave propagating along the metal/dielectric interface interacts with free electrons in thin continuous metal thin film (see Fig. 2.18b). The occurrence of LSPR also results in a strong absorption of incident light. The position of the LSPR spectral band (shown in Fig. 2.19) depends on sizes, shapes, and type of materials of the nanoparticles or nano-structures.

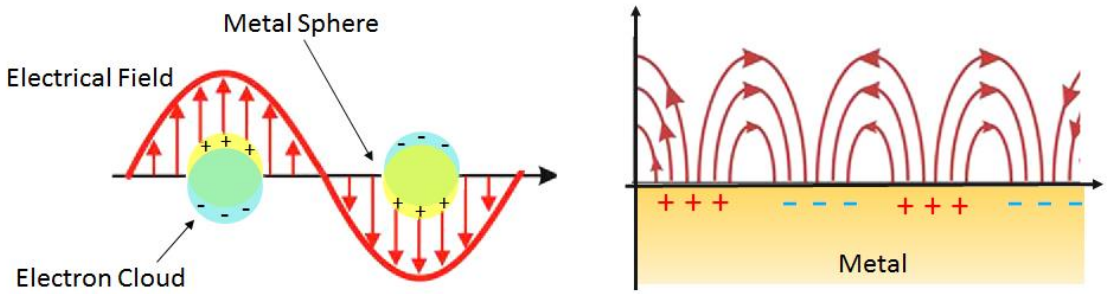

Figure 2.18 Interaction of EM wave with surface plasmons localized in metal nanoparticles (a), and surface plasmons in continuous metal film (b).

For gold and silver spherical nano-particles, the LSPR absorption bands are located in the visible spectral region, making these materials particularly suitable for different sensing applications. In addition, changes in the local medium surrounding the nanoparticles, caused for example by molecular adsorption, result in a shift of the LSPR band, which actually constitutes the main principle of LSPR biosensing.

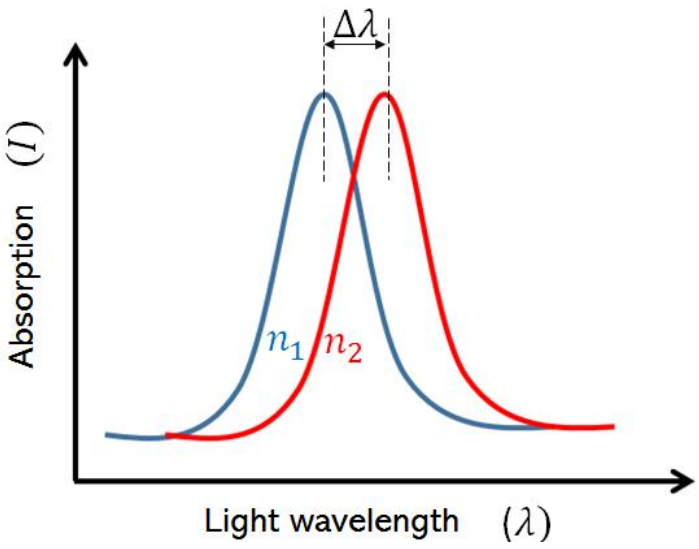

Figure 2.19 Typical LSPR spectra in the media of different refractive indices [68].

The dependence of the LSPR wavelength shift on the refractive index changes has been described by the following relationship [67]:

$$\Delta\lambda = S\Delta n \, exp\left(\frac{-2d}{\chi}\right) \tag{2.10}$$

where Δn is the change in refractive index of a medium, S is the refractive index sensitivity of LSPR transducer measured in nm per refractive index unity (nm/RIU), d is the effective thickness of the molecular layer (in nm) and χ is the characteristic electromagnetic field decay length (in nm). The expression given in Eq. (2.10) forms a basis for LSPR wavelength-shift based sensors. In terms of biosensing, the binding of analyte molecules to the surface of the nanoparticle causes changes in local refractive index near the nanoparticle surface, which in turn causes the shift the LSPR peak. LSPR sensor technique employs such changes as a sensing indicator for the presence of the target molecules. The exponential decay of the LSPR transducer response in Eq. 2.9 demonstrates the limitation of LSPR method which is related to a rather short evanescent field decay length (in tens of nanometers) as compared to that in traditional SPR (around 150-300nm) [10] (see the illustration in Fig. 2.20). As a consequence of this, the thickness (d) of a bio-sensing layer (for example, a layer of immobilized antibodies) should be smaller than χ, otherwise the sensitivity of LSPR will be compromised. Therefore, the use of small size bio-receptors, such as split antibodies, nano-bodies, or aptamers is beneficial for LSPR sensors [68].

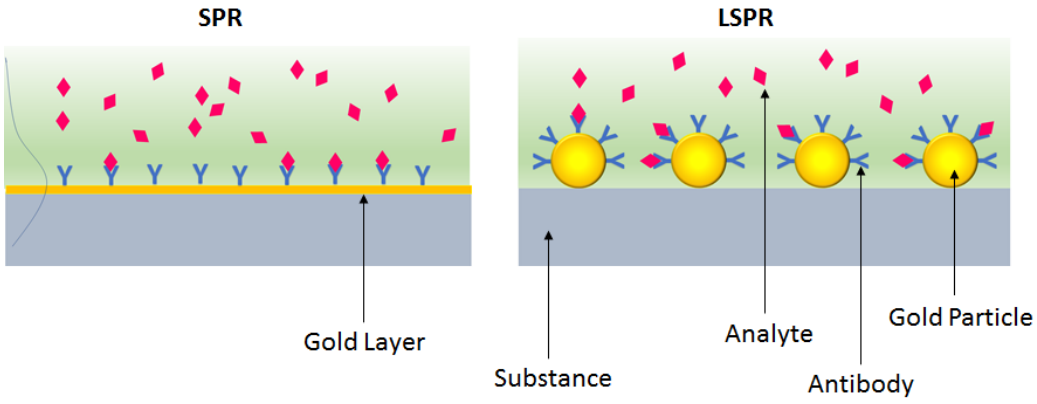

Figure 2.20 Comparison of the effect of evanescent field decay length in conventional SPR (A) and LSPR (B) biosensing.

The LSPR sensors can be fabricated either by depositing metal nanoparticles (NPs) on the surface of glass slides or optical fiber, or by simply suspending metal NPs in solution to form a solution-phase LSPR sensor. Various optical geometries can be used in LSPR sensors; the two most common geometries and modes of operation are transmission and reflection modes are shown in Figure 2.21.

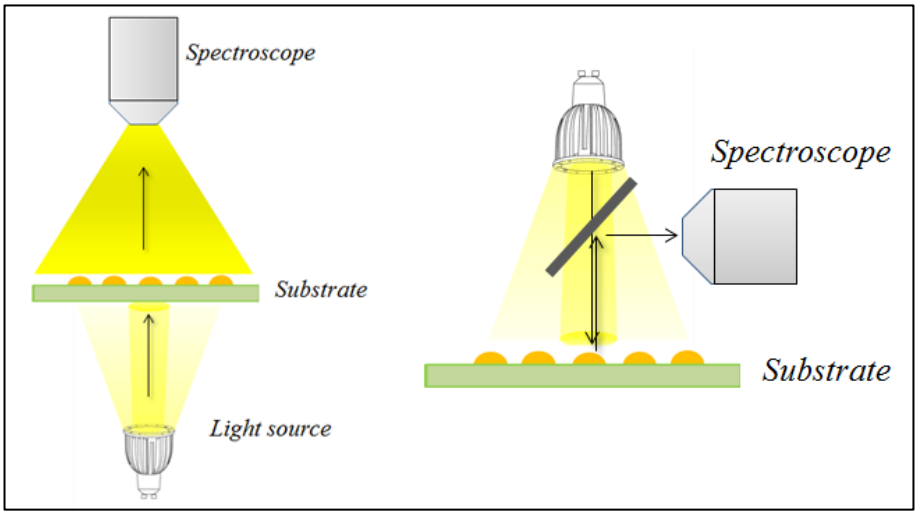

Figure 2.21 LSPR detection modes: transmission (left) and reflection (right).

The use of metal nanoparticles is only one possibility for LSPR sensing. These days, many other types of metal nanostructures are utilized in LSPR sensing, which

includes non-spherical nano-particles or nano-rods [69] , nano-islands [70], and nano-holes [71] which can be either random in their shapes, sizes, and lateral distribution or ordered metal nanostructures formed by different types of nano-lithography, e.g. electron-beam lithography [72], interference lithography [73], colloid nano-sphere lithography [74], etc. Several metals can be used in such nano-structures, most commonly gold [75] and silver [76].

The effect of LSPR is typically exploited in biosensing by monitoring the spectral shift of the LSPR band caused by binding of analyte molecules to metal nanoparticles, which could be functionalized with specific bio-receptors, e.g. antibodies, or aptamers. The refractive index sensitivity (S) of LSPR biosensor found from the gradient of a linear dependence of the LSPR frequency versus refractive index [77, 78].

2.3.7 Ellipsometry based biosensors.

The method of ellipsometry, which will be described in detail later in Ch. 3, is based on detection of changes in polarization of light upon its reflection from the investigated sample. In ellipsometry, the polarization of light is described by two parameters Ψ and Δ which are, respectively, the ratio of the reflection amplitudes r_p and r_s and the phase shift between them. The relations between the above reflection coefficients for p- and s- polarizations of light with the optical constants of the reflective surface are established through Fresnel's equations (in Ch.3). For example, in the case of a thin film on the surface of metals or semiconductors, the values of the thickness (d), refractive index (n) and extinction coefficient (k) can be

found from the recorded values of Ψ and Δ, In spectroscopic ellipsometry, the spectra of Ψ(λ) and Δ((λ) yield the dispersion characteristics of *n(λ)* and *k(λ)* the thin film as well as its thickness *d*. Ellipsometry is a very sensitive analytical tool typically used for characterization of materials in semiconductor industry and microelectronics. The accuracy of ellipsometry measurements (which depends on the instrumentation used) can reach 10^{-5} for *n* and *k*, while the thickness accuracy can go down to 10^{-3} nm.

The ellipsometry is also capable of detection of molecular adsorption on the surface and thus can be used in chemical- and bio-sensing. However traditional (external reflection) ellipsometry is hardly used in sensing due to several reasons, mainly because of the fact that the light goes through the detected medium, as shown in Fig. 2.22. This method may work reasonably well in gas-sensing; in biosensing, however, the changes in the medium refractive index due to injection of different solutions can affect the measurements. Cloudy solutions cause more problems due to the light scattering. The design of a cell for ellipsometry sensing create additional challenges: (i) the cell has tobe made of chemically

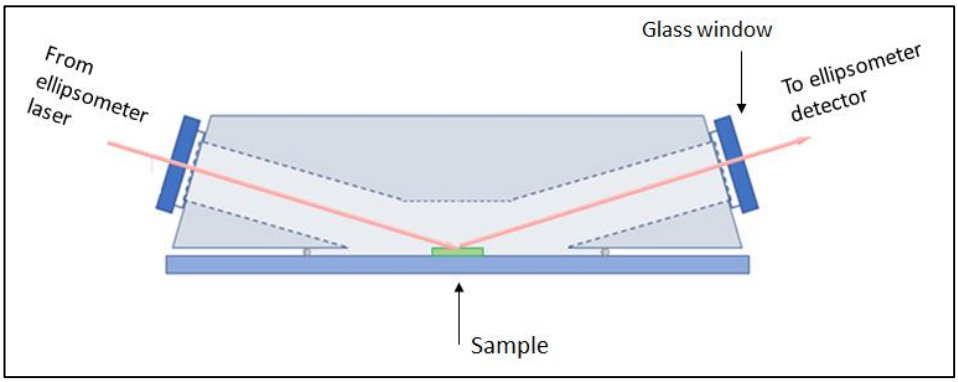

Figure 2.22 External reflection ellipsometry sensor geometry

inert material such as PTFE; (ii) it is supposed to have transparent windows which do not alter polarization of light; (iii) the cell must have a small volume to be suitable for bio-sensing applications. The latter demand is particularly difficult (practically impossible) to achieve. The above limitations of exploiting ellipsometry in chemical and biosensing can be overcome with the use of total internal reflection ellipsometry (TIRE) [79, 80, 81]. This method combines the advantages of highly accurate spectroscopic ellipsometry instrumentation with experimental convenience of Kretchmann SPR geometry. As shown in Figure 2.23a, the addition of a 68^{o} prism to

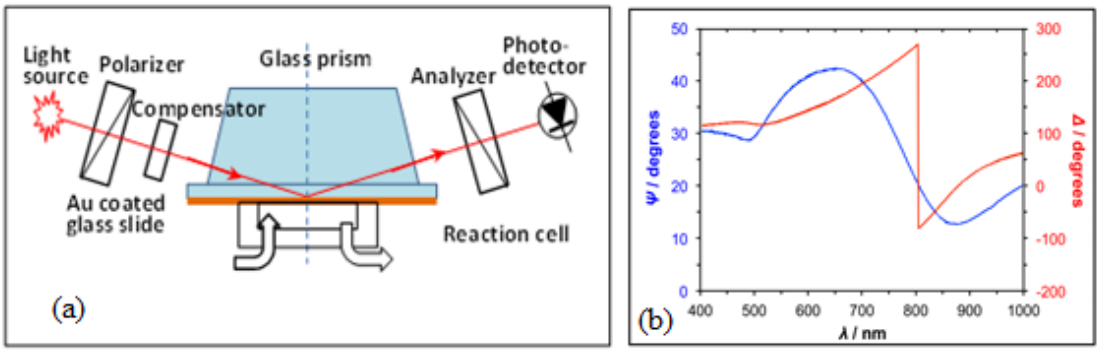

Figure 2.23 The scheme of TIRE (a) and typical Ψ and Δ TIRE spectra of gold-coated glass slide (b).

standard spectroscopic instrument allows coupling light into a thin metal film at conditions close to total internal reflection (between glass n=1.515 and water n=1.33). A cell of a very small volume can be attached underneath to perform various biochemical reactions. The main difference between SPR and TIRE is that in TIRE the spectra of two parameters, e.g. amplitude related Ψ ($\Psi = tan^{-1} r_p/r_s$)

and phase-related Δ ($\Delta = \varphi_p - \varphi_s$) can be recorded, while only the amplitude of p-polarized light was recorded in SPR. As one can see from Fig. 2.23b, the spectrum of $\Psi(\lambda)$ closely resembles the SPR curve $R(\theta)$. At the same time, the spectrum of $\Delta(\lambda)$ exhibits a sharp, almost vertical drop from 270^o to 90^o at the wavelength close to the surface plasmon resonance. The parameter Δ is about 10 times more sensitive than Ψ to changes in the thickness or refractive index of a molecular layer on the surface of gold, so that $\Delta(\lambda)$ spectra are mostly used in TIRE bio-sensing [82].

The method of TIRE was successfully exploited for detection of small molecules of mycotoxins, pesticides, alkyl-phenols [83] in low concentrations down to 0.1 ng/ml in direct immuno-assay form with specific antibodies immobilized on the surface of gold, while the sensitivity of conventional SPR was not sufficient for such tasks. Recently, the transducing method of TIRE was successfully adapted for LSPR bio-sensing because of 3 to 4 times higher refractive index sensitivity (RIS) in comparison with traditional UV-vis absorption spectroscopy [84]. With the use of small-size bio-receptors, i.e. split-antibodies and aptamers, covalently immobilized on the surface of gold nano-islands on glass slides, the detection of mycotoxins on concentrations down to 0.01 ng/ml was achieved [85].

2.3.8 Interferometry sensing methods.

The extraordinary sensitivity of interferometry sensors is due to their operational principle which is based on the interference of two electromagnetic (EM) waves having different optical path lengths. In a typical interferometry sensor, one of the EM waves interacts with the medium (it could be named as a sensing channel), while the other one is not affected by the surrounding medium as thus serves as a

reference. When both waves meet and interfere, the intensity of the resulting light (I) is a periodic function of phase variation ($\Delta\varphi$) [86]:

$$I_{Output}(\Delta\varphi) = I_R + I_S + 2\sqrt{I_R I_S}\cos(\Delta\varphi) \quad (2.11)$$

where I_S and I_R are the light intensities of the sensing and reference channels, respectively. This dependence is shown in Fig. 2.24 where each peak corresponds to 2π phase shift between the sensing and reference channels. This phase variation can be related to the changes in the medium refractive index or to molecular adsorption or bio-molecular interaction in the sensing channel, [87].

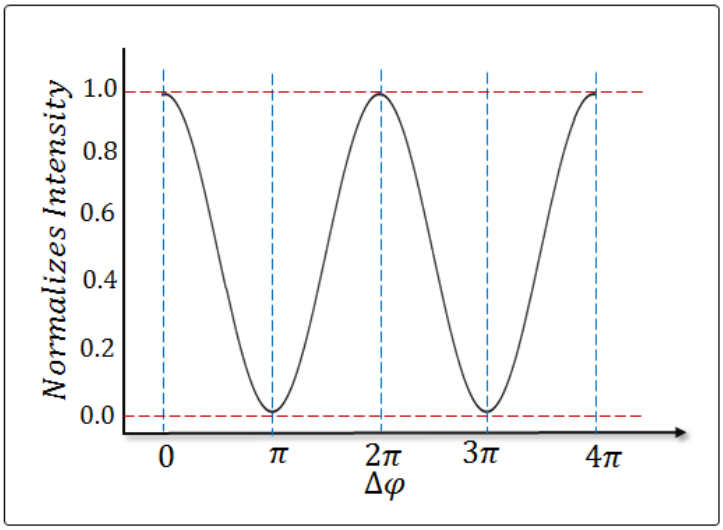

Figure 2.24 Interference pattern: the variation of the light intensity vs phase shift

A large number of interferometry methods have been developed, some of them were utilized in biosensing applications. The most common interferometry sensors are outlined in the following sections below.

2.3.8.1 The Fabry-Perot interferometry

Biosensors based on interferometry are the most sensitive optical devices. There are several interferometry methods which are employed in biosensing, and the Fabry-Perot interferometer based on porous silicon (PS) is one of the simplest examples of those [74]. This method relies on the interference of light reflected from the two interfaces, e.g. Si/PS and PS/medium, as shown in Fig. 2.25 [88].

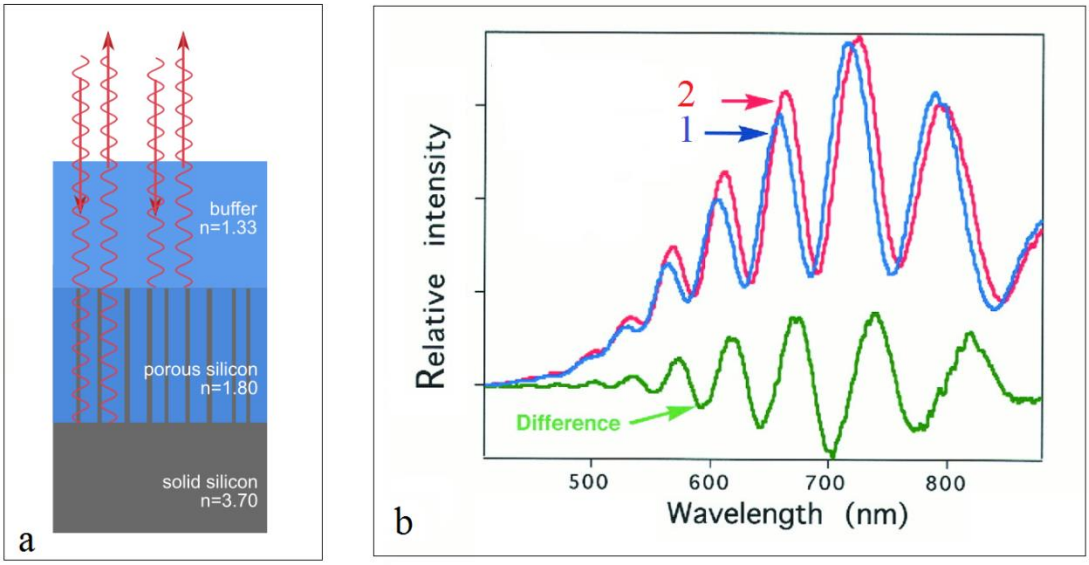

Figure 2.25 The structure of Fabry-Perot interferometry biosensor based on porous silicon (a), and typical interference spectra patterns (b); the shift between the spectra 1 and 2 is caused by protein adsorption.

The observed interferometry fringes appeared as a result of constructive interference following the conditions for the maximal intensity,[89]:

$$m\lambda = 2nd \tag{2.12}$$

where n and d are the refractive index and the thickness of the PS layer, respectively, and $m = 1, 2, 3..$ The number and positions of interference fringes depend on the refractive index n of PS layer, which consisted with Si columns separated by voids. Changes in the refractive index caused by adsorption of guest molecules, such as proteins, in the voids of PS layer lead to the shift of the interference pattern (see Fig. 2.27b). The concentration of absorbed molecules could be quantified by such spectral shift. Despite its simplicity, the method of Fabry-Perot interferometry has an advantage of a large surface area, which may absorb analyte molecules in much larger concentrations (from 10^2 to 10^3 times) than that on the flat surface, which leads to the substantial changes in refractive index, and subsequently to a large spectral shift of the interference pattern, and thus high sensitivity of molecular detection.

2.3.8.2 Mach-Zehnder (MZ) interferometer

In an MZI device a polarized monochromatic light is coupled into a channel waveguide and split at a Y-junction into two branches as shown in Figure 2.26. One of the branches represents a reference arm while the other one, having a sensing window, can interact interacting with the sample. The two spited light beams are recombined again by another Y-junction, where the two light beams have a phase difference due to the changes in the refractive index that occur in the sensing path.

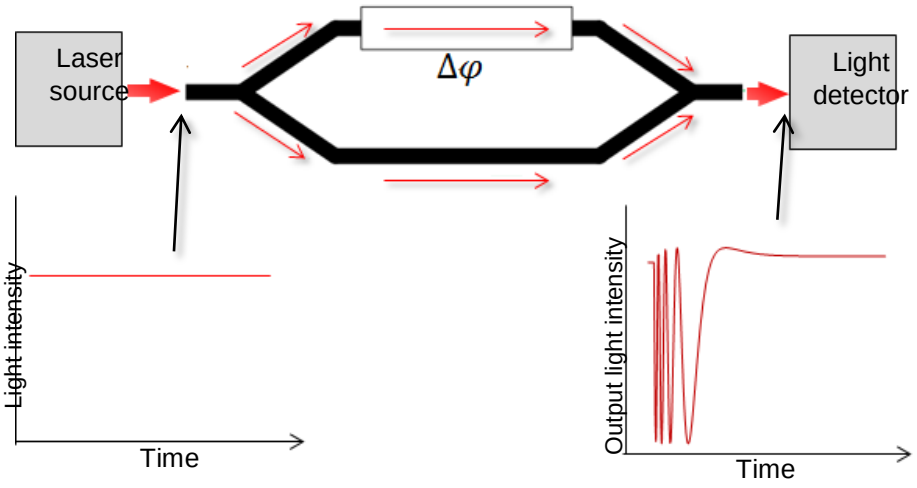

Figure 2.26 Schematic diagram of Mach–Zehnder interferometric sensor.

The phase variation can be expressed as [90-95]:

$$\Delta\varphi = \frac{2\pi}{\lambda} L\Delta N_{eff} \tag{2.13}$$

where L is the length of the sensor area, λ is the wavelength of the light and N_{eff} is the effective refractive index. The phase variation leads to variation in the intensity of the output light which can be collected by a photodetector or a CCD camera:

$$I \propto [1 + Vcos\Delta\phi] \tag{2.14}$$

where $\Delta\phi = (\phi_R - \phi_S)$ is the phase variation between the guided modes in the reference (ϕ_R) and sensing arm (ϕ_S) .

The visibility factor (V) determines the difference between the maximum and minimum intensities; it depends on the coupling factor of the divisor and on the propagation losses of the guided mode in the interferometer arms.

The relevant parameters influencing the sensitivity of a MZI configuration are the interaction length (L), the visibility factor (V) and the relative phase variation between the sensor and the reference arm (ΔN_{eff}). This configuration has achieved

high sensitivity. However, there are still some drawbacks of this method due to the cosine-type intensity distribution of the interference pattern, that involves: (i) a phase ambiguity of the signal due to its periodicity, (ii) possible misinterpretation of the signal due to intensity fluctuations of the light source and (iii) sensitivity fading when the signal is tuned close to one of the extreme values of the transmission curve [96, 97, 98, 100].

2.3.8.3 The Hartman interferometer (HI)

In this method, the light is divided into two beams by a splitter outside the chip, which then are coupled to the slab waveguide using gratings. In the chip, the light pass through contiguous regions one of them functionalized with specific (sensing path) or non-specific receptors (reference path), as shown in Fig. 2.27. The light outputs from both regions using gratings, then combined via a lens, generating an interferogram in a CCD camera. This configuration overcomes the issues related to the sinusoidal signal by signal processing using fast Fourier transform (FFT).

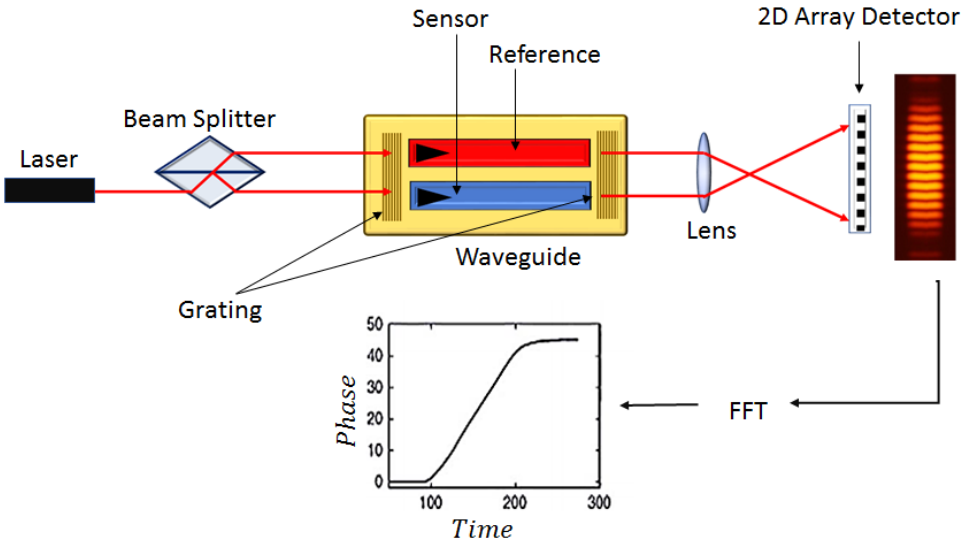

Figure 2.27 Schematic diagram of Hartman interferometer.

The crosstalk effect between sensing and reference beams which highly increases the noise in the detection, limits the sensitivity of this sensor configuration. Moreover, [101].

2.3.8.4 The Young interferometer (YI)

In this method the light is coupled in a channel waveguide then split by a Y-divisor into two beams, one of them travels through the sensing area and the other through the reference path, as shown in Fig. 2.28. The output light from both paths is projected onto a CCD sensor; the recorded interferogram is analysed using FFT.

In this configuration the optical path length Δl difference of the two beams interfering on x position at the CCD array at position is given by, [98, 102]:

$$\Delta l = \frac{nw}{D} y \tag{2.14}$$

where n is the refractive index, w is the distance between the two outputs of the integrated optical y branch, and D is the distance between the chip edge and diode array, respectively; normally $D \gg w$. The phase difference $\Delta\phi$ between the two beams is given by:

$$\Delta\phi = \frac{2\pi}{\lambda_o} \Delta l = \frac{2\pi}{\lambda_o} \frac{nw}{D} y \tag{2.15}$$

Where λ_o is the wavelength in vacuum.

The Young Interferometer sensors can achieve high sensitivity and unambiguous signals, however the required distance between the waveguide output and the CCD sensor makes it more affected by mechanical vibrations and less suitable to use it as portable device [103].

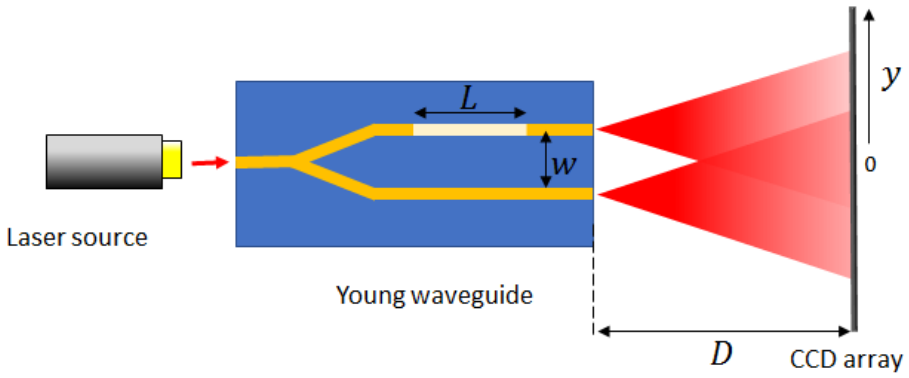

Figure 2.28 Schematic diagram of Young interferometer

2.3.8.5 Dual polarization interferometry (DPI):

This sensor (shown Figure 2.29) uses two slab waveguides and an additional layer is placed between both waveguides to provide effective optical isolation, the lower layer is the reference waveguide and the upper layer (opened to environment) is the sensing one [14]. The resulted diffraction pattern is projected at CCD array for data processing. The diffraction pattern can be described by a set of fringes modulated in the y direction and enveloped in Gaussian function. For a propagation over a distance D maxima and minima of intensity should be separated by a distance a according to:

$$a = \frac{\lambda D}{w} \tag{2.16}$$

Where λ is the wavelength and, w the separation of the sources.

There is a linear relationship between the position and phase, and it is possible to find the relative position shift Δx of the fringe maxima in terms of the $\Delta\phi$ [58, 104, 105];

$$\Delta\phi = \frac{2\pi \Delta y}{a} \tag{2.17}$$

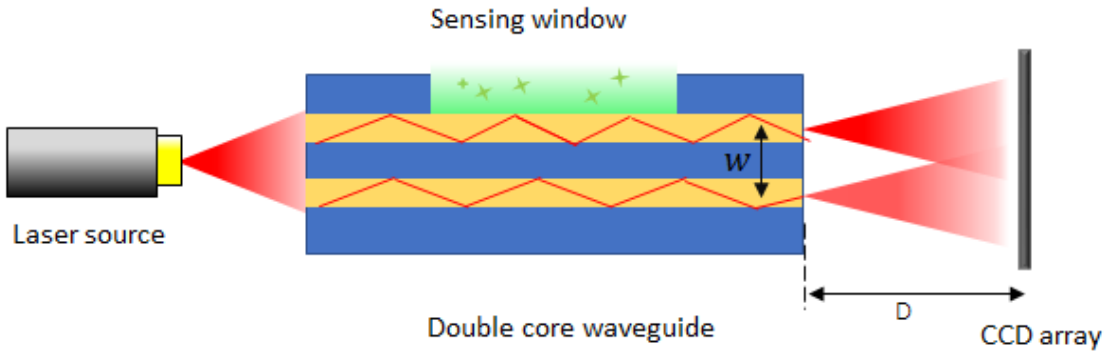

Figure 2.29 Schematic diagram of Dual polarization interferometry.

2.3.8.6 Bimodal Waveguide interferometer (BIMW)

In this technique two modes of light of the same polarization and wavelength but of different orders (TE0 and TE1) travel while interfering in a straight waveguide. Light is coupled in a single-mode waveguide in which only TE0 can propagate, then after some distance, light is coupled into another waveguide can support two transversal modes. So that, in the step junction, TE0 and TE1 are excited and both propagate until the end of the chip. The interference of both modes when a bio-interaction occurs on the sensor area produces a phase variation according to [98]:

$$\Delta\phi = \frac{2\pi}{\lambda} L \Delta N_{eff} = \frac{2\pi}{\lambda} L(N_{eff}(TE_1) - N_{eff}(TE_o)) \tag{2.18}$$

Where L is the length of the sensor area and l is the working wavelength.

In this device shown in Fig. 2.30 the output light is projected on a two-section photodetector generating currents I_{up} and I_{down} in the upper and lower sections, respectively. These values are employed to calculate the signal (S) which is proportional to the phase variation $\Delta\phi$ according to the expression, [98]:

$$S = \frac{I_{up} - I_{down}}{I_{up} + I_{down}} \propto \cos(\Delta\phi(t)) \tag{2.19}$$

From this equation it can be deduced that the interference pattern is independent of the light intensity and the output signal is not sensitive to fluctuations in the coupling efficiency. Furthermore, the signal will not vary by fluctuations in the input light [98, 106].

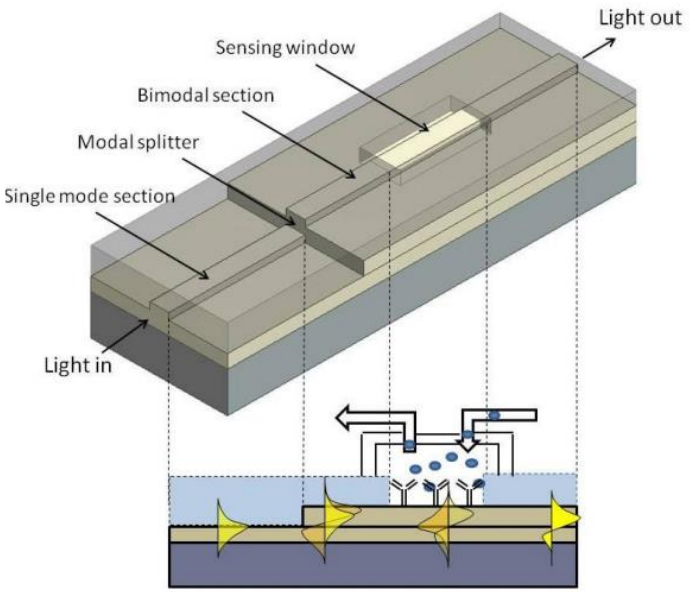

Figure 2.30 Schematic diagram of Bimodal Waveguide, and distributions of electromagnetic fields sketched in several points through the waveguide [107].

The BiMW device has demonstrated high sensitivity. However, this configuration also has drawbacks of phase ambiguity which leads to sensitivity fading that requires normalizing the signal output to solves the misinterpretation. It is easy to conclude from the above, that the devices that consist of channel waveguides (MZI, YI) are more complex for fabrication than the devices based on slab waveguides (HI, DPI). While, the signal processing of slab waveguides is more difficult for multiplexed detection since parasite light and crosstalk must be minimized, [98, 107].

2.3.8.7 Polarization interferometer

This device consists of a single channel planar waveguide. The widow in the upper cladding layer exposes the core to environment. When the polarized light propagates through the core of the waveguide and pass the sensing window, its p-component (parallel to the plane of incidence) penetrate into the medium and could be affected by changes in the medium refractive index. At the same time, s-component of polarized light (perpendicular to the place of incidence) is much less affected (practically not affected) by the medium and it can serve as a reference. A phase shift between p- and s- components of polarized light can be employed as indicator of the changes in the refractive index or optical property of the medium. As illustrated in Fig. 2.31, such changes can be caused by molecular adsorption or binding of analyte molecules to bio-receptors immobilized on the surface. The output signal of polarization interferometer forms by converting changes in polarization of light to the light intensity using a linear polarizer. The resulted multi-periodic output signal is described by according to Malus's formula [108, 109]:

$$I_{(\theta)} = I_O Cos^2\theta \tag{2.20}$$

Where θ is the angle between polarizer axes and polarization of light, I_o and I_{in} are the intensity of the light before and after polarizer, respectively.

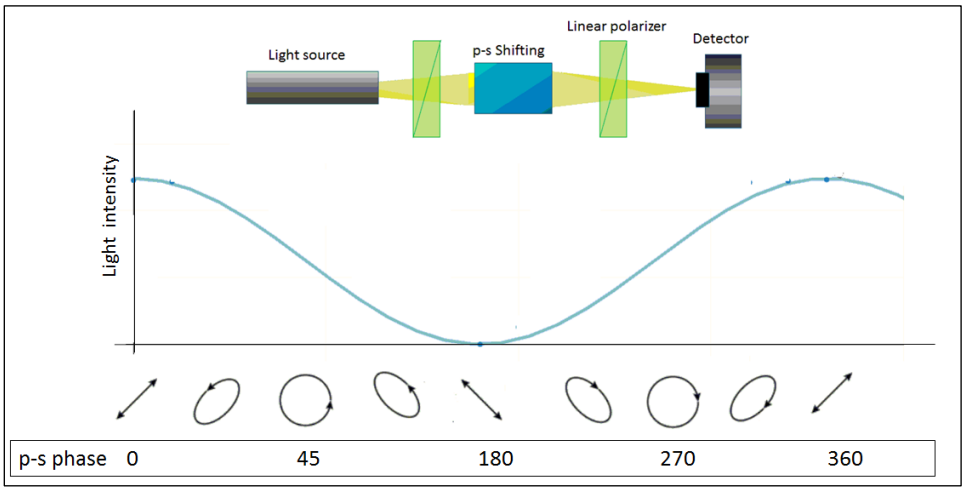

Figure 2.31 Mechanism of generate PI signal, convert the change in polarization state to change in light intensity via linear polarizer.

The operation principle of PI is very similar to that of MZ interferometer; but the main advantage of PI is in the simplicity of its design which makes it very attractive for biosensing applications. There were several attempts of utilizing OPW PI devices in bio-sensing and demonstrating potentially remarkable sensitivity of such devices [110, 111], but they were not followed by commercial applications. The current PhD

project mainly focuses on further development of OPW PI biosensors as a platform biosensing technology for a wide range of applications.

2.3.9 Fiber-Optic Bio-Sensors:

The light travelling through the optical fibre is not usually affected by surrounding environment unless suitable configuration changes were made to allow the EM wave interacting with the external medium. The removal of the cladding layer allows the evanescent field of the core mode to react with the surrounding medium. The penetration of the evanescent field outside the core boundary can be exploited to probe the surrounding environment using different sensing techniques which include [112]:

- changes in the output power due to refractive index changes alone
- evanescent field absorption,
- fluorescence,
- Surface Plasmon Resonance.

When light propagates through an optical fibre by repeating total internal reflection at the core-cladding interface, in absence of the cladding layer in the part which is designed to work as a sensor, the radiation extends a short distance from the guiding region into the medium via evanescent field which accompany the total internal reflection. The evanescent wave may interact with the environment by means of refractive index changes, absorption, or scattering; the power associated power losses can be described as [113]:

$$P_{out} = P_{in} \frac{(n_1^2 - n_s^2)}{(n_1^2 - n_2^2)} \tag{2.21}$$

where n_1 is the refractive index of the core, n_2 is the refractive index of the cladding, n_s is the refractive index of the sample surrounding the core, P_{in} represents the power coupled into the guided modes of the fibre from the source, and P_{out} is the power coming out of the fibre sensing region to reach the detector [114].

2.3.9.1 Evanescent field absorption:

This method relies on fact of decreasing the output light intensity due to its absorption by the analyte which depends on the analyte concentration. The power transmitted by an optical fibre whose cladding has been replaced locally by an absorbing medium may be written in the form:

$$P(z) = P(o)\exp(-\gamma z) \tag{2.22}$$

where $P(O)$ is the power transmitted in the absence of absorbing species, z is the distance along the un-cladded fibre length, and γ is an evanescent absorption coefficient [115, 116].

2.3.9.2 Fluorescence. number sections properly

This method relies on detection of fluorescence that can be induced by the evanescent field, and which indicates the presence of the analyte (see Fig. 2.32). The most common method is the use of sandwich assay, with primary antibodies covalently bonded to the surface of the fibre. Then, the target analyte molecule that binds to the antibody is introduced; the presence of this biomolecule is then confirmed by binding a secondary fluorescent-labelled antibody, which fluoresces when excited by the evanescent wave in the optical fibre [109, 117].

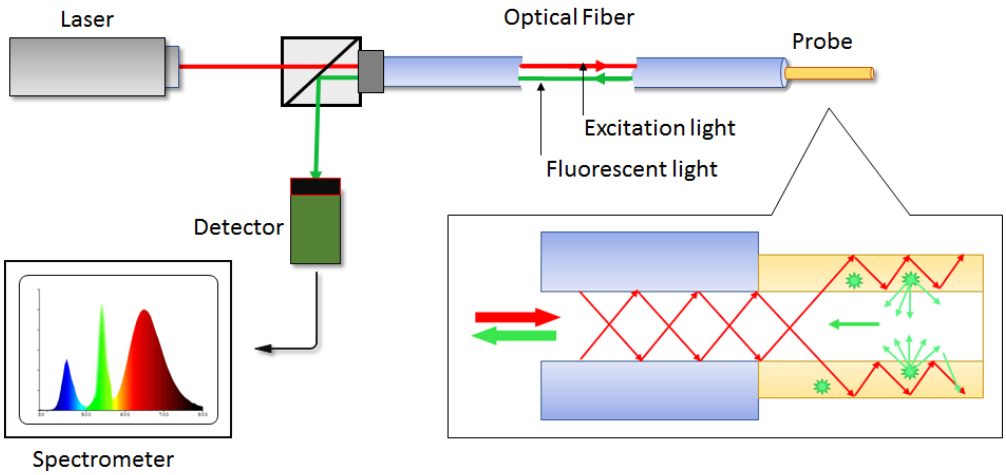

Figure 2.32 The principle of optical fibre sensing based on fluorescence.

In this method, the surface plasmons, e.g. the oscillations of free electrons in thin metal layer coted the fibre core, are stimulated by evanescent field. When SPR occurs, the intensity of reflected light is greatly reduced. The shift of the resonance due to adsorption (or binding) of analyte molecules on the fibre core surface can be monitored by the angle or wavelength of the output light, similar to Kretschmann SPR. Moreover, the use of optic fibres has certain advantages over traditional prism-based SPR, i.e. more simple, small, and flexible design which also allows for multi-channel and remote sensing [118].

2.3.9.3 Fibre grating sensor

Optical fibre grating sensors can be classified into two groups having either (i) short-period gratins with the grating pitch in order of hundreds of nanometres and called fibre Bragg grating sensors (FBGS), or (ii) long-period gratings sensors (LPGS) when the modulation period ranges between 100 μm and 700 μm, [119, 120]. Fibre Bragg Grating (FBG), in simple words, is a mirror for a narrow band of

wavelengths passing through optical fibre, as illustrated in Fig. 2.33. It is transparent for other wavelengths, which pass unchanged through the fibre. This wavelength specific, mirror-like effect is achieved by creating a periodic change in the effective refractive index of the fibre core. If the wavelength propagating through the FBG has a period which is a multiple of the period of the Bragg Grating, such that all the reflected components interfere constructively (while forward waves have destructive interference), the wavelength will be reflected. For the case of a constant periodical index modulation, the backward constructive interference occurs in a narrow range of wavelengths around the Bragg condition which can be written down as, [121]:

$$\lambda = 2n_{eff}\,\Lambda \tag{2.23}$$

Where λ is the wavelength of a light, n_{eff} is the effective refractive index of the core mode and Λ is the period of the refractive index modulation.

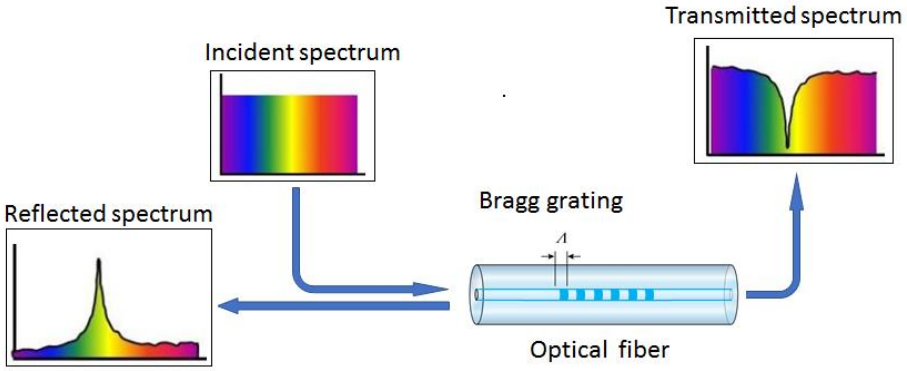

Figure 2.33 Fibre Optic Bragg Grating sensor principle

The reflectivity of Bragg grating is affected by grating strength and length. The increase of the magnitude of the refractive index changes of the grating structure enhances the reflectivity (Fig. 2.34). Moreover, increasing the Bragg grating length increases the reflectivity which can reach almost 100% in a few centimetres long section of a fibre.

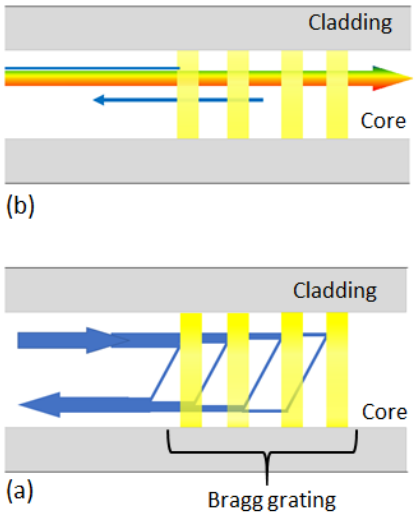

Figure 2.34 The effect of the grating length on reflectivity. All light spectrum going through the grating zone except Bragg wavelength (a), Each line of the grating contributes to reflect part of the light for the particular wavelength, each line in the grating reflects back some of the light for the particular wavelength hundreds of lines enough to complete reflection all of the wavelength is reflected back (b).

The Bragg wavelength of an optical fibre grating is a function of a grating period (Λ) and the effective refractive index (n_{eff}) of the fibre core according to equation (2.23). Thus, any changes in the refractive index or the grating period due to external factors, e. g. molecular absorption, will change the Bragg wavelength of the device

and can be detected in either the reflected or transmitted spectra of FBGs. Therefore, fibre gratings are excellent elements for sensing applications, and the basic principle of its operation is the monitoring of the shift in Bragg wavelength, λ_B with the changes in refractive index [122].

2.3.9.4 Long Period Gratings:

A Long Period Grating (LPG) is a periodically changing structure along the fibre, similar to that of a Bragg grating. The period is however, much large, on the scale of a hundred of micrometers or even millimeters, so that Long Period gratings are generally easier to inscribe; they can be written directly into the cladding on the external surface of the optical fibre. While the Bragg grating acts as a mirror for the light propagating through the core mode, the Long Period grating couples the light from the core modes to the co-propagating cladding modes. As light cannot efficiently propagate in the cladding, meaning that it is scattered and attenuated quite fast, the Long Period Grating takes away the core wavelengths which phase-matched with its period, as shown in Figure 2.35 [123, 124, 125].

For the wavelengths of the light propagating trough the fibre, which match the LPG period, upon interaction, LPG changes the modes direction and the core mode is coupled into the cladding mode. As light cannot propagate far through the cladding due to scattering, the LPG acts as a wavelength filter.

The phase matched wavelengths occur in the transmission spectrum as a loss dip in the spectrum, the coupling wavelength is given by the phase-matching conditions described by the following equation [123]:

$$m\lambda_{LPG} = \left(n_{Core}(\lambda) - n^{i}_{Cladding}(\lambda)\right)\Lambda \tag{2.24}$$

with m being the order of coupling, Λ is the period of the grating, $n^{i}_{Cladding}(\lambda)$ is the refractive index of the i mode of the cladding, and $n(\lambda)$ is the refractive index of the core. If the LPG changes due to the temperature, humidity, as well as mechanical stresses, the parameters of the coupling equation do also change, resulting in the loss wavelength shift at the output end.

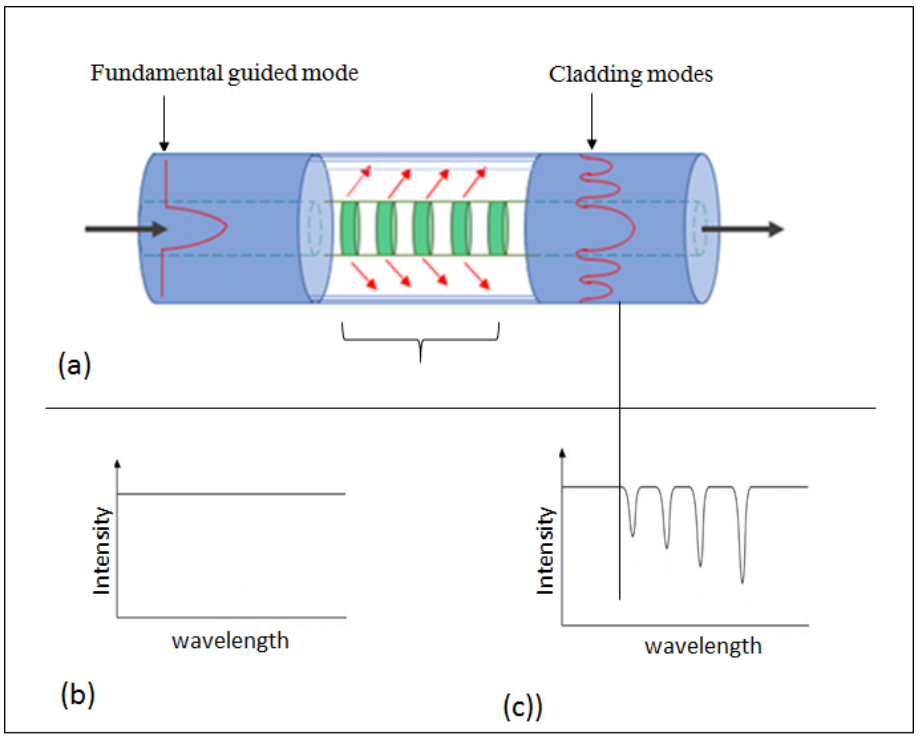

Figure 2.35 (a) Schematic illustration of principles of LPG, and (b) transmission spectra of LPG fibre.

Therefore, in LPGS several attenuation bands at discrete wavelengths appear in the transmitted spectrum, with each attenuation band corresponding to the coupling to a specific cladding mode. [126]. LPG sensor consists of long period grating fibre

coated by biological recognition layer which enables the surface of the fibre to bind the target molecules. Binding the target molecules give rise the changes in the refractive index that surrounded the fibre and thus shifts the Bragg reflected wavelength in FBG sensor or change the transmission spectrum in LPG sensor [127, 128].

2.3.10 Raman spectroscopy and SERS biosensors

The method of Raman spectroscopy, particularly its latest version of surface enhanced Raman spectroscopy (SERS) is one of most promising spectroscopic techniques for bio-sensing applications. It is worth to be mentioned here because it is strongly linked with the metal nanostructures. Raman spectroscopy is based on the phenomenon of inelastic light scattering and can provide characteristic IR spectral signature characteristics for a wide variety of chemicals (Fig. 2.36).

When photons are incident to the sample, they can be scattered elastically (with no changes in energy) or in-elastically (with changes in energy). Raman spectroscopy is based on inelastic scattering of photons following their interaction with vibrating molecules of the sample. During this interaction, photons transfer energy to/from molecules as vibrational energy. Thus, the energy change of the scattered photons corresponds to the vibrational energy levels of the sample molecules (see Figure 2.33A) [129, 130, 131].

subsequently focused on an array of detectors, such as a high sensitivity charge coupled device (CCD). The spectrometer is equipped with a filter to reject the elastically scattered photons, which have the same (high) energy as the laser photons and produce an intense peak which diminishes all much weaker Raman peaks. There

is another technique, when optical microscope is coupled to the spectrometer named Raman micro-spectroscopy to enable both excitation and collection of Raman spectra in micro scale.

Since the probability of Raman scattering event is very low (in one out of million molecules), the Raman vibration spectral lines have very low intensity, which constitutes the major drawback of traditional Raman spectroscopy.

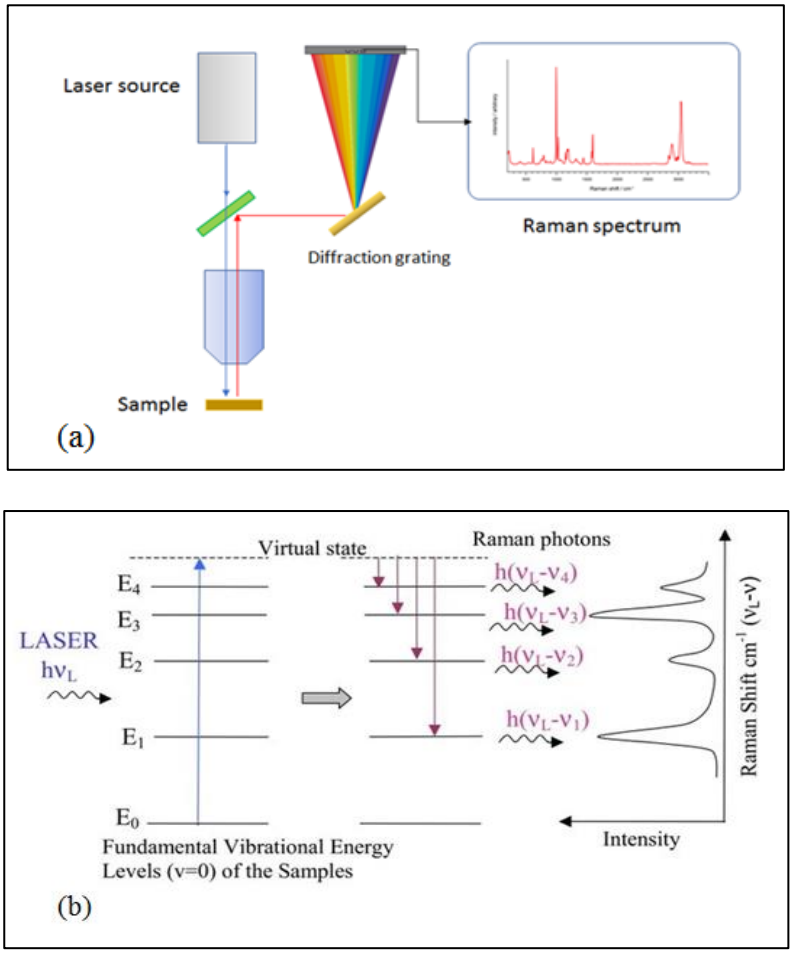

Figure 2.36 (a) experimental set-up for Raman spectroscopy measurements, (b) Schematic representation of Raman (Stokes) scattering of photons by vibrating

molecules in the sample: energy is transferred by photons to the molecules as vibrational energy, the energy loss correspond to the vibrational energy levels of the molecules (E1, E2, …)

The recent progress in this field is associated with the phenomenon of surface enhanced Raman spectroscopy (SERS),[132] in which the probability of Raman scattering events is substantially enhanced (up to 10^9 times according to some reports) if they occur on a rough surface. There are several chemical and physical factors behind the Raman enhancement, the main factor is the enhancement of EM field on sharp edges. The initial SERS experiments were performed on electrochemically roughen silver surface [133.]. These days a substantial Raman enhancement (of 10^6-10^7 folds) was observed on metal nanostructures [134]; this effect goes side-by-side with LSPR. Recent progress in nanotechnology, particularly in fabrication of metal-nanostructures, promoted the application of SERS in biosensing [135.].

2.4 Conclusion

There are two main trends in mycotoxin detection methods: the traditional analytical techniques and biosensors. Traditional techniques involve wide range of methods from rapid tests which are easy to conduct, to high precision and high performance methods which are more time consuming and more expensive.

The rapid methods include through membrane based immunoassay, enzyme linked immunosorbent assay (ELISA), fluorometric assay with immuno-affinity clean-up column, immuno-chromatographic assay, and fluorescence polarization method. These rapid methods have detection limits range between 1 to 20 ppb and requires time (5-25) minutes, and the basic principle of each of these have been briefly explained in this chapter. The traditional analytical equipment that have more accurate and lower detection limits are the high performance liquid chromatography (HPLC) and mass spectrometry, they provide detection limit in the range of ng/ml. These techniques are laboratory based, complex and more expensive comparing with other traditional methods.

The other trend is the biosensors which are integrated devices, easy to use, and providing satisfying sensitivity. Biosensors typically consist of three main parts: bio-receptor, transducer, and signal processing system. Classification and brief review of different types of biosensors was given in this chapter.

Since this work focuses on the development of novel optical biosensing technologies, optical biosensors were discussed in more detail. Traditional optical biosensors are based on detection of changes in the optical properties of the materials induced by reaction of target molecules with bio-receptors, for example changes in

absorption spectrum, fluorescence, refractive index, polarization, etc. Among a large number of optical biosensors, the interferometry-based methods offer the highest sensitivity. For example, the biosensors based on Mach-Zehnder interferometers are capable of detection of molecules in sub-ppb range.

Therefore, this project was dedicated to further development of interferometry-based biosensors, using polarization interferometry principles and simple planar waveguide geometry. The aims and objectives of this work were outlined in Chapter 2.

2.5 References

1. Kumar, P., Mahato, D. K., Kamle, M., Mohanta, T. K., & Kang, S. G. (2017). Aflatoxins: a global concern for food safety, human health and their management. *Frontiers in microbiology*, *7*, 2170.
2. World Health Organization. (2017). Evaluation of certain contaminants in food: eighty-thrid report of the Joint FAO/WHO Expert Committe on food additives. In Evaluation of certain contaminants in food: eighty-thrid report of the Joint FAO/WHO Expert Committe on food additives.
3. Verstraete, F. (2008). European Union Legislation on mycotoxins in food and feed. Overview of the decision-making process and recent and future developments. Mycotoxins: Detection methods, management, public health and agricultural trade, 77-99.
4. van Egmond, H. P., Schothorst, R. C., & Jonker, M. A. (2007). Regulations relating to mycotoxins in food. Analytical and bioanalytical chemistry, 389(1), 147-157.
5. Bezuidenhout, S. C., Gelderblom, W. C., Gorst-Allman, C. P., Horak, R. M., Marasas, W. F., Spiteller, G., & Vleggaar, R. (1988). Structure elucidation of the fumonisins, mycotoxins from Fusarium moniliforme. Journal of the Chemical Society, Chemical Communications, (11), 743-745.
6. Meurant, G. (2012). Handbook of toxic fungal metabolites. Elsevier.
7. Sittig, M. (1981). Handbook of toxic and hazardous chemicals.
8. rSilva, O., Gomes, E. T., Wolfender, J. L., Marston, A., & Hostettmann, K. (2000). Application of high performance liquid chromatography coupled with ultraviolet spectroscopy and electrospray mass spectrometry to the characterisation of ellagitannins from Terminalia macroptera roots. Pharmaceutical research, 17(11), 1396-1401.
9. Liang, Q., Qian, H., & Yao, W. (2005). Identification of flavonoids and their glycosides by high-performance liquid chromatography with electrospray ionization mass spectrometry and with diode array ultraviolet detection. European Journal of Mass Spectrometry, 11(1), 93-101.
10. Kralj Cigić, I., & Prosen, H. (2009). An overview of conventional and emerging analytical methods for the determination of mycotoxins. International journal of molecular sciences, 10(1), 62-115.
11. Ismail, B. P. (2017). Basic principles of chromatography. In Food Analysis (pp. 185-211). Springer, Cham.
12. Mangold, H. K., & Stahl, E. (1969). Thin-layer chromatography.
13. Geiss, F. (1987). Fundamentals of thin layer chromatography.
14. Sherma, J., & Fried, B. (Eds.). (2003). Handbook of thin-layer chromatography (Vol. 89). CRC press.
15. Jeppsson, J. O., & Sjöquist, J. (1967). Thin-layer chromatography of PTH amino acids. Analytical Biochemistry, 18(2), 264-269.

16. Lindsay, S., & Kealey, D. (1987). High performance liquid chromatography.
17. Ishii, D., Asai, K., Hibi, K., Jonokuchi, T., & Nagaya, M. (1977). A study of micro-high-performance liquid chromatography: I. Development of technique for miniaturization of high-performance liquid chromatography. Journal of Chromatography A, 144(2), 157-168.
18. Buttriss, J. L., & Diplock, A. T. (1984). [15] High-performance liquid chromatography methods for vitamin E in tissues. In Methods in enzymology (Vol. 105, pp. 131-138). Academic Press.
19. Mochamad, L., & Hermanto, B. (2017). High-performance liquid chromatography ultraviolet-photodiode array detection method for aflatoxin B1 in cattle feed supplements. Veterinary world, 10(8), 932.
20. Thammana, M. (2016). A review on high performance liquid chromatography (HPLC). RRJPA, 5(2), 22-28.
21. Shih, J. J. (2008). Microfabricated high-performance liquid chromatography (HPLC) system with closed-Loop flow control (Doctoral dissertation, California Institute of Technology).
22. https://microbenotes.com/high-performance-liquid-chromatography-hplc/
23. Skoog, D. A., & West, D. M. (1980). Principles of Instrumental Analysis, (Saunders golden sunburst series).
24. Belguidoum, K., Amira-Guebailia, H., Boulmokh, Y., & Houache, O. (2014). HPLC coupled to UV–vis detection for quantitative determination of phenolic compounds and caffeine in different brands of coffee in the Algerian market. Journal of the Taiwan Institute of Chemical Engineers, 45(4), 1314-1320.
25. Marriott, P., & Shellie, R. (2002). Principles and applications of comprehensive two-dimensional gas chromatography. TrAC Trends in Analytical Chemistry, 21(9-10), 573-583.
26. Terry, S. C., Jerman, J. H., & Angell, J. B. (1979). A gas chromatographic air analyzer fabricated on a silicon wafer. IEEE transactions on electron devices, 26(12), 1880-1886.
27. Karasek, F. W., & Clement, R. E. (2012). Basic gas chromatography-mass spectrometry: principles and techniques. Elsevier.
28. Jerman, J. H., & Terry, S. C. (1984). U.S. Patent No. 4,471,647. Washington, DC: U.S. Patent and Trademark Office. (more in http://delloyd.50megs.com/moreinfo/gaschrom.html)
29. Engvall, E., & Perlmann, P. (1972). Enzyme-linked immunosorbent assay, ELISA: III. Quantitation of specific antibodies by enzyme-labeled anti-immunoglobulin in antigen-coated tubes. The Journal of Immunology, 109(1), 129-135.
30. Voller, A., Bidwell, D. E., & Bartlett, A. (1979). The enzyme linked immunosorbent assay (ELISA). A guide with abstracts of microplate applications. Dynatech Europe, Borough House, Rue du Pre..
31. Gan, S. D., & Patel, K. R. (2013). Enzyme immunoassay and enzyme-linked immunosorbent assay. J Invest Dermatol, 133(9), e12.

32. file:///C:/Users/A/Downloads/Enzyme-linked%20immunosorbent%20assay%20(ELISA)%20(1).pdf
33. Bahadır, E. B., & Sezgintürk, M. K. (2016). Lateral flow assays: Principles, designs and labels. TrAC Trends in Analytical Chemistry, 82, 286-306.
34. Anfossi, L., D'Arco, G., Calderara, M., Baggiani, C., Giovannoli, C., & Giraudi, G. (2011). Development of a quantitative lateral flow immunoassay for the detection of aflatoxins in maize. Food Additives and Contaminants, 28(2), 226-234.
35. Zhang, G., Zhu, C., Huang, Y., Yan, J., & Chen, A. (2018). A lateral flow strip based aptasensor for detection of Ochratoxin a in corn samples. Molecules, 23(2), 291.
36. Lata, K., & Sharma, R. (2013). Lateral Flow Assay Concept and its Applications in Food Analysis. Lateral, 32(5).
37. Maragos, C. M., & Kim, E. K. (2004). Detection of zearalenone and related metabolites by fluorescence polarization immunoassay. Journal of food protection, 67(5), 1039-1043.
38. Liu, Y., Liu, R., Boroduleva, A., Eremin, S., Guo, Y., & Zhu, G. (2016). A highly specific and sensitive fluorescence polarization immunoassay for the rapid detection of triazophos residue in agricultural products. Analytical Methods, 8(36), 6636-6644.
39. Oberleitner, L., Eremin, S. A., Lehmann, A., Garbe, L. A., & Schneider, R. J. (2015). Fluorescence polarization immunoassays for carbamazepine–comparison of tracers and formats. Analytical Methods, 7(14), 5854-5861.
40. Nielsen, K., Lin, M., Gall, D., & Jolley, M. (2000). Fluorescence polarization immunoassay: detection of antibody to Brucella abortus. Methods, 22(1), 71-76.
41. Davies, A. M. C. (2014). An introduction to near infrared (NIR) spectroscopy. A Journal of Near Infrared Spectroscopy.
42. Dalm, M., Buxton, M. W., van Ruitenbeek, F. J., & Voncken, J. H. (2014). Application of near-infrared spectroscopy to sensor based sorting of a porphyry copper ore. Minerals Engineering, 58, 7-16.
43. Lucas, P., Solis, M. A., Le Coq, D., Juncker, C., Riley, M. R., Collier, J., ... & Bureau, B. (2006). Infrared biosensors using hydrophobic chalcogenide fibers sensitized with live cells. Sensors and Actuators B: Chemical, 119(2), 355-362.
44. https://byjus.com/chemistry/infrared-spectroscopy/
45. Absalan, F., & Ronaghi, M. (2007). Molecular inversion probe assay. In Comparative Genomics (pp. 315-330). Humana Press.
46. Wang, Y., Cottman, M., & Schiffman, J. D. (2012). Molecular inversion probes: a novel microarray technology and its application in cancer research. Cancer genetics, 205(7-8), 341-355.
47. Herbert, C. G., & Johnstone, R. A. (2002). Mass spectrometry basics. CRC press.
48. Siuzdak, G. (1996). Mass spectrometry for biotechnology. Elsevier.

49. Guillarme, D., Schappler, J., Rudaz, S., & Veuthey, J. L. (2010). Coupling ultra-high-pressure liquid chromatography with mass spectrometry. TrAC Trends in Analytical Chemistry, 29(1), 15-27.
50. Ramos Catharino, R., de Azevedo Marques, L., Silva Santos, L., Baptista, A. S., Glória, E. M., Calori-Domingues, M. A., ... & Eberlin, M. N. (2005). Aflatoxin screening by MALDI-TOF mass spectrometry. Analytical chemistry, 77(24), 8155-8157.
51. Santos, A., Vaz, A., Rodrigues, P., Veloso, A., Venâncio, A., & Peres, A. (2019). Thin Films Sensor Devices for Mycotoxins Detection in Foods: Applications and Challenges. *Chemosensors*, *7*(1), 3.
52. Food Safety AUTHORITY OF IRELAND, Mycotoxins in Food, ISSUE NO. 1 | MAY 2009
53. http://www.premierbiosoft.com/tech_notes/mass-spectrometry.html.
54. Monošík, R., Streďanský, M., & Šturdík, E. (2012). Biosensors-classification, characterization and new trends. Acta Chimica Slovaca, 5(1), 109-120.
55. Ahn, J. M., Hwang, E. T., Youn, C. H., Banu, D. L., Kim, B. C., Niazi, J. H., & Gu, M. B. (2009). Prediction and classification of the modes of genotoxic actions using bacterial biosensors specific for DNA damages. Biosensors and Bioelectronics, 25(4), 767-772
56. Koshelev, M., Lohrenz, T., Vannucci, M., & Montague, P. R. (2010). Biosensor approach to psychopathology classification. PLoS Computational Biology, 6(10), e1000966.
57. Mulchandani, A., & Bassi, A. S. (1995). Principles and applications of biosensors for bioprocess monitoring and control. Critical reviews in biotechnology, 15(2), 105-124.
58. Turner, A., Karube, I., & Wilson, G. S. (1987). Biosensors: fundamentals and applications. Oxford university press.
59. Mohanty, S. P., & Kougianos, E. (2006). Biosensors: a tutorial review. Ieee Potentials, 25(2), 35-40. Dey, D., & Goswami, T. (2011). Optical biosensors: a revolution towards quantum nanoscale electronics device fabrication. BioMed Research International, 2011.
60. Patel, P. N., Mishra, V., & Mandloi, A. S. (2010). Optical biosensors: Fundamentals & trends. JERS, 1(1), 15-34.
61. Zhang, J., Zhang, L., & Xu, W. (2012). Surface plasmon polaritons: physics and applications. Journal of Physics D: Applied Physics, 45(11), 113001.
62. Nguyen, H., Park, J., Kang, S., & Kim, M. (2015). Surface plasmon resonance: a versatile technique for biosensor applications. Sensors, 15(5), 10481-10510.
63. Sahoo, P. R., Swain, P., Nayak, S. M., Bag, S., & Mishra, S. R. (2016). Surface plasmon resonance based biosensor: A new platform for rapid diagnosis of livestock diseases. Veterinary
64. Gwon, H. R., & Lee, S. H. (2010). Spectral and angular responses of surface plasmon resonance based on the Kretschmann prism configuration. Materials transactions, 51(6), 1150-1155.

65. Yanase, Y., Hiragun, T., Ishii, K., Kawaguchi, T., Yanase, T., Kawai, M., ... & Hide, M. (2014). Surface plasmon resonance for cell-based clinical diagnosis. Sensors, 14(3), 4948-4959
66. Webster, J. G. (1998). The measurement, instrumentation and sensors handbook. CRC press.
67. Nabok, A. (2005). Organic And Inorganic Nanostructures (Artech House Mems and Sensors Library) (Vol. 286). Artech House Publishers Hardcover
68. Willets, K. A., & Van Duyne, R. P. (2007). Localized surface plasmon resonance spectroscopy and sensing. Annu. Rev. Phys. Chem., 58, 267-297.
69. Al Rubaye, A., Nabok, A., Catanante, G., Marty, J. L., Takacs, E., & Szekacs, A. (2018). Detection of ochratoxin A in aptamer assay using total internal reflection ellipsometry. Sensors and Actuators B: Chemical, 263, 248-251.
70. Kabashin, A. V., Evans, P., Pastkovsky, S., Hendren, W., Wurtz, G. A., Atkinson, R., ... & Zayats, A. V. (2009). Plasmonic nanorod metamaterials for biosensing. Nature materials, 8(11), 867.
71. Vigderman, L., & Zubarev, E. R. (2013). High-yield synthesis of gold nanorods with longitudinal SPR peak greater than 1200 nm using hydroquinone as a reducing agent. Chemistry of Materials, 25(8), 1450-1457.
72. Brolo, A. G., Gordon, R., Leathem, B., & Kavanagh, K. L. (2004). Surface plasmon sensor based on the enhanced light transmission through arrays of nanoholes in gold films. Langmuir, 20(12), 4813-4815.
73. Watt, F., Bettiol, A. A., Van Kan, J. A., Teo, E. J., & Breese, M. B. H. (2005). Ion beam lithography and nanofabrication: a review. International Journal of Nanoscience, 4(03), 269-286.
74. Kravchenko, A., Shevchenko, A., Ovchinnikov, V., Priimagi, A., & Kaivola, M. (2011). Optical Interference Lithography Using Azobenzene-Functionalized Polymers for Micro-and Nanopatterning of Silicon. Advanced materials, 23(36), 4174-4177.
75. Wood, M. A. (2006). Colloidal lithography and current fabrication techniques producing in-plane nanotopography for biological applications. Journal of the Royal Society Interface, 4(12), 1-17.
76. Murray, W. A., & Barnes, W. L. (2007). Plasmonic materials. Advanced materials, 19(22), 3771-3782.
77. Shrivas, K., Sahu, S., Patra, G. K., Jaiswal, N. K., & Shankar, R. (2016). Localized surface plasmon resonance of silver nanoparticles for sensitive colorimetric detection of chromium in surface water, industrial waste water and vegetable samples. Analytical Methods, 8(9), 2088-2096.
78. Unser, S., Bruzas, I., He, J., & Sagle, L. (2015). Localized surface plasmon resonance biosensing: current challenges and approaches. Sensors, 15(7), 15684-15716.
79. Damborský, P., Švitel, J., & Katrlík, J. (2016). Optical biosensors. Essays in biochemistry, 60(1), 91-100.]

80. Westphal, P., & Bornmann, A. (2002). Biomolecular detection by surface plasmon enhanced ellipsometry. Sensors and Actuators B: Chemical, 84(2-3), 278-282.
81. Arwin, H., Poksinski, M., & Johansen, K. (2004). Total internal reflection ellipsometry: principles and applications. Applied optics, 43(15), 3028-3036.
82. Nabok, A. V., Tsargorodskaya, A., Hassan, A. K., & Starodub, N. F. (2005). Total internal reflection ellipsometry and SPR detection of low molecular weight environmental toxins. Applied Surface Science, 246(4), 381-386.
83. Nabok, A., & Tsargorodskaya, A. (2008). The method of total internal reflection ellipsometry for thin film characterisation and sensing. Thin Solid Films, 516(24), 8993-9001
84. Al-Rubaye, A. G., Nabok, A., & Tsargorodska, A. (2017). LSPR Biosensor Based on Nanostructured Gold Films: Detection of Mycotoxins. Procedia technology, 27, 131-132.
85. Nabok, A., Al-Rubaye, A. G., Al-Jawdah, A. M., Tsargorodska, A., Marty, J. L., Catanante, G., ... & Takacs, E. (2019). Novel optical biosensing technologies for detection of mycotoxins. Optics & Laser Technology, 109, 212-221
86. Al-Rubaye, A., Nabok, A., Abu-Ali, H., Szekacs, A., & Takacs, E. (2017, October). LSPR/TIRE bio-sensing platform for detection of low molecular weight toxins. In 2017 IEEE SENSORS (pp. 1-3). IEEE.
87. Schmitt, K., & Hoffmann, C. (2010). High-refractive-index waveguide platforms for chemical and biosensing. In Optical Guided-wave Chemical and Biosensors I (pp. 21-54). Springer, Berlin, Heidelberg.
88. Schmitt, K., & Hoffmann, C. (2010). High-refractive-index waveguide platforms for chemical and biosensing. In Optical Guided-wave Chemical and Biosensors I (pp. 21-54). Springer, Berlin, Heidelberg.
89. [Min, H. K., Yang, H. S., & Cho, S. M. (2000). Extremely sensitive optical sensing of ethanol using porous silicon. Sensors and Actuators B: Chemical, 67(1-2), 199-202.
90. Nabok, A. (2005). Organic And Inorganic Nanostructures (Artech House Mems and Sensors Library) (Vol. 286). Artech House Publishers Hardcover.
91. Prieto, F., Sepúlveda, B., Calle, A., Llobera, A., Domınguez, C., & Lechuga, L. M. (2003). Integrated Mach–Zehnder interferometer based on ARROW structures for biosensor applications. Sensors and actuators B: Chemical, 92(1-2), 151-158.
92. Sepúlveda, B., Del Rio, J. S., Moreno, M., Blanco, F. J., Mayora, K., Domínguez, C., & Lechuga, L. M. (2006). Optical biosensor microsystems based on the integration of highly sensitive Mach–Zehnder interferometer devices. Journal of Optics A: Pure and Applied Optics, 8(7), S561.
93. Liu, Q., Tu, X., Kim, K. W., Kee, J. S., Shin, Y., Han, K., ... & Park, M. K. (2013). Highly sensitive Mach–Zehnder interferometer biosensor based

on silicon nitride slot waveguide. Sensors and Actuators B: Chemical, 188, 681-688.
94. Fu, H., Zhao, N., Shao, M., Li, H., Gao, H., Liu, Q., ... & Qiao, X. (2015). High-sensitivity Mach–Zehnder interferometric curvature fiber sensor based on thin-core fiber. IEEE Sensors Journal, 15(1), 520-525.
95. Heideman, R. G., Kooyman, R. P. H., & Greve, J. (1993). Performance of a highly sensitive optical waveguide Mach-Zehnder interferometer immunosensor. Sensors and Actuators B: Chemical, 10(3), 209-217.
96. Schubert, T., Haase, N., Kück, H., & Gottfried-Gottfried, R. (1997). Refractive-index measurements using an integrated Mach-Zehnder interferometer. Sensors and Actuators A: Physical, 60(1-3), 108-112.
97. Yuan, D., Dong, Y., Liu, Y., & Li, T. (2015). Mach-zehnder interferometer biochemical sensor based on silicon-on-insulator rib waveguide with large cross section. Sensors, 15(9), 21500-21517.
98. Chalyan, T., Pasquardini, L., Falke, F., Zanetti, M., Guider, R., Gandolfi, D., ... & Pavesi, L. (2016, April). Biosensors based on Si3N4 asymmetric Mach-Zehnder interferometers. In Optical Sensing and Detection IV (Vol. 9899, p. 98991S). International Society for Optics and Photonics.
99. Wu, D., Zhao, Y., & Li, J. (2015). PCF taper-based Mach–Zehnder interferometer for refractive index sensing in a PDMS detection cell. Sensors and Actuators B: Chemical, 213, 1-4.
100. González-Guerrero, A. B., Maldonado, J., Herranz, S., & Lechuga, L. M. (2016). Trends in photonic lab-on-chip interferometric biosensors for point-of-care diagnostics. Analytical Methods, 8(48), 8380-8394.
101. Schneider, B. H., Edwards, J. G., & Hartman, N. F. (1997). Hartman interferometer: versatile integrated optic sensor for label-free, real-time quantification of nucleic acids, proteins, and pathogens. Clinical chemistry, 43(9), 1757-1763.
102. Hartman, N. F. (1997). U.S. Patent No. 5,623,561. Washington, DC: U.S. Patent and Trademark Office.
103. Ymeti, A., Greve, J., Lambeck, P. V., Wink, T., van Hövell, S. W., Beumer, T. A., ... & Kanger, J. S. (2007). Fast, ultrasensitive virus detection using a young interferometer sensor. Nano letters, 7(2), 394-397.
104. Ymeti, A., Kanger, J. S., Greve, J., Besselink, G. A. J., Lambeck, P. V., Wijn, R., & Heideman, R. G. (2005). Integration of microfluidics with a four-channel integrated optical Young interferometer immunosensor. Biosensors and Bioelectronics, 20(7), 1417-1421.
105. Wang, Y., Zheng, Y., Yang, F., & Yang, X. (2012). Dual polarisation interferometry for real-time, label-free detection of interaction of mercury (II) with mercury-specific oligonucleotides. Chemical Communications, 48(23), 2873-2875.
106. Thompsett, A. R., & Brown, D. R. (2007). Dual polarisation interferometry analysis of copper binding to the prion protein: Evidence for two folding states. Biochimica et Biophysica Acta (BBA)-Proteins and Proteomics, 1774(7), 920-927.

107. González-Guerrero, A. B., Lechuga, L. M., & Domínguez, C. Simple and compact integrated silicon interferometer device for biosensing platforms devices.
108. Zinoviev, K. E., González-Guerrero, A. B., Domínguez, C., & Lechuga, L. M. (2011). Integrated bimodal waveguide interferometric biosensor for label-free analysis. Journal of Lightwave Technology, 29(13), 1926-1930.
109. Tolles, W. M., Nibler, J. W., McDonald, J. R., & Harvey, A. B. (1977). A review of the theory and application of coherent anti-Stokes Raman spectroscopy (CARS). Applied Spectroscopy, 31(4), 253-271.
110. Zhang, X., Tan, Q. H., Wu, J. B., Shi, W., & Tan, P. H. (2016). Review on the Raman spectroscopy of different types of layered materials. Nanoscale, 8(12), 6435-6450.
111. Herrero, A. M. (2008). Raman spectroscopy a promising technique for quality assessment of meat and fish: A review. Food Chemistry, 107(4), 1642-1651.
112. Monteiro, M., Stari, C., Cabeza, C., & Martí, A. C. (2017). The polarization of light and Malus' law using smartphones. The Physics Teacher, 55(5), 264-266.
113. Dong, X., Tam, H. Y., & Shum, P. (2007). Temperature-insensitive strain sensor with polarization-maintaining photonic crystal fiber based Sagnac interferometer. Applied physics letters, 90(15), 151113.
114. Leung, A., Shankar, P. M., & Mutharasan, R. (2007). A review of fiber-optic biosensors. Sensors and Actuators B: Chemical, 125(2), 688-703.
115. Sheeba, M., Rajesh, M., Vallabhan, C. P. G., Nampoori, V. P. N., & Radhakrishnan, P. (2005). Fibre optic sensor for the detection of adulterant traces in coconut oil. Measurement Science and Technology, 16(11), 2247.
116. Mignani, A. G., Falciai, R., & Ciaccheri, L. (1998). Evanescent wave absorption spectroscopy by means of bi-tapered multimode optical fibers. Applied spectroscopy, 52(4), 546-551.
117. Ruddy, V., MacCraith, B. D., & Murphy, J. A. (1990). Evanescent wave absorption spectroscopy using multimode fibers. Journal of Applied Physics, 67(10), 6070-6074.
118. Hale, Z. M., Payne, F. P., Marks, R. S., Lowe, C. R., & Levine, M. M. (1996). The single mode tapered optical fibre loop immunosensor. Biosensors and Bioelectronics, 11(1-2), 137-148.
119. Anderson, G. P., Golden, J. P., & Ligler, F. S. (1993). A fiber optic biosensor: combination tapered fibers designed for improved signal acquisition. Biosensors and Bioelectronics, 8(5), 249-256
120. Sharma, A. K., & Gupta, B. D. (2005). On the sensitivity and signal to noise ratio of a step-index fiber optic surface plasmon resonance sensor with bimetallic layers. Optics Communications, 245(1-6), 159-169
121. Vengsarkar, A. M., Lemaire, P. J., Judkins, J. B., Bhatia, V., Erdogan, T., & Sipe, J. E. (1996). Long-period fiber gratings as band-rejection filters. Journal of lightwave technology, 14(1), 58-65.
122. Bhatia, V. (1999). Applications of long-period gratings to single and multi-parameter sensing. Optics express, 4(11), 457-466.

123. Campanella, C., Cuccovillo, A., Campanella, C., Yurt, A., & Passaro, V. (2018). Fibre Bragg Grating Based Strain Sensors: Review of Technology and Applications. Sensors, 18(9), 3115.
124. Du, W., Tao, X. M., Tam, H. Y., & Choy, C. L. (1998). Fundamentals and applications of optical fiber Bragg grating sensors to textile structural composites. Composite Structures, 42(3), 217-229.
125. Hou, R., Ghassemlooy, Z., Hassan, A., Lu, C., & Dowker, K. P. (2001). Modelling of long-period fibre grating response to refractive index higher than that of cladding. Measurement Science and Technology, 12(10), 1709.
126. Del Villar, I., Matías, I. R., Arregui, F. J., & Lalanne, P. (2005). Optimization of sensitivity in long period fiber gratings with overlay deposition. Optics Express, 13(1), 56-69.
127. Singh, A., Rana, S. B., Singh, M., & Sharma, A. (2014). Study and investigation of long period grating as refractive index sensor. Optik-International Journal for Light and Electron Optics, 125(7), 1860-1863.
128. Rego, G. (2013). A review of refractometric sensors based on long period fibre gratings. The Scientific World Journal, 2013.
129. Chiavaioli, F., Baldini, F., Tombelli, S., Trono, C., & Giannetti, A. (2017). Biosensing with optical fiber gratings. Nanophotonics, 6(4), 663-679.
130. Bandyopadhyay, S., Biswas, P., Chiavaioli, F., Dey, T. K., Basumallick, N., Trono, C., ... & Bandyopadhyay, S. (2017). Long-period fiber grating: a specific design for biosensing applications. Applied optics, 56(35), 9846-9853.
131. Thévenot, D. R., Toth, K., Durst, R. A., & Wilson, G. S. (2001). Electrochemical biosensors: recommended definitions and classification. Analytical Letters, 34(5), 635-659.
132. Ronkainen, N. J., Halsall, H. B., & Heineman, W. R. (2010). Electrochemical biosensors. Chemical Society Reviews, 39(5), 1747-1763.
133. Grieshaber, D., MacKenzie, R., Voeroes, J., & Reimhult, E. (2008). Electrochemical biosensors-sensor principles and architectures. Sensors, 8(3), 1400-1458.
134. Wang, J. (1999). Amperometric biosensors for clinical and therapeutic drug monitoring: a review. Journal of pharmaceutical and biomedical analysis, 19(1-2), 47-53.
135. Su, L., Jia, W., Hou, C., & Lei, Y. (2011). Microbial biosensors: a review. Biosensors and bioelectronics, 26(5), 1788-1799.
136. Gerard, M., Chaubey, A., & Malhotra, B. D. (2002). Application of conducting polymers to biosensors. Biosensors and bioelectronics, 17(5), 345-359.
137. Atkins, P., & De Paula, J. (2011). Physical chemistry for the life sciences. Oxford University Press, USA.
138. Pisoschi, A. M. (2016). Potentiometric biosensors: concept and analytical applications-an editorial. Biochem Anal Biochem, 5, 19-20.

139. Wang, Y., Chen, Q., & Zeng, X. (2010). Potentiometric biosensor for studying hydroquinone cytotoxicity in vitro. Biosensors and Bioelectronics, 25(6), 1356-1362.
140. Muhammad-Tahir, Z., & Alocilja, E. C. (2003). A conductometric biosensor for biosecurity. Biosensors and Bioelectronics, 18(5-6), 813-819.
141. Syu, Y. C., Hsu, W. E., & Lin, C. T. (2018). Field-Effect Transistor Biosensing: Devices and Clinical Applications. *ECS Journal of Solid State Science and Technology*, *7*(7), Q3196-Q3207.
142. Shul'ga, A. A., Soldatkin, A. P., El'skaya, A. V., Dzyadevich, S. V., Patskovsky, S. V., & Strikha, V. I. (1994). Thin-film conductometric biosensors for glucose and urea determination. Biosensors and Bioelectronics, 9(3), 217-223.
143. Jaffrezic-Renault, N., & Dzyadevych, S. (2008). Conductometric microbiosensors for environmental monitoring. Sensors, 8(4), 2569-2588.
144. Marrakchi, M., Dzyadevych, S. V., Lagarde, F., Martelet, C., & Jaffrezic-Renault, N. (2008). Conductometric biosensor based on glucose oxidase and beta-galactosidase for specific lactose determination in milk. Materials Science and Engineering: C, 28(5-6), 872-875.
145. Lisdat, F., & Schäfer, D. (2008). The use of electrochemical impedance spectroscopy for biosensing. Analytical and bioanalytical chemistry, 391(5), 1555.
146. Bogomolova, A., Komarova, E., Reber, K., Gerasimov, T., Yavuz, O., Bhatt, S., & Aldissi, M. (2009). Challenges of electrochemical impedance spectroscopy in protein biosensing. Analytical Chemistry, 81(10), 3944-3949.
147. Bogomolova, A., Komarova, E., Reber, K., Gerasimov, T., Yavuz, O., Bhatt, S., & Aldissi, M. (2009). Challenges of electrochemical impedance spectroscopy in protein biosensing. Analytical Chemistry, 81(10), 3944-3949.

Chapter 3: Physical foundations of optical waveguides

3.1 Introduction

This chapter presents the theoretical background of light propagation through the waveguide which is required for both the waveguide design and simulation of its performance.

The phenomenon of total internal reflection which is the key point for understanding of EM wave propagation through the waveguide, is described in detail using Fresnel's equations. In addition to describing the amplitudes of reflected and transmitted EM waves, Fresnel's theory was used in this project for calculation of the phase shift between p- and s- components of polarized light.

The Goos-Hanchen theory describing the lateral shift of the EM waves during total internal reflection was considered in this work when calculating the number of reflections in the waveguide.

The waveguiding modes of EM waves propagating through the waveguides were described using two alternative approaches, e.g. the geometrical optic-ray and Maxwell's equations approaches.

3.2 Theoretical foundations

A waveguide is a structure confining and guiding the electromagnetic waves in a particular direction. Optical waveguides are the key elements of photonic devices that perform guiding, coupling, switching, splitting, multiplexing and de-multiplexing of optical signals [1]. In this project, the interaction of the light propagated through the waveguide core with the surrounding medium was utilized for sensing applications. The propagation of the electromagnetic waves through the waveguide is governed by Maxwell's equations, so the required parameters of the waveguide can be found by solving Maxwell equations. This approach, however, could be quite challenging, while an alternative much simpler classical geometric approach of ray optics can provide good approximation for waveguide modelling [2, 3, 4, 5].

To understand the mechanism of propagation of electromagnetic waves and physics events accompanied it, we need to review the physics of waves and how they interact with the medium, particularly, at the interface's boundary. Therefore, this chapter begins with outlining the main physics parameters and phenomena of the traveling EM waves, which include the total internal reflection, Fresnel equations, modes of propagation, and the accompanying changes in phase and polarization. Then the calculation the waveguide parameters, such as propagation angle, number and type of modes, polarization, will carried out using both the geometric ray optics (condition equation) method and Maxwell's equations approach.

3.2.1 p- and s- polarized waves

To analyze the behavior of crossing the boundary between two different media it is convenient to consider two types of linearly polarized waves which are based on the electric field vector direction [3]. Fig. 3.1 illustrates the reflection of EM wave (light) in which "p" polarization wave has the electric field vector parallel to the plane of incidence, while the magnetic field vector perpendicular to it, and it is also called as transverse magnetic (TM) mode. The "s" polarization wave has the electric field vector perpendicular to the plane of incidence and it is also called as transverse electric (TE) mode; the magnetic field vector lies in the plane of incidence. Because, the majority of optical phenomena considered in this work are related to electric field, the notations of s- and p- polarizations will be used throughout the thesis.

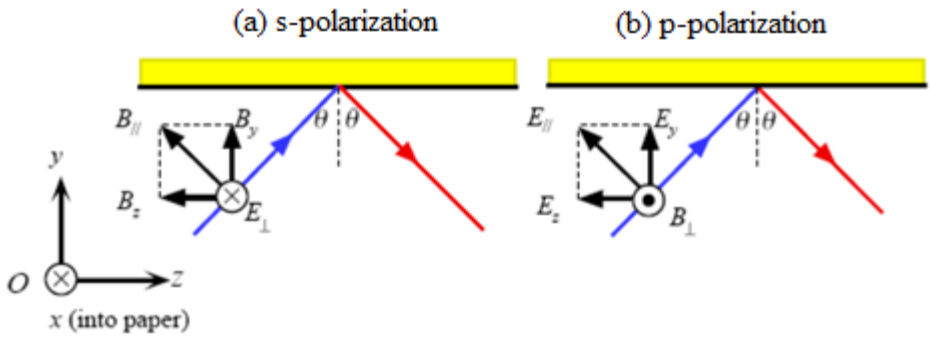

Figure 3.1 Definitions of s- polarizations (a), and p- polarizations (b) of light [3].

Any other electric field direction can be resolved through electric field components E// (or E_p) and $E_\perp$ (or E_s). These two components experience different phase changes, $\varphi_{\|}$ and $\varphi_\perp$, and consequently require different angles to propagate along the waveguide, [3, 6, 7, 8].

3.2.2 Interaction of light with medium

In this section we briefly review the interaction of EM waves with the materials, which can be discriminated to dielectric materials (or insulators) that have no free electric charges and conducting materials (metals and semiconductors) which have mobile electric charges.

The electromagnetic wave (light) induces polarization and oscillations of electric charges in molecules and atoms in the medium. The ability of a medium to respond to this excitation is described by electric permittivity ε, and the magnetic permeability μ. Maxwell's theory uses these quantities in equations to describe the propagation of EM waves in a medium.

Maxwell's equations can be solved for a dielectric medium. If the medium is assumed to be insulating, nonmagnetic, and isotropic, so the relative permittivity ε_r is independent of the direction, then the solution becomes quite simple and leads to Maxwell's EM wave phase velocity v, and wavelength λ, both of which depend on ε_r . In a dielectric medium of relative permittivity ε_r , the phase velocity v is given by [9,10]:

$$v = \frac{1}{\sqrt{\varepsilon_r \varepsilon_o \mu_o}} \tag{3.1}$$

The ratio of the speed of light in free space to its value in a medium is called the refractive index n of the medium which can be written as:

$$n = \frac{c}{v} = \sqrt{\varepsilon_r} \tag{3.2}$$

In non-crystalline materials (such as glasses and liquids) the value of refractive index doesn't change with direction of the light propagation, because the composition of

the material is homogeneous in all directions. While in crystalline materials refractive index is not the same for all propagation directions due to difference in the atomic arrangement and interatomic interaction. Moreover, the refractive index has dependence on the frequency of light, so that the difference of the refractive index on the light frequency for the medium is considered to be one of the most important characteristics materials.

The EM wave may lose its intensity due to the light absorption, when the light energy matches the available energy state in the atoms or molecules, or due to scattering from molecules or atoms. This attenuation is generally accounted by describing the medium in terms of a complex relative permittivity (or dielectric constant) ε_r, that is [10]:

$$\varepsilon_r = \varepsilon_r' - j\varepsilon_r'' \tag{3.3}$$

Similarly, the waves that travel in a medium and experience attenuation can be generally described in terms of complex refractive index N

$$N = n - jk\ , \tag{3.4}$$

where n is the real part, and k is the imaginary part of the refractive index, called as extinction coefficient. Typically, the optical properties of materials are described by frequency dependencies of n and k .

The solution of Maxwell's equations is a planar wave propagating along z direction, which is described as [10]:

$$E = E_o\ e^{-\alpha z}.e^{i(kz-\omega t)} \tag{3.5}$$

Where E_o is the constant complex vector that represents the transverse electric field in the $Z = 0$ plane, k is the attenuation coefficient of the optically isotropic medium, ω is the angular frequency, and t is the time. The factor $e^{-\alpha z}$ indicates that the amplitude of wave decreases exponentially with distance, which is illustrated in Fig. 3.2. This means that the energy of the wave is absorbed by the medium during the wave propagation.

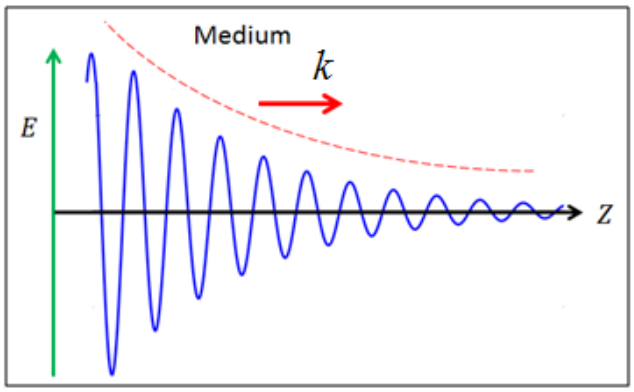

Figure 3.2 The attenuation of light propagating through the absorbing medium.

Figure 3.3 shows the normal dispersion characteristics, e.g. frequency dependences, of n and k which is typically exhibited by transparent substances. The absorption is strongest at the resonance frequency ω_o.

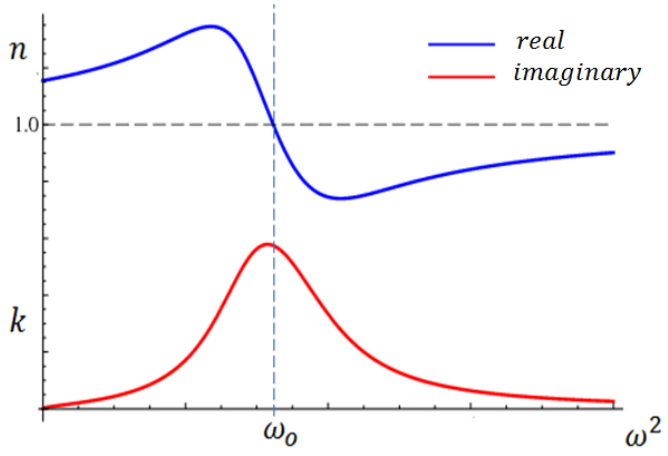

Figure 3.3 Dispersion characteristics of refraction and extinction coefficients in dielectrics [11].

In conduction medium the electrons are not bound, so there is no elastic restoring force as there was in case of dielectric, so that the real and imaginary parts of refractive index are equal and are given by:

$$n \approx k \approx \sqrt{\frac{\sigma}{2\omega\epsilon_o}} \tag{3.6}$$

So the amplitude of an EM electromagnetic wave reduces exponentially and reaches e^{-1} of its value at the distance of δ which so-called "skin depth"

$$\delta = \sqrt{\frac{2}{\omega\sigma\mu_o}} \tag{3.7}$$

This explains why the highly conductive materials are opaque and have a small skin depth. The typical behavior of n and k against ω is shown in Fig. 3.4, the index of refraction n is less than unity for wide range of frequency, while the extinction coefficient k is very large at low frequencies, so that the metal seem to be more transparent at high frequencies.

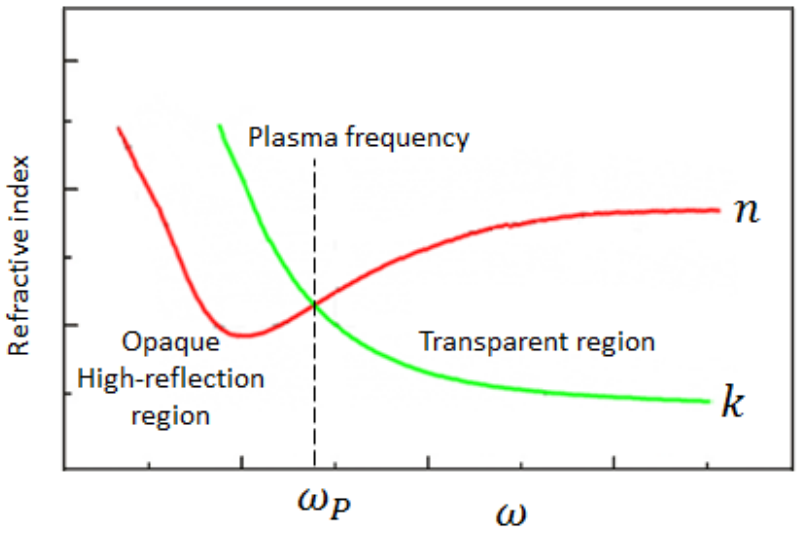

Figure 3.4 Dispersion characteristics of refraction and extinction coefficients for metals [10].

If the optical frequency is lower than ω_o, the electric field will penetrate into the material. If the material is thick enough, all the incoming wave will be reflected. If the optical frequency is higher than ω_o, the material becomes transparent.

The presence of both free and bound electrons in semiconductors or poorly conducting materials contribute to their optical properties and make the theoretical calculations complicated, so that the experimental approaches seem to be much easier [10, 11].

3.2.3 Fresnel equations

The Fresnel equations, that determine the reflection and transmission of light at and the interface between two media having different refractive indices, are among the most fundamental findings of classical optics. Fresnel equations provide explanation

and mathematical rules for optical phenomena, which determines the performance of the optical systems, particularly the waveguides. These equations were derived by Augustin-Jean Fresnel in 1823, and they relate the amplitudes, phases, and polarizations of the transmitted and reflected waves at the interface between two transparent media having different refraction indices. The results of this theory are fully consistent with the rigorous treatment of light in the framework of Maxwell equations. Derivation of these equations are based on Snell's law and the boundary conditions for the electric and magnetic fields at an interface between two media with different electromagnetic properties. One of the first results of this theory in 1872 was estimating the intensity of light reflected from the surface of a dielectric, as a function of the incidence angle.

Fresnel equations predict the ratios of the intensity of the reflected and transmitted light to the intensity of the incident light, and these ratios were called the reflection coefficient $r = E_r/E_i$ and transmission coefficient $t = E_t/E_i$ (see the illustration in Figure 3.5).

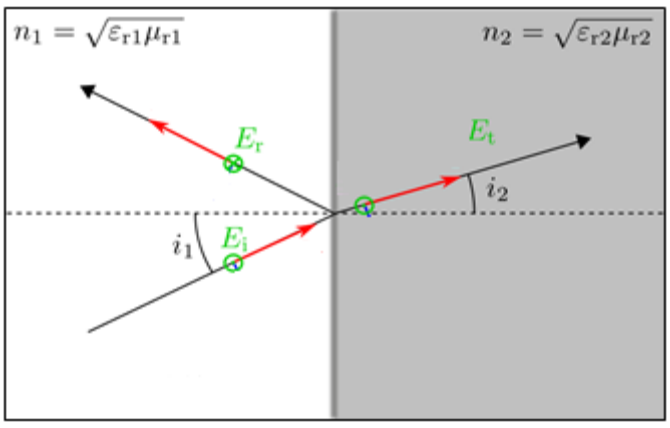

Figure 3.5 Definition of Fresnel parameters.

The polarization of the incident EM wave perpendicular to the plane of reflection can be distinguished as *s*-polarization (transverse electric TE mode); and *p*-polarization (transverse magnetic TB mode) corresponds to EM wave lying in the plane of reflection. Each one of these polarization states has its own reflection and transmission coefficients. Fresnel equation presents the reflection coefficient $r = Er/E$, and transmission coefficient $t = E_t/E$, for these two modes. Thus, for s-polarization, the reflection coefficient of reflected waves beam is descripted b y[3, 12, 13].:

$$r_s = \frac{\cos\theta - \sqrt{n^2 - sin^2\theta}}{\cos\theta + \sqrt{n^2 - sin^2\theta}} \tag{3.8}$$

And, the transmission coefficient of the transmitted wave beam is described as following;

$$t_s = \frac{2\cos\theta}{\cos\theta + \sqrt{n^2 - sin^2\theta}} \tag{3.9}$$

While for p-polarized incident beam the reflection and transmission coefficients are:

$$r_p = \frac{-n^2\cos\theta - \sqrt{n^2 - sin^2\theta}}{n^2\cos\theta + \sqrt{n^2 - sin^2\theta}} \tag{3.10}$$

$$t_p = \frac{2n^2\cos\theta}{n^2\cos\theta + \sqrt{n^2 - sin^2\theta}} \tag{3.11}$$

When light approaches the boundary from the higher index side, that is $n_1 > n_2$, the reflection is said to be internal reflection and at normal incidence there is no phase change. On the other hand, if light approaches the boundary from the lower index side, that is $n_1 < n_2$ it is called external reflection.

3.2.4 Intensity of reflectivity and transmissivity:

For practical purposes, the intensities of the reflected and transmitted waves (Fig. 3.6) are more useful than reflection and transmission coefficients, thus the Fresnel equations can be written in terms of waves intensity as [14]:

$$R = \frac{|E_r|^2}{|E_i|^2} = |r|^2 \tag{3.12}$$

$$R_P = \frac{tan^2(\theta_i - \theta_t)}{tan^2(\theta_i + \theta_t)} \tag{3.13}$$

$$R_S = \frac{sin^2(\theta_i - \theta_t)}{sin^2(\theta_i + \theta_t)} \tag{3.14}$$

$$T_P = \frac{4\,sin\,\theta_i\ sin\,\theta_t\,cos\,\theta_i\,cos\,\theta_t}{sin^2(\theta_i+\theta_t)cos^2(\theta_i-\theta_t)} \tag{3.15}$$

$$T_S = \frac{4\,sin\,\theta_i\ sin\,\theta_t\,cos\,\theta_i\,cos\,\theta_t}{sin^2(\theta_i+\theta_t)} \tag{3.16}$$

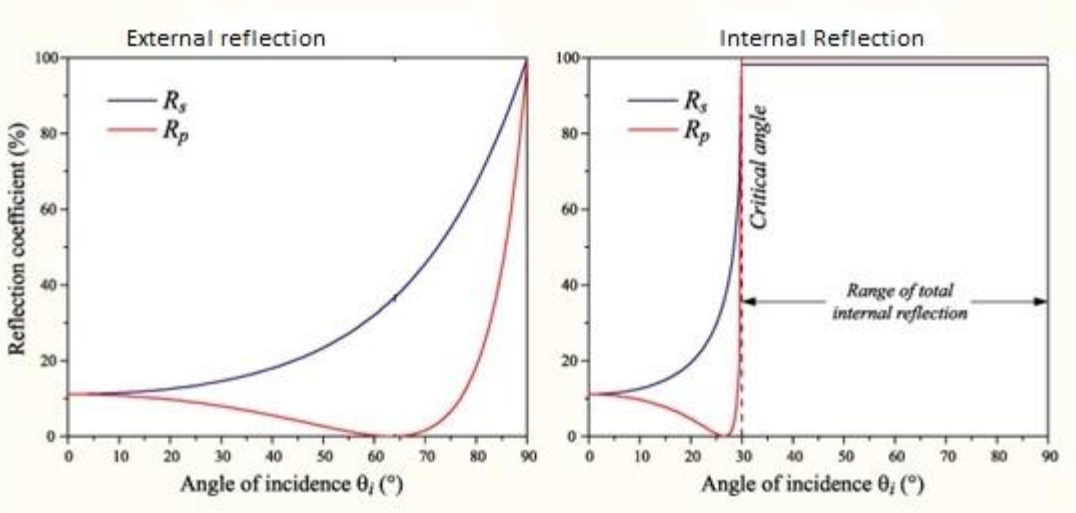

Figure 3.6 Magnitude of the reflection coefficients rs and rp vs. angle of incidence for external (a) and internal (b) reflections [14].

3.2.5 Brewster's Effect

At particular incidence angle called Brewster angle θ_B, the reflected and refracted light rays are perpendicular to each other (Figure 3.7). Simple geometrical considerations give the following formula for Brewster angle:

$$tan\,\theta_B = \frac{n_2}{n_1} \tag{3.17}$$

According to Fresnel equations the value of reflection coefficient of p-polarized waves (R_P) will be zero. So, in this condition there is no p-polarized light reflected, and the reflected light will be linearly polarized.

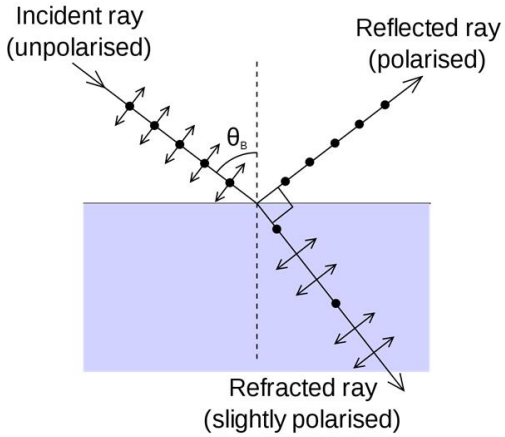

Figure 3.7 Brewster's Effect

3.2.6 The phase of the reflected and transmitted waves

By analysing equations 1,2 3,4, we can find the following: when $n_1 < n_2$, there is π phase shift for s-polarized light reflected for all incident angles, while p-polarized light experienced π phase shift for incidence angle less than Brewster angle, and no phase shift for incidence angle exceed the Brewster angle. For internal reflection (when $n_1 > n_2$) , for s-polarized wave there is no phase shift for all incident angles less than the critical angle $\theta_i < \theta_C$, and there is a phase shift $\varphi_{(\theta)}$ for incident angle larger than critical angle $\theta_i > \theta_C$. The p-polarized light wave does not suffer any phase shift for all incident angels less than the Brewster angle $\theta_i < \theta_P$, while above Brewster angle there is π phase shift appeared until the critical angle, for incident angles exceed the critical angle there is phase shift $\varphi_{(\theta)}$ as shown in Fig. 3.8 [15].

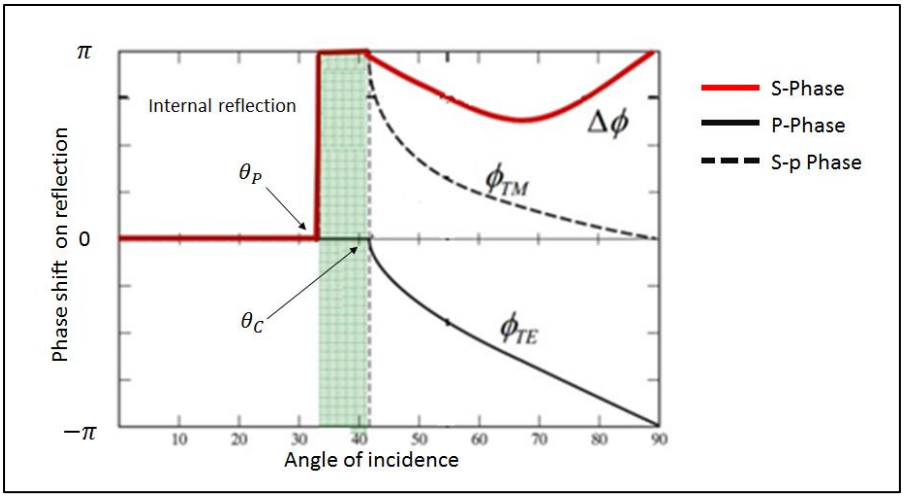

Figure 3.8 Phase shift due to the internal reflection [17].

3.2.7 Total Internal Reflection:

Another phenomenon that can be derived from Fresnel equations is the changing of phase shift between *p*-polarized and *s*- polarized reflected waves with changes of the incidence angle, during total internal reflection. Total internal reflection occurs at the angles of incidence higher than critical angle, $\sin\theta_c = \frac{n_2}{n_1}$

The result is that the incident wave is totally reflected and the intensity of transmitted waves decays exponentially with distance from the interface at which they are formed, this fading field called evanescent field. The Fresnel equations treatment for this situation gives two notes. Firstly, the phase shift (with respect to the incident wave) is different for p-polarization and s- polarization and depends on incident angle, n_1 and n_2. It is worth mentioning that the phase shift between *p* and *s* leads to changes in the polarization state of the reflected light.

$$\delta_p = 2\ tan^{-1}\left[\frac{N\sqrt{N^2 sin^2\theta - 1}}{cos\ \theta}\right] \tag{3.18}$$

$$\delta_S = 2\ tan^{-1}\left[\frac{\sqrt{N^2 sin^2\theta - 1}}{N\ cos\ \theta}\right] \tag{3.19}$$

$$\delta_{P-S} = 2\ tan^{-1}\left[\frac{\sqrt{N^2 sin^2\theta - 1}}{N\ sin\theta\ tan\theta}\right] \tag{3.20}$$

So, it can be summarized that at internal reflection conditions, the amplitudes of reflected and incident waves are equal, but the phase has shift between them is determined by Eqs. (11), (12), and (13), [18].

According to Maxwell theory the phase between p and s determines the polarization state of the electromagnetic waves.

The polarization state is described by the geometric figure traced by the electric field vector upon a stationary plane perpendicular to the direction of wave's propagation (Fig. 3.9). When the electric field and magnetic field can be described by:

$$E_x(z,t) = E_{ox}Cos(t + \delta_x) \tag{3.21}$$

$$B_y(z,t) = B_{oy}Cos(t + \delta_y) \tag{3.22}$$

The locus of points in space that generate a curve whose form can be derived by:

$$\frac{E_x^2}{E_{ox}^2} + \frac{B_y^2}{B_{oy}^2} - 2\frac{E_x}{E_{ox}}\frac{B_y}{o_y}\cos(\delta) = sin^2(\delta) \tag{3.23}$$

$$\text{Where} \quad \delta = \delta_x - \delta_y \tag{3.24}$$

This equation gives an ellipse.

There are specific cases which can be observed for the polarization state:

when $\delta = 0$, the equation (26) will represents the line with 45^o slope, which is called linear polarization;

at $\delta = 90^o$ the equation represents circular polarization when the E vector rotates a draw a circle; any other values of (δ) give elliptical curve characterized by the

orientation angle ψ between the x-axis and main ellipse axis and a ratio factor which ε = a/b, as in Fig. 3.9.

All the above polarization sets are shown in Fig. 3.10.

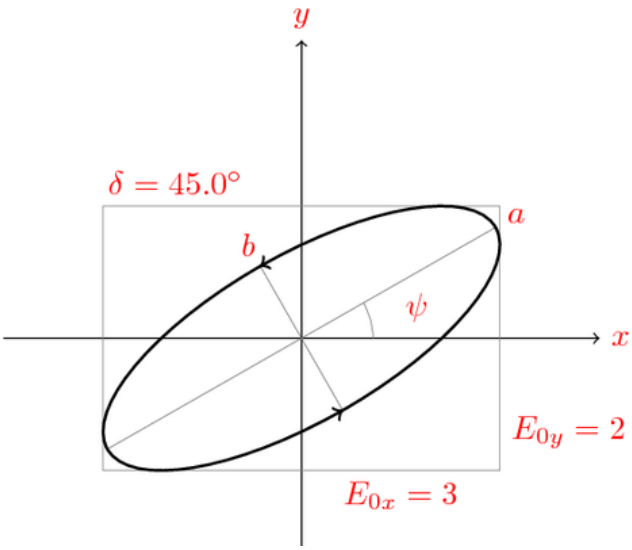

Figure 3.9 Parameters of elliptically polarized light.

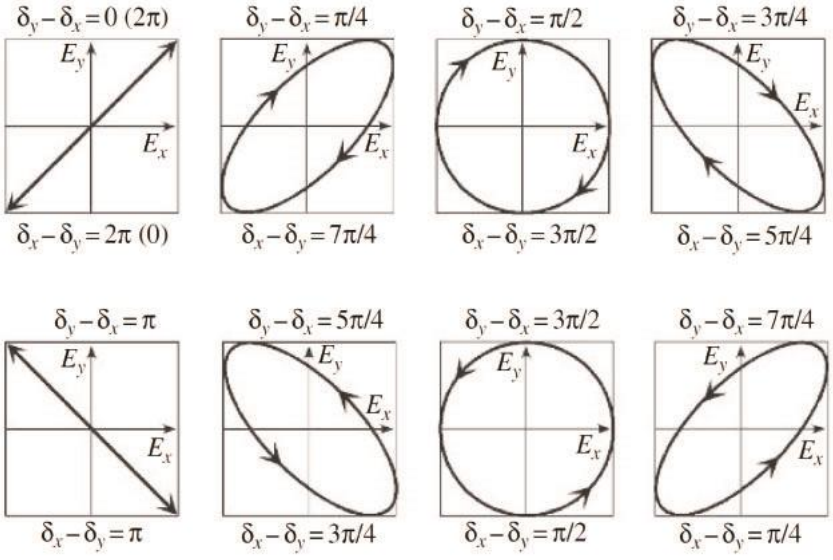

Figure 3.10The polarization states of light

3.2.8 Evanescent wave

The solution of Maxwell's equations for the total internal reflection predicts the existence of an electromagnetic field in the less dense medium with the intensity decaying exponentially away from the interface. In fact, the incident light waves are not completely reflected at the interface surface but penetrate into low refractive index medium to the distance (d) (Fig. 3.11) which is close to the wavelength of incident light λ, before it completely reflected.

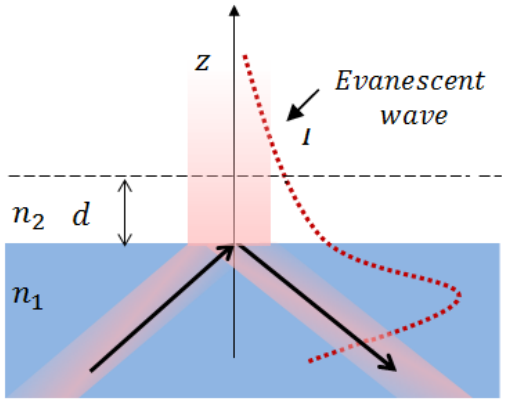

Figure 3.11 Evanescent wave propagating along the interface, with its magnitude decaying into the low refractive index medium direction.

The intensity of the evanescent and penetrating deep are affected by incident angle as shown in Figure 3.12 and Figure 3.13. The exponential decay exponentially in z direction is given by [3]:

$$I_z = I_o e^{-z/\gamma} \tag{3.25}$$

where the decay length γ is given by:

$$\gamma = \frac{\lambda_o}{4\pi n_1 \sqrt{\sin^2\theta - n^2}}, \qquad n = n_2/n_1 \tag{3.26}$$

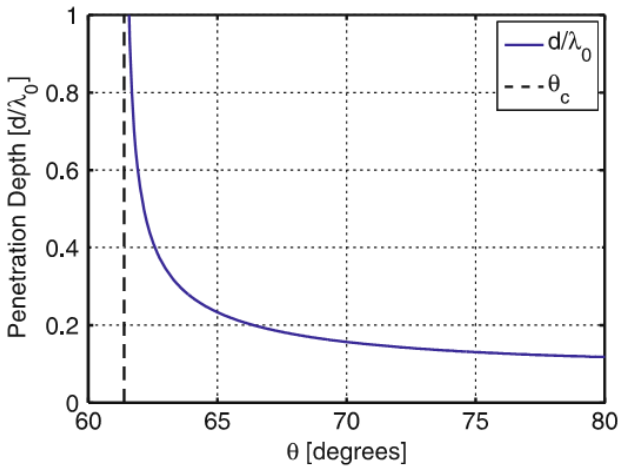

Figure 3.12 Penetration depth of the evanescent wave as a function of the incident angle θ for a typical glass–water interface with n_w/n_{glass} = 0.878 [19].

It is worth mentioning, that the polarization of the incident beam does not affect the penetration depth, but it affects the amplitude (the intensity) of the evanescent field.

For plane waves incident on the interface with the intensity $I_o$in the dense medium, the amplitude of the field in the less dense medium I is given by:

$$I^{\parallel} = I_o^{\parallel} \frac{4cos^2\theta\,(2sin^2\theta - n^2)}{n^4\,cos^2\theta + sin^2\theta - n^2} \tag{3.27}$$

$$I^{\perp} = I_o^{\perp} \frac{4cos^2\theta}{1 - n^2} \tag{3.28}$$

The dependence of $I^{\parallel}$ and $I^{\perp}$ on the incident angle as shown in Fig. 3.15

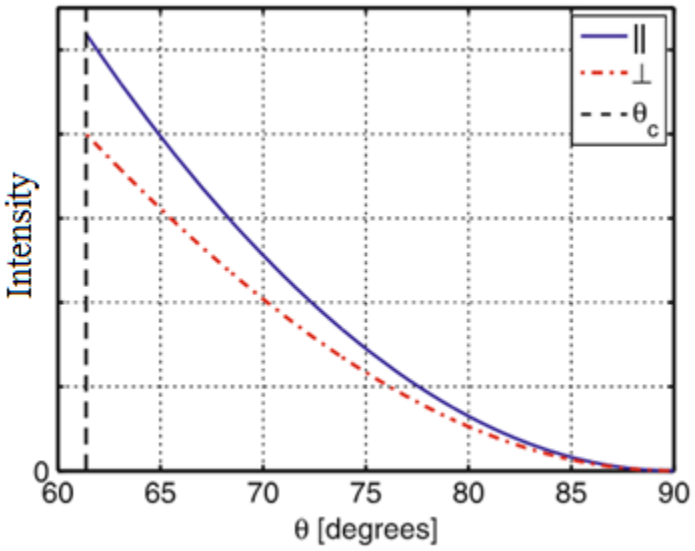

Figure 3.13 Intensities of the evanescent field at the interface in the low index material for both parallel and perpendicular polarization vs the incident angle [19].

When a free charge, e.g. electrons, are exposed to this evanescent field, the energy can be absorbed. So that if there is a thin metal layer present at the interface, free electrons in metals as resonator. The oscillation of the free electrons in the metal generates electromagnetic waves propagating along the interface, these waves called surface plasmon (Fig.3.14). So that, the surface plasmon is an electromagnetic (EM) mode caused by oscillation arising from the interaction of light with mobile surface chargers in a metal (typically gold or silver). If the plasmon happen inside the metal the accompanying electromagnetic wave will be damped, therefore the metal film should be sufficiently thin (less than ~50 nm) in order to produce surface plasmons, so that the evanescent wave penetrates through the metal film and couples with a surface plasmon at the outer boundary of the film. The coupling occurs when momentum of the incoming light matches the momentum of resonance vibration of the free charge in the metal. For given TIR mediums, metal thin film and incident light wavelength, there specific incident angle can satisfy the moment matching and

give rise to emerge the plasmon waves along the two mediums interface [18, 19, 20, 21].

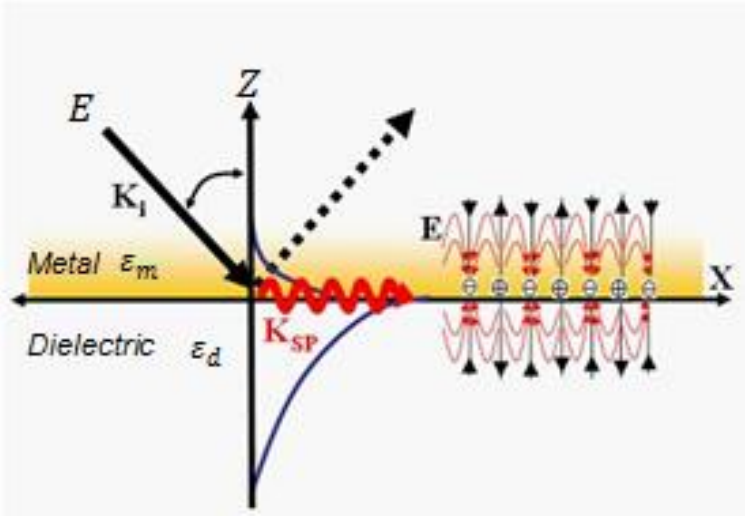

Figure 3.14 Evanescent field interacting with surface plasmons [20].

3.2.9 Goos–Haenchen shift

Because the EM waves penetrates into the lower index material to some distance, the reflected beam suffers lateral shift along the direction of propagation as if reflected from a virtual plane inside the lower refractive index medium (see the illustration in Fig. 3.15). This lateral shift is named Goos-Hanchen shift, and it can be calculated it by knowing the penetration depth γ:

$$x = 2\gamma \tan\theta \tag{3.29}$$

Goos–Haenchen shift, can also be expressed as the derivative of the reflection phase

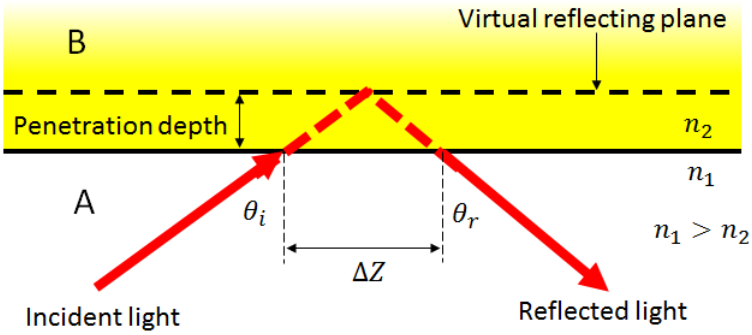

Figure 3.15 Goos–Haenchen shift, The reflected light beam in total internal reflection appears to have been laterally shifted by an amount Δz.

loss with respect to the EM wave lateral wavenumber according to equation (31):

$$S = \frac{d\phi_r}{d\beta} \tag{3.30}$$

Here, S is the Goos- Haenchen shift, ϕ_r is the reflection phase loss and β is the lateral wavenumber of the beam.

The corresponding Goos-Hanchen shift is different for perpendicular (s) and parallel (p) polarization which can be derived by substituting Eq. 1.5 into Eq.1.6 [23]:

$$S_s = \frac{\lambda_1 \sin\theta_i}{\pi\sqrt{\sin^2 - n_r^2}} \tag{3.31}$$

$$S_p = \frac{n_r^2}{\sin^2\theta_i(1+n_r^2)} S_s \tag{3.32}$$

The dependences of S_s and S_p against the angle of incidence are shown in Fig. 3.16

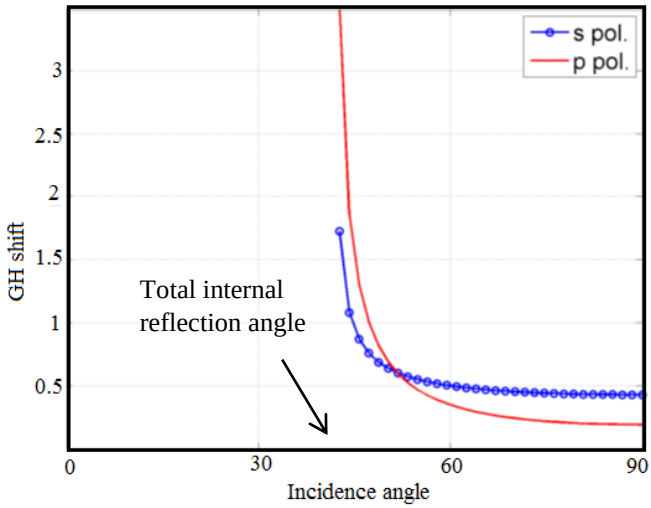

Figure 3.16 Goos–Haenchen shift vs incidence angle for p- and s-polarization [23].

The theory further pointed out that the lateral shift is not vanishing even at the incident angles below the critical angle. Moreover, the negative reflective index can lead to a negative shift, which is quite small in comparison to the wavelength of light, [24, 25].

3.3 Optical waveguide:

The term “waveguide” in general refers to a structure that is able to confine and guide electromagnetic waves. In the simplest case, the waveguide is a material having a refractive index sufficiently high compared to the ambient medium, and appropriate dimensions, to guide wavelengths by total internal reflections.

An optical waveguide is an optical structure having the ability to confine the light electromagnetic waves and force them to propagate in one dimension. Optical

waveguide deals with an optical range of the electromagnetic spectrum, its performance based on the principle of optical confinement by repeating the total internal reflection at the core-cladding boundaries.

3.3.1 Classification of waveguides

The transverse profile of refractive index of the waveguide determines the majority of its characteristics, so that the waveguides can be classified depending on their transverse profile of the refractive index in (x, y) cross section.

The optical waveguides can be classified into two types: the step-index waveguide having an abrupt change of refractive index at the interface between the core and cladding and producing the total internal reflection effect, and the graded-index waveguide having when gradual and continuous change of refractive index between the core and cladding which produces a refracted wave rather than a reflected wave. These two types of waveguides are shown in Fig.3.17.

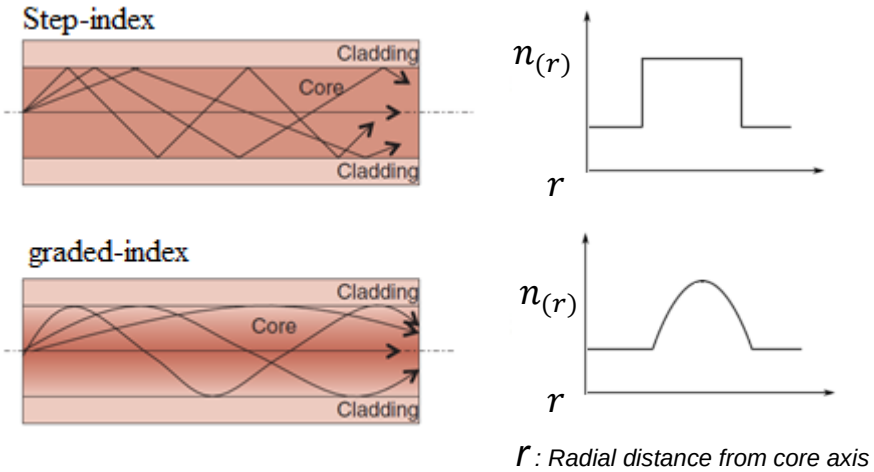

Figure 3.17 Step-index (above) and graded-index (below) waveguides

The waveguide can accommodate either single or multi-mode waves, and called respectively, single- or multi-mode waveguide, [27]. The waveguide modes will be introduced properly later in this chapter. Briefly, the term "mode" here is related to the presence of standing waves across the waveguide. i.e. a single mode propagation corresponds to a half-wave fit into the core, while in multi-mode propagation the core accommodates several half-waves [28].

Waveguides can be classified by their geometrical cross-section, as illustrated by Fig.3.20.

Planar waveguide corresponds to two-dimensional the optical confinement of EM waves a in rectangular shape waveguide, with the core layer sandwiched between two cladding layers (see Figure3.20b),

Channel waveguide, also having rectangular geometry, is formed by a high-index core buried in a low-index surrounding medium; this waveguide has two possible geometries of ridge and rib (see below).

Ridge waveguide has a strip core on top of the planar one; this waveguide has strong optical confinement because it is surrounded on three sides by low index cladding material or air (see Figure3.20c),

Rib waveguide which is a strip channel emerged from high refractive index plane acting as a guide (see Figure3.20a).

Cylindrical waveguide or optical fibre has a cylindrical geometry with high refractive index core surrounded by cladding (see Figure3.20d).

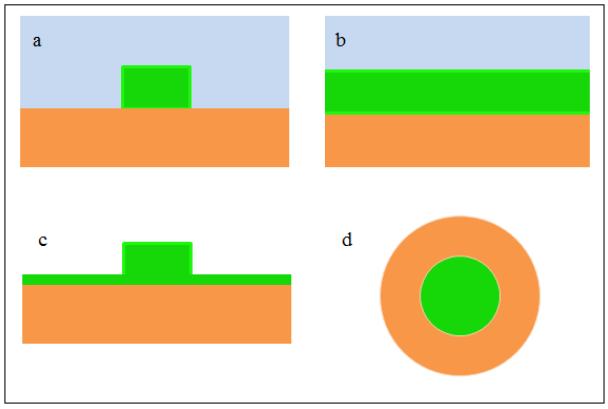

Figure 3.18 Schematic representation of different waveguides cross section geometry (a) ridge waveguide. (b) planar waveguide, (c) rib waveguide, (d) cylindrical waveguide.

3.4 Propagation parameters

3.4.1 Wave vector model of the waveguide (Ray Optics approach)

The Condition equation of the light propagation in optical waveguides is fully described by Maxwell's equations. The classical geometric approach using ray optics provides good approximation.

The ray of light is defined as the beam light with the diameter much smaller than the core thickness, and it is represented by a line. The light rays having an angle of incidence (θ) at the core–cladding interface greater than the critical angle will propagate through the core in zigzag fashion as shown in Fig 3.19.

In the realistic case, when the whole end of the core is illuminated by light, there are only certain reflections angles can provide constructive interference of EM waves, and hence only specific rays belong to specific propagation angles can exist in the

waveguide. The constructive interference produces a spatial distribution of optical energy in the direction (y) perpendicular to the wave propagation (z) that remains stable with time and it is called a propagation mode [3, 29].

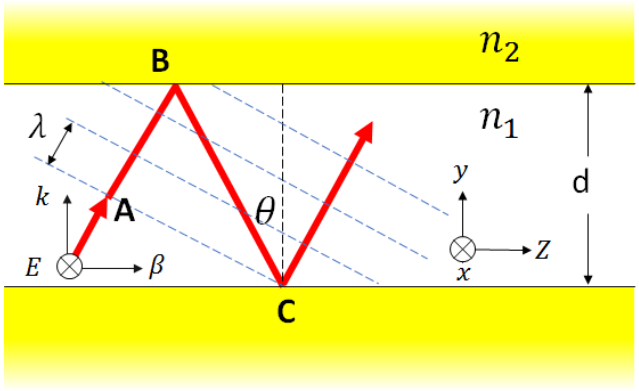

Figure 3.19 The formation of standing waves across the waveguide (y-direction) due to constructive interference of EM waves propagating in z-direction.

When the waves reflected at boundary overlap, the condition to satisfy the constructive interference is that a total phase shift must be equal to an integer multiple of 2π. For waveguide with thickness d, and waves propagating at the angle θ, the total phase shift between two consecutive reflection can be written as:

$$\frac{2\mathrm{d}\sin\theta}{\lambda} - 2\varphi = \mathrm{m}(2\pi) \tag{3.33}$$

Thus, for the wave propagating along the waveguide we need:

$$\left[\frac{2\pi n_1 d}{\lambda}\right] cos\theta_m - \varphi_m = m\pi \tag{3.34}$$

This is called waveguide condition equation. The reflection phase angle (φ) depends on both the incident angle (θ) and the polarization of the incident wave, thus for

each kind of polarization there is a different change in phase leads to different suitable propagation angles θ_m, for s-polarization;

$$\tan\frac{\varphi_s}{2} = \frac{\sqrt{N^2 sin^2\theta - 1}}{N\,cos\theta} \tag{3.35}$$

for p-polarization;

$$\tan\frac{\varphi_p}{2} = \frac{N\sqrt{N^2 sin^2\theta - 1}}{cos\theta} \tag{3.36}$$

Using the expressions of φ from equation (3.34) in equations (3.35 or 3.36) one can obtain equation (3.37) which can be solved graphically to find the available values of m.

$$tan\left[\left(\frac{2\pi n_1 d}{\lambda}\right)cos\theta_m - m\frac{\pi}{2}\right] = \frac{\sqrt{sin^2\theta - \left(\frac{n_2}{n_1}\right)^2}}{cos\theta_m} \tag{3.37}$$

The solutions therefore fall into odd and even categories. The left-hand side (LHS) of this formula simply reproduces itself whenever *m* is even integer *m*=0, 2, 4, but it becomes a cotangent function when *m* is odd integer, m=1, 3. Fig. 3.20 show the graphical solution of this equation

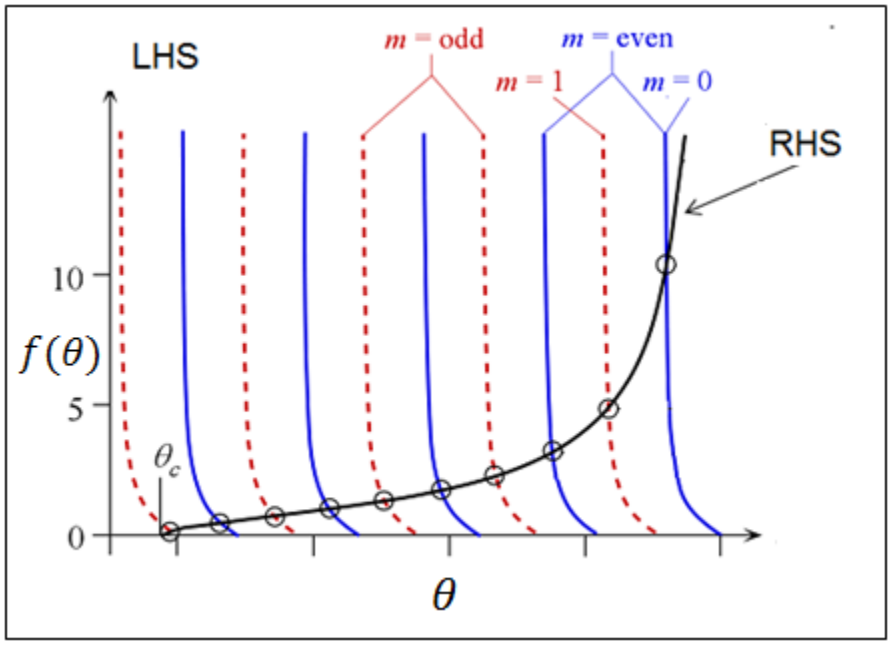

Figure 3.20 Graphical solution of equation 3.37 [3].

Fig. 2.20 shows the graphical solution of equation (3.37). The intercepts of LHS with RHS of eq. 3.37 gives the available mode values (m) as well as the propagation angles θ_m.

3.4.2 Waveguide mode

Since there are only specific reflection angles satisfy the propagation condition, each propagation angle provides a distinct field pattern across the core section $E_m(y)$. Such field patterns are called propagation modes. The integer number m identifies such modes and is called as the mode number, [3, 30].

So, there are specific angles available for the light to propagate through the waveguide, while other propagation angles are not supported. For each propagation angle θ_m, there are upward and downward waves traveling in opposite directions along y, and therefore setting up standing waves along y-direction, which are called as mode patterns. We can resolve the wave vector k into two propagation constants, β and k, along and perpendicular to the guide axis z as shown in Fig. 3.21.

$$\beta_m = k \sin\theta_m = \left(\frac{2\pi n_1}{\lambda}\right) \sin\theta_m \quad (3.38)$$

$$k_m = k \cos\theta_m = \left(\frac{2\pi n_1}{\lambda}\right) \cos\theta_m \quad (3.39)$$

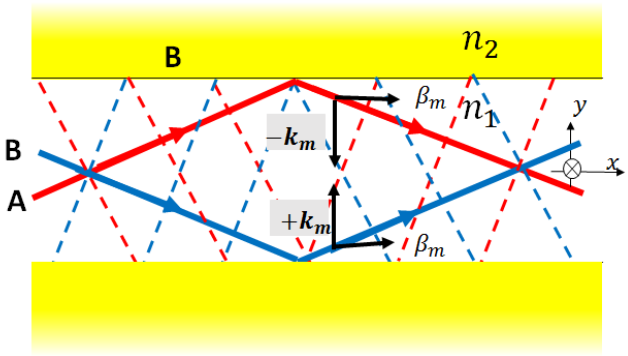

Figure 3.21 Interference of upward and downward traveling waves having equal but opposite sign wave vectors.

For a given m, there are upward and downward traveling waves, indicated as waves A and B in Figure 3.21. These upward and downward traveling waves both propagate along z with the same propagation constant β_m, but travel in opposite directions along y with equal but opposite propagation constants $\pm\beta_m$ as shown in Figure 3.21; their interference sets up standing waves along y-direction, illustrated in Figure 3.22. The EM field in the waveguide can be written as:

$$E(y,z,t) = E_m(y)\cos(\omega t - \beta_m + \delta) \tag{3.40}$$

In which $E_m(y)$ is the field distribution along y. The field pattern in the core exhibits a harmonic variation across the waveguide (in y-direction) representing standing waves as shown in Fig. 3.22.

The field does not vanish immediately at the boundary of core–cladding (unless the boundaries are mirrors) and decay exponentially in y direction:

$$E_x = A.\exp(-\beta_m.z) \tag{3.41}$$

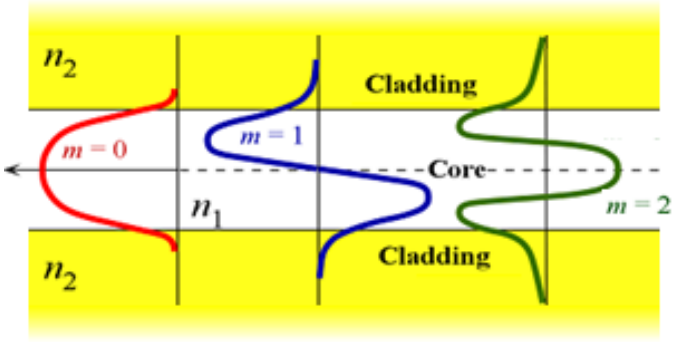

Figure 3.22 The electric field pattern of standing waves across the waveguide.

Traveling wave in the z-direction is described by Eq. (2.1.6) with a particular propagation constant β_m which defined by Eq. (2.1.4). Each of these traveling waves, with a distinct field pattern $E(y)_m$, constitutes a mode of propagation. The integer m identifies these modes and is called the mode number. The light energy can be transported along the guide only by one or more of these possible modes of propagation as illustrated in Fig. 3.22.

3.4.3 Number of modes:

To estimate the maximum number of allowed modes, and to find out approximate relationship that defines the allowed propagation angle one can start with the self-consistency condition:

$$\sin\theta_m = m\frac{\lambda}{2d} \qquad m = 1,2,.... \tag{3.42}$$

Since $\sin\theta_m < 1$, the maximum value of m should be the integer greater than $(2d/\lambda)$, considering that the total internal reflection occurs only at $\theta \leq \theta_c$, therefore the total number of modes M can be given:

$$M = Int(\frac{2d\ \sin\theta_c}{\lambda}) \tag{3.43}$$

or in terms of refractive index:

$$M \doteq \frac{2d\sqrt{n_1^2 - n_2^2}}{\lambda} \tag{3.44}$$

When $\lambda/2d > \sin\bar{\theta}_c$ there is only one mode is allowed. The waveguide is then called a single mode waveguide. This occurs when the core thickness is sufficiently thin, or the wavelength is sufficiently long. For given waveguide parameter there is a cut-off frequency ω_c below which waveguiding cannot occur, this ω_c corresponds to a long wavelength cut-off λ_c [31].

3.4.4 Number of reflections:

The angle of propagation and the core thickness determine the horizontal displacement for each reflection, then by knowing the length of the waveguide the whole number of reflections can be calculated.

From simple geometric consideration shown in Fig. 3.23, the horizontal distance for each reflection (x) can be defined as:

$$x' = 2h \tan\theta \tag{3.45}$$

Where h is the core thickness and θ is the bounce angle.

Due to the penetration of the waves in the cladding layer, the reflected beam appears to be reflected from a virtual plane inside the cladding layer. So, it seems there is a virtual core thickness determines the propagation process, not the physical boundaries. Therefore, the reflected ray at the real interface seems to undergo a lateral shift. This lateral displacement depends on the mode of propagation, and for each mode the lateral displacement can be given as [33, 34]:

$$Z_s = 2(n_{core}^2 . sin^2\theta - n_{cladding}^2)^{-\frac{1}{2}} tan\vartheta \ \frac{1}{k_o} \tag{3.46}$$

$$Z_p = Z_s \left(\frac{n_{core}^2 . sin^2\theta}{n_{cladding}^2} + sin^2\theta - 1\right)^{-1} \tag{3.47}$$

Therefore:

$$x = x' + 2z_{(s\ or\ p)} \tag{3.48}$$

So, the number of reflection on each side of the waveguide of the length L is equal to:

$$N = L/x \tag{3.49}$$

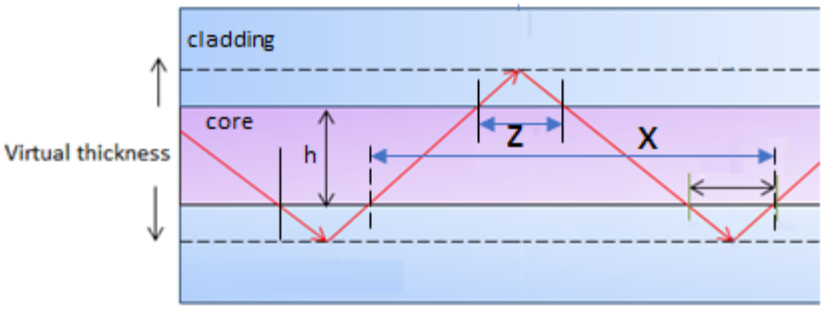

Figure 3.23 The geometry for calculation of the number of reflections.

3.4.5 The changes of polarization of light during propagation through the waveguide

As was mentioned previously, during the light propagation through the waveguide by repeated total internal reflection, a phase shift between p and s components of polarized light develops at each reflection. Therefore, at the waveguide output, all these phase shifts will be summed up, thus effecting and the polarization state of out-

coming light. Therefore, output light polarization state will be sum of all single phase shift during all reflections. That means the length of the waveguide works as amplifying to the amount of p-s phase shift.

3.5 Electromagnetic description of waveguiding (Maxwell's equation approach)

In this section light propagation through the waveguide will be treated according to Maxwell's equations, and guided mode dispersion equation as well as the distribution of the electromagnetic field in the guide will be found using theoretical approach.

The waveguide which consists of three dielectric media that are homogeneous, isotropic, linear and lossless and their magnetic permeability is considered to be constant, as a simple three-layer planar waveguiding structure of . Figure 3.24

The propagation of the light will be assumed in Oz direction, and the structure is taken as infinite with invariant properties in the Oy direction.

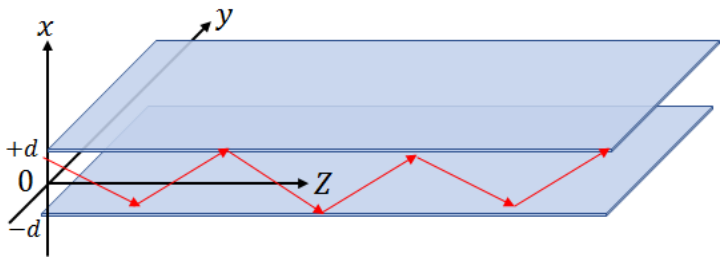

Figure 3.24 Schematic diagram of planar optical waveguide.

3.5.1 Propagation equation

Maxwell Equations which are appropriate to this optical system are:

$$\vec{\nabla} \wedge \vec{E} = -\mu_o \frac{\partial \vec{H}}{\partial t} \tag{3.50}$$

$$\vec{\nabla} \wedge \vec{H} = \varepsilon_o n^2 \frac{\partial \vec{E}}{\partial t} \tag{3.51}$$

$$\vec{\nabla}\, \vec{E} = 0 \tag{3.52}$$

$$\vec{\nabla}\, \vec{H} = 0 \tag{3.53}$$

$$\vec{B} = \mu_o \vec{H} \text{ and } \vec{D} = \varepsilon \vec{E} \tag{3.54}$$

Taking into account the applicability of the boundary conditions, the solution takes the form of EM waves propagation in OZ direction which

$$\vec{E} = \vec{E} \exp i(\omega t - \overrightarrow{kr}) = \vec{E} \exp i(\omega t - \beta z) \tag{3.55}$$

$$\vec{H} = \vec{H} \exp i(\omega t - \overrightarrow{kr}) = \vec{H} \exp i(\omega t - \beta z) \tag{3.56}$$

As the structure is infinite in Oy direction, the problem has no dependence on ($\frac{\partial}{\partial y} = 0$).

An electromagnetic field can be considered as a sum of two polarized field TE and TM, corresponding to a TE (Transverse Electric) wave with $\vec{E}$ parallel to Oy and a TM (Transverse Magnetic) wave where $\vec{H}$ is transverse. Then, from Maxwell's equations, it can be written that:

For TE mode:

$$\frac{\partial^2 E_y}{\partial x^2} + (k^2 n^2 - \beta^2) E_y = 0 \tag{3.57}$$

$$H_x = -\frac{\beta}{\omega \mu_o} E_y \tag{3.58}$$

$$H_z = -\frac{1}{i\omega\mu_o}\frac{\partial E_y}{\partial x} \tag{3.59}$$

For TM mode:

$$\frac{\partial^2 H_y}{\partial x^2} + (k^2 n^2 - \beta^2) H_y = 0 \tag{3.60}$$

$$E_x = -\frac{\beta}{\omega\mu_o} H_y \tag{3.61}$$

$$E_z = -\frac{1}{i\omega\mu_o}\frac{\partial H_y}{\partial x} \tag{3.62}$$

Note that the previous separation in TE and TM modes can be performed in the case of a planar optical waveguide with a refractive index n(x) which depends on one transverse coordinate only.

Generally speaking, we have to solve the following Helmholtz's equation:

$$\frac{\partial^2 F}{\partial x^2} + (k^2 n^2 - \beta^2) F = 0 \tag{3. 63}$$

With $F = E \; or \; H$ depending on the light polarization.

It is necessary to solve the previous equation in the three mediums, n, n_s and n_a

TE modes:

Equation (63) can be written for the three layers as:

$$\frac{\partial^2 E_y}{\partial x^2} + q^2 E_y = 0 \quad \text{medium } n_a \tag{3.64}$$

$$\frac{\partial^2 E_y}{\partial x^2} + h^2 E_y = 0 \quad \text{medium } n_s \tag{3.65}$$

With: $q^2 = \beta^2 - k^2 n_a^2$, $h^2 = k^2 n^2 - \beta^2$, $p^2 = \beta^2 - k^2 n_s^2$.

β is the propagation constant given by: $\beta = kN = kn \; sin\theta$ (N is the guided mode effective index).

The guiding condition imposes the existence of a sinusoidal solution within the central layer n ($h^2 \geq 0$), with evanescent waves into mediums n_a and n_s

Both q^2 and $p^2 \geq 0$, so $kn \geq \beta \geq kn_s \geq kn_a$

The electric field E_y has the general form:

$$E_y(x) = \begin{cases} C\exp(-qx) & 0 \leq x \leq \infty \\ A\cos(hx) + B\sin(hx) & -d \leq x \leq 0 \\ D\exp[p(x+d)] & -\infty \leq x \leq -d \end{cases} \quad (3.66)$$

Where A, B, C and D are constants that can be determined by matching the boundary conditions which require the continuity of E_y and H_z. Note that for $\vec{D}$ and $\vec{B}$ the continuity conditions concern their normal components. Thus, at the interfaces (n, n_a) and (n, n_s), we can write:

$$E_y\big|_n = E_y\big|_{n_s} \quad (3.67)$$

$$\frac{\partial E_y}{\partial x}\Big|_n = \frac{\partial E_y}{\partial x}\Big|_{n_s} \quad (3.\ 68)$$

$$E_y\big|_n = E_y\big|_{n_a} \quad (3.69)$$

$$\frac{\partial E_y}{\partial x}\Big|_n = \frac{\partial E_y}{\partial x}\Big|_{n_a} \quad (3.70)$$

These conditions allow us to write previous equations (1.31) in the following form:

$$E_y(x) = \begin{cases} C\exp(-qx) & 0 \le x \le \infty \\ C\left[\cos(hx) + (q/h)\sin(hx)\right] & -d \le x \le 0 \\ C\left[\cos(hd) + (q/h)\sin(hd)\right]\exp[p(x+d)] & -\infty \le x \le -d \end{cases} \quad (3.71)$$

$\vec{H}$ can be determined from equations [56].

The equation system allows us to determine the electric field profile of each guided mode propagating within the structure. However, to determine the constants C and E, this can be done by use the derivative continuity of the electromagnetic field in the guide. After simplification, we can find:

$$\tan(hd) = \frac{p+q}{h-\frac{pq}{h}} \quad (3.72)$$

This relation can be transformed into:

$$dh = \arctan\left(\frac{q}{h}\right) + \arctan\left(\frac{p}{h}\right) + m\pi \quad (3.73)$$

Where m is an integer ≥ 0 this defines the guided mode order.

(For the previous calculation, we can use: $\tan(a+b) = \frac{\tan(a)+\tan(b)}{1-\tan(a)\tan(b)}$)

Finally, equation (73) represents the TE guided mode dispersion equation. By replacing p , q and h in (72), we obtain equation (35) previously described during consideration of the optic-ray approach. Finally, we need to determine the constant C in order to obtain a complete description of the guided modes travelling within the structure. For that, we use the normalization condition calculation:

$$C_m = 2h_m\sqrt{\frac{\omega\mu_o}{|\beta_m|\left(d+\frac{1}{q_m}+\frac{1}{p_m}\right)\left(h_m^2+q_m^2\right)}} \quad (3.74)$$

As an example, the solutions of the problem are schematically displayed in Fig. 3.25 [34, 35, 36]

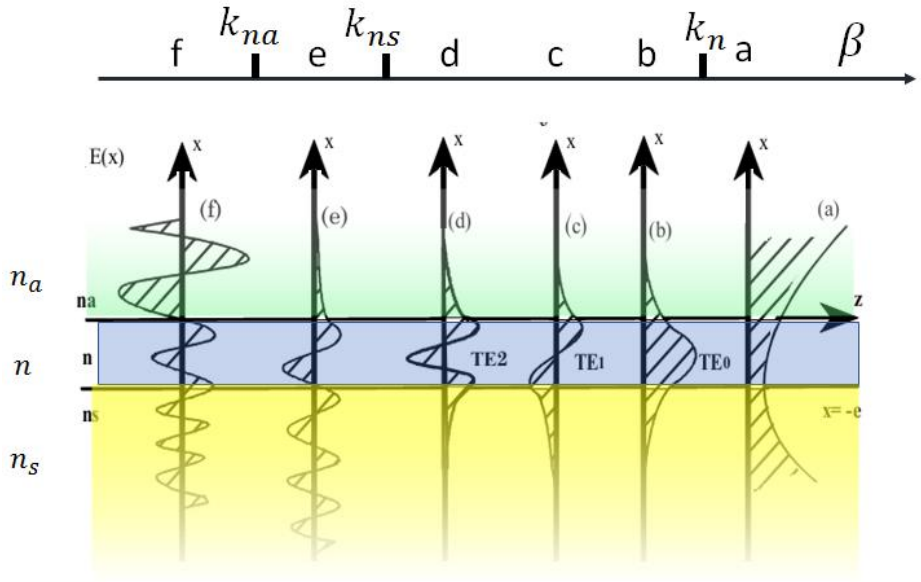

Figure 3.25 Guided mode electric field distribution in a planar optical waveguide structure: (a) represents an unacceptable physical solution because k the three mediums; (b), (c) and (d) represent the electric field distribution of well guided modes (TE), (e) represents a substrate mode – the optical energy is well confined at the interface (n, na) but it varies sinusoidally in the substrate; (f) shows the electric field distribution of a radiation mode, kin the three mediums – this is an oscillatory solution in the three mediums (free extension outside the guide).

3.5.2 Mode number and Cut-Offs

Due to the fact that specific angles can allow propagation and each propagation angle represents a mode state; thus, there are limited numbers of allowed modes. This number can be estimated it using the results of ray-optics approach as well as by use electromagnetic Maxwell's approach. Examine the graph solution of the transverse resonance condition equation (Figure. 4) shows the abscissa is divided into equal intervals of width (λ/2d). each one of these represent available state of

mode. This extends to angle $(sin\theta < sin\theta_c)$ so, the number of these state M is obviously the smallest integer greater than:

$$M \doteq sin\theta_c/(\lambda/2d) \tag{3.76}$$

Using numerical aperture, [2]:

$$Sin\theta_c = \sqrt{n_1^2 - n_2^2} \tag{3.77}$$

So that:

$$M = \frac{2d}{\lambda}\sqrt{n_2^2 - n_3^2} \tag{3.78}$$

The electromagnetic approach which relay on Maxwell equation to deal with waveguide parameters has given the number of modes in the same equation form. [3, 37]:

The cut-off wavelength is the minimum wavelength in which the waveguide system still acts as a single mode waveguide. Above the cut-off wavelength, the system will only allow the LP01 mode to propagate through the core. Below the cut-off wavelength, higher order modes will be able to propagate (the system becomes a multimode). The wavelengths which leads to $M < 1$ correspond to the waveguide which does not support any of these modes for this or longer wavelengths. Therefore, the longest wavelength that can be guided by the structure, can be given by [3]:

$$\lambda_{max} = 2d \tag{3.79}$$

3.6 Conclusions

The main purpose of this chapter is to provide theoretical background of light propagation through the waveguide which is required for both the design and modelling of polarization interferometry biosensor based on optical waveguide.

The main idea of the proposed biosensor devices lies on modulation of the polarization state of light propagation through the planar waveguide caused by changes in the refractive index of surroundings medium. Therefore, Fresnel's theory, which describes the change of amplitudes and phase of the electromagnetic waves transmitted and reflected at the interface between two transparent media, is the key part of this chapter. Changes in the phase and polarization of electromagnetic waves described by Fresnel's equation are of particular importance for this work; it allows the theoretical estimation of the waveguide performance.

The Goos-Hanchen model presented in this chapter describes mathematically the effect of the evanescent field during the total reflection on the EM wave propagation through the waveguide and allowed calculating precisely the number of reflections in the waveguide of particular geometry.

The two approaches in description of the propagation the light through the waveguide using either geometrical optical-ray method or and Maxwell's equations were explored in this chapter. In the optical-ray approach, the propagation of the light is described as a zig-zag path along the waveguide caused by reflections of rays at the boundaries between the core and cladding. The constructive interference waves results in certain allowed reflection angle.

The waveguide condition equation allowed us to the propagation angle for particular waveguide modes.

Alternatively, Maxwell's equations are used to describe the propagation of electromagnetic waves through the waveguide consisting of three dielectric mediums (core and two cladding). Applying the Helmholtz's equation (e.g. Maxwell's equation in differential time harmonic form) for the plane EM waves propagation through the waveguide and can diction stable EM field distribution in the core and vanishing field in cladding. The results are very much similar to these obtained by optic-ray approach.

Both approaches were reviewed in detail in this chapter and results obtained match each other.

3.7 References

1. Saleh, B. E., & Teich, M. C. (2019). Fundamentals of photonics. John Wiley & Sons.
2. Snyder, Allan W., and John Love. *Optical waveguide theory*. Springer Science & Business Media, 2012.
3. Kasap, S. O., & Sinha, R. K. (2001). *Optoelectronics and photonics: principles and practices* (Vol. 340). New Jersey: Prentice Hall.
4. Review on Optical Waveguides By Shankar Kumar Selvaraja and Purnima Sethi Submitted: November 27th 2017Reviewed: April 10th 2018Published: August 1st 2018 DOI: 10.5772/intechopen.77150.
5. F. Graham Smith, Terry A. King, Dan Wilkins, An introduction Optical and Photonics, WL 535.GR
6. Bass, M., Van Stryland, E. W., & Williams, D. R. (1995). Handbook of optics (Vol. 2, pp. 33-66). W. L. Wolfe (Ed.). New York: McGraw-Hill.
7. Pedrotti, F. L., Pedrotti, L. M., & Pedrotti, L. S. (2017). Introduction to optics. Cambridge University Press.
8. Pedrotti, F. L., Pedrotti, L. M., & Pedrotti, L. S. (2017). Introduction to optics. Cambridge University Press
9. Benson, T. M., Kendall, P. C., Stern, M. S., & Quinney, D. A. (1989). New results for rib waveguide propagation constants. *IEE Proceedings J (Optoelectronics)*, *136*(2), 97-102.
10. Pedrotti, F. L., Pedrotti, L. M., & Pedrotti, L. S. (2017). *Introduction to optics*. Cambridge University Press.
11. http://www.superstrate.net/pv/optical/absorption.html
12. Skaar, J. (2006). Fresnel equations and the refractive index of active media. *Physical Review E*, *73*(2), 026605.
13. Obukhov, Y. N., & Rubilar, G. F. (2002). Fresnel analysis of wave propagation in nonlinear electrodynamics. *Physical Review D*, *66*(2), 024042.
14. Peatross, J., & Ware, M. (2011). *Physics of light and optics* (pp. 101-119). Brigham Young University, Department of Physics.
15. Obukhov, Y. N., & Rubilar, G. F. (2002). Fresnel analysis of wave propagation in nonlinear electrodynamics. *Physical Review D*, *66*(2), 024042.
16. Azzam, R. M. A. (2004). Phase shifts that accompany total internal reflection at a dielectric–dielectric interface. *JOSA A*, *21*(8), 1559-1563.
17. https://www.coursehero.com/file/p2iqe6d/TE-TM-t-23-3-Phase-changes-on-reflection-18-0-TE-T-TE-TM-TE-TM-M-the-phase-r-is/
18. Svirko, Y. P., & Zheludev, N. I. (2000). Polarization of light in nonlinear optics. *Polarization of Light in Nonlinear Optics, by Yu. P. Svirko, NI Zheludev, pp. 240. ISBN 0-471-97640-7. Wiley-VCH, January 2000.*, 240.
19. https://www.coursehero.com/file/p2iqe6d/TE-TM-t-23-3-Phase-changes-on-reflection-18-0-TE-T-TE-TM-TE-TM-M-the-phase-r-is.
20. Chiu, N. F., Huang, T. Y., & Lai, H. C. (2013). Graphene oxide based surface plasmon resonance biosensors. Advances in Graphene Science, 280.
21. Garland, P. B. (1996). Optical evanescent wave methods for the study of biomolecular interactions. Quarterly reviews of biophysics, 29(1), 91-117.
22. Messica, A., Greenstein, A., & Katzir, A. (1996). Theory of fiber-optic, evanescent-wave spectroscopy and sensors. Applied o
23. ptics, 35(13), 2274-2284.

24. Anderson, G. P., Golden, J. P., Cao, L. K., Wijesuriya, D., Shriver-Lake, L. C., & Ligler, F. S. (1994). Development of an evanescent wave fiber optic biosensor. IEEE Engineering in Medicine and Biology Magazine, 13(3), 358-363.
25. RUI YANG, (2012). Theory and Applications of Goos-H□anchen Shift Based On Guided Mode Resonance. Submitted as partial ful_llment of the requirements for the degree of Doctor of Philosophy in Electrical and Computer Engineering in the Graduate College of the University of Illinois at Chicago, 2016 https://indigo.uic.edu/bitstream/handle/10027/20911/Yang_Rui.pdf?sequence=1
26. . Stenmark, T., Word, R. C., & Könenkamp, R. (2016). Determination of the Goos-Hänchen shift in dielectric waveguides via photo emission electron microscopy in the visible spectrum. Optics Express, 24(4), 3839-3848.
27. Snyder, A. W., & Love, J. D. (1976). Goos-Hänchen shift. Applied optics, 15(1), 236-238.
28. A. W. Snyder and J. D. Love, Optical Waveguide Theory, Chapman and Hall, London (1983)
29. Shankar Kumar Selvaraja and Purnima Sethi, Review on Optical Waveguides, Submitted: November 27th 2017Reviewed: April 10th 2018Published: August 1st 2018. DOI: 10.5772/intechopen.77150
30. https://www.lehigh.edu/imi/teched/GlassProcess/Lectures/Lecture%2019_Messaddeq_Dielectricwaveguide.pdf
31. Younès Messaddeq, Introduction to Dielectric Waveguide, https://www.lehigh.edu/imi/teched/GlassProcess/Lectures/Lecture%2019_Messaddeq_Dielectricwaveguide.
32. https://www.electronics-notes.com/articles/antennas-propagation/rf-feeders-transmission-lines/waveguide-modes-te-tm-tem.php
33. Saleh, B. E., & Teich, M. C. (2019). Fundamentals of photonics. John Wiley & Sons. p. 250-252.
34. Tamir, T., & Bertoni, H. L. (1971). Lateral displacement of optical beams at multilayered and periodic structures. JOSA, 61(10), 1397-1413.
35. Stenmark, T., Word, R. C., & Könenkamp, R. (2016). Determination of the Goos-Hänchen shift in dielectric waveguides via photo emission electron microscopy in the visible spectrum. Optics Express, 24(4), 3839-3848.
36. Azzedine Boudrioua, Photonic Waveguides Theory and Applications, Includes bibliographical references and index. ISBN 978-1-84821-027-1.
37. Farhan Rana, Semiconductor Optoelectronics, Chapter 8, Integrated Optical Waveguides,
38. Schmitt, K., & Hoffmann, C. (2010). High-refractive-index waveguide platforms for chemical and biosensing. In Optical Guided-wave Chemical and Biosensors I (pp. 21-54). Springer, Berlin, Heidelberg.
39. Hunsperger, R. G. (1995). Integrated optics (Vol. 4), Chapter 2, OpticalWaveguide Modes. Springer Verlag.

Chapter 4: Waveguide design and experimental set-up

4.1 Introduction

This chapter described the detail of the design and fabrication of planar waveguide as a main element of the developed biosensor. The detailed option chosen of all technical aspects of the development of the experimental setup was also provided in this chapter.

4.2 Planar waveguide transducer

The optical planar waveguide is a key element in this work. The waveguide is designed to accommodate a single mode of 635 nm of light wavelength. The main idea of employing the optical waveguide as a sensor lies in its unique feature which is the ability to amplify the sensing signal by repeating the total internal reflection.

In our case the planar optical waveguide has a step-index structure consisting of a high refractive index silicon nitride core layer surrounded on both sides with lower refractive index silicon oxide cladding which provides conditions of total internal reflection at the core-cladding interfaces. In addition to the values of refractive indices of materials used and the wavelength of the light, the thickness of the core layer plays a crucial role in achieving the single mode wave propagation of the waveguide. The mode number (m) can be found form the following formula [1]:

$$m \leq \frac{2V}{\pi} \tag{4.1}$$

Where V-parameter (also called as the normalized thickness) is a defined as [1]:

$$V = \frac{\pi d}{\lambda}\sqrt{n_{core}^2 - n_{cladding}^2} \tag{4.2}$$

where λ is operation wavelength, $n_{core}$is the core refractive index, and $n_{cladding}$ is a cladding refractive index. Choosing the core thickness close to λ/2 makes V-

parameter value less than $(\pi/2)$ and $m = 0$, which means that only the fundamental mode (m=0) propagates along the waveguide.

The waveguide used in this work shown schematically in Fig 4.1 was acquired from National Centre for Scientific Research "Demokritos" (Athens, Greece). It was produced by standard silicon planar technologies, where the Si_3N_4 waveguide core layer of 190 nm thickness was deposited by LPCVD process on a SiO_2 layer with a thickness of 3 μm

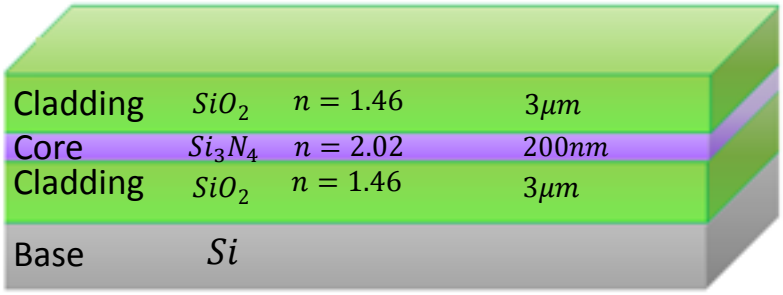

Figure 4.1 The scheme of an optical planar waveguide used

produced by thermal oxidation of Si wafer. The Si_3N_4 layer was covered with another 3 μm thick SiO_2 layer using CVD deposition process. The refractive indices are typically 1.46 and 2.02 for SiO_2 and Si_3N_4 layers, respectively. The above parameters for core and cladding layers were chosen to provide a single mode light propagation [39], and this condition was confirmed by calculations using equation (4.1, 4.2), which gives m = 0 at λ = 635 nm.

$$V = \frac{3.14 \times 190}{635}\sqrt{2.02^2 - 1.42^2}$$

(4.3)

$$V = 1.351, \quad m \leq 0.85, \; m = 0$$

(4.4)

The optical system includes a CCD camera (LC100/M - Smart Line Camera, USB 2.0, Thorlabs. This CCD camera model is equipped with ultra-high sensitivity linear image sensor ILX554B (Sony), containing 2048 pixels (pixel size: 14µm × 56µm), and operating within 350 - 1100 nm spectral range. LC100 CCD camera has an analog providing DC output in a voltage range of 0 - 4V in 4096 increments; the maximal current is 16 mA. The analog output can be programmed as a static or variable. In a static mode, a constant, adjustable output voltage can be assigned, while in a variable mode, the output voltage represents the light intensity of a selected pixel. Fig. 4.2. shows the control panel and a typical signal from a pixel.

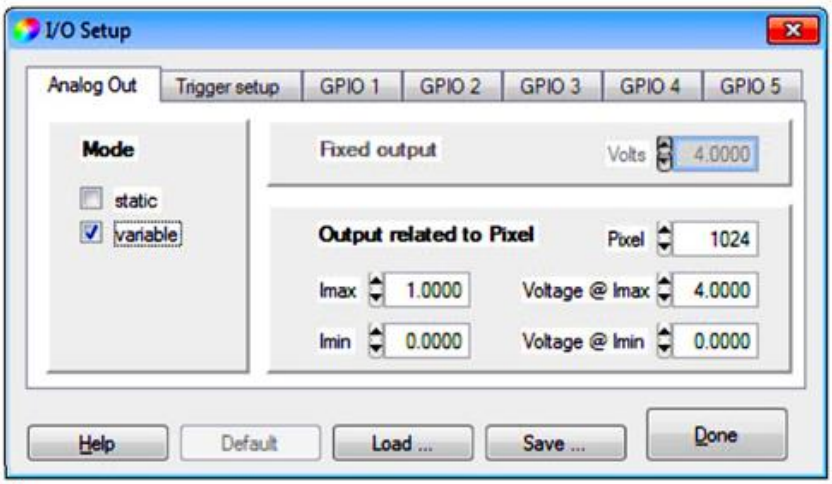

(a)

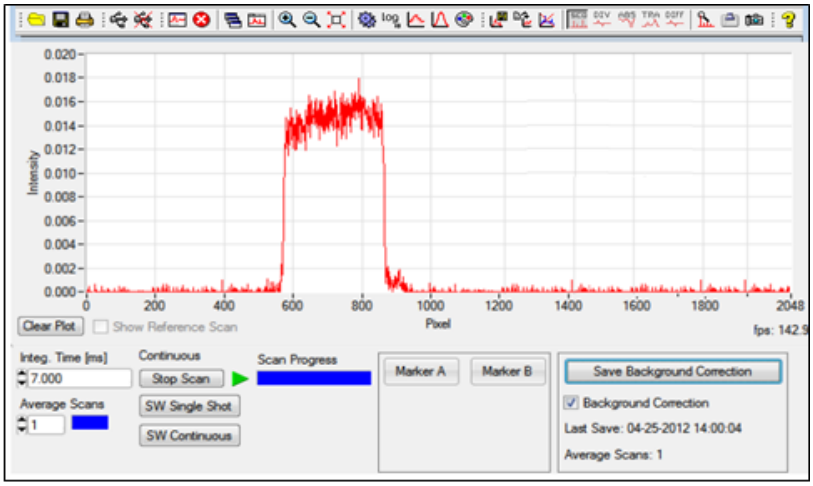

(b)

Figure 4.2 LC 100 output signal control panel (a); typical output signal (b)

The recorded data can be displayed as the light intensity for each pixel. The spectrum chart gives a possibility to monitor the intensity vs number of the pixel to find the most active area of CCD array.

As shown in Fig. 4.3, the analog output signal is recorded with Pico Scope connected to PC via USB. Alternatively, the signals can be processed using SPLICCO software provided by Thorlabs for LC100 CCD camera.

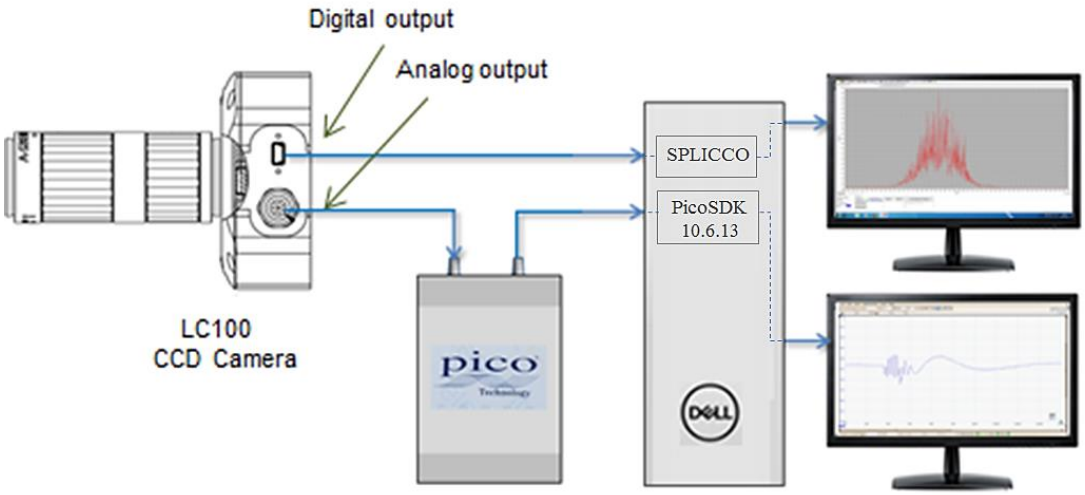

Figure 4.3 LC 100 CCD interfacing to PC via PicoScope.

Semiconductor laser diode (ADL-63054TL) providing a 12^{o} degree fan beam of 630 nm wavelength with 5mW power was used as a light source. Among the three common techniques of light coupling light coupling, i.e. direct end-coupling, prism coupling and grating coupling, the direct coupling was chosen. The light was coupled into the waveguide via a slant edge of the waveguide cut at 47^{o}. This was an optimal light coupling solution which provided enough light intensity propagating through the waveguide. The slant edge coupling shown in Fig. 4.4 is hybrid method combining the prism and end-coupling methods. Slanted edge was obtained by abrading and polishing of the silicon chip. This method has raised the level of output power to ~200μW as compared to single nW in the earlier versions of the OPW set-up [2,3].

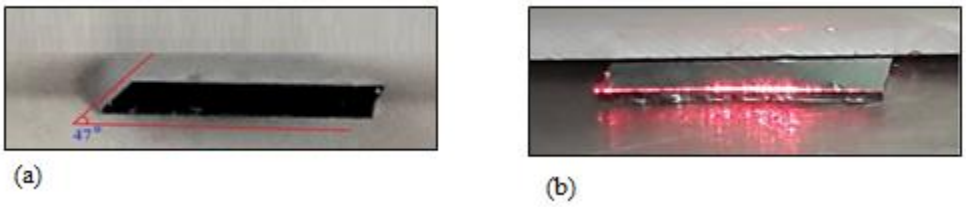

Figure 4.4 Waveguide slant edge (a) and the light propagation through the waveguide (b).

The operation of the system as a sensor requires opening a sensing window in the upper SiO_2 layer of the waveguide. In order to achieve the best performance of the OPW biosensor, the optical system has undergone several stages of development which are outlined in the following sections below.

4.3 OPW set-up, version I

In the first setup, the fan beam laser shined directly at the slant edge of the waveguide piece. The laser source was fixed on an angular moving arm as shown in Fig. 4.5, allowing to adjust the coupling angle and to obtain the maximum output light intensity. The CCD array was placed close to the other side of the waveguide to collect the out-coming light. A polarizer was placed between the waveguide and CCD detector to convert the polarization changes to the variation of the light intensity.

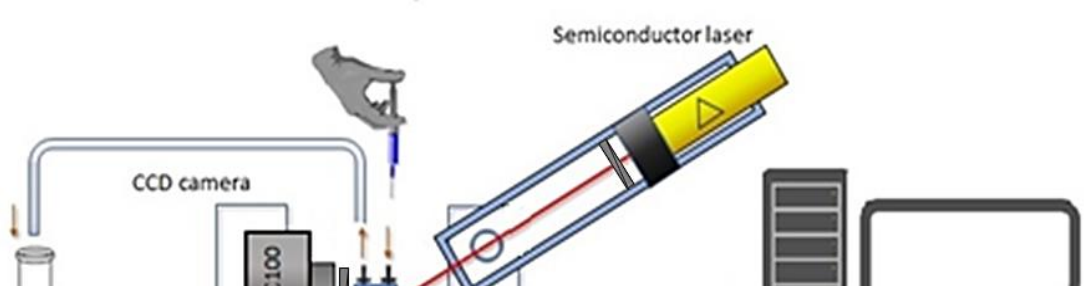

Figure 4.5 The schematic diagram of the 1st version of OPW experimental set-up.

The reaction cell having a volume of $0.072\ cm^3$ was made of nylon and connected with the inlet and outlet micro-tubes. The reaction cell was tightly sealed against the sensing widow using a square shape rubber frame (see Fig. 4.6). The waveguide was sandwiched between the base nylon piece and the cell; the rubber seal had a 6 x 6 mm square opening in the middle to avoid any contact with the surface of the waveguide window. The sensing window was etched in the top SiO_2 cladding layer by injecting diluted (1:10) hydrofluoric acid into the reaction cell. The light intensity was monitored during the etching; when the etching reaches the edge of the core layer, the polarization state of the propagated light became affected and resulted in the oscillation of the light intensity, also the light intensity dropped. At that point the system was flashed with distilled water to stop the etching process and to remove the reaction products.

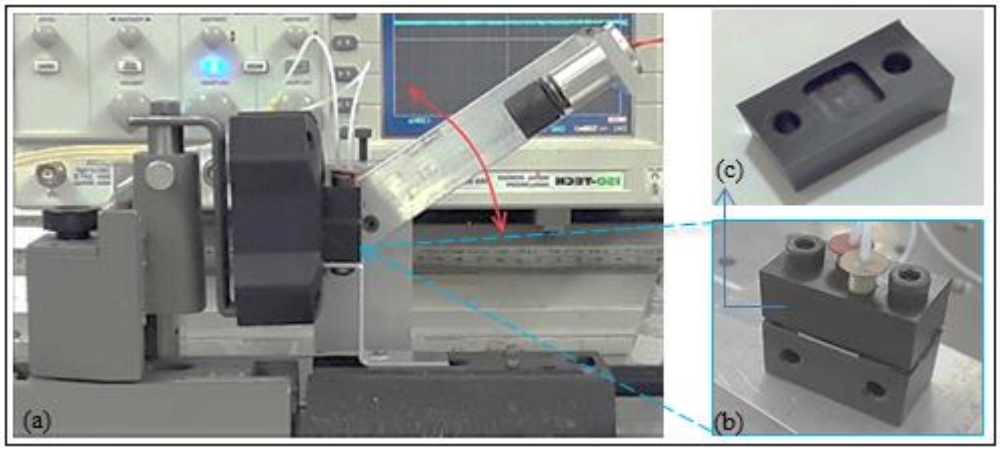

Figure 4.6 The view of the version I setup (a), waveguide placed between the reaction cell and a nylon base (b), reaction cell (c).

Then the waveguide piece was rinsed, dried and checked for thickness in the seining window using ellipsometry. This method ensured that the sensing window was identical to the cell dimensions and it also gives opportunity to monitor the etching process. Finally, the waveguide chip was installed matching the positions of the sensing window against the rubber frame, and the system was ready for testing.

The refractive index sensitivity (RIS) was assessed experimentally by injecting different concentrations of NaCl aqueous solutions into the cell and monitoring the resulting polarization changes of the output light. A typical example of the system response on injection of NaCl is shown in Figure 6a. As one can see, the output waveform doesn't show clear periodic behavior and may consist of several overlapping signals as illustrated by the spectral analysis of the waveform in Figure 4.7a. Spectral analysis of the waveform in Fig. 7b confirmed that of the output waveform is a superposition of more than one signals with different phases and amplitudes. There are two possible explanations for that: (i) there were differences in the light path length across the core due to irregular geometric dimensions of the sensing window, which led to the variation of light polarization across the core; (ii)

each pixel of the CCD array sensor received signals of different phase, therefore, in order to achieve the best system response, the pixels which the least affected by interference and overlapping of the rays must be selected.

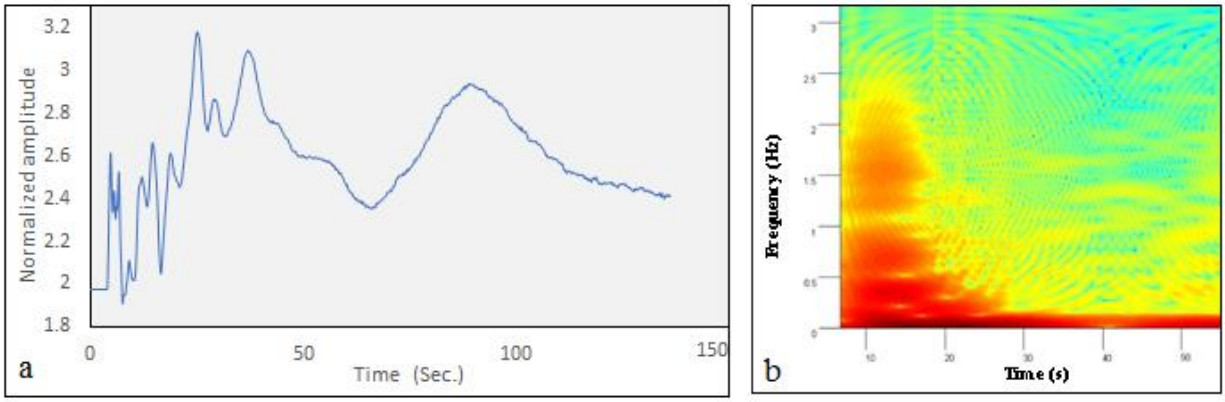

Figure 4.7 The response waveform for for injection of 5% NaCl solution into the cell (a) and the corresponding spectrogram of the output signal (b).

Despite all those difficulties, it was possible to estimate roughly the number of the periods of phase changes from the waveforms presented in Fig. 4.8a. The results obtained are given as a linear dependence of the number of periods of the phase changes against the refractive index in Fig. 4.8b which allows estimating the refractive index sensitivity (RIS) of PW sensors using the following formula [4,5]:

$$RIS = \frac{2\pi N}{\Delta n} \tag{4.3}$$

where N is the number of periods of oscillations,

$$\Delta n = n_{NaCl} - n_{water} \tag{4.4}$$

The refractive index sensitivity (RIS) was found to be around 1200 radians per refractive index unity (RIU). This value of sensitivity was higher than in other traditional optical methods such as SPR and TIRE., but it was lower than reported

for MZ-based sensors (Nabok, 2016). Nevertheless, the first experiment results on detection of three types of mycotoxin were obtained with the 1st version of the setup, and they are presented in Ch. 6.

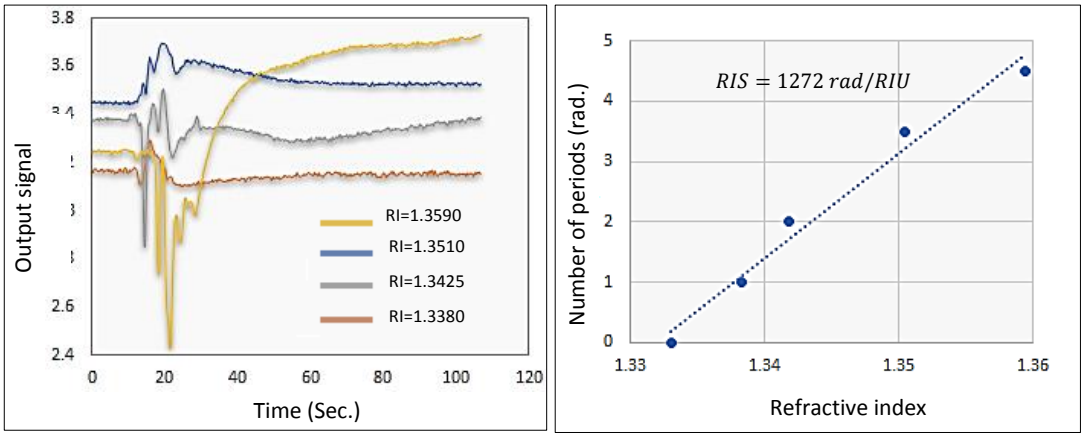

Figure 4.8 The output signals recoded during injections NaCl solutions of different concentrations into the cell (a), and the evaluation of RIS (b).

4.4 OPW set-up, version II

The fist alteration was in the use of a point-beam laser diode as a light source, instead of fan-beam laser diode producing highly divergent light beams of about 12^{o} which is not suitable for this application, in order to reduce the overlap due to reflection from the sides of waveguide channel, in this waveguide dimensions the divergence should be less than 6 degree . Therefore, to meet this requirement, the laser beam has to be collimated using cylindrical lenses. Therefore, in the second setup, a micro cylindrical lens set SM1NR05 - SM1 Zoom Housing (Thorlabs) was placed in front of the laser diode, as shown in Fig. 4.9.

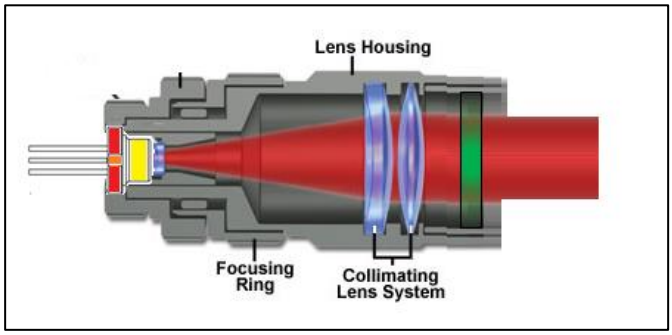

Figure 4.9 The formation the light beam with SM1NR05 - SM1 Zoom Housing.

In addition to reducing the beam divergence, the cylindrical lenses set gave other advantages in reducing astigmatism, improving the wave-front quality, focusing the beam to a small circular spot. As a result, a narrow collimated laser beam (less than 1mm in diameter) has been formed which results in the reduction of noise caused by internal reflections of light within the waveguide overlapping with the main beam. The second alteration was the addition of a quarter wave plate to change polarization from linear to circular. A zero-order quarter-wave plate WPQ10M-266 - Ø1 (from Thorlabs) shown in Fig. 4.10 was used in the set-up, version II.

Figure 4.10 WPQ10M-266 - Ø1" Zero-Order Quarter-Wave Plate.

Another problem appeared in the 1st set-up was the inhomogeneous etching of the sensing window. The calibration of the etching time has been done by performing ellipsometry measurements after a certain etching time. Using the calibration data shown in Fig.4.11 the etching could be performed outside the reaction cell and resulted in homogeneous sensing window.

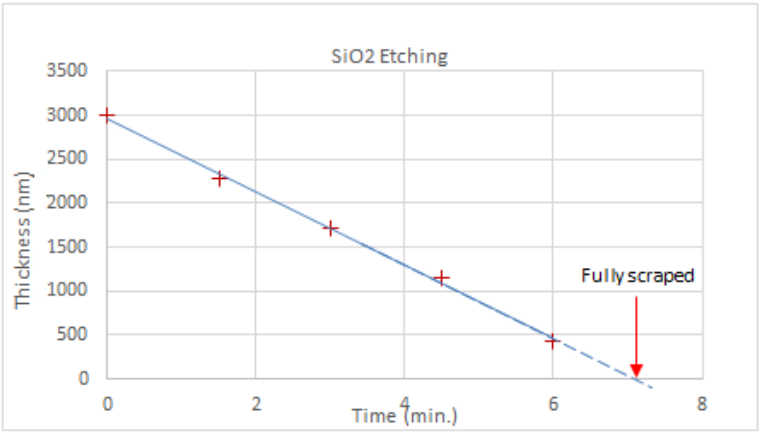

Figure 4.11 Etching kinetics of the SiO2

In the OPW set-up version II shown in Fig. 4.12, in addition to the changes in the optical system, a peristaltic rotary micro-pump was used to deliver the liquid sample to the cell.

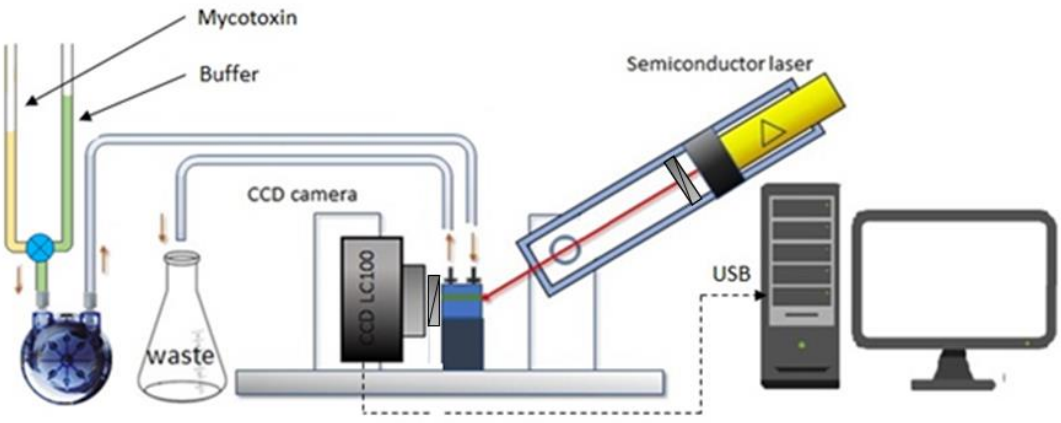

Figure 4.12 The scheme of setup version II of OPW set-up.

The performance of this setup was evaluated by injecting NaCl of different concentrations into the cell. The resulted waveforms shown in Fig. 4.13a appeared to be less noisy and without interferences which allows much easier calculation of the phase change

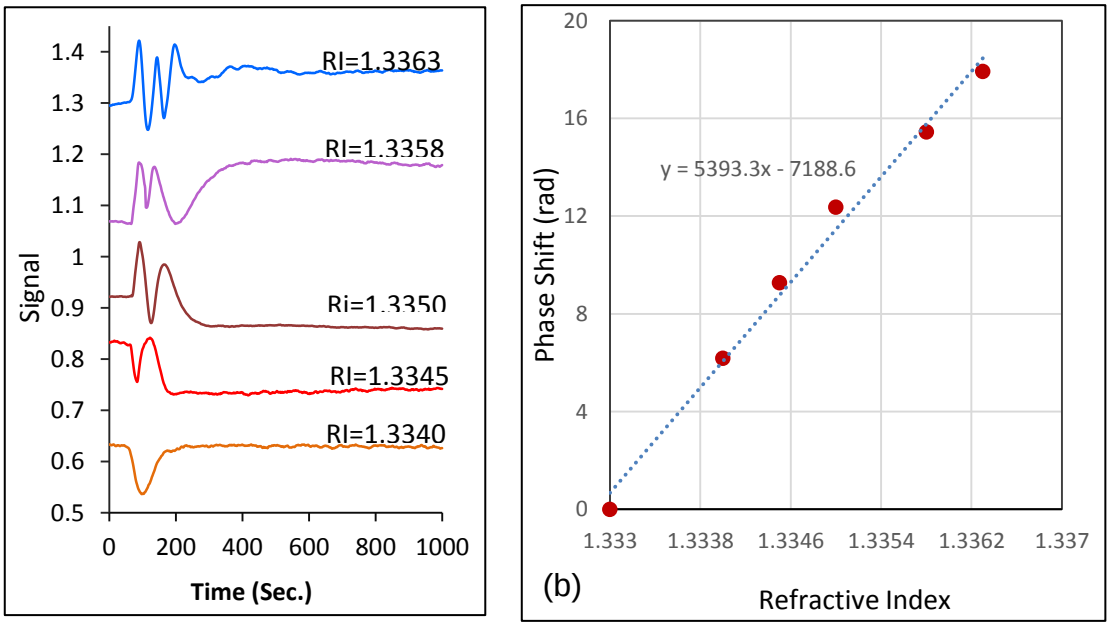

Figure 4.13 Evaluation of refractive index sensitivity for the OPW setup II.

The calibration dependence in Fig.4.13b yields the RIS value of about 5200 rad/RIU which is much higher than in the previous set-up. However, the quality of the output signals was still insufficient for auto calculation of the phase shift, so the number of periods has been calculated manually. The phase variation of the output signal was attributed to the irregular etching of the sensing window which affected the light

pass length within the sensing window and resulted in different phases in the signal at different pixels of CCD array. An additional cause of signal instability was the result of overlapping of rays having different phases.

The shape of the waveform and was also strongly affected by the injection of liquid in the cell. The manual injection was used in the first set-up, while a peristaltic rotary pump was used for liquid samples delivery in the second set-up. Both injection methods could not achieve a smooth constant flow of liquid in the in the reaction cell.

4.5 OPW set-up, version III

All the deficiencies of the second experimental set-up outline above were eradicated in the third version, by improving the waveguide design, the signal collection and processing, and the use of microfluidic system.

In this set-up, the channel waveguide was fabricated using photolithography instead of a planar waveguide in the previous set-ups. The first step was to cut and refine the waveguide piece with regular geometric dimensions. It follows by grinding and polishing the slant edges in both ends of the waveguide piece, and then test them for light propagation. After making sure that the slant edges provide effective light coupling, the waveguide piece was subjected to photolithography processes which are outlined in more detail in the following sections.

4.5.1 Photolithography process

4.5.1.1 Substrate preparation

To prevent complete or partial delamination of the photoresist during pattern developing using wet etching or plating, the substrate surface must be properly cleaned and dehydrated prior to coating with photoresist. Trace residues, including surface moisture, will allow the developer, etchant, or plating solution to penetrate the photoresist layer and undercut the photoresist pattern. Therefore, a thorough cleaning of the surface is a significant step proceed before deposition of the photoresist layer on the waveguide piece. There are two common methods for cleaning the silicon wafer, e.g. wet and dry cleaning. Cleaning processes with use of liquid chemicals are generally referred to as wet cleaning. They utilize a combination of solvents, acids and water to spray, scrub, etch and dissolve contaminants from the wafer surface, while dry cleaning processes use gas phase chemistry or plasma etching for wafer cleaning. In this work wet cleaning was chosen because it is easier and less expensive than dry cleaning which require specialized equipment.

Contaminants can be classified into organic impurities, i.e. skin flakes, skin grease, bacteria, and inorganic ones, i.e. dust particles, salt residues, moisture, etc. After visual inspection the waveguide piece via the optical microscope, the waveguide piece was soaked in acetone with ultrasonic agitation for 30 minutes to dissolve and remove the organic impurities. This process was repeated again using isopropyl alcohol. Finally, the waveguide piece was dried using nitrogen gas and heated up to 100 C^{o} in the oven, to remove all moisture and alcohol residues.

4.5.1.2 Photoresist deposition

Spin coating is the most common method for applying photoresist to a substrate surface. Other less common methods include spraying, roller coating, dip coating,

and extrusion coating. For testing purposes, several photoresist coatings were deposited using different rotation speed in order to optimize the rotation speed and to obtain homogeneous coating with the thickness of about $1\mu m$. The rotation speed of 2500 rpm was found to be optimal. Photolithography is a complex procedure whch consits of several processes shown schematically in Fig. 4.14 and outlined step-by-step below.

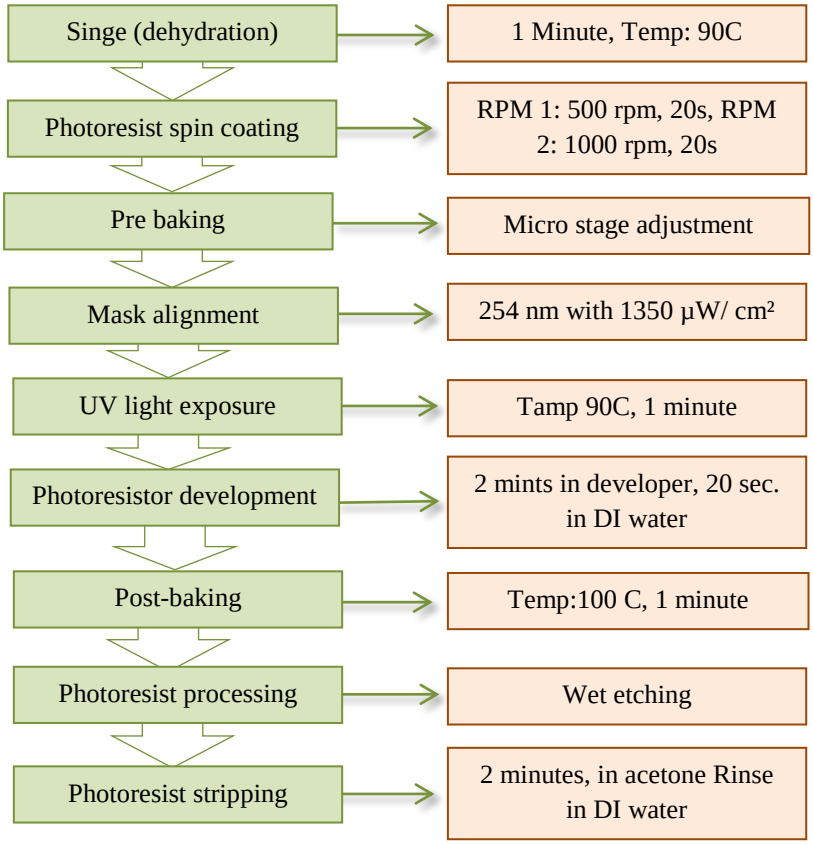

Figure 4.14 Photolithography process steps.

4.5.1.3 Pre-bake (or soft bake)

After spin coating, the solvent concentration in the coated film reduces from 85 to about 10%. The solvent retention is primarily due to its entrapment within nano-capillaries in the polymer layer. The remaining solvent can be removed from the photoresist during the soft baking stage. This stage also anneals the residual stresses that accumulated in the film during spin coating due to evaporation of the solvent and non-equilibrium conformations of long chain polymer molecules. Soft baking was performed at 90-100°C for 20 min in ventilated or convection oven.

4.5.1.4 Photoresist exposure

A negative photoresist ethyl L-lactate 651761 form Sigma Aldrich was used for photolithography. The waveguide pieces coated with a photoresist layer were exposed to UV light through the mask which was aligned and positioned on top of the waveguide. Photoresist was exposed to UV light for 60 s using UVGL-58 source, which provides two UV wavelengths: 365 nm with 1200 µW/cm² intensity, and 254 nm with 1350 µW/cm² intensity. It followed by post- illumination backing treatment, i.e. by gradually (during 30 min) increasing the temperature to 80 ^{o}C, keeping at 80 ^{o}C for 30 min, then reducing gradually the temperature to room temperature during 60 min, to polymerize photoresist layer and make it insoluble during the developing process.

4.5.1.5 Photoresist development

Development is a process of removing unexposed areas of photoresist. The developing was performed by immersing the waveguide pieces in a bath of

developer solution (65,178-8 Resist Developer- Sigma-Aldrich) with stirring for 60 sec, followed by a rinsing several times with isopropyl alcohol. Then the surface was dried by pressurized nitrogen gas.

4.5.1.6 Post-develop baking

A post-develop baking is necessary for stabilizing and hardening the undeveloped photoresist prior to further processing steps, e.g. wet etching, and to ensure complete removal of solvent, improving adhesion in wet etch. This process is usually conducted at 90 -120 ºC using convection oven.

4.5.1.7 **Photoresist Removal (stripping)**

This process consists in complete removal of the photoresist layer after the etching procedure is done. The removal solution has been used to swell the photoresist and then remove it from the wafer.

4.5.2 Etching processes

To fabricate the channel waveguide two types of etching were needed: (i) etching the SiO_2 top cladding layer in order to make the sensing window, and second, (ii) etching the Si3N4 core layer to form the ridge waveguide. Diluted hyrdro-fluoric acid (HF) is typically used for SiO_2 etching, while hot (160 C^o) phosphoric acid (H_3PO_4) was used to etch the Si_3N_4 layer, [6,7, 8, 9, 10].

The speed of these two etching reactions was calibrated using ellipsometry measurements, and the obtained calibrations are presented in Fig. 4.15. These graphs were used to estimate the time required for each etching process. It has to be noted that Si_3N_4 is practically not etched in diluted HF, and *vise-versa* SiO_2 is not etched in

H_3PO_4, therefore the HF etching stops automatically when reaching Si_3N_4 core, and H_3PO_4 etching stops when reaching the SiO_2 cladding underlayer.

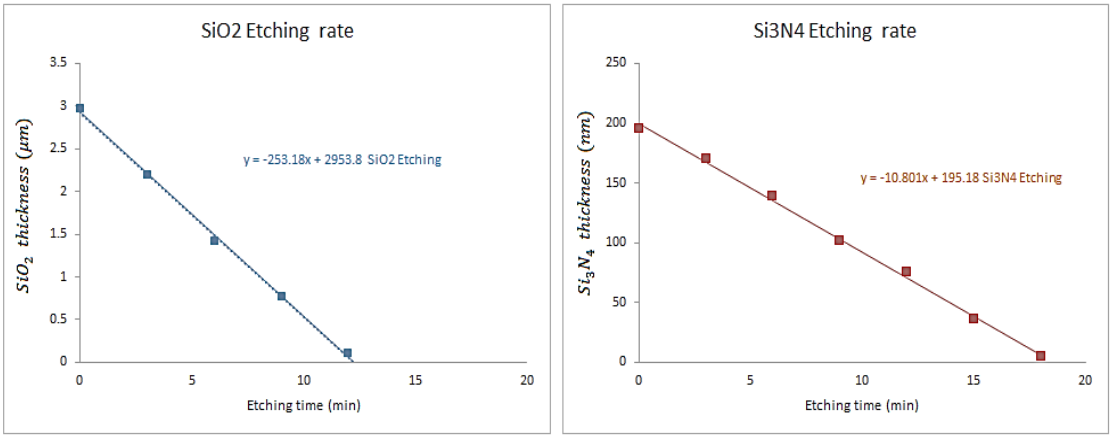

Figure 4.15 Calibration of the etching rate for SiO2 (a) and Si3N4 (b).

4.5.2.1 Fabrication the channel waveguide

The formation of the channel waveguide had required two stages of photolithography. The first step was to remove the upper SiO_2 layer from the whole waveguide piece except the area A and B (see Fig. 4.16) where its existence is necessary to guide the light from the source trough the sensing area and to the detector sensor array. The mask 1 was used for this photolithography step. After preforming photolithography, and etching SiO_2 layer in (1:10) diluted HF, we obtained the structure shown on the right side of Fig. 4.16 with SIO_2 remaining in the areas of A and B.

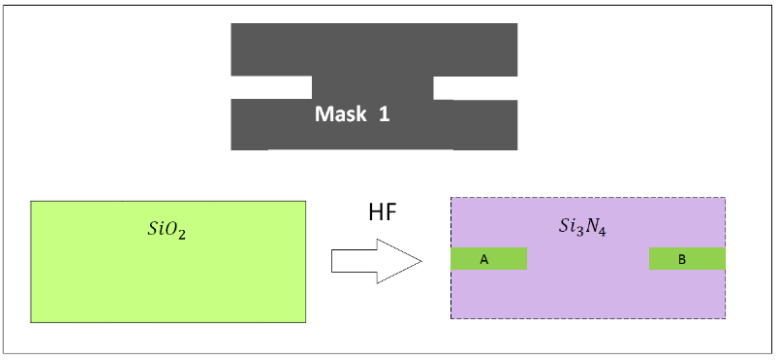

Figure 4.16 The first step of the channel waveguide fabrication.

The second stage was fabricating the Si_3N_4 channel core which is shown in Fig. 4.17. The mask 2 was used in photolithography. The core channel was formed by etching the whole Si_3N_4 layer except the core area using the window in photoresist layer as a stencil. The etching has been done in hot (120 C^o) phosphoric acid. The resulted structure is shown on the right side of Fig. 4.17.

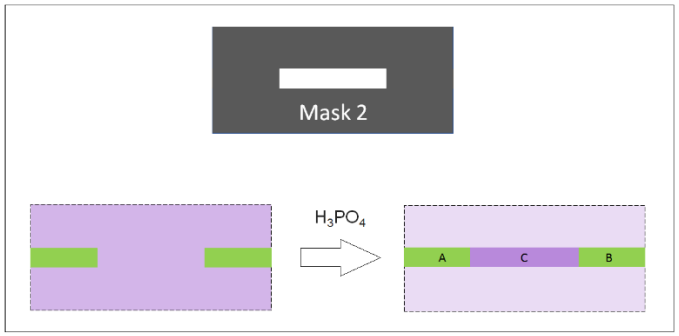

Figure 4.17 The second step the channel waveguide fabrication.

The whole process of the channel waveguide formation is illustrated in Fig. 4.18

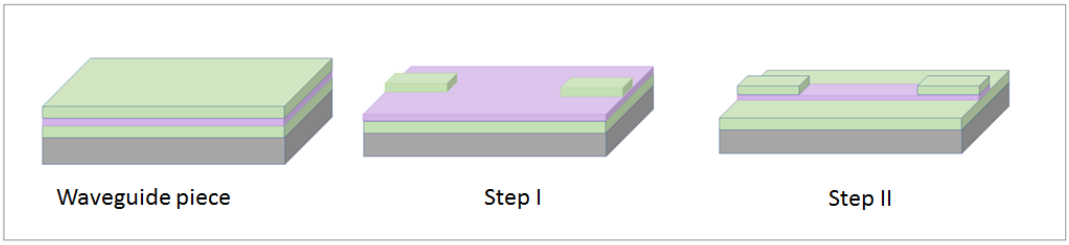

Figure 4.18 Channel waveguide fabrication in two-steps.

4.6 Collection of the output light beam

In both previous setups, the direct contact between the CCD array and the waveguide output end was used to collect the light that coming out of the waveguide core. Because of high diversion of the out-coming light beam, the signal in each pixel of the CCD array was formed by overlapped beams emitted from different points of the wave-front having different phase shifts (see the diagram in Fig. 4.19a) thus resulting in unstable and noisy output signal.

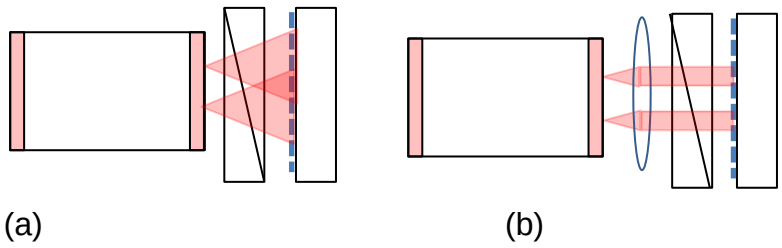

Figure 4.19 The collection of the outcoming beam: directly (a) and using the lens (b).

To eradicate such problem, the optical beam collimation objective was used to create a parallel light beams with minimized overlapping on pixels and thus more stable signal (see fig. 4.19b). The optical element used was zoom housing tube containing a

lens set and linear polarizer (Zoom Housing for Ø1" Optics, Non-Rotating, SM1NR1 - SM1, Thorlabs shown in Figure 4.20). This optical element together with the CCD camera was assembled on angular adjustable arm which gives some flexibility to the set-up. The resulted output signal quality was substantially improved.

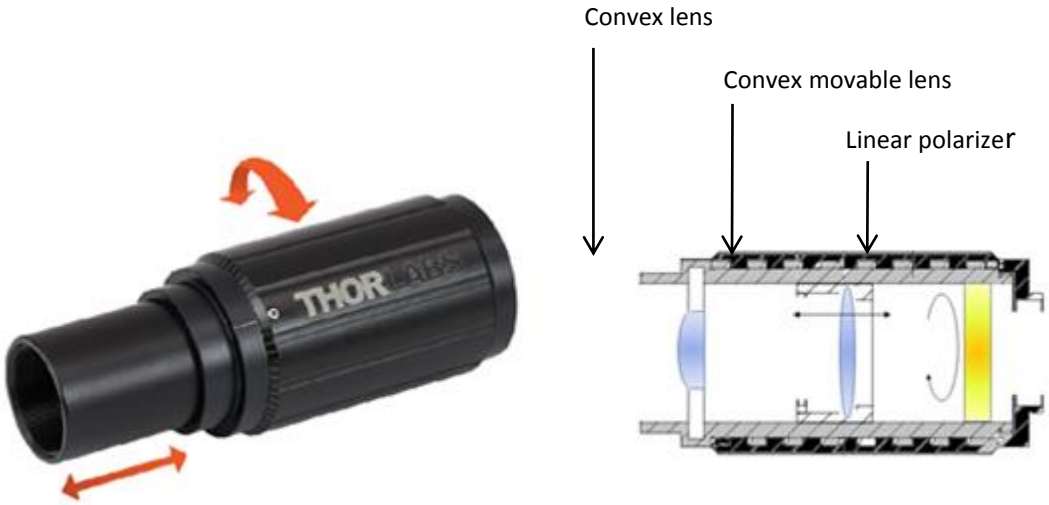

Figure 4.20 SM1NR1 - SM1 Zoom Housing.

4.7 Reaction cell and microfluidic system

The detailed analysis of the performance of previous experimental set-ups showed that both the geometric shape of the reaction cell and microfluidic system have significant effects on the resulting sensor signal. The injection of liquid samples of into a wide cell usually produces uneven lateral distribution of concentration chemicals within in the cell, which is illustrated in Fig. 4.21a. Such transversally inhomogeneous properties of liquid may cause instability of the output signal. The use of narrow cells with dimensions $(1 \times 1 \times 8)mm$ in the setup version III results

in more homogeneous liquid mixture (see Fig. 4.21b) and thus eliminates this source of signal instability (see Fig. 4.22).

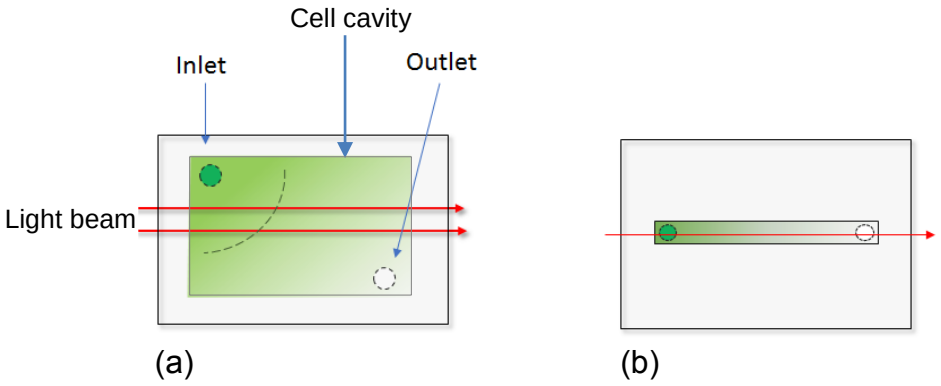

Figure 4.21 The effect the reaction cell width on homogeneity of liquid samples.

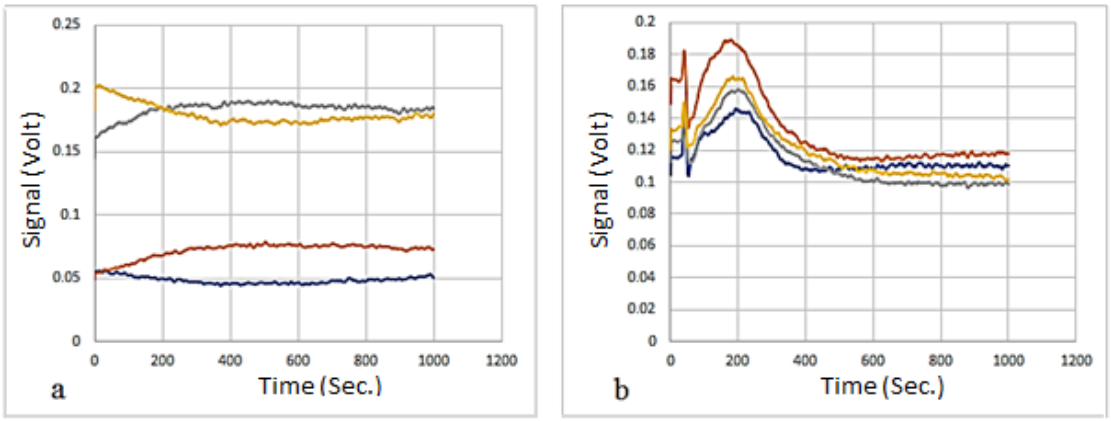

Figure 4.22 The effect of the cell width on the output signal: (a) the signal from different pixels in a 6 mm wide cell, (b) the same signals in a narrow (1mm) cell.

The use of a rotary peristaltic pump for injection of liquid samples into the cell causes additional instability of the flow and thus in the sensor signal in the set-up version II (not to mentioning an obvious flow instability during manual injection

used in the set-up version I. Therefore, the replacement of peristaltic pump with a syringe pump has significantly improved the sensing signal. In the set-up version III shown schematically in Fig. 4.23a and photograph in Fig. 4.23b, all the changes mentioned above were combined which allowed us to overcome the difficulties and achieve a stable output signal and eventually improve the sensitivity of detection.

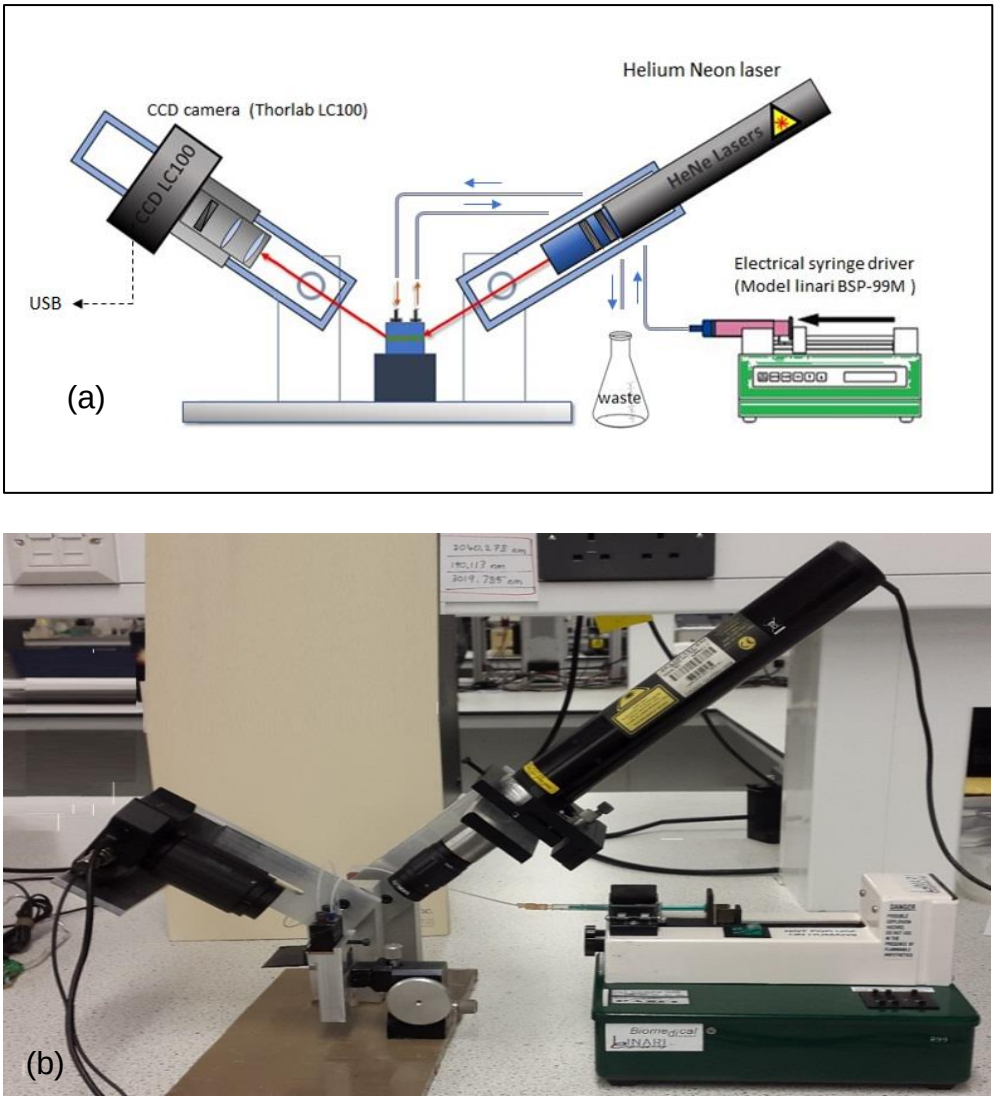

Figure 4.23 OPW experimental set-up, version III: Schematic diagram (a) and photograph (b).

4.8 Signal processing

The periodical output of the signal is produced due to the rotation of the polarization of the light coming out of the waveguide which is related to a variable phase shift between p- and s- components of polarized light developing on course of changes in the refractive index of external medium or molecular adsorption, as was described in detail in Ch.3. The phase shift, which constitutes the actual sensor response, can be found from the recorded waveforms. Such phase shift can be roughly estimated by counting the number of periods of oscillations of the output signal, which has been done in the first two versions of the experimental set-up; the accuracy of such estimation is rather poor, e.g. from ½ to ¼ of a period. Poor quality of the output signal did not allow more precise calculation of the phase shift by automatic processing of the output signal. In the version III set-up, the quality of the signal was sufficient for more accurate calculation of the phase shift which has be done in the following steps. First, the original output signal shown in Fig. 4.24 a has to be normalized as illustrated in Fig. 4.24 b.

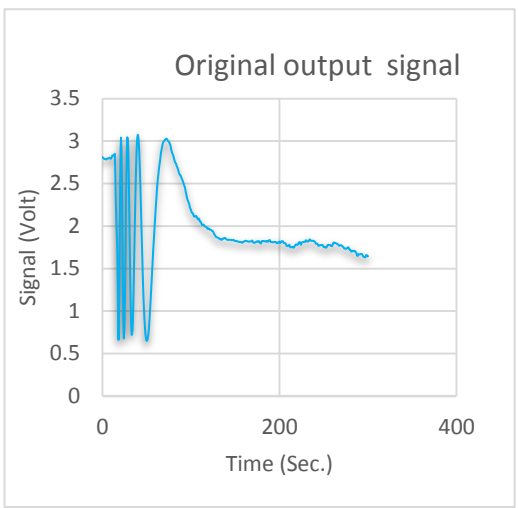

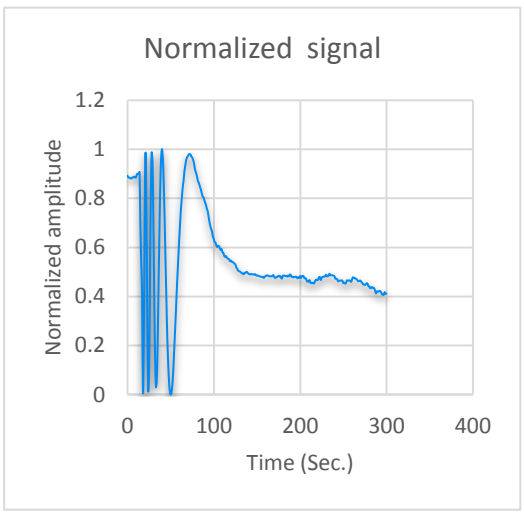

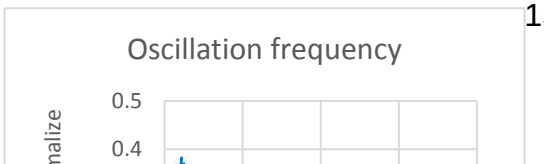

Figure 4.24 Signal processing: original signal (a), normalized signal (b), absolute values of the rotation frequency (c), and the phase shift (d)

Knowing that the phase shift (φ)is a function of rotation frequency $\omega(t)$

$$\varphi = f[\omega(t)] \tag{4.5}$$

the rotation frequency can be found by differentiating the normalized waveform, then taking the absolute values of the obtained parameters:

$$\omega(\mathrm{t}) = \left|\frac{d\varphi(t)}{\mathrm{dt}}\right| \tag{4.6}$$

The resulted graph is shown in Fig. 4.24c. The area under the angular frequency $\omega(\mathrm{t})$ represents the total amount of phase displacement, which can be by integrating the $\omega(\mathrm{t})$ curve over the whole period of measurements (T)

$$\varphi = \int_0^{\mathrm{T}} \omega(\mathrm{t})\mathrm{dt} \tag{4.7}$$

The resulted time dependence of the phase shift is shown in Fig. 4.24d response is the actual sensor response. The signal processing described above was carried out using Origin 8.0 software; the screen shots in Fig. 4.25 demonstrate the procedure.

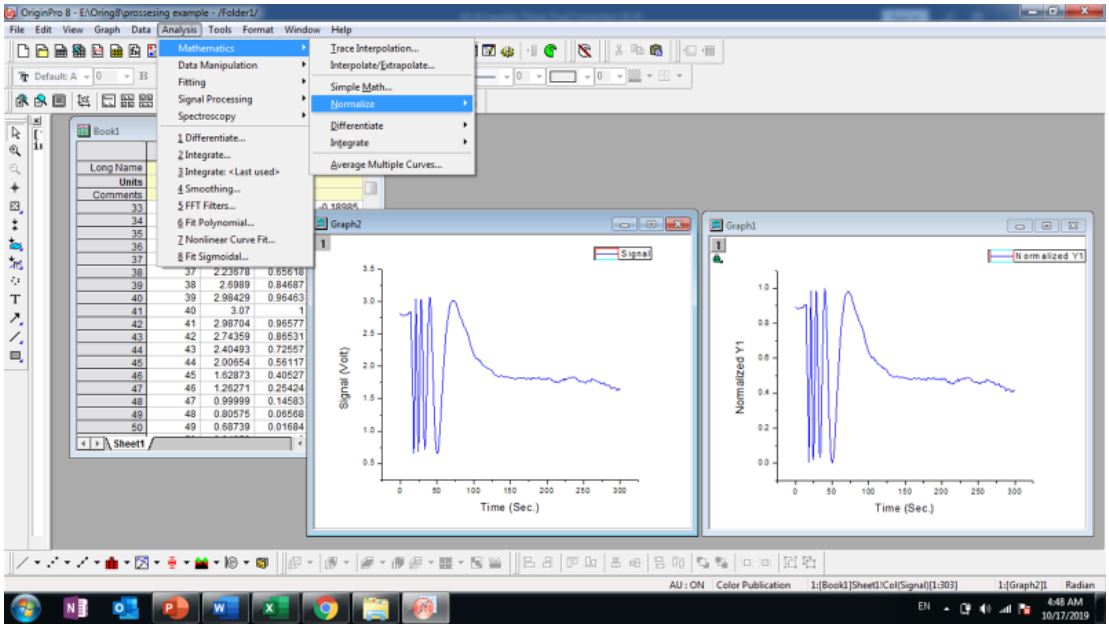

(a)

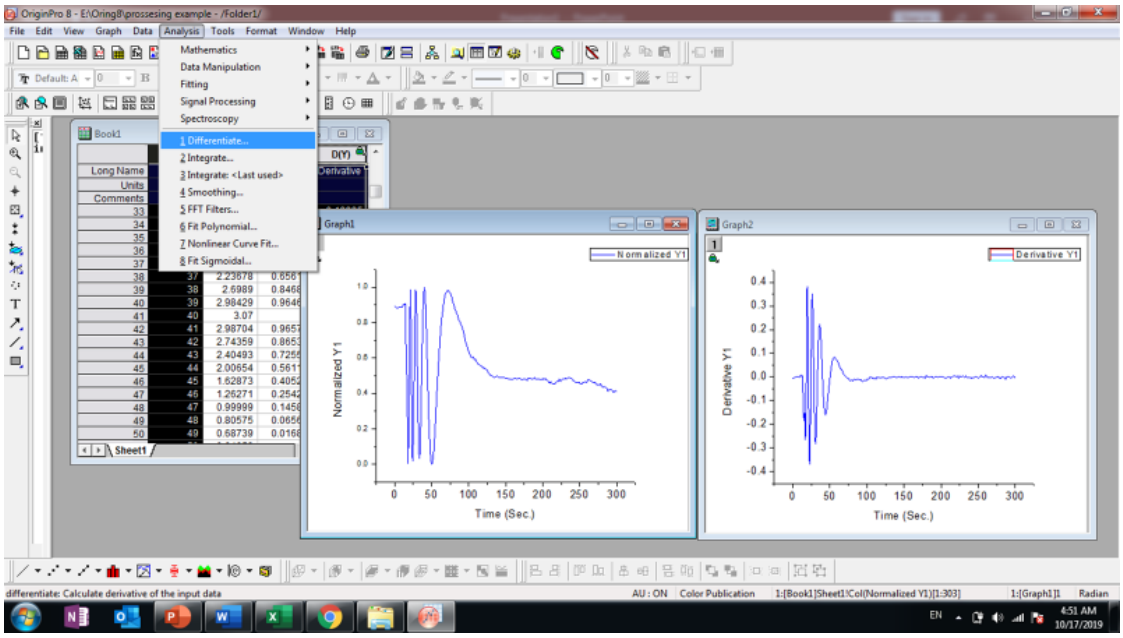
Mathematics
Data Manipulation
Fitting
Signal Processing
Spectroscopy
1 Differentiate...
2 Integrate...
3 Integrate: <Last used>
4 Smoothing...
5 FFT Filters...
6 Fit Polynomial...
7 Nonlinear Curve Fit...
8 Fit Sigmoidal...
Graph1
Normalized Y1
Graph2
Derivative Y1
Time (Sec.)

(b)

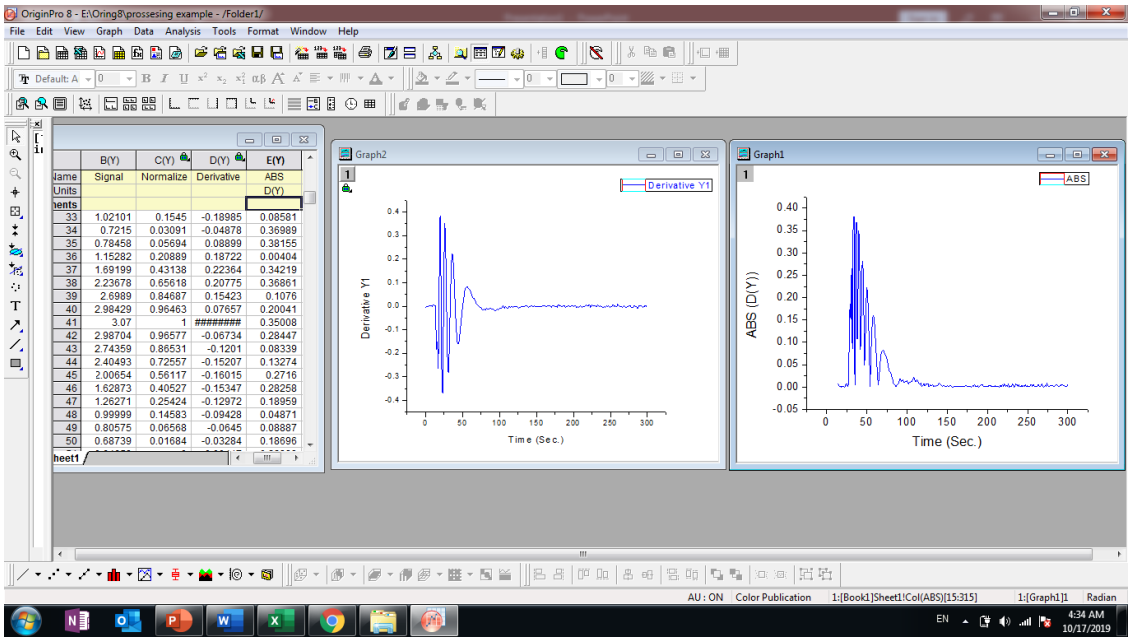
Graph2
Derivative Y1
Graph1
ABS
ABS (D(Y))
Time (Sec.)

(c)

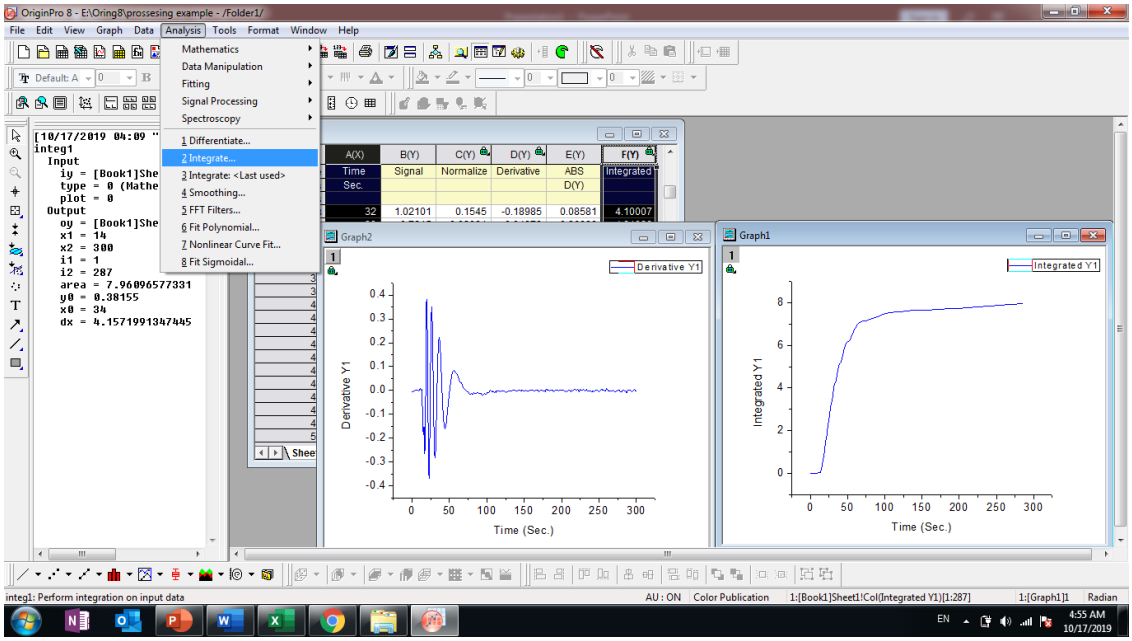

(d)

Figure 4.25 Origin-8.0 screen shots demonstrating all stages of signal processing: normalization (a), derivation (b), taking absolute values of the derivative (c), and integrate of absolute values of the derivative (d).

4.9 The evaluation of the sensitivity of the final setup

The evaluation of sensitivity the final version of the UPW PI set-up was carried out the same way as before, e.g. injecting solutions of sodium chloride of different concentrations, recording the corresponding waveforms and evaluation of the phase shift signal processing described above. The results are shown in Fig. 4.25.

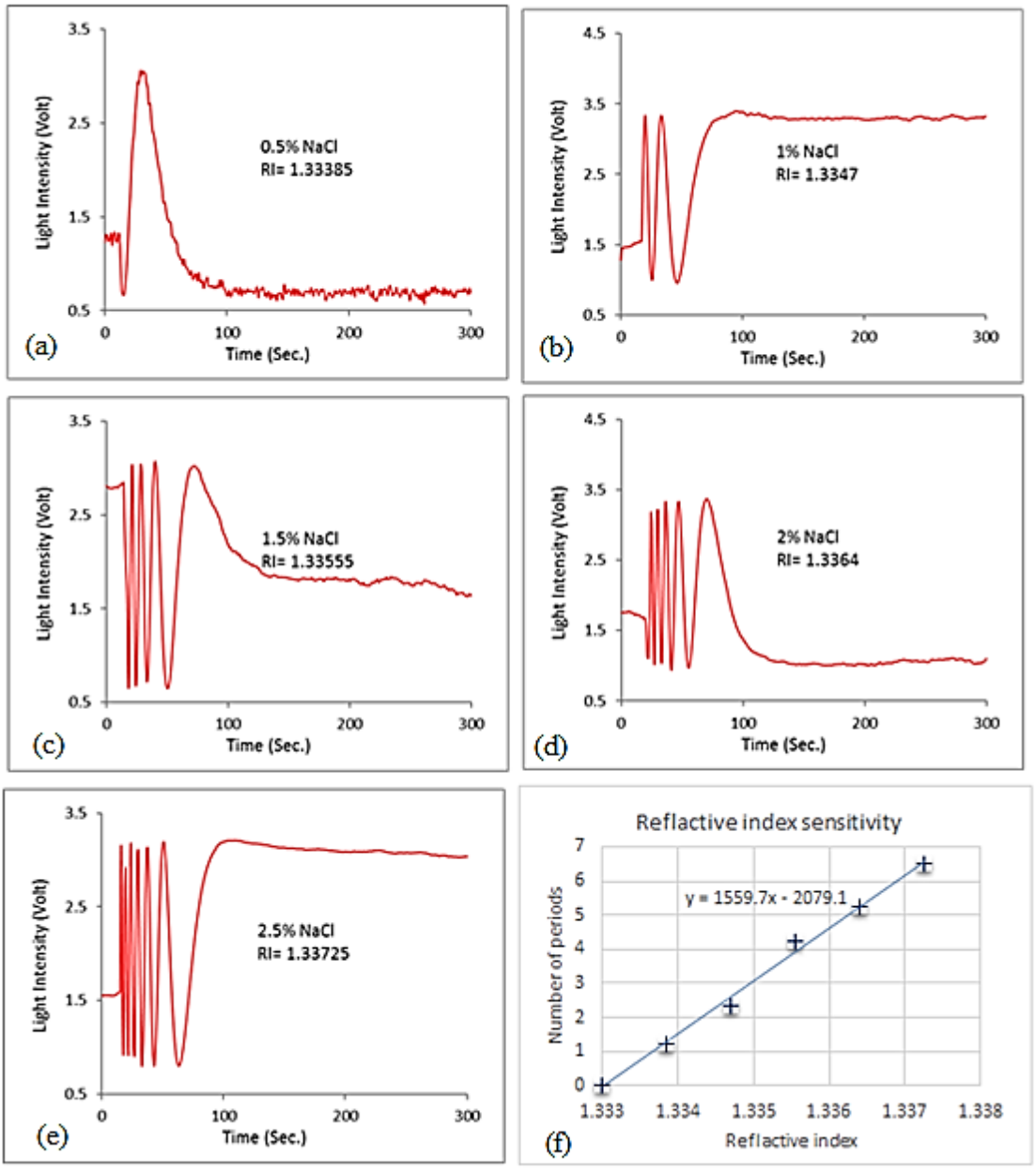

Figure 4.26 The output wave forms corresponding to different concentrations of NaCl (a, b, c, d, e) and dependence of the phase shift on refractive index (f).

As one can see, the obtained signals of much better quality than before represent values of the phase shift between the p- and s- components of polarized light caused by variations in the refractive index of the medium. The refractive index sensitivity can be evaluated from the gradient of linear dependence of the phase shift vs refractive index in Fig. 4.26f. The value of 1.559.5 (in number of periods per

refractive index unity) given on the graph can be converted in more conventional units of radians per RIU to become 9800 rad/RIU. The obtained value is very close to that obtained earlier by modeling of the waveguide, e.g. RIS=9300 rad/RIU. The obtained value is the largest among the reported RIS values for other interferometry biosensors, such as MZ interferometers [11, 12, 13, 14].

4.10 Conclusion

Both design and fabrication of the waveguide were described in this chapter. The system has undergone three stages of developments by optimizing optical system,

liquid sample delivery system and waveguide design. Each stage of development has resulted in an increase in sensitivity and performance improvement.

Table 4.1 summarizes all features of each set-up as well as the resulted refractive index sensitivity (RIS), for the experimental set ups.

Parameter	Set up 1	Set up 2	Set up 2
Light source	Laser diode, 5 mW, fan beam, 638 nm wavelength.	Laser diode, 5mW, Parallel beam, 638 nm wavelength.	Helium Neon laser, 5mW, point beam, wavelength 632.8 nm
Optical	Single cylindrical lens, planer focusing	Two cylindrical lenses, two-axises focusing	Quarter-Wave Plate, two cylindrical lenses, two-axises focusing
Cell	Wide cell (6×6×2 mm)	Wide cell (8×6×2 mm)	Channel cell (8×1×1mm)
Sample delivering	Manual injection	micro pump	Syringe pump
RIS	2500 rad/RIU	5300 rad/RIU	9800 rad/RIU

4.11 References

1. Kasap, S. O., & Sinha, R. K. (2001). *Optoelectronics and photonics: principles and practices* (Vol. 340). New Jersey: Prentice Hall.

2. Anna Tsargorodska, (2007). RESEARCH and DEVELOPMENT in OPTICAL BIOSENSORS for DETERMINATION of TOXIC ENVIRONMENTAL POLLUTANTS, PhD thesis.
3. Nabok, A., Haron, S., & Ray, A. (2004). Registration of heavy metal ions and pesticides with ATR planar waveguide enzyme sensors. *Applied surface science*, *238*(1-4), 423-428.
4. Chalyan, T., Pasquardini, L., Falke, F., Zanetti, M., Guider, R., Gandolfi, D., ... & Pavesi, L. (2016, April). Biosensors based on Si3N4 asymmetric Mach-Zehnder interferometers. In *Optical Sensing and Detection IV* (Vol. 9899, p. 98991S). International Society for Optics and Photonics.
5. Nabok, A. (2005). *Organic And Inorganic Nanostructures (Artech House Mems and Sensors Library)* (Vol. 286). Artech House Publishers Hardcover.
6. Verhaverbeke, S., Teerlinck, I., Vinckier, C., Stevens, G., Cartuyvels, R., & Heyns, M. M. (1994). The etching mechanisms of SiO2 in hydrofluoric acid. *Journal of The Electrochemical Society*, *141*(10), 2852-2857.
7. Kang, J. K., & Musgrave, C. B. (2002). The mechanism of HF/H 2 O chemical etching of SiO 2. *The Journal of chemical physics*, *116*(1), 275-280.
8. Verhaverbeke, S., Teerlinck, I., Vinckier, C., Stevens, G., Cartuyvels, R., & Heyns, M. M. (1994). The etching mechanisms of SiO2 in hydrofluoric acid. *Journal of The Electrochemical Society*, *141*(10), 2852-2857.
9. Van Gelder, W., & Hauser, V. E. (1967). The etching of silicon nitride in phosphoric acid with silicon dioxide as a mask. *Journal of the Electrochemical Society*, *114*(8), 869-872.
10. Seo, D., Bae, J. S., Oh, E., Kim, S., & Lim, S. (2014). Selective wet etching of Si3N4/SiO2 in phosphoric acid with the addition of fluoride and silicic compounds. *Microelectronic Engineering*, *118*, 66-71.
11. Yuan, D., Dong, Y., Liu, Y., & Li, T. (2015). Mach-zehnder interferometer biochemical sensor based on silicon-on-insulator rib waveguide with large cross section. *Sensors*, *15*(9), 21500-21517.
12. Mukundan, H., Anderson, A., Grace, W. K., Grace, K., Hartman, N., Martinez, J., & Swanson, B. (2009). Waveguide-based biosensors for pathogen detection. *Sensors*, *9*(7), 5783-5809.
13. Duval, D., González-Guerrero, A. B., Dante, S., Dominguez, C., & Lechuga, L. M. (2012, May). Interferometric waveguide biosensors based on Si-technology for point-of-care diagnostic. In *Silicon Photonics and Photonic Integrated Circuits III* (Vol. 8431, p. 84310P). International Society for Optics and Photonics.
14. Nabok, A. (2016). Comparative studies on optical biosensors for detection of bio-toxins. In *Biosensors for Security and Bioterrorism Applications* (pp. 491-508). Springer, Cham.

Chapter 5: Chemical part

5.1 Introduction

This chapter provides comprehensive analytes (mycotoxins) used in this project as well as their specific bio-receptors such as antibodies and aptamer, special attention was given to immobilization of antibody and aptamer on translucent surface.

5.2 Biomaterial, which are targeted by experiment

5.2.1 Mycotoxin, general description

The word "mycotoxin" is derived as a combination of Greek name for fungus "mykes" and Latin word ‘toxicum’ which means poison. This term generally identifies a group of toxic substances excreted as secondary products of fungi metabolism [1], probably, as a chemical protection of the mould from other microorganisms [2]. Such moulds (or fungi) have the ability to grow on food and feed stuff at certain environmental conditions of elevated temperature and moisture which are quite common, particularly in tropical countries, therefore these fungi are widespread [3].

Mycotoxins being relatively small molecules with molecular weight in hundreds of Daltons are known by their highly toxic effects on human and animals [4, 5]. Usually, crops that stored in a damp environment (60-80% humidity) at the temperatures in the range of 30-40°C for few days become a potential field for fungi growth and therefore mycotoxin contamination [6]. The classification of mycotoxins is complicated, due to the large variety of their originating fungi species and chemical structure. The most important mycotoxins from the perspective of agriculture and food industry, and public health are: aflatoxins, ochratoxins, zearalenone, and fumonisins.

5.3 Mycotoxins selected for this study

5.3.1 Aflatoxins

Aflatoxins are secondary metabolites of *Aspergillus* fungi strains. Aflatoxins have received great deal of attention because of their toxic and carcinogenic properties and also because of the fact that they are most frequent contaminants in agriculture products associated food [8]. The optimal temperatures for the production of aflatoxins by *A. flavus* and A. *parasiticus* are reported to be between 25 and 30 °C which made them very common contaminants worldwide [9, 10]. Molecular structure of aflatoxin B1 is shown in Fig. 5.1

Molecular Formula: C17H12Cl2O6

Molecular Weight: 383.179580 g/mol

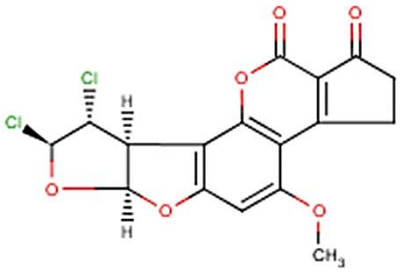

Figure 5.1 Molecular structure of aflatoxin B1 from Aspergillus flavus [11].

The humans and live stock can be exposured to aflatoxins through the products such as maize, rice, groun- and tree- nuts, cocoa beans, figs and other dried foods, spices, crude vegetable oils, and many other derivative products, which could be contaminated with fungi before and after the harvest. Aflatoxin B1 was classified as

group I carcinogen by the International Agency for Cancer Research [12]. For example aflatoxin B1 in concentrations as low as 1 ppb in the diet of trout [13] can cause malignant hepatocellular carcinomas. Such propertires made aflatoxin B1 one of the most abundant, toxic and potent naturally occurring carcinogenic substance known, Many countries have sitted a lower level for aflatoxins ranges are between 0.02 and 5 ppb, with 0.05 ppb the most common [14]. EU has Setted limits for Aflatoxin in range (0.01-10 ppb) depend on kind of food and type of aflatoxin [15, 16]. There are approximately 16 known types of aflatoxins. The four major aflatoxins that cause illness in humans are B1, B2, G1, G2, M1 [17, 18]. Among those, aflatoxin B1 is the most common contaminant in food [19,20], and M1 is most common in milk contamination, [21]. Figure 5.2 shows the fluorescence images of *Aspregillus flavus* generating aflatoxin B1,[21]. Fig. 5.2 shows the fluorescence images of *Aspregillus flavus* generating aflatoxin B1.

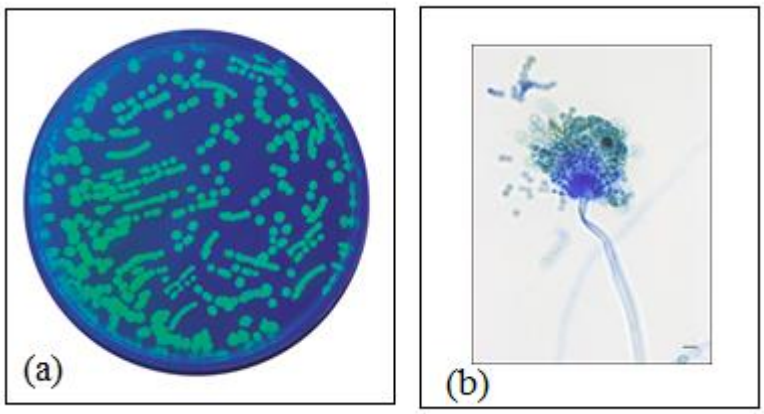

Figure 5.2 UV fluorescent microscopy images of Aspergillus flavus containing aflatoxin B1.

5.3.1.1 Physical and chemical properties

Aflatoxins are a colorless to pale-yellow crystals at room temperature. They are slightly soluble in water and hydrocarbons, soluble in methanol, acetone, and chloroform, and insoluble in non-polar solvents. Crystalline aflatoxins and their solutions stored in dry and dark environment are extremely stable and can be still active for years [19,20]. Aflatoxins are relatively unstable in light and air, particularly in their solutions in polar solvents, or under exposure to oxidizing agents or UV light. At their melting points (237 °C - 299 °C) aflatoxins decompose but are not destroyed under normal cooking conditions. They can be completely destroyed by autoclaving in the presence of ammonia or by treatment with bleach [21]. Destruction in aflatoxin molecules can occur by braking the lactone ring followed by decarboxylation at high temperatures in aqueous solution at pH 7. The lactone ring is a subject to alkaline hydrolysis, for example by treatment with potassium permanganate, sodium hypochlorite, sodium perborate, chlorine, ozone, and hydrogen peroxide; therefore, these oxidizing agents can be used for aflatoxins decontamination [22].

5.3.1.2 Toxicological Profile

Aflatoxins induce DNA damage, negatively affect the DNA damage repair, and alter DNA base compositions of genes [23]. Aflatoxins are associated with both toxicity and carcinogenicity in human and animal populations. Aflatoxin B1 is considered as responsible for both toxicity as well as carcinogenicity. The diseases caused by the consumption of aflatoxins are known as aflatoxicoses with liver being the main target organ.

5.3.2 Ochratoxin

Ochratoxin A (OTA) is a mycotoxin produced by secondary metabolism of many filamentous species belonging to the genera *Aspergillus* and *Penicillium* [1–4]. The chemical structure of OTA is given in Fig. 5.4.

Molecular Formula: C20H18ClNO6

Molecular Weight: 403.815 g/mol

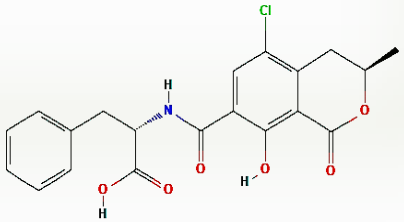

Figure 5.3 Chemical structure of Ochratoxin A [11].

There are three types of ochratoxins, with ochratoxin A (OTA) being the most toxic and commonly detected in foodstuff. The primary source of ochratoxin contamination in food and feed stuff is cereal commodities (maize, oats, barley and wheat) in addition to groundnuts, dried fruits and coffee beans [25, 26,27].

5.3.2.1 Physical and chemical properties

OTA is unstable when exposed to light, especially in very humid conditions; however, it is stable in the dark in ethanol solutions [28]. OTA is also thermally stable; in cereal products, up to 35% of the toxin survives autoclaving for up to 3 hours [29]. OTA is a weak organic acid with a pKa value of 7.1, and a molar mass of 403.8 g/mol. OTA crystals are varying from colourless to white, this molecule possesses an intense green fluorescence under UV light in acid medium and blue fluorescence in alkaline conditions [30]. In acid and neutral pH, OTA is slightly soluble in water, moderately soluble in chloroform, soluble in polar organic solvents

(alcohols, ketones, acetonitrile, methanol, and ethylacetate), and insoluble in petroleum ethers and saturated hydrocarbons. While in alkaline conditions, this molecule is soluble in aqueous sodium bicarbonate solution and in all alkaline solutions in general. It has a melting point of about 90 °C when crystallized from benzene as a solvent, however, non-solvated crystals has a melting point of 169 °C. OTA solution prepared in polar organic solvents such as ethanol or methanol can be stored for more than a year without any loss of activity if kept cold and in the dark conditions. Crystalline OTA is colourless, in the absence of moisture, are extremely stable up to 3 hours of autoclaving, if kept away from light and UV radiation [31,32].

5.3.2.2 Toxicological Profile

Nephropathy and neurotoxicity are the major toxic effect of OTA. It has been shown that the OTA induced damage in the central nervous system. OTA can be regarded as a possible cause of certain lesions as well as damage at the cerebral level. Thus, this substance seems to be highly toxic for the nervous cells and able to reach at any time the neural tissue (brain, retina, etc.) [33].

5.3.3 Zearalenone

Zearalenone (ZEN) is a common contaminant of all major cereal grains worldwide; it is a nonsteroidal estrogenic mycotoxin produced by several *Fusarium* species, including *Fusarium graminearum* (*Gibberella zeae*), *F. culmorum, F. cerealis, F. equiseti*, and *F. semitectum.* It is found worldwide in a number of cereal crops such as maize, barley, oats, wheat, rice and sorghum, and also in bread [34]. The trivial

name zearalenone is derived from Gibberella zeae and it chemical structure is shown in Fig. 5.5.

Molecular Formula: $C_{18}H_{22}O_5$

Molecular Weight: 318.369 g/mol

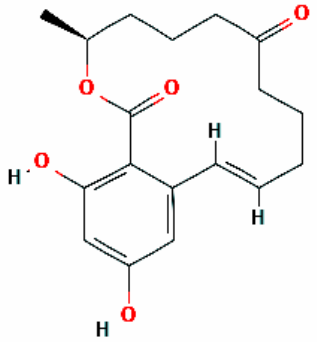

Figure 5.4 Chemical structure of zearalenone [11].

ZEN has been associated with increasing incidences of breast cancer. The International Agency for Research on Cancer (IARC) has placed ZEN in the category group 3 [34].

5.3.3.1 Physical properties

Zearalenone is a white crystals having melting-point of 164–165 °C. Molecular formula: $C_{18}H_{22}O_5$, and Molecular weight: 318.4 g/mol. The structure is shown in Fig. 5.4 [35].

The solubility of zearalenone at 25 °C in percent by weight are: 0.002% in water, 0.05% in n-hexane, 1.13% in benzene, 8.6% acetonitrile, 17.5% in dichloromethane, 18% in methanol, 24% in ethanol, and 58% in acetone. ZEA is a stable compound,

both during the storage and processing (cooking) of food, and it does not degrade at high temperatures at 120 °C. It can be decomposed by 29% when heated at 150 °C for 60 minutes, and by 69% at 200 °C for 60 minutes. Zearalenone is stable to hydrolysis in neutral or acid buffer solutions.

5.3.3.2 Toxicological Profile

Zearalenone has been associated with different negative effects on humans and animals especially on the reproductive system. ZEN acts as Oestrogen mimicking agent, the toxic effects of ZEA are lipid peroxidation, cell death and the inhibition of protein and DNA synthesis, so it causes functional, morphological alterations in reproductive organs [35].

5.4 Bio-receptors for detection of mycotoxins

5.4.1 Antibodies

The antibody is a type of glycoprotein protein having Y-shape molecular structure. Antibody is one of the main elements of the immune system in mammals produced by B-lymphocytes after exposure to a given antigen. The main function of antibodies in the organism is to bind foreign species, e.g. molecules, toxins, etc., which are called generally as antigens and remove them from the body of mammals. The remarkable property of antibodies is a high degree of affinity of binding specific antigens [36,37]. Such specific binding properties of antibodies made them an ideal bio-receptor in various biosensing applications. The whole branch of biosensors utilizing antibodies is called immunogens. Antibodies specific to the mycotoxins,

e.g. aflatoxin B1, ochratoxin A, and zearalenone, were also used as bioreceptors in this project [38].

5.4.1.1 ANTIBODY STRUCTURE:

An antibody is an aggregation of molecules having a Y- shape and the size of about 10 nm. In general, all antibodies have very similar structure. As shown in Figure 5.6, the antibody consists of four polypeptide chains: two light chains and two heavy chains which are joined together by di-sulfide bridges to form a "Y" shaped molecule called Immunoglobulin (IgG). Each chain is composed from about 70 to 110 amino acids and are classified into different categories according to their size and function. All antibodies have very similar structure except small variable parts at the tips of the light chains called as hyper-variable regions. There are only five types of mammalian Ig heavy chain denoted by the Greek letters: α, δ, ε, γ, and μ. while there are only two kinds of immunoglobulin light chain are named as κ and λ. Each side of the top of the "Y" of an antibody have a variable structure of amino-acids which can be tuned to accommodate a particular antigen in key-lock type of interaction [39,40]. Such interaction explains extremely high selectivity of antibodies to specific targets (antigens).

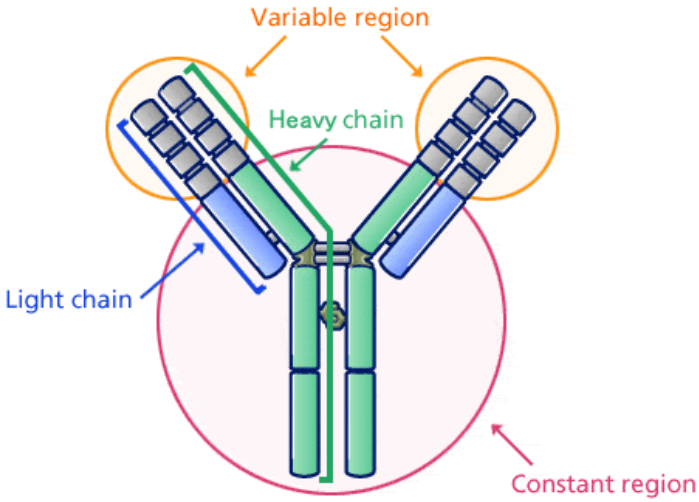

Figure 5.5 The schematic diagram of IgG molecule [45].

5.4.1.2 Antibody-Antigen Interaction

The interaction of an antibody antigen is a reversible binding reaction which follows the basic thermodynamic principles of reversible bimolecular interaction due to several non-covalent interactions involving electrostatic, hydrophobic and hydrogen bonding (Figure 5.7). The antigen to antibody binding is due to the formation of multiple non-covalent bonds between the amino acids in Fab-fragments of antibody and the antigen. The antibody-antigen reaction is characterized by affinity which is the strength of antibody-antigen bonding produced by summation of the attraction and repulsion forces, such as Van-der-Waals interactions, salt bridges, hydrophobic forces, and hydrogen bonds [46].

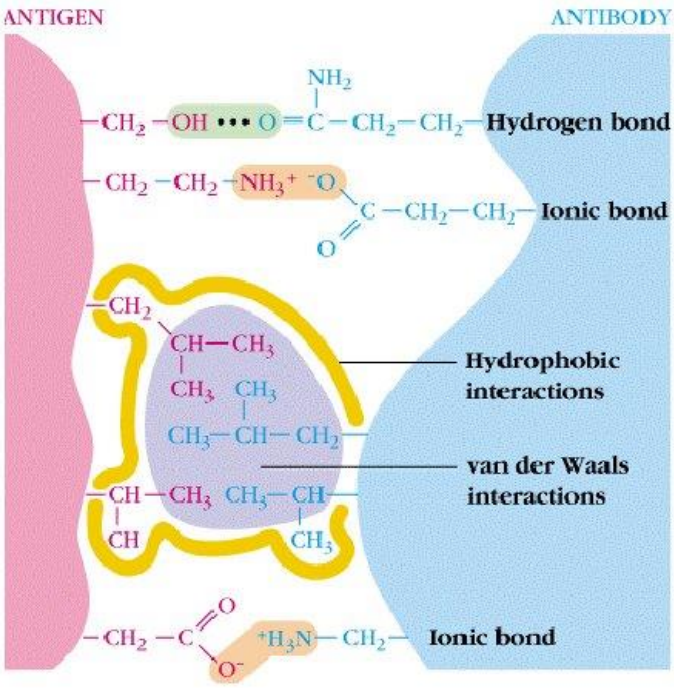

Figure 5.6 The noncovalent interactions that form the basis of antigen-antibody (Ag-Ab) binding [47].

The affinity factor of antibody-antigen is affected by molar concentration, temperature, pH, ionic strength, and the rate of diffusion, the parameters which plays important roles in determining the equilibrium of binding reaction, [48, 49,50]. The parameters which represent the antibody-to-antigen binding strength are the association constant K_A (mol^{-1}) = k_a / k_d which is the ratio of rates of adsorption (k_a) and desorption (k_d), or its reciprocal parameter called affinity coefficient K_D (mol) = $1/K_A = k_d / k_a$, [49, 50, 51].Typically for IgG-based antibodies, the values for K_A are in the range of 10^6 to 10^8 mol^{-1} or K_D of 10^{-6} to 10^{-8} mol, [51].

The immobilization of antibodies and their orientation control on the surface of transducers is very important for sensor performance,[52]. Immobilization methods

involving covalent binding of antibodies to the surface are the most common since they provide the highest stability [53]. Electrostatic immobilization of antibodies is also quite strong (Coulomb interaction is the second strongest after the covalent one) and thus very popular and commonly used in various biosensing applications [54]. This can be achieved using the layers of polyelectrolytes adsorbed on the surface. For example, on the glass which is usually negatively charged due to OH^- groups on the surface, a layer of polycations, such as polyallylamine hydrochloride (PAH), has to be adsorbed first. Then the negatively charged antibodies from their buffer solutions with pH about 7.5 -8 can be immobilized on top as shown in Fig. 5.8a. [55]

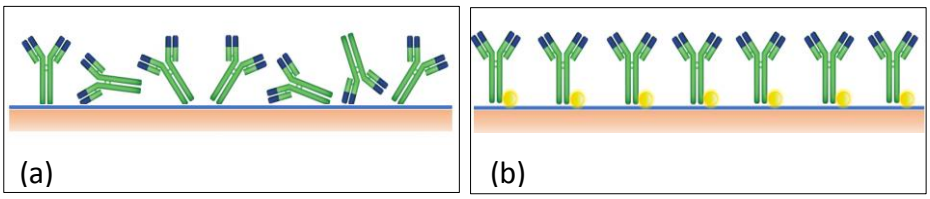

Figure 5.7 (a) Randomly oriented antibodies immobilized directly on polycation layer; (b) vertically oriented antibodies immobilized via intermediate layer of protein G (or A) [55]

The problem with such method of immobilization is the random orientation of antibodies with their Fab-fragments not available for binging antigens. To achieve the maximal efficiency of antibody-antigen binding, the antibodies should be immobilized on the surface of transducer in such way that antibody's binding sites were available for binding, i.e. oriented in normal direction to the surface. This could be done using intermediate layer of protein A (or G) which have a binding side to the constant domain of antibodies (see Fig. 5.8b) [56]. Therefore, protein A (or G) being negatively charged in the buffer solution with pH 7.5-8 have to be immobilized first.

Then antibodies are bound to protein A (or G). This process is described in detail in Ch.6.

5.5 Aptamers

The term “aptamer” was coined by its inventor Andrew D. Ellington, and this word is stemming from Latin terms “aptus” which means fit, and “meros” which means part. In 1990, Robertson and Joyce developed the *in-vitro* selection protocol to adapt the sequence of oligonucleotides in DNA or RNA to accommodate specifically the target molecules. These efforts paved the way for *in-vitro* generation of various DNA or RNA oligonucleotides with new properties and characteristics [57].

Aptamers are typically produced by SELEX method (Figure 5.9) [58], which is schematically outlined in Fig. 5.19, from a random library of nucleic acids incubated together with a target molecule, in that way some nucleic acids are getting adsorbed on the target in a particular sequence. The non-bound nucleic acids are separated from those to a target. Then the chains of bound nucleic acids is polymerized and separated from the target. The resulted polynucleotide is then amplified by PCR (polymerase chain reaction) and used in the binding of next cycles. Such procedure is repeated from 6 to 12 times and resulted in polynucleotide chain highly specific to the target molecule [59, 60, 61].

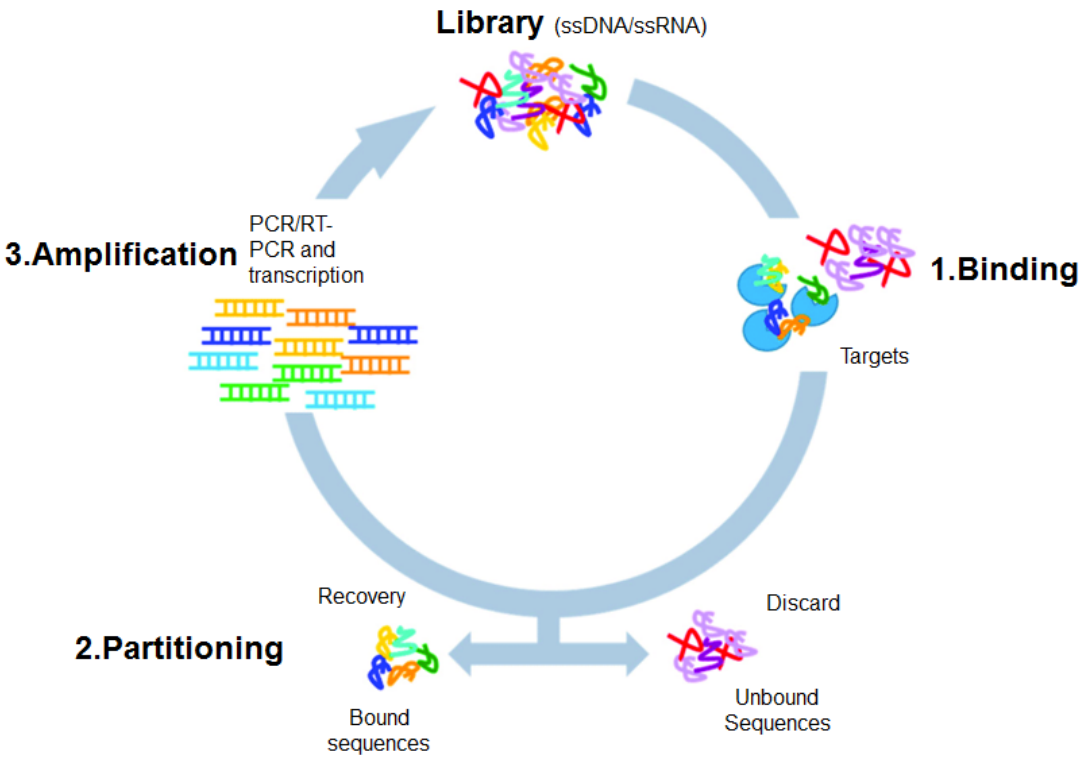

Figure 5.8 Scheme of SELEX process of producing aptamers [58].

Aptamers depending of their nucleotide sequences have different types of secondary structures (Figure 5.10) in buffer solutions due to the interactions nucleic acids and subsequent formation of base pairs, e.g. cytosine (C) with guanine (G), and adenine (A) with thymine (T) in DNA or uracil (U) in RNA. The presence of MgCl salt in the buffer solution plays a vital role in maintaining stability of secondary structures [62, 63]. Several examples of such secondary structures are shown in Fig. 5.10.

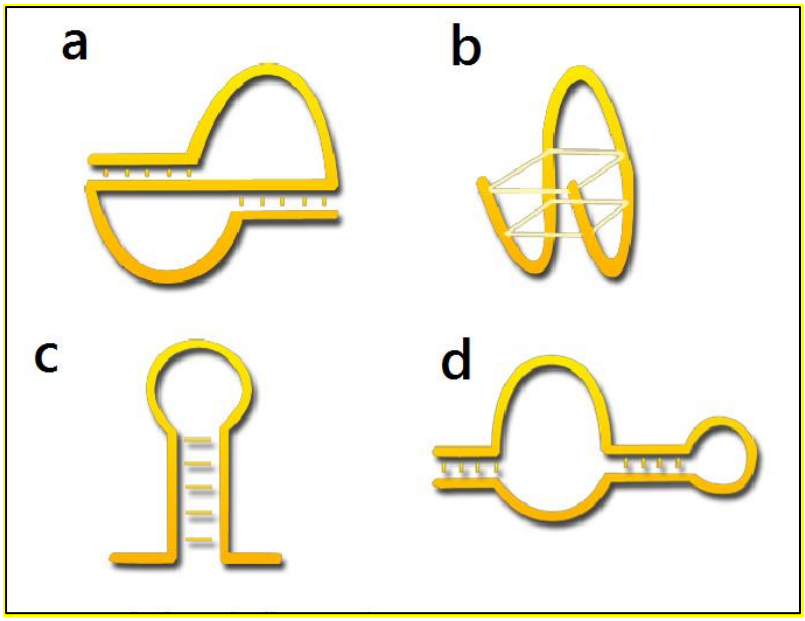

Figure 5.9 Example of aptamers' secondary structures: (a) pseudo-knot, (b) G-quadruple, (c) stem loop/ bulge, (d) hairpin [62].

Aptamers change their secondary structures upon interaction with their specific targets by engulfing or wrapping around the target molecules. Such phenomenon can be utilized for detection of target molecules in various biosensing applications.

There are several possibilities for biosensing depending of the type of aptamers used and on the presence of particular functional groups. Aptamer can be immobilized on the surface via functional groups typically attached at C3 terminal, for example SH group can be used for immobilization on gold surface. On the other end, typically C5 terminal, the aptamers can be labeled with either redox or fluorescent functional groups. As shown schematically in Fig. 5.11 for labeled aptamers immobilized on the surface of gold, the labels may come closer to the electrode surface as a result of biding the target molecule thus either increasing the electron transfer between redox group and the electrode (in electrochemical sensors) or quenching

fluorescence in close proximity to the gold surface (in fluorescence sensors), [63, 64, 65].

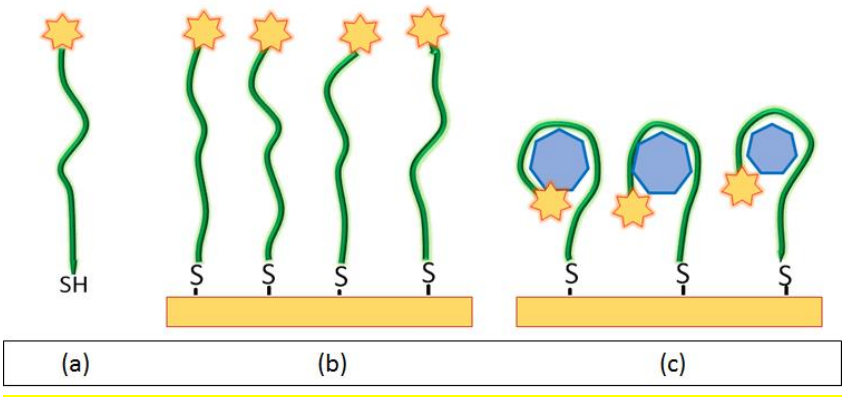

Figure 5.10 Labelled aptamers (a) immobilized on the surface of gold (b) and binding the target molecules (c).

If unlabeled aptamers are used, the molecular binding could be detected as changes in the molecular layer thickness or refractive index using the detections methods of SPR, TIRE, LSPR, and planar waveguides. The above situations outline the so-called direct assay format when the target is binding to a receptor immobilized on the surface (see Fig. 5.12 a, b). There are other types of assays formats possible, for example sandwich assay, when a secondary aptamer or antibody can bind to a target (see Fig. 5.12 c, d) or competitive assay, when the target is immobilized on the surface and aptamers (or antibodies) compete for binding to the target molecules on

the surface and free target analytes in solutions (see Fig. 5.12 e). All these formats can be utilized in apta-sensing, [66, 67].

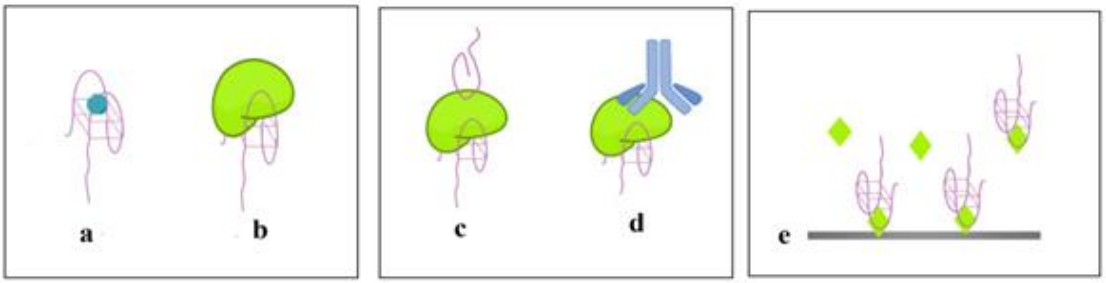

Figure 5.11 Direct aptamer assay with small (a) and large (b) target molecules; sandwich assay using secondary aptamers (c) or antibodies (d); and competitive assay (e) [68].

Aptamers have several advantages over traditional antibodies:

1. Simple and inexpensive synthesis with no ethical restrictions;
2. Thermal stability and less sensitivity to environment (buffer solutions);
3. Possibility of adding functional groups, i.e. SH groups for immobilization on gold; surface, and functional groups (redox or fluorescent labels);
4. Simple aptamers recovery by thermo-cycling (using PCR units);
5. Small size, which makes aptamers more suitable for direct assay sensing format.

Because of their advantages aptamers are becoming increasingly popular in biosensing and practically substituted antibodies in the market.

Aptamer have several applications in biomedical diagnostic; they can be particularly useful in biomedical diagnosis for the development of disease biomarker. A diagnostic based aptamer kit was developed for detection of mycotoxins and aflatoxins in particular [69, 70]. Biotechnology company Aptagen developed an

interesting technology known as the aptamer – beacon (Apta-beacon) which can be utilized for quick biomarker development. Apta-beacon is potentially great for point of care treatment of patients [71]. The development of a biosensor for the rapid and simple detection of aflatoxin B1 may lead to the advance of several aptasensors for AFB1 analysis in food. This technique is used as a molecular identification probe for the detection of AFB1 and demonstrate y an extensive detection range for aflatoxin B1 from 0.1 to 10 ng/ml [72, 73]. The detection method is based on chemiluminescence competitive assay utilizing G quadruplex horseradish peroxidase- like DNAzyme (HRP-DNAzyme) connected to AFB1 aptamer. The assay permitted the detection of AFB1 in spiked corn sample with LOD=0.35nM [74, 75, 76, 77].

5.6 Conclusion

The target analytes (e.g. mycotoxins) used in this work were described in chapter five in detail including their origins, main physical, chemical properties and basement effect on human and animal. The allowed limits of mycotoxins in food and animal feed are typically in the ranges of 0.1 to 1 μg. Two types of biosensors used in this project for selective binding of mycotoxins are antibody and aptamers. The chemical structure and functioning of antibodies were described in detail including the methods of their immobilization on surface of transducers. The electrostatic immobilization method which was chosen in this work was outlines in more detail. Aptamer type of biosensors were described in this chapter including their synthesis, chemical structure, main properties and advantages over traditional antibodies.

5.7 References

1- Turner, N. W., Subrahmanyam, S., & Piletsky, S. A. (2009). Analytical methods for determination of mycotoxins: a review. *Analytica chimica acta*, *632*(2), 168-180.

2- Medeiros, F. H. V. D., Martins, S. J., Zucchi, T. D., Melo, I. S. D., Batista, L. R., & Machado, J. D. C. (2012). Biological control of mycotoxin-producing molds. *Ciência e agrotecnologia*, *36*(5), 483-497.

3- Speijers, G. J. A., & Speijers, M. H. M. (2004). Combined toxic effects of mycotoxins. *Toxicology letters*, *153*(1), 91-98.

4- Turner, N. W., Subrahmanyam, S., & Piletsky, S. A. (2009). Analytical methods for determination of mycotoxins: a review. *Analytica chimica acta*, *632*(2), 168-180.

5- Turner, N. W., Bramhmbhatt, H., Szabo-Vezse, M., Poma, A., Coker, R., & Piletsky, S. A. (2015). Analytical methods for determination of mycotoxins: An update (2009–2014). *Analytica Chimica Acta*, *901*, 12-33.

6- xxxxxx

7- Medeiros, F. H. V. D., Martins, S. J., Zucchi, T. D., Melo, I. S. D., Batista, L. R., & Machado, J. D. C. (2012). Biological control of mycotoxin-producing molds. *Ciência e agrotecnologia*, *36*(5), 483-497.

8- Klich, M. A. (2007). Aspergillus flavus: the major producer of aflatoxin. *Molecular plant pathology*, *8*(6), 713-722.

9- Lillehoj, E. B. (1983). *Effect of environmental and cultural factors on aflatoxin contamination of developing corn kernels*(No. 87-031148. CIMMYT.).

10- Agag, B. I. (2004). Mycotoxins in foods and feeds: 1-aflatoxins. *Ass. Univ. Bull. Environ. Res*, *7*(1), 173-205

11- Aptamers based on Electrochemical impedance spectroscopy, Doctoral Thesis, Cristina Ocana Tejada, University Autonoma de Barcelona, 2015.

12- Hsieh, D. P. H. (1985). An assessment of liver cancer risk posed by aflatoxin M 1 in the Western world. *Trichothecenes and other mycotoxins. New York, John Wiley & Sons*, 521-8.

13- Cheeke, P. R. (1998). *Natural toxicants in feeds, forages, and poisonous plants* (No. Ed. 2). Interstate Publishers, Inc., PO Box 50.

14- Unnevehr, L., & Grace, D. (Eds.). (2013). *Aflatoxins: Finding solutions for improved food safety* (Vol. 20). Intl Food Policy Res Inst.

15- Aflatoxin European Commission https://ec.europa.eu/food/safety/chemical_safety/contaminants/catalogue/aflatoxins_en
16- EU Food & Aflatoxin Legislation https://www.peanutsusa.org.uk/eu-food-aflatoxin-legislation
17- World Health Organization, Food Safety Digest, February 2018. https://www.who.int/foodsafety/FSDigest_Aflatoxins_EN.pdf
18- Bbosa, G. S., Kitya, D., Lubega, A., Ogwal-Okeng, J., Anokbonggo, W. W., & Kyegombe, D. B. (2013). Review of the biological and health effects of aflatoxins on body organs and body systems. *Aflatoxins-recent advances and future prospects*, *12*, 239-265.
19- Saini, S. S., & Kaur, A. (2012). Aflatoxin B1: Toxicity, characteristics and analysis: Mini review. *Global Advanced Research Journal of Chemistry and Material Science*, *1*(4), 063-70.
20- Fouad, A. M., Ruan, D., El-Senousey, H. K., Chen, W., Jiang, S., & Zheng, C. (2019). Harmful Effects and Control Strategies of Aflatoxin B1 Produced by Aspergillus flavus and Aspergillus parasiticus Strains on Poultry. *Toxins*, *11*(3), 176.
21- Galvano, F., Galofaro, V., & Galvano, G. (1996). Occurrence and stability of aflatoxin M1 in milk and milk products: a worldwide review. *Journal of Food protection*, *59*(10), 1079-1090.
22- Bueno, D., Muñoz, R., & Marty, J. L. (2014). Common methods to detect mycotoxins: a review with particular emphasis on electrochemical detection. *Sensing in Electroanalysis.(K. Kalcher, R. Metelka, I. Švancara, K. Vytřas; Eds.). 2013/2014, Volume 8.*
23- Battilani, P., Pietri, A., Barbano, C., Scandolara, A., Bertuzzi, T., & Marocco, A. (2008). Logistic regression modeling of cropping systems to predict fumonisin contamination in maize. *Journal of Agricultural and Food Chemistry*, *56*(21), 10433-10438.
24- https://www.who.int/ceh/capacity/mycotoxins.pdf
25- Richard, J. L. (2007). Some major mycotoxins and their mycotoxicoses—An overview. *International journal of food microbiology*, *119*(1-2), 3-10.
26- Carnaghan, R. B. A., Hartley, R. D., & O'kelly, J. (1963). Toxicity and fluorescence properties of the aflatoxins. *Nature*, *200*(4911), 1101.
27- El Khoury, A., & Atoui, A. (2010). Ochratoxin A: general overview and actual molecular status. *Toxins*, *2*(4), 461-493.
28- Malir, F., Ostry, V., Pfohl-Leszkowicz, A., Malir, J., & Toman, J. (2016). Ochratoxin A: 50 years of research. *Toxins*, *8*(7), 191.
29- El Khoury, A., & Atoui, A. (2010). Ochratoxin A: general overview and actual molecular status. *Toxins*, *2*(4), 461-493.
30- Richard, J. L. (2007). Some major mycotoxins and their mycotoxicoses—An overview. *International journal of food microbiology*, *119*(1-2), 3-10.

31- Varga, J., Kevei, E., Rinyu, E., Téren, J., and Z. Kozakiewicz,1996. Ochratoxin production by Aspergillus species. Applied and Environmental Microbiology, 62, 4461-4464.
32- Pfohl-Leszkowicz, A., Manderville, R.A., 2007. Ochratoxin A: An overview on toxicity and carcinogenicity in animals and humans. Molecular nutrition & food research, 51(1), 61-99.
33- Clark, H.A., Snedeker, S.M., 2006. Ochratoxin A: its cancer risk and potential for exposure. Journal of Toxicology and Environmental Health, Part B: Critical Reviews, 9(3), 265-296.
34- Akron. 2010. The Chemical Database. The Department of Chemistry at the University of Akron. http://ull. chemistry.uakron.edu/erd and search on CAS number. Last accessed: 3/8/10.
35- World Health Organization, & International Agency for Research on Cancer. (1993). Some naturally occurring substances: food items and constituents, heterocyclic aromatic amines and mycotoxins. *IARC Monographs on the Evaluation of the Carcinogenic Risk of Chemicals to Humans*, *56*.
36- HSDB. 2010. Hazardous Substances Data Bank. National Library of Medicine. http://toxnet.nlm.nih.gov/ cgi-bin/sis/htmlgen?HSDB and search on CAS number. Last accessed: 3/10.
37- El Khoury, A., & Atoui, A. (2010). Ochratoxin A: general overview and actual molecular status. *Toxins*, *2*(4), 461-493.
38- Zhang, L., Dou, X. W., Zhang, C., Logrieco, A., & Yang, M. H. (2018). A review of current methods for analysis of mycotoxins in herbal medicines. *Toxins*, *10*(2), 65.
39- Sorrenti, V., Di Giacomo, C., Acquaviva, R., Barbagallo, I., Bognanno, M., & Galvano, F. (2013). Toxicity of ochratoxin a and its modulation by antioxidants: a review. *Toxins*, *5*(10), 1742-1766.
40- Zinedine, A., Soriano, J. M., Molto, J. C., & Manes, J. (2007). Review on the toxicity, occurrence, metabolism, detoxification, regulations and intake of zearalenone: an oestrogenic mycotoxin. *Food and chemical toxicology*, *45*(1), 1-18.
41- Taheur, F. B., Fedhila, K., Chaieb, K., Kouidhi, B., Bakhrouf, A., & Abrunhosa, L. (2017). Adsorption of aflatoxin B1, zearalenone and ochratoxin A by microorganisms isolated from Kefir grains. *International journal of food microbiology*, *251*, 1-7.
42- Drzymala, S. S. (2015). Instrumental analysis, metabolism and toxicity of cis-and trans-zearalenone and their biotransformation products.
43- Gromadzka, K., Waskiewicz, A., Chelkowski, J., & Golinski, P. (2008). Zearalenone and its metabolites: occurrence, detection, toxicity and guidelines. *World Mycotoxin Journal*, *1*(2), 209-220.
44- Smeesters, L., Meulebroeck, W., Raeymaekers, S., & Thienpont, H. (2015). Optical detection of aflatoxins in maize using one-and two-photon induced fluorescence spectroscopy. *Food Control*, *51*, 408-416.
45- https://microbiologyinfo.com/antibody-structure-classes-and-functions/

46- Rogowska, A., Pomastowski, P., Sagandykova, G., & Buszewski, B. (2019). Zearalenone and its metabolites: Effect on human health, metabolism and neutralisation methods. Toxicon.
47- Kim, S. D., Shin, K. R., & Zhang, B. T. (2003, December). Molecular immunocomputing with application to alphabetical pattern recognition mimics the characterization of ABO blood type. In *The 2003 Congress on Evolutionary Computation, 2003. CEC'03.* (Vol. 4, pp. 2549-2556). IEEE.
48- Peraica, M., Radić, B., Lucić, A., & Pavlović, M. (1999). Toxic effects of mycotoxins in humans. Bulletin of the World Health Organization, 77(9), 754.
49- Zhang, Y., Jia, Z., Yin, S., Shan, A., Gao, R., Qu, Z., ... & Nie, S. (2014). Toxic effects of maternal zearalenone exposure on uterine capacity and fetal development in gestation rats. Reproductive Sciences, 21(6), 743-753.
50- Köhler, G., & Milstein, C. (1975). Continuous cultures of fused cells secreting antibody of predefined specificity. *nature*, *256*(5517), 495.
51- Riechmann, L., Clark, M., Waldmann, H., & Winter, G. (1988). Reshaping human antibodies for therapy. *Nature*, *332*(6162), 323.
52- Nabok, A. V., Mustafa, M. K., Tsargorodskaya, A., & Starodub, N. F. (2011). Detection of aflatoxin B1 with a label-free ellipsometry immunosensor. *BioNanoScience*, *1*(1-2), 38-45.
53- Holder, A. A. (2009). The carboxy-terminus of merozoite surface protein 1: structure, specific antibodies and immunity to malaria. *Parasitology*, *136*(12), 1445-1456.
54- Janeway, C. A., Travers, P., Walport, M., & Shlomchik, M. (1996). *Immunobiology: the immune system in health and disease* (Vol. 7, p. 26). London: Current Biology.
55- Mason, D. W., & Williams, A. F. (1980). The kinetics of antibody binding to membrane antigens in solution and at the cell surface. *Biochemical Journal*, *187*(1), 1-20.
56- Welch, N. G., Scoble, J. A., Muir, B. W., & Pigram, P. J. (2017). Orientation and characterization of immobilized antibodies for improved immunoassays. *Biointerphases*, *12*(2), 02D301.
57- Babacan, S., Pivarnik, P., Letcher, S., & Rand, A. G. (2000). Evaluation of antibody immobilization methods for piezoelectric biosensor application. *Biosensors and Bioelectronics*, *15*(11-12), 615-621.
58- Catuogno, S., & Esposito, C. L. (2017). Aptamer cell-based selection: Overview and advances. *Biomedicines*, *5*(3), 49.
59- Nabok, A. (2005). *Organic And Inorganic Nanostructures (Artech House Mems and Sensors Library)* (Vol. 286). Artech House Publishers Hardcover.
60- Nabok, A., Al-Rubaye, A. G., Al-Jawdah, A. M., Tsargorodska, A., Marty, J. L., Catanante, G., ... & Takacs, E. (2019). Novel optical biosensing technologies for detection of mycotoxins. *Optics & Laser Technology*, *109*, 212-221.

61- Hirao, I., Kimoto, M., & Lee, K. H. (2018). DNA aptamer generation by exSELEX using genetic alphabet expansion with a mini-hairpin DNA stabilization method. Biochimie, 145, 15-21.
62- https://metarna.wordpress.com/2016/01/19/what-are-aptamers/
63- Hirao, I., Kimoto, M., & Lee, K. H. (2018). DNA aptamer generation by exSELEX using genetic alphabet expansion with a mini-hairpin DNA stabilization method. Biochimie, 145, 15-21.
64- Catuogno, S., & Esposito, C. L. (2017). Aptamer cell-based selection: Overview and advances. *Biomedicines*, *5*(3), 49.
65- Kimoto, M., Matsunaga, K. I., & Hirao, I. (2016). DNA aptamer generation by genetic alphabet expansion SELEX (ExSELEX) using an unnatural base pair system. In Nucleic Acid Aptamers (pp. 47-60). Humana Press, New York, NY.
66- Nutiu, R., & Li, Y. (2003). Structure-switching signaling aptamers. *Journal of the American Chemical Society*, *125*(16), 4771-4778.
67- Spiridonova, V. A., Glinkina, K. A., Gainutdinov, A. A., & Arutyunyan, A. M. (2014). Production of thrombin complexes with DNA aptamers containing G-quadruplex and different duplexes. *J. Nephrol. Ther*, *4*, 149-154.
68- Aptamers based on Electrochemical impedance spectroscopy, Doctoral Thesis, Cristina Ocana Tejada, University Autonoma de Barcelona, 2015.
69- Balamurugan, S., Obubuafo, A., Soper, S. A., & Spivak, D. A. (2008). Surface immobilization methods for aptamer diagnostic applications. *Analytical and bioanalytical chemistry*, *390*(4), 1009-1021.
70- Song, S., Wang, L., Li, J., Fan, C., & Zhao, J. (2008). Aptamer-based biosensors. *TrAC Trends in Analytical Chemistry*, *27*(2), 108-117.
71- Sassolas, A., Blum, L. J., & Leca-Bouvier, B. D. (2011). Optical detection systems using immobilized aptamers. *Biosensors and Bioelectronics*, *26*(9), 3725-3736.
72- Stojanovic, M. N., De Prada, P., & Landry, D. W. (2001). Aptamer-based folding fluorescent sensor for cocaine. *Journal of the American Chemical Society*, *123*(21), 4928-4931.
73- Tombelli, S., Minunni, M., & Mascini, M. (2007). Aptamers-based assays for diagnostics, environmental and food analysis. *Biomolecular engineering*, *24*(2), 191-200.
74- Citartan, M., Gopinath, S. C., Tominaga, J., Tan, S. C., & Tang, T. H. (2012). Assays for aptamer-based platforms. *Biosensors and Bioelectronics*, *34*(1), 1-11.
75- Kaur, H., Bruno, J. G., Kumar, A., & Sharma, T. K. (2018). Aptamers in the therapeutics and diagnostics pipelines. *Theranostics*, *8*(15), 4016.
76- Chandola, C., Kalme, S., Casteleijn, M. G., Urtti, A., & Neerathilingam, M. (2016). Application of aptamers in diagnostics, drug-delivery and imaging. *Journal of biosciences*, *41*(3), 535-561.

77- https://pdfs.semanticscholar.org/1a98/1885bb54a3aa2e7fd0ae9d537d65444fb7a6.pdf

Chapter 6: Bio-sensing tests

6.1 Introduction

The experimental results of detection of mycotoxins were presented in this chapter. Because of continuous development of the experimental set up during the project, the results are split into three parts corresponding to particular setup used. Preliminary results of detection in the 1st set up having poor quality of the output signal and relatively low RISK were used to prove the concept of OPW, PI sensor. Much improved 2nd setup allowed the detection of three mycotoxin indirect immunoassay with their specific antibodies, immobilized electrostatically on the waveguide. In the last batch of results obtained using the 3rd version of the setup, aptamers were used as bio receptors for specific binding of aflatoxin b1 and ochratoxin A, the obtained results showed reusable sensitivity in sub ppt concentration ranges.

6.2 Immobilization of antibodies on the waveguide surface

In biosensors, the biological receptors have to be properly deposited onto the transducer; this process is known as immobilization [1]. Several well- established methods of immobilization of proteins are widely exploited, such as physical adsorption, covalent binding, entrapment [2, 3, 4] and a recently developed electrostatic self-assembly technique (also known as layer-by-layer deposition) [5]. The purpose of any immobilization method is to retain maximal activity of the biological receptors on the surface of the transducer. The selection of an appropriate immobilization method depends on the nature of the biological receptor, the type of the transducer used, the properties of the analyte, and the operating conditions of the biosensor, the layer-by-layer (LbL) electrostatic deposition has been used in this project for immobilization of antibodies. This method has been first developed for deposition of alternatively charged layers of polyelectrolytes, and as poly-allylamine hydrochloride (PAH) as polycation and poly-sterylsulphonate sodium salt (PSS) as polyanion. Both polycations and polyanions dissociate in water and result, respectively, in positively and negatively charged polymer chains with counter ions Cl^- and Na^+ left in solutions. Those polymer chains can be deposited layer-by-layer on the substrates (which supposed to be initially charged) using simple procedure of dipping the sample in beakers containing PAH and PSS with intermediate rinsing in pure water. The LbL electrostatic deposition is schematically outlined in Fig. 6.1. The thickness of a layer depends on both the underlying surface and the deposition condition, e.g. the type of material, the surface roughness and condition factors such as concentration of polyelectrolytes, adsorption time, temperature, rinsing time, dipping speed, drying time, etc. [6].

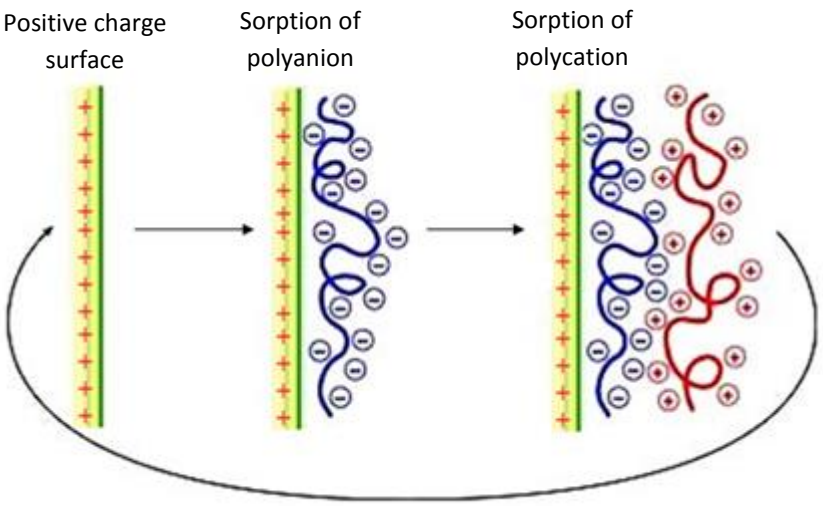

Figure 6.1 Fabrication of polyelectrolyte multilayers using layer-by-layer electros deposition

The method of electrostatic Lb L can be expanded by including other types of electrically charged objects, such as organic molecules functionalised with electrically charge groups, e.g. SO_3^- or NH_2^+, nanoparticles, and proteins having electric charge which depends on the pH of solutions [7].

Proteins (including antibodies) are typically immobilized on the surface of transducer by methods of covalent binding, entrapment into polymers, hydrogels or any other network. In this project the electrostatic binding was used for immobilization of proteins. This technology was developed by Y.LVOV and G.Decher [8]. The polymer poly (allylamine hydrochloride) (PAH) has been used as polycation for immobilization of antibodies. PAH is fully ionized at a pH lower than

7.0 [9]. The advantage of using PAH was that its charge is located at the far end of the side chain, which was easily accessible for the compensation by other ionic molecules. The chemical structure of PAH is shown in Fig.6 2. The molecular weight of PAH was about 70000 g/mole. It has a pH of 4.37 when diluted to 10^{-5} M concentration in ultrapure water. The concentration of PAH used for the deposition was 2 mg/ml ($2.857 \cdot 10^{-5}$ M). This concentration was considered to be appropriate to provide enough charge for LbL deposition as demonstrated by [10]. Another common polycation is polyethylenimine (PEI), having molar mas of 43.04; it is a branched polymer with repeating unit composed of the amine group and two carbon aliphatic CH_2CH_2 spacers. Polycations are water soluble, and they dissociate into positivity charged polymer chain due to NH_2^+ groups and counter ions, typically Cl^- .

One of the most common polyanions, is poly sterylsulphonate sodium salt (PSS). Its chemical structure is shown in Fig. 6.2, and its average molecular weight is about 9,000-11,000. PSS is a polymer consisting of two parts: poly(3,4-ethylenedioxythiophene) a conjugated polymer carries negative charges associated with SO_3^- groups and counter ions Na^+

(a) (b)

Figure 6.2 Molecular structures of PSS (a) and PAH (b) [11].

Multi layers can be deposited onto the surface by consecutive deposition of PAH and PSS. This technology is called Electrostatic self-assembly of layer-by-layer deposition (LbL) has become a popular method for making organic films. The method of LbL is quite versatile and can be used for making composite films containing some other electrically charged, such as nanoparticle, proteins, cells, etc.

In this project, the thickness of the polyelectrolyte bilayer was determined by ellipsometry using M2000 J.A. Woollam spectroscopic ellipsometer unit. The thickness and refractive index of the films produced were found by ellipsometry data fitting using Cauchy model. Ellipsometric measurements on dried films shown a good approximation of the thickness, the average thickness of the PAH/PSS bilayer was estimated at 2.9 , which is in good agreement with the literature value of $(2{\sim}3\ nm)$ previously reported in the literature [12, 13].

Proteins can carry electrical charge depending on the pH of solution. At pH above the iso-electric point proteins are negativity charged due to $COOH^-$ groups, while at pH lower than iso-electric point they have positive charge due to NH_2^+ groups. For example, IgG being negatively charged at $pH > 7$ can be alternated with PAH. This property has been used in this work by immobilizing IgG based antibodies on top of PAH layer.

Antibodies immobilized on PAH are randomly oriented as shown in Fig. 6.3a, so some of the Fab fragments are not available for binding antigens. In order to improve the orientation of the antibodies, protein A has been used as an intermediate body. This mechanism has been explained in earlier in section (4.3.1.2). The electrostatic immobilization of antibodies proved to be successful in our research

group previous research, and we also used it in the current work. It has to be mentioned that the antibodies have to be immobilized on the surface of silicon nitride in the sensing window of the waveguide. However, after etching the top oxide layer in HF and rinsing in deionised water, a thin layer of oxide may still remain on the surface and contain negative surface charge due to F^- and HO^- groups. The immobilization procedure, which was carried out in the cell starts by injection of PAH 1 mg/ml aqueous solution into the cell and incubation for 15–20 min, followed by purging the cell with deionised water. Then protein A (0.01 mg/ml solution in 35 mM Tris-HCl buffer, pH 7.5 was injected and incubated for 15 min, and then IgG-based antibodies (typically 1μg/ml solution in Tris-HCl buffer pH 7.5 was injected and incubated for 15 min. Obviously, the intermediate 3-times rinsing with buffer after protein A deposition was used. All the chemicals used were acquired from Sigma Aldrich.

6.3 Detection of mycotoxin in direct assay with specific antibody:

The first biosensing tests were carried out using the 1st version of the experimental set-up (described in detail in Ch 4.) which has the refractive index sensitivity of approximately 1200 rad/RIU.

Aflatoxin B1 (AFT B1) was detected in direct immunoassay with specific antibodies electrostatically immobilized on the surface of Si_3N_4 in the sensing window via intermediate layers of PAH, and protein A (as was described in detail above). The biosensing tests were carried out by recording the OPW PI sensor responses caused by sequential injections of solutions of PAH, protein A, anti-AFT B1 antibodies, and

AFT B1 increasing order of concentrations, e.g. 0.01, 0.1, 1, 10, 100, and 1000 ng /ml. Typical sensor responses are shown in Fig. 6.3. As one can see, the signals were quite noisy and unstable in that 1st version of the experimental set-up, but the main features of the responses can still be noticed, and the number of periods of phase change can be roughly estimated. Deposition of a very thin (of about 1nm) layer of PAH (in Fig. 6.3a) causes only half-a period phase shift between p- and s-components of polarized light. Absorption of much larger molecules of protein A causes about 2 full periods of phase change (Fig. 6.3b). Much larger molecules of anti-AFT B1 caused about 3.5 periods of phase change (Fig. 6.3c). And finally, quite small concentration of AFT B1 (1ng/ml) yields about half-a-period of phase changes, as shown in Fig. 6.3d as an example. In the second set-up version having much higher refractive index sensitivity of around 5600 rad./RIU, the output signals were less noisy with more stable amplitudes, so the

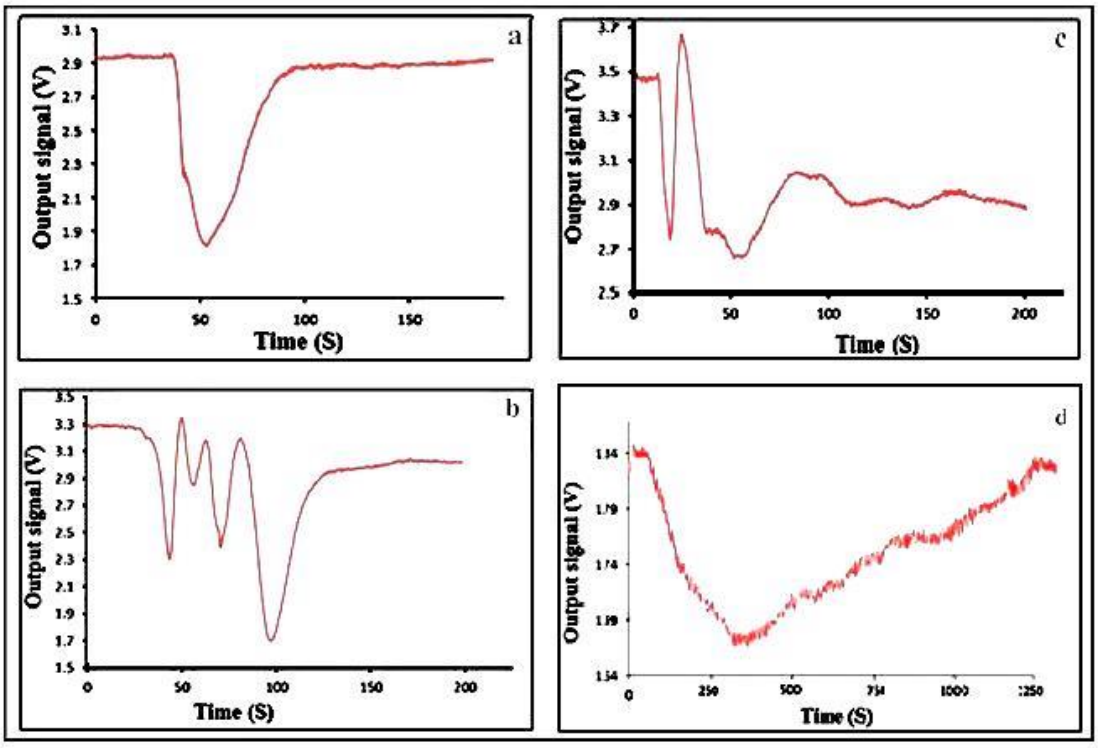

Figure 6.3 Output signal waveforms recorded during absorption of layers of PAH (a), protein A (b), antibodies (c) and aflatoxin B1, 1ng/ml concentration (d). Arrows indicate the moment of injections.

evaluation of the phase shift was more precise though still carried out manually. With this set-up all three mycotoxins, aflatoxin B1, ochratoxin A, and zearalenone, were detected in a wide range of concentrations, e.g. 0.01, 0.1, 1.0, 10.0, 100.0, and 1000.0 (ng/ml). As before, the biosensing tests were carried out by sequential injections of the above-mentioned mycotoxins starting from the smallest concentration. Each injection was followed by rinsing the cell with pure buffer solution in order to remove unbound mycotoxin molecules.

Typical responses to injections of different concentrations of aflatoxin B1 are shown in Figure 6.4. The number of periods of signal oscillation at each injection which corresponds to the phase shift between p and s components of the polarized light were summarized in Figure. 6.5 as we can see the increase in the number of oscillation periods increases with the increase in AFT B1. The sensitivity of detection of AFB1 is provided by the antibodies used.

The previous research in our research group showed high specificity of the antibodies used [14], with typical values of the affinity coefficients in 10^{-7} - 10^{-8} mol. Nevertheless, the negative control tests were carried out in order to eliminate cross-sensitivity. The results of negative control tests are presented in Fig. 6.6, the injection of non-complementary target molecule, e.g. ochratoxin A (OTA) showed no response at all (Fig. 6.7a) as compared to a noticeable phase change caused by AFT B1 (Fig. 6.7b). The injection of pure buffer (Fig. 6.7c) solutions typically

causes about ¼ of a period phase changes due to washing out non-specifically bound toxins. This is actually constitutes the base-line of our experiments.

As was shown in Fig. 6.5, the minimal detection concentration of AFT B1 was 0.01 ng/ml which is similar to the results obtained earlier using the of TIRE [15]. The situation of the sensor response in Fig. 6.5 at high concentration of AFT B1 is associated with the saturation of binding sites of antibodies. Much higher sensitivity of OPW PI could be achieved by rectifying the problems existence in the 2nd set up version.

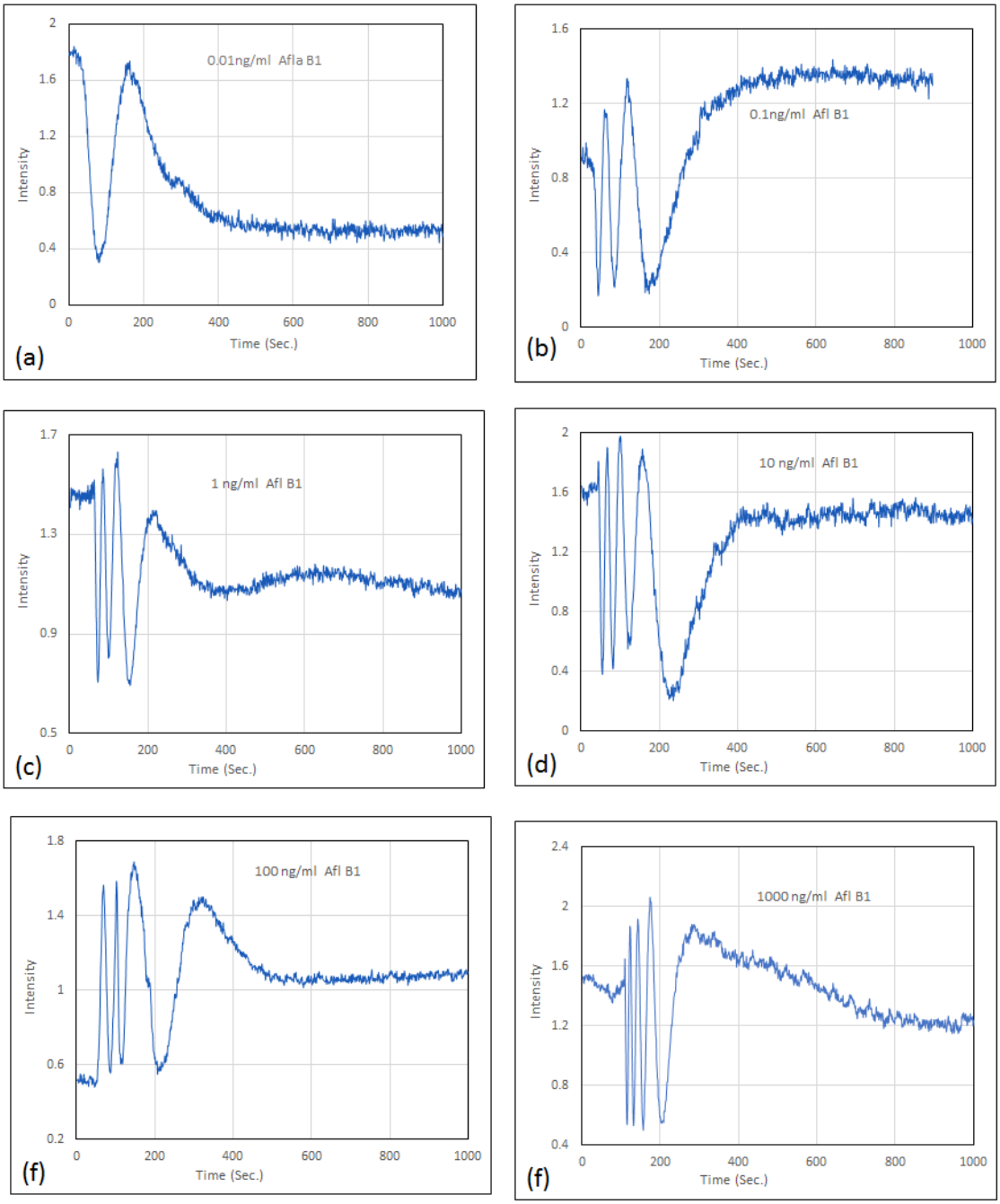

Figure 6.4 Output signals for different concentrations of AFT B1: 0.01 ng/ml (a), 0.1 ng/ml (b), 1 ng/ml (c), 10 ng/ml (d), 100 ng/ml l (f), and 1000 ng/ml (g).

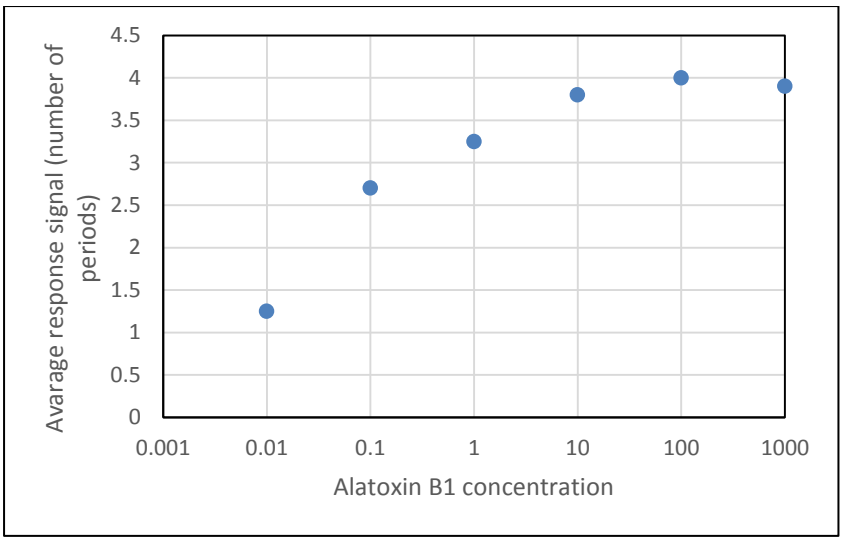

Figure 6.5 Calibration curve: the dependence of the phase shift vs. concentration of AFT B1.

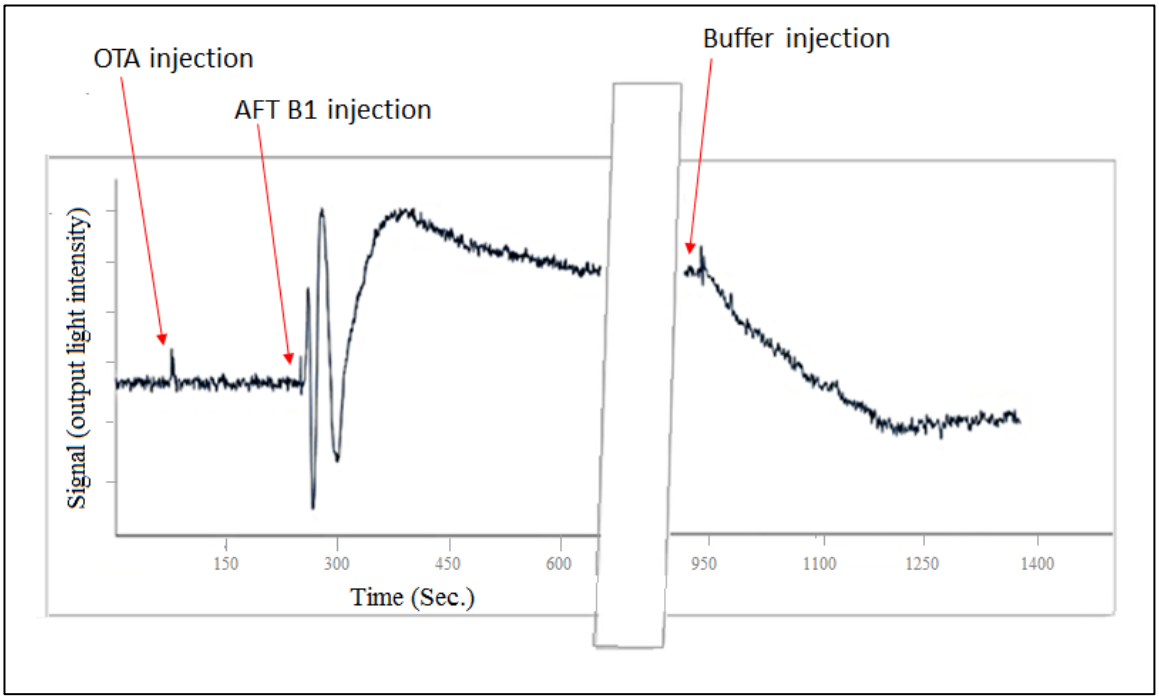

Figure 6.6 Negative control test: responses of OPW PI sensor with immobilized anti-AFT B1 to AFT B1 (a) , to OTA (b) and buffer injection (c).

Similar experiments were carried out for other mycotoxins. Using the setup version II the set up typical results of detection of ochratoxin A in the immune assay with specific antibodies are shown in Fig. 6.7, and the calibration curve in Fig. 6.8 presents the values of the evaluated phase shift vs concentration of OTA.

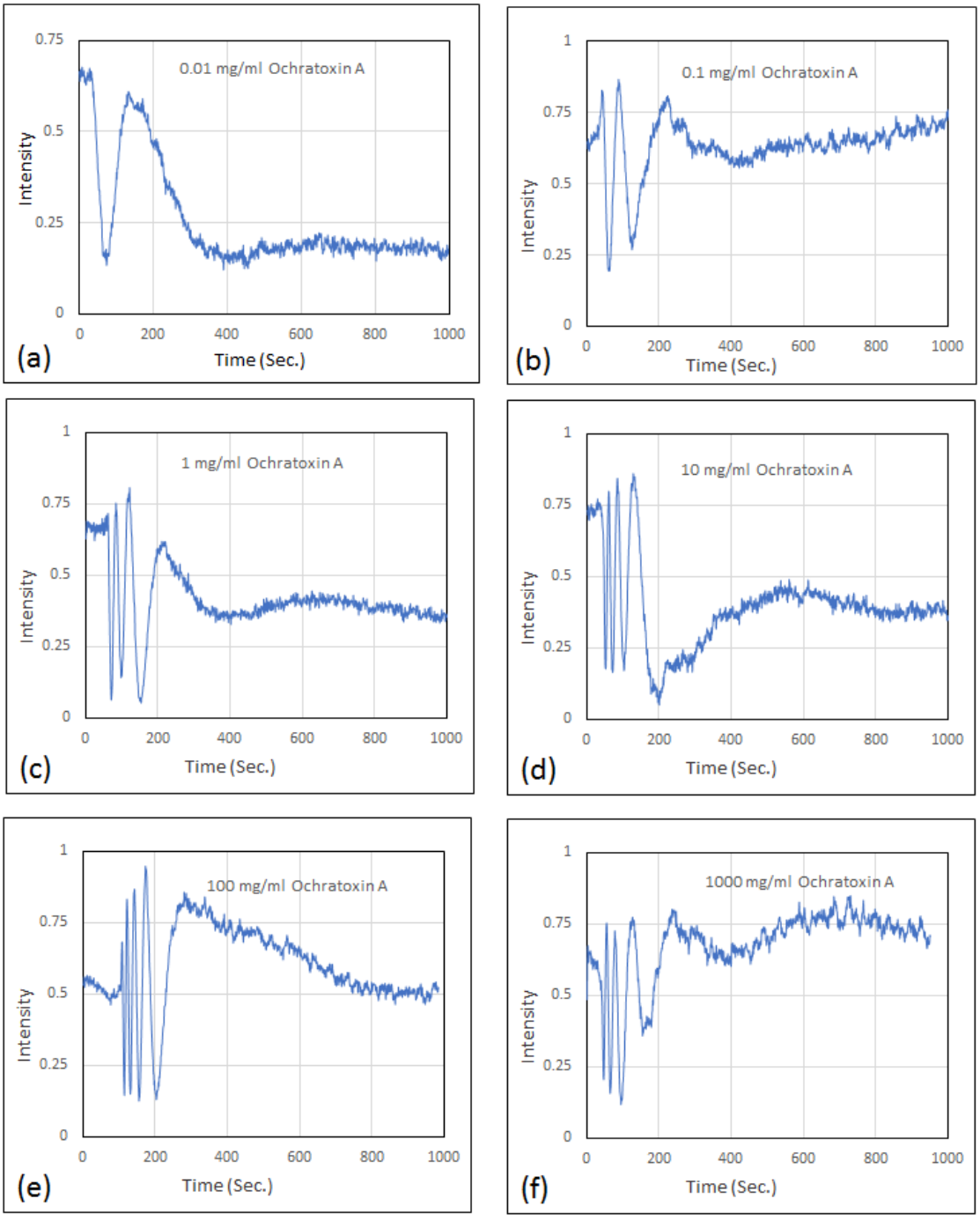

Figure 6.7 Output signals for different concentrations of Ochratoxin A: 0.01 ng/ml (a), 0.1 ng/ml (b), 1 ng/ml (c), 10 ng/ml (d), 100 ng/ml l (f), and 1000 ng/ml (g).

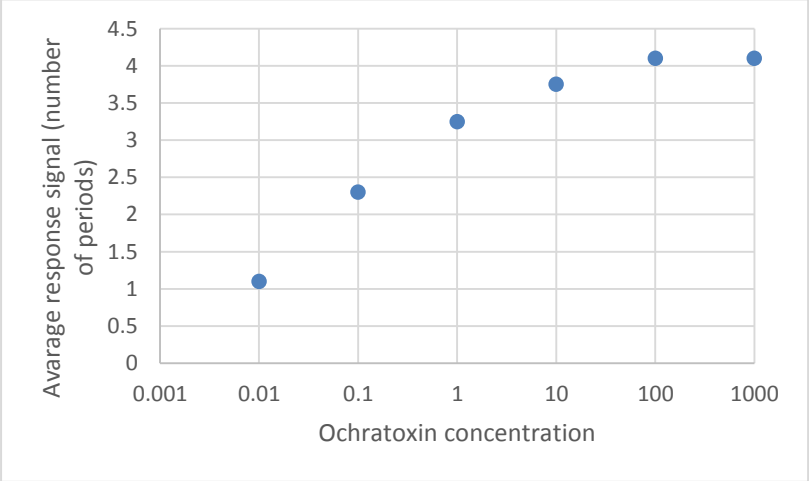

Figure 6.8 Calibration curve for Ochratoxin A.

Further down, the results of detection of zearalenone (ZEN) are shown in Fig. 6.9 and 6.10. The results are quite similar to those given earlier for AFT B1 and OTA, the small all of the response is due to the saturation of binding sits of antibodies.

The analysis of detection of all three mycotoxins in direct immunoassay with respective specific antibodies was carried out by plotting the accumulated responses on the same graph. Because the biosensing tests have been performed in sequential manner from the lowest to the highest concentration, the accumulated sensor responses can be calculated in a following way: The values of phase shifts at each injection have to be added up, while the phase shifts caused by washing out have to be subtracted. Such accumulated responses for all three mycotoxins are given in Fig. 6.11.

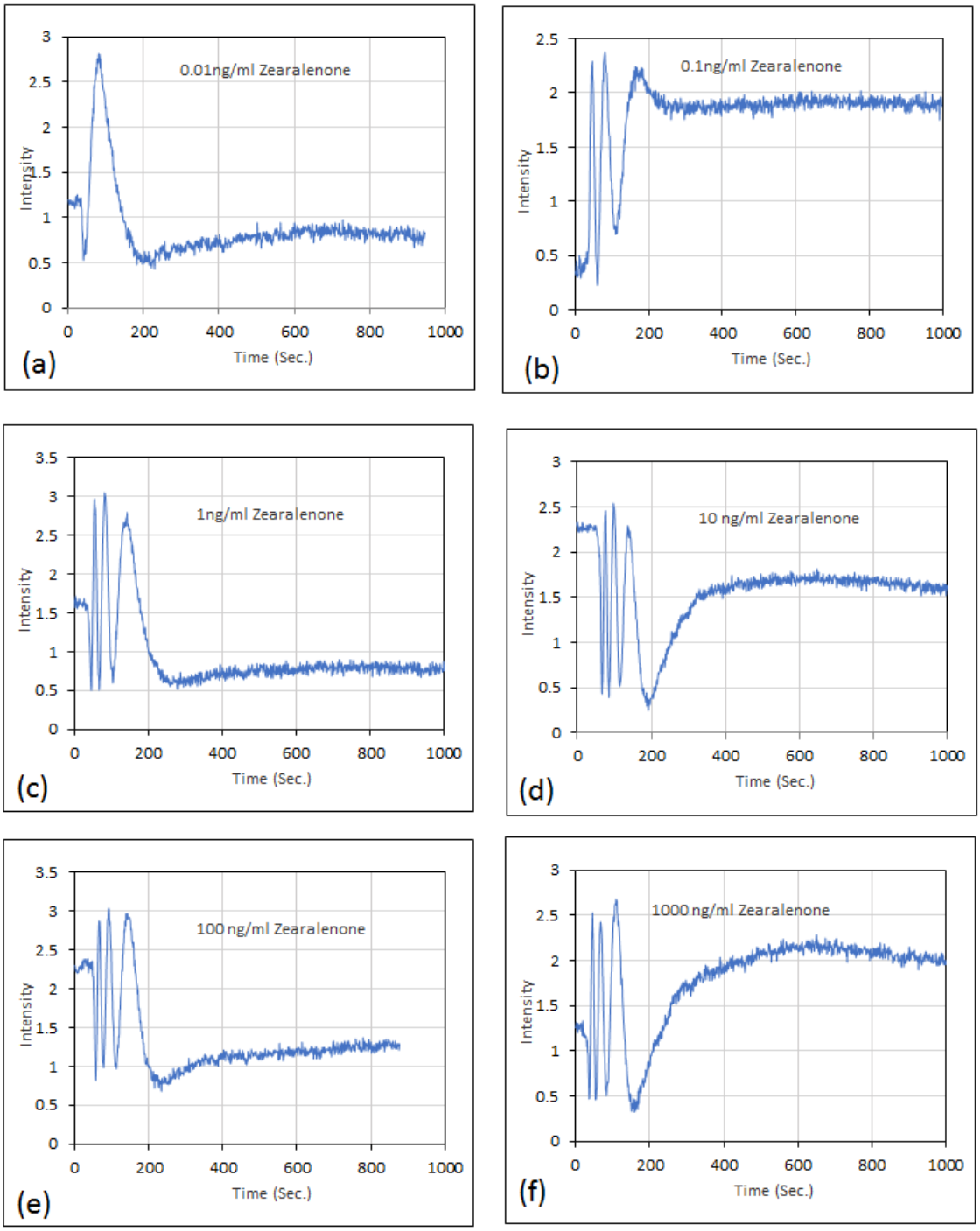

Figure 6.9 Output signals for different concentrations of Zearalenone: 0.01 ng/ml (a), 0.1 ng/ml (b), 1 ng/ml (c), 10 ng/ml (d), 100 ng/ml l (f), and 1000 ng/ml (g).

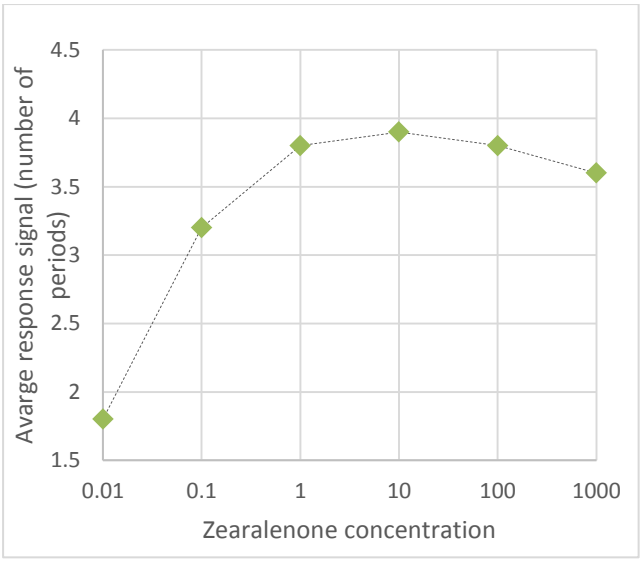

Figure 6.10 Calibration curve for Zearalenone (ZEN).

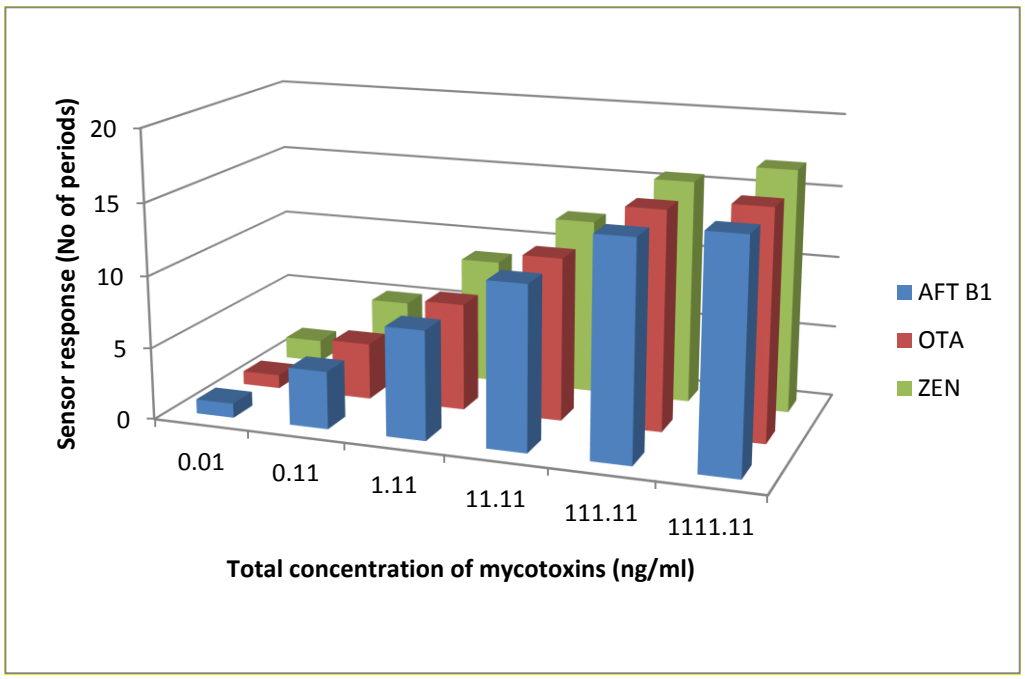

Figure 6.11 The summary: accumulated sensor responses vs total concentration of mycotoxins.

The responses of OPW PI sensor to all three mycotoxins are quite similar in terms of values and the general behavior. The minimal detected concentration was of 0.01 ng/ml, while the detection limit is at least an order of magnitude smaller since the base line was about 0.25 periods. The linear response range is of four orders of

magnitude (from 0.01 to 100 ng/ml); the saturation of the responses was typically occur at 1mg/ml concentrations due to the saturation of antibody binding sites. These results are very impressive, particularly considering direct immunoassay format. Therefore, the OPW PI sensor exceeded the sensitivity of TIRE method by at least one order of magnitude. The sensitivity could be further increased by improving the signal and using automated and more precise calculation of the phase changes.

6.4 Bio sensing tests using aptamer bioreceptors

6.4.1 Introduction

The optimization of the experimental set-up which was focused on improvements of optical sensitivity and signal processing was achieved in the 3rd version of the set-up, which was described in detail in Ch. 4. In addition to that, a novel type of bioreceptors, e.g. aptamers, was exploited, and the results were presented in this section.

Aptamers represent a new biosensing strategy which became increasingly popular in the last few years. Aptamers are also known as chemical antibodies, they are synthetic oligonucleotide or peptide molecules that reproduce a similar to antibodies function, i.e. specific binding of particular target molecules. Aptamers are typically based on RNA or DNA oligonucleotides of particular sequence complementary to that of target molecules they are assembled from a vast pool of nucleic acids using the SELEX (which was described in detail) procedure. The popularity of using aptamers as bio-receptors has rocketed in the last decade, and nowadays aptamers were commercially produced by specification for a wide range of targets.

Aptamers have a number of advantages over traditional antibodies which include better stability, much simpler and more ethical (without the use of immunization of small animals) synthesis, and, not least, the lower price. These features lead to substantial improvement the system performance. Aptamers are about ten times smaller than antibodies; the molecular weight of IgG-based antibodies is in the range of 150 – 170 kDa, while the aptamers containing from 30 to 80 nucleotides have molecular weight of 12 to 30 kDa. This makes the aptamers more suitable for optical non-labelled detection; it also allows aptamers to be much closed to the surface of transducer which could be particularly important for LSPR biosesnors [16].

Antibodies are usually very sensitive to the environment, i.e. the changes in temperature and pH may lead to their denaturation, also their recovery after binding the analytes is problematic. While the aptamers are fairly stable at ambient temperature and their secondary structure can be easily restored by thermocycling, the same way aptamer can be recovered after binding the target analytes.

The aptamers change their conformation upon binding the target molecule (in simple terms, wrapped around the target molecules) which leads to changes in the aptamer layer thickness and/or refractive index; such changes can be detected with the sensitive transducer such as OPW PI sensor developed in the current project.

6.4.2 Preparation of aptamers and their immobilization on OPW

In the current work, we used non-labeled aptamer (from Microsynth, Switzerland) for AFT B1 which has the following nucleotide sequence which was established in

[17, 18]: SH-5′-GTTGGGCACGTGTTGTCTCTCTGTGTCTCGTGCCCTTCGCTAGGCCCACA-3′.

There was no label attached at 3' terminal, while the thiol group was attached to 5' terminal to allow aptamer's immobilization directly on the gold surface. In our case, of immobilization the surface of silicon nitride within a sensing window, the immobilization protocol was more complicated. The aptamers were delivered in lyophilized form. The aptamer stock solution is prepared at 100 µM by adding an appropriate volume of sterilized water. Then, the stock solution is aliquoted and stored at -20°C. All other chemicals, i.e. sodium phosphate (Na_2HPO_4), potassium phosphate (KH_2PO_4), potassium chloride (KCl), magnesium chloride ($MgCl_2$), dithiothreitol (DTT), sulfo-succinimidyl-4-(N-maleimidomethyl) cyclohexane-1-carboxylate (Sulfo-SMCC), and sodium chloride (NaCl) were procured from Sigma-Aldrich (France). Aflatoxin b1 was purchased from Sigma-Aldrich (UK). All reagents were of analytical grade. Deionized Milli-Q water was used for preparation of reagents throughout the experiments.

The 100 mM PBS binding buffer (PBB) was prepared by dissolving 10 mM Na_2HPO_4, 1.76 mM KH_2PO_4, 3 mM $MgCl_2$, 2.7 mM KCl, and 137 mM NaCl, in deionised water. The pH of the buffer was adjusted to 7.4. Before immobilization, the stock solution of aptamers was diluted at desired concentration with PBB supplemented with 2 mM of DTT, then diluted aptamer solution was thermo-cycled in PCR unit, e.g. heated to 90C° for 5 min and cooled down to 4 C° for 5 min. The presence of thiol groups at 5' terminal allows immobilization on gold surface. In our case, however, we need to immobilize this aptamer in the sensing window of the planar waveguide on the surface Si_3Ni_4. The process of aptamers immobilization is illustrated in Fig. 6.12. At first, the silicon nitride surface was aminated using (3-

aminopropyl) triethoxysilane; this provides NH_2 groups on the surface (Fig. 6.13a) to bind SMCC molecules 4-(N-maleimidomethyl) cyclohexanecarboxylic acid) (Fig. 6.13b). To do that, 30 µl of 10 mM SMCC solution in PBS buffer, pH 7.4 was added into each aminated surface and incubated for one hour at room temperature.

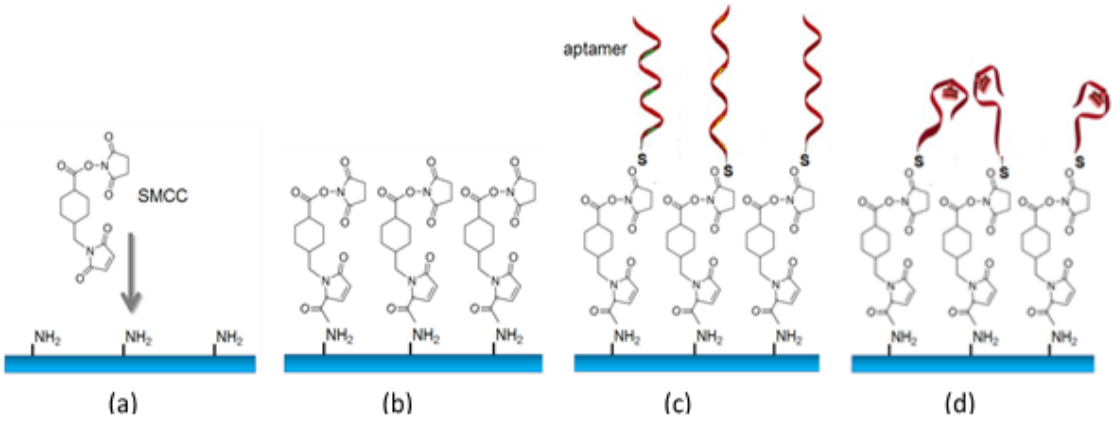

Figure 6.12 Aptamer immobilization protocol: aminated surface of Si3N4 (a), SMCC activated surface (b), aptamers immobilized (c), aptamers binding target analyte molecules (d).

The plates were then washed with deionized water three times. Finally, aptamers were attached to SMCC layer using the specific reaction between C5-terminal cysteines and the maleimide-activated surfaces (Fig. 6.12c). This was achieved by dropping 30 µl of 2 µM aptamer solution (preheated with thermal cycler) in binding buffer pH 7.4 with the addition of 1 mM DTT (dithiothreitol) on the SMCC-activated plates. The samples were incubated for 4 hours at room temperature in the dark. After the conjugation reaction was complete, the plates were washed three times for 2 minutes in binding buffer.

Normally aptamers have their secondary structures stabilized in the presence of $MgCl_2$ salt in the binding buffer, but they change their 3D conformation when bind to the target analyte, literally wrapping around the target (Fig.6.12d). This process which is associated with changes in the molecular layer thickness can be easily detected by OPW PI sensor.

6.4.3 Detection of Aflatoxin B1 with PI OPW sensor in aptamer assay.

Aflatoxin B1 (AFT B1) stock solution (1 mg/ml) was prepared in acetonitrile. Further dilutions of AFT B1 were done in PBB. All of the working AFT B1 solutions of 1pg/ml, 0.01 ng/ml, 0.1 ng/ml, 1 ng/ml, 10 ng/ml, 100 ng/ml, and 1 μg/ml were prepared by multiple dilution in PBB and stored at 4 C^o when not in use.

A series of PI measurements were carried out by sequential injections of AFT b1 solutions of different concentrations in PBB (starting with the smallest concentration of 1 pg/ml) into the cell. Intermediate washing the cell by purging it with 1ml of PBB solution was carried out after each injection in order to remove non-specifically bound toxin molecules. The signals were recorded during binding of AFT b1 to their specific aptamers with the exposure time of around 40 minutes. The recorded waveforms are shown in Fig. 6.13 (blue curves) along with the corresponding phase changes (black curves). The values of phase shift were calculated by processing the recorded waveforms as described in Ch.4

As one can see, the lowest concentration of AFT B1 used was 1pg/ml, which causes a noticeable 5.84 rad. (nearly the whole period) of phase change. The saturation of

the response typically occurs after 400 s to 500 s of exposure which is similar to the time of immune reaction, e.g. binding target analyte to respective antibodies [19].

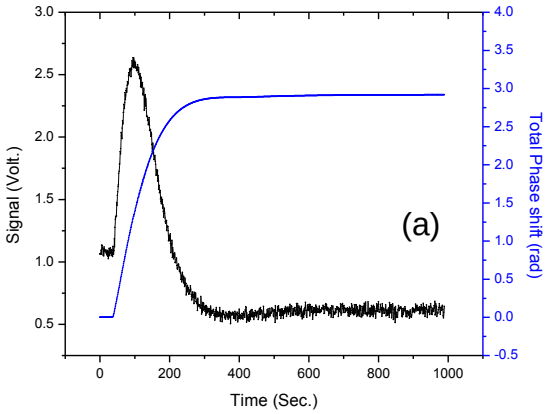

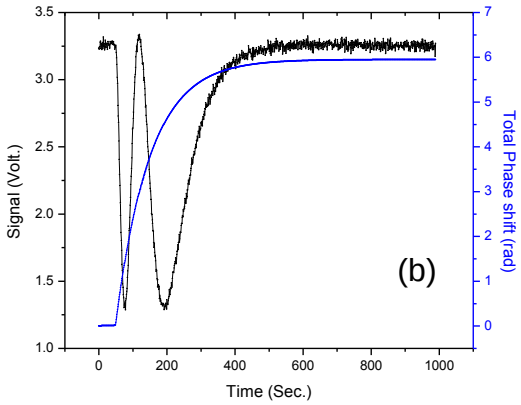

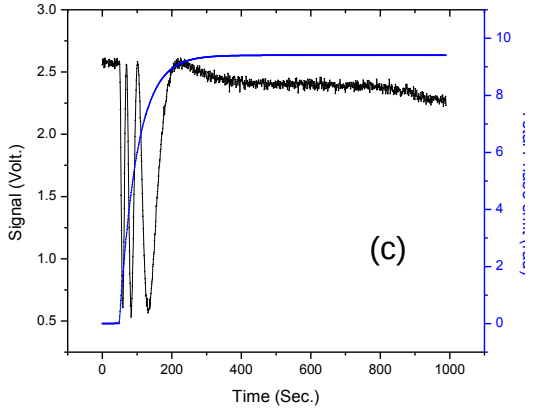

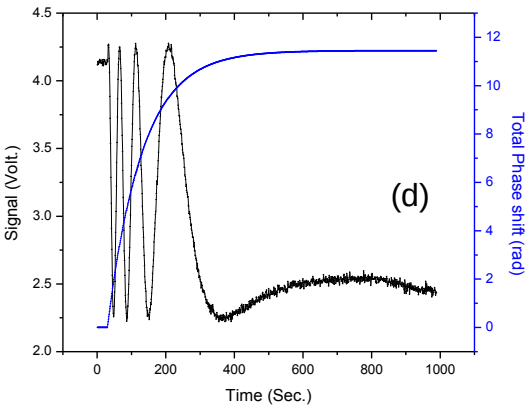

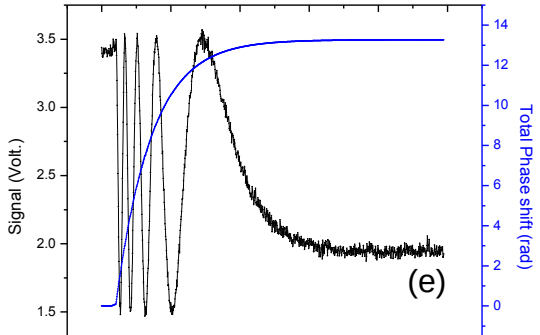

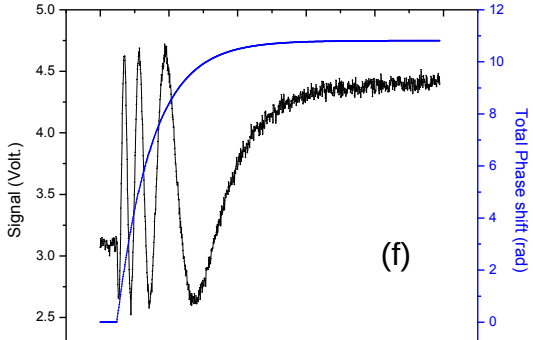

Figure 6.13 Output signals (left) and corresponding phase shifts (right) for different concentrations of AFT b1: 0.001 ng/ml (a), 0.01 ng/ml (b), 0.1 ng/ml (c), 1 ng/ml (d), 10 ng/ml (e), 100 ng/ml (f), and 1000 ng/ml (g).

The PI OPW sensor responses, e.g. the phase shift values, recorded for consecutive injections of different concentrations of AFT B1, are summarised in Fig. 6.14a (blue poles).

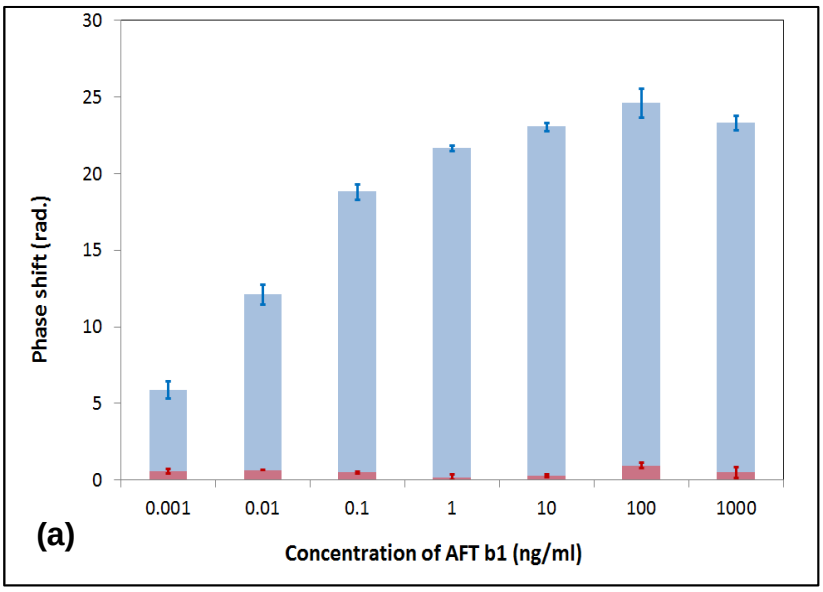

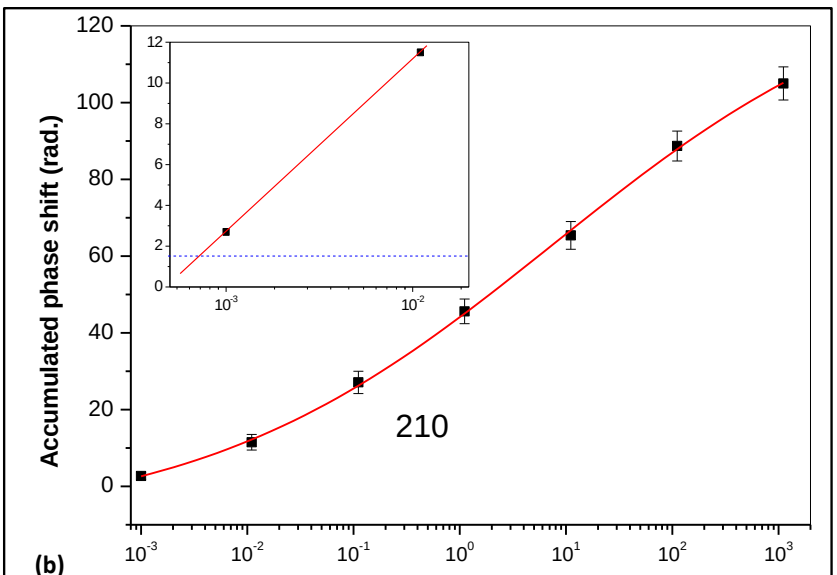

Figure 6.14 (a) Concentration dependence of phase shifts caused by consecutive injections of AFT b1 (blue dots) and during toxin washing out toxins (red dots); (b) Accumulated phase shift vs the total concentration of AFT b1.

A monotonous increase of the phase shift with the increase of AFT b1 concentration is observed. A small drop in the response at the highest concentration of 1μg/ml is most-likely caused by saturation of binding cites, e.g. aptamers. The signal recordings, which were performed during washing out non-specifically bound toxin molecules after each binding stage, typically yield 2.36 ± 0.14 rad. of phase change (see Fig. 6.14a, red poles). The fact that this value is practically independent on the AFT B1 concentration indicates that non-specific adsorption most-likely takes place in the voids between immobilized aptamers. Negative control tests were also carried out by injecting a different mycotoxin, e.g. ochratoxin A, which is not supposed to be bound to this kind of the aptamer. The response was at the noise level. Also, the injection of pure buffer solution (with no AFT b1 added) yielded a zero response.

Because the measurements were carried out in sequence of steps of injections of toxins in progressively increased concentration, further analysis of the data obtained was carried out in order to work out the accumulated response. For that purpose, the phase changes at each stage were added, and the responses to washing out toxins

were subtracted. The resulted calibration curve in Fig. 6.14b shows a wide linear dynamic detection range (from 0.01 ng/ml to100 ng/ml) with the trend of flattening at both low and high concentrations. The results obtained are similar to those reported earlier for the PI detection of aflatoxin B1 in direct immunoassay with specific antibodies [20, 21], though the sensitivity was much higher due to the use of improved (version III) OPW PI experimental set-up. The accuracy of phase shift measurements was estimated as ±0.5 rad. which allows the evaluation of low detection limit as 0.7pg/ml by linear approximation of calibration curve to the level of 1.5 rad. (see the inset in Fig. 6.14b). The obtained LDL value in sup ppt (part-per-trillion) range is quite remarkable. It is much lower to LDL values reported in optical biosensing methods, and it is comparable with high-tech analytical methods such as mass-spectroscopy.

6.4.4 Detection of ochratoxin A in aptamer assay with PI OPW sensor.

Similar tests were performed on detection OTA in direct assay with specific aptamer purchased from Microsynth (Switserland) having a following nucleotide sequence:

5'-SH-GATCGGGTGTGGGTGGCGTAAAGGGAGCATCGGACA-3' [22].

The immobilization protocol was similar to that of anti-AFT B1 aptamer described earlier in this chapter. The detection of OTA was carried out in sequential injections of OTA in increasing concentrations from 1 pg/ml up to 1μg/ml. The results, e.g. the recorded waveforms (blue curves) and calculated phase shift (black curves) are shown in Fig. 6.15. Similar to aflatoxin B1 data, the response tend to saturate due to the saturation of aptamers,

though the saturation happened at much smaller concentrations of OTA (see Fig. 6.15h).

Following the procedure developed earlier for AFT B1, the accumulated sensor responses for OTA was plotted against the total concentration of OTA in Figure 6.16 Similarly, to

AFT B1, the calibration curve fits well into sigmoid function. The results obtained are similar to those reported earlier [23, 24], though the sensitivity of OTA detection was much higher. The low detection limit of 0.6 pg/ml was evaluated by extrapolation of the dependence to the level of 1.5 rad. corresponding to a tripled noise level. The latest upgrade of PI OPW sensor in combination with aptamer bio-receptors is clearly more sensitive as previous versions and thus capable of detection of much smaller concentrations of aflatoxins (aflatoxin B1 and ochratoxin A) in sub-ppt range. An additional advantage of using aptamers was a simple procedure of sensor recovery. The OPW sensor chips with immobilized aptamers can be restored to its initial state after performing a heating/cooling cycle in PCR unit (which unravels aptamers and releases the toxin) followed by washing out the toxins in PBB buffer containing $MgCl_2$. The recovered OPW chips could be used again straight after this treatment; such attempts were carried out with the re-used OPW chips and showed similar responses. Alternatively the OPW chips immersed in PBB could be stored in a fridge at 4 C^o for few weeks.

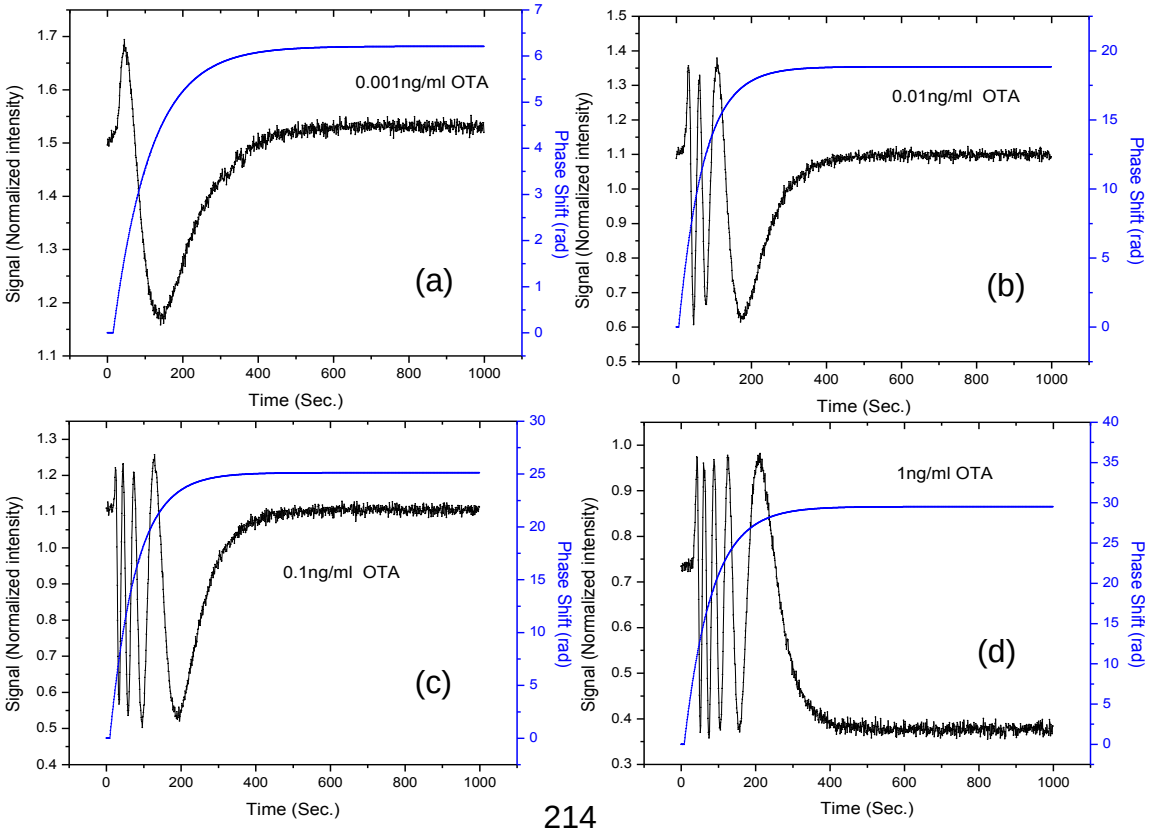
0.001ng/ml OTA
(a)
0.01ng/ml OTA
(b)
0.1ng/ml OTA
(c)
1ng/ml OTA
(d)
Signal (Normalized intensity)
Phase Shift (rad)
Time (Sec.)

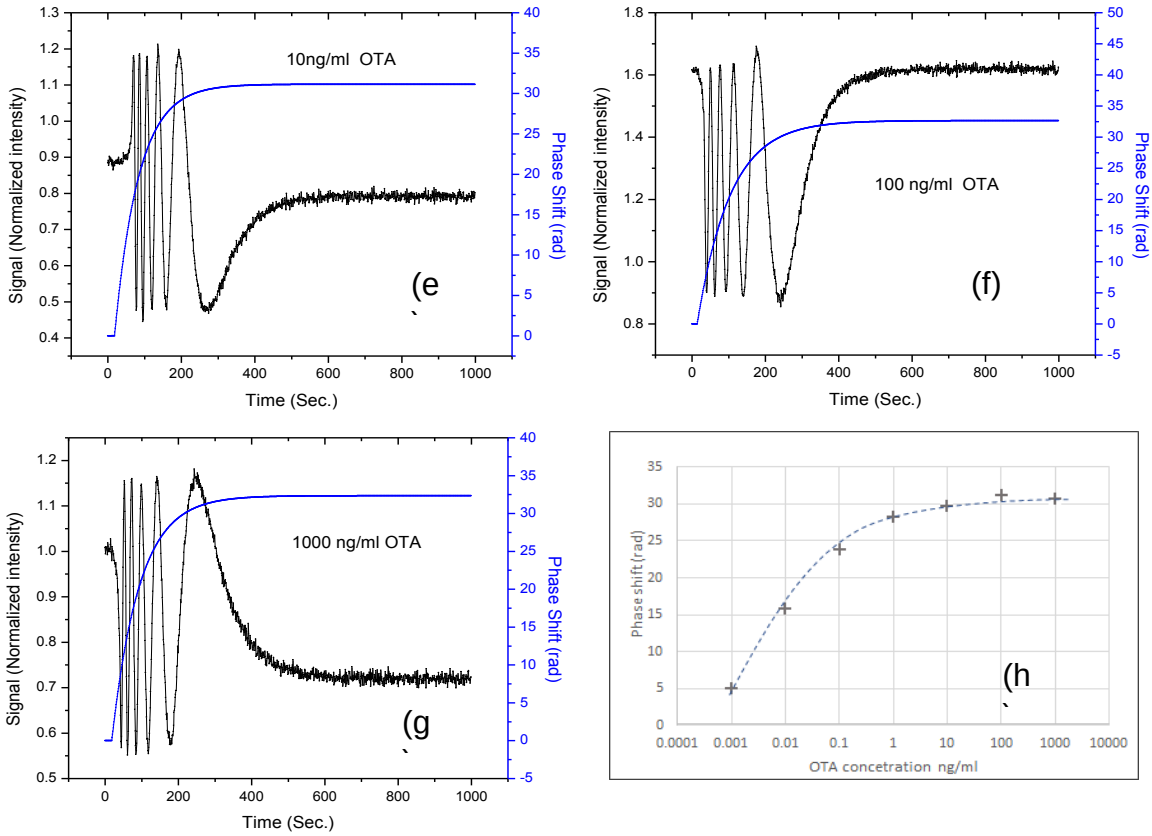

Figure 6.15 Output signals (black curves) and corresponding phase shifts (blue curves) for different concentrations of ochratoxin: 0.001 ng/ml (a), 0.01 ng/ml (b), 0.1 ng/ml (c), 1 ng/ml (d), 10 ng/ml (e), 100 ng/ml (f), and 1000 ng/ml (g); summarised individual phase shifts (h).

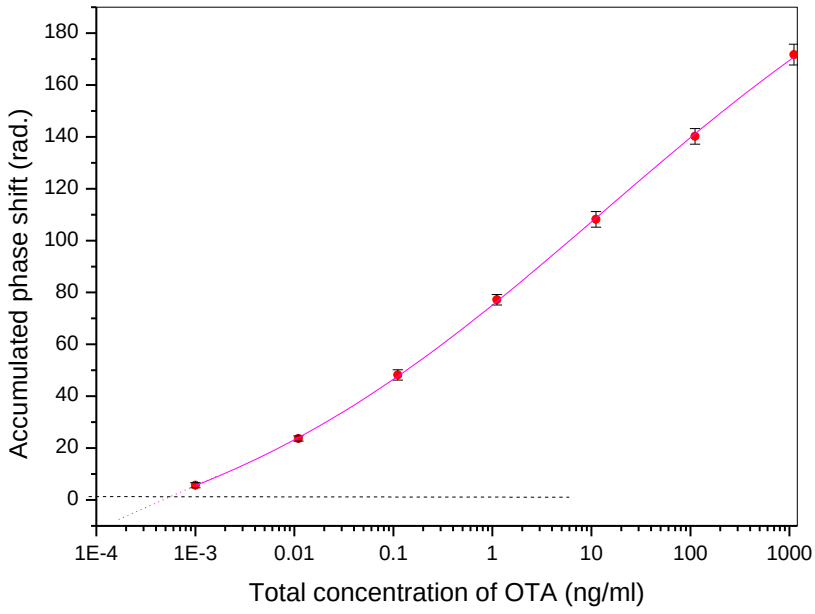

Figure 6.16. The accumulated sensor responses against the total concentration of OTA.

The repeating of a thermo-cycle is advisable before the use. The selectivity of the sensor system has been examined by inject different mycotoxin, the system did not show any response can be considered as a signal Fig. 6.17, which means the sensor can discriminate and select its targets which is designed for them.

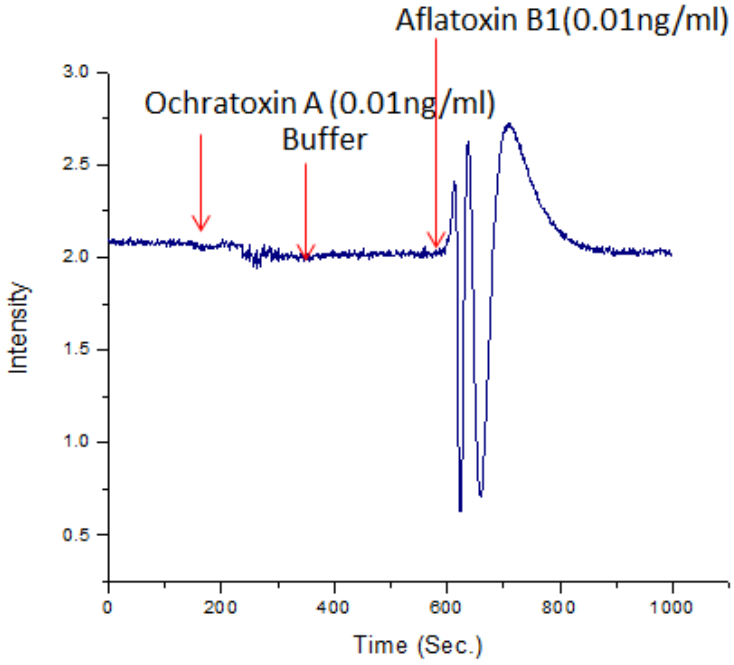

Figure 6.16 Selectivity test signal

Table 6.1 bio tests parameters

Mycotoxin concentration (ng/ml)	Aflatoxin		Ochratoxin		Zearalenone
	Antibody receptor response (rad)	Aptamer receptor response (rad)	Antibody receptor response (rad)	Aptamer receptor response (rad)	Antibody receptor response (rad)
0.001	–	6.0	–	5.0	–
0.01	9.42	12.5	9.4	16	11.9
0.1	18.8	18.8	13.8	24	20.4
1.0	20.4	22.9	20.4	28	23.8
10.0	25.1	23.6	20.7	30	24.5
100.0	27.0	24.8	26.7	32	23.3
1000.0	23.4	22.7	24.2	31	22.6

6.5 Conclusions

The biosensing tests performed using OPW PI set-up were successful. The 1st set-up version provided the proof of concept of detection of molecular adsorption. The 2th much improved version of the set-up allowed the detection of three types of mycotoxins (AFT B1, OTA, and ZEN) in concentrations down to 0.01 ng/ml in direct immunoassay with specific antibodies which was similar to the results obtained previously with TIRE methods [15]. There was an obvious possibility of further improvement of the sensitivity, which was eventually achieved with the final

(3rd) version of the set-up an automated signal processing. The detection of AFT B1 and OTA in concentration down to 1pg/ml or (ppt) was achieved in the direct assay with aptamers. The LDL of 0.7ppt use estimated which is much lower than if repented in any biosensors, and it is comparable with high -tech methods of HPLC and mass-spectroscopy.

6.6 References

1. Guisan, J. M. (Ed.). (2006). Immobilization of enzymes and cells (Vol. 22). Springer Science & Business Media.
2. Johnsson, B., Löfås, S., & Lindquist, G. (1991). Immobilization of proteins to a carboxymethyldextran-modified gold surface for biospecific interaction analysis in surface plasmon resonance sensors. Analytical biochemistry, 198(2), 268-277.
3. Peluso, P., Wilson, D. S., Do, D., Tran, H., Venkatasubbaiah, M., Quincy, D., ... & Witte, K. (2003). Optimizing antibody immobilization strategies for the construction of protein microarrays. Analytical biochemistry, 312(2), 113-124.

4. Hodneland, C. D., Lee, Y. S., Min, D. H., & Mrksich, M. (2002). Selective immobilization of proteins to self-assembled monolayers presenting active site-directed capture ligands. Proceedings of the National Academy of Sciences, 99(8), 5048-5052.
5. Dubas, S. T., Kumlangdudsana, P., & Potiyaraj, P. (2006). Layer-by-layer deposition of antimicrobial silver nanoparticles on textile fibers. Colloids and Surfaces A: Physicochemical and Engineering Aspects, 289(1-3), 105-109.
6. Kotov, N. A., Dekany, I., & Fendler, J. H. (1995). Layer-by-layer self-assembly of polyelectrolyte-semiconductor nanoparticle composite films. The Journal of Physical Chemistry, 99(35), 13065-13069.
7. Lvov, Y., Ariga, K., Onda, M., Ichinose, I., & Kunitake, T. (1997). Alternate assembly of ordered multilayers of SiO2 and other nanoparticles and polyions. Langmuir, 13(23), 6195-6203.
8. Lvov, Y., Decher, G., & Moehwald, H. (1993). Assembly, structural characterization, and thermal behavior of layer-by-layer deposited ultrathin films of poly (vinyl sulfate) and poly (allylamine). *Langmuir*, *9*(2), 481-486.
9. Mendelsohn, J., & Baselga, J. (2000). The EGF receptor family as targets for cancer therapy. *Oncogene*, *19*(56), 6550.
10. Lvov, Y., Ariga, K., Ichinose, I., & Kunitake, T. (1995). Assembly of multicomponent protein films by means of electrostatic layer-by-layer adsorption. *Journal of the American Chemical Society*, *117*(22), 6117-6123.
11. An, Q., Zhou, Y., Zhang, Y., Zhang, Y., & Shi, F. (2014). A facile method for the fabrication of covalently linked PAH/PSS layer-by-layer films. *RSC Advances*, *4*(11), 5683-5688.
12. Kim, D., Karns, K., Tia, S. Q., He, M., & Herr, A. E. (2012). Electrostatic protein immobilization using charged polyacrylamide gels and cationic detergent microfluidic western blotting. Analytical chemistry, 84(5), 2533-2540.
13. Jang, H., Kim, S., Cho, J., & Char, K. (2003). Spin-coated ultrathin multilayers and their micropatterning using microfluidic channels.
14. Michel, M., Toniazzo, V., Ruch, D., & Ball, V. (2012). Deposition mechanisms in layer-by-layer or step-by-step deposition methods: From elastic and impermeable films to soft membranes with ion exchange properties. ISRN Materials Science, 2012.
15. Al-Rubaye, A., Nabok, A., Abu-Ali, H., Szekacs, A., & Takacs, E. (2017, December). LSPR/TIRE bio-sensing platform for detection of low molecular weight toxins. In *2017 IEEE SENSORS* (pp. 1-3). IEEE.
16. Mustafa, M. K., Nabok, A., Parkinson, D., Tothill, I. E., Salam, F., & Tsargorodskaya, A. (2010). Detection of β-amyloid peptide (1–16) and amyloid precursor protein (APP770) using spectroscopic ellipsometry and QCM techniques: A step forward towards Alzheimers disease diagnostics. Biosensors and Bioelectronics, 26(4), 1332-1336.
17. Nabok, A., Al-Rubaye, A. G., Al-Jawdah, A. M., Tsargorodska, A., Marty, J. L., Catanante, G., ... & Takacs, E. (2019). Novel optical biosensing

technologies for detection of mycotoxins. Optics & Laser Technology, 109, 212-221.
18. Blind, M., & Blank, M. (2015). Aptamer selection technology and recent advances. Molecular Therapy-Nucleic Acids, 4, e223.
19. Barton, J. L., Bunka, D. H., Knowling, S. E., Lefevre, P., Warren, A. J., Bonifer, C., & Stockley, P. G. (2009). Characterization of RNA aptamers that disrupt the RUNX1–CBFβ/DNA complex. Nucleic acids research, 37(20), 6818-6830.
20. Platt, M., Rowe, W., Knowles, J., Day, P. J., & Kell, D. B. (2008). Analysis of aptamer sequence activity relationships. Integrative Biology, 1(1), 116-122.
21. Al-Rubaye, A. G., Nabok, A., & Tsargorodska, A. (2017). Spectroscopic ellipsometry study of gold nanostructures for LSPR bio-sensing applications. Sensing and Bio-Sensing Research, 12, 30-35.
22. A. Al-Jawdah, A. Nabok, A. Al-Rubaye, A. Holloway, A. Tsargorodska, E. Takacs, A. Szekacs, Mycotoxin biosensor based on optical planar waveguide, Toxins, 10(7), 2018, 272.
23. A. Nabok, A.M. Al-Jawdah, A.Tsargorodska, Development of planar waveguide-based immunosensor for detection of low molecular weight molecules such as mycotoxins, Sensors & Actuators - B Chemical, 247 (2017), 975–980
24. Al Rubaye, A., Nabok, A., Catanante, G., Marty, J. L., Takacs, E., & Szekacs, A. (2018). Detection of ochratoxin A in aptamer assay using total internal reflection ellipsometry. Sensors and Actuators B: Chemical, 263, 248-251.

Chapter 7: Conclusions and future work

7.1 Conclusions

The main aim of this project, e.g. the development of novel highly sensitive optical planar waveguide biosensor for detection of low molecular weight analytes such as mycotoxins, was achieved. The developed biosensor is based on the optical planar waveguide operating as polarization interferometer capable of detection of mycotoxins in very low concentrations below the ppt level in direct assay with either specific antibodies or aptamers.

A comprehensive literature review was carried out on existing optical bio-sensing technologies as well as on theoretical background of light propagation through the waveguide. The latter review provided useful guidance for modelling and designing of our planar waveguide- based biosensor.

The major part of work was in the design and development of the experimental set-up; this work lasted more than two years and went through several stages.

The waveguide with the structure of $SiO_2/Si_3N_4/SiO_2$ was fabricated on Si wafers using standard microelectronics technologies; the SiO_2 cladding layer was about 2-3 μm thick and its the refractive index was of 1.46, while the core Si_3N_4 layer has the refractive index of 2.02 and the thickness of around 200 nm. With such parameters, the waveguide provided a single mode propagation for red light of 630-650 nm in wavelength. Due to a large number of reflections (estimated as 500 per mm) the waveguide can provide high refractive index sensitivity estimated as 1550 rad/RIU/mm.

The light was coupled into the waveguide via slant edge cut at 47^o angle corresponding to the main angle of light propagation; this provided a simple and

cost-effective light coupling solution which deliver the sufficient amount of light. Another important design feature was shaping the core layer in a narrow (1mm) strip which provided high quality of the output signal. The light source could be either semiconductor laser diode (630-650 nm) or HeNe (633 nm) laser. The latter provided better stability of light intensity, though the former one is more suitable for miniaturized experimental set-up which is currently under development. Quarter-wavelength plate was used to make the light circularly polarised. The light coming out of the waveguide after passing a polarizer was collected by CCD array interfaced to PC. The polarizer role was to visualise the variations of the polarization of light by converting it to the variations of the light amplitude. The multi-periodic output signal caused by the phase shift between p- and s- components of polarized light has to be processed in order to obtain the values of the phase shift which actually constitutes the sensor response. This has been done ex-situ using Origin 8.0 software. The sensing window etched in the top SiO_2 layer was used for detection of biochemical reactions. For that purpose a reaction cell of about 0.1 ml in volume was hermetically sealed against the sensing window. the cell was equipped with in-let and out-let tubes connected to a syringe micro-pump which provided a stable flow of liquid through the cell. The developed OPW PI experimental set-up was tested by recording the signals during injection of solutions of NaCl of different concentrations into the cell. The refractive index sensitivity (RIS) was found to be of 9683.5 ± 153.9 rad/RIU for a 6 mm long sensing window which is about 1600 rad/RIU/mm corresponding well to theoretical estimation. To our knowledge, the obtained RIS was the highest reported for optical biosensors.

In parallel to the OPW PI sensor development, the work was carried out on the optimization of the immobilization protocol of bio-receptors on the Si_3N_4 surface the

waveguide sensing window. Two types of specific bio-receptors for mycotoxins were used, e.g. antibodies and aptamers.

Immobilization of antibodies was achieved by electrostatic binding via the layers of polycation (PAH) and protein A (or G). Immobilization of aptamers terminated with SH groups was achieved on aminated Si_3N_4 surface using SMCC binding layer. A series of biosensing tests of detection mycotoxins, i.e. aflatoxin B1, ochratoxin A, and zearalenone, were carried out in direct assay with either antibodies or aptamers immobilized on the planar waveguides. All three above mentioned mycotoxins were detected using their corresponding specific antibodies; the minimal detected concentrations were of 0.01 ng/ml (or 10 ppt). The sensitivity could be at least an order of magnitude higher but was restricted by poor quality of output signals in earlier versions of the experimental set-up.

Aftaloxin B1 and ochratoxin A were both detected in direct assay with their corresponding specific aptamers using the latest (improved) version of the experimental set-up. The results were very impressive: the minimal detected concentration of the above mycotoxins was 1 pg/ml (or 1 ppt), with the LDL of about 0.6 -0.7 pg/ml. The obtained LDL are the lowest among known optical bio-sensing technologies and comparable with the sensitivities of advanced analytical methods of HPLC and mass-spectroscopy. The results are particularly remarkable considering the label-free and detection in the most cost-effective direct assay format. The developed novel bio-sensor is particularly suitable for detection of low molecular weight analytes, for example toxins. Detection of large molecules is also possible, as well as the use of other bio-sensing formats, such as sandwich or competitive assay which may increase the sensitivity and selectivity even further.

The developed biosensor could be considered as a platform biosensing technology for a wide range of applications, such as environmental control, agriculture and food industry, bio-medical. The application could be altered by selecting suitable bio-receptors, e.g. antibodies, or aptamers. The use of aptamers is particularly attractive because of their low-cost, simple and flexible synthesis, thermal and environmental stability, a simple recovery procedure.

7.2 Future Work

Although considerable time and efforts were put in this work to achieve the main aim, there is still plenty of work ahead. The nearest task is to develop a portable sensor prototype capable of point-of-need detection of target analytes (mycotoxins) in low concentrations in real samples of water and food.

Such task, which is currently underway, requires scaling down the optical system using miniature optical components, e.g. laser diode, lenses, quarter wavelength plate, polarizer, and CCD array without housing. The waveguide chips containing three channels in the core have to be produced using industrial microelectronics technology including photolithography. The electronics for signal acquisition and processing should be placed on one portable PCB and interfaced to PC via NI card. LabView software has to be developed for data acquisition which includes the simultaneous recording of signals in all three channels and in-situ signal processing to evaluate the phase shift. The detection of mycotoxins in real samples of water and food is planned with this portable device.

Because of the use of three sensing channels, simultaneous detection of several analytes could be explored as well. An option of remote sensing wirelessly connected to the data processing centre could also be interesting to explore.

Further development which depends on the funding available may target commercial development of OPW PI sensors for different applications, such as detection of other toxins, for example phenols, petrochemicals, pesticides for environmental and agriculture applications, or hormones and bio-medical markers for different disease for biomedical applications.

There are also, some interesting the fundamental science aspects could be studied in more detail. These may include the use of metal nano-structures possessing LSPR phenomenon in combination with planar waveguide. Other materials, instead of silicon oxide and silicon nitride, can be explored for wave-guiding. A combination of planar waveguide with LPG could be interesting to explore.

The current work may lead to several projects of both fundamental research and R&D types which can be carried out in a small scale (through UG, MSc and PhD projects) as well as large scale research projects funded by UK Research Councils (EPSRC, BBSRC), European Commission (H2020 and beyond), NATO, etc.